

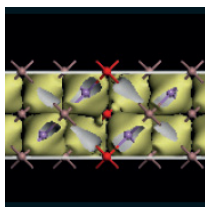
# INTERNATIONAL WORKSHOP ON COMPUTATIONAL NANOTECHNOLOGY

**5–9 June 2017**

**Low Wood Hotel, Windermere, UK**

Organised by the IOP Nanoscale Physics and Technology Group

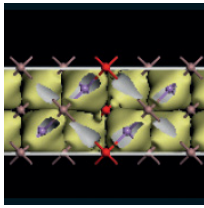
<http://iwcn2017.iopconfs.org/>



# International Workshop on Computational Nanotechnology

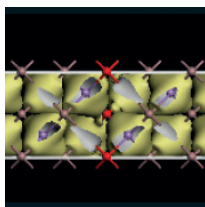
## Contents

Welcome .....	2
Programme .....	3-12
Oral .....	3-9
Posters .....	10-12
Abstracts	
Oral .....	13-113
Posters .....	114-174



## International Workshop on Computational Nanotechnology

**Welcome** to the English Lake District – long-time inspiration for poets, artists and other creatives, but now for us engineers and scientists attending the International Workshop on Computational Nanotechnology (IWCN). IWCN continues a 27 year history of workshops focused around the development and application of simulation tools for investigating and designing electronic and photonic semiconductor devices. This period has seen aggressive scaling of transistor dimensions in microprocessor and memory chips; it has seen both “the end of silicon” and “the end of Moore’s Law” predicted and then disproved, time and time again; it has seen the emergence of nanotechnology as a global research & development phenomenon, and the emergence of new materials which have captured the imagination of experts and laypeople alike. This workshop series, under its previous name “International Workshop on Computational Electronics” has mirrored both the industry trajectory and the ongoing emergence of new research ideas in this field. A key part of the original vision of the workshop was to bring together simulation developers and users from a range of disciplines in order to integrate ideas on techniques, algorithms and applications. The new conference title, International Workshop on Computational Nanotechnology, reflects not only the fact that present-day electronics is fundamentally dependent on nanoscience and nanoscale manufacturing, but also the convergence of physics, electronics, chemistry, biology and materials science which now underpins much of the innovation in both research and product development. IWCN2017 is, of course, just one small snapshot of a vast field of global activity. Its success depends not only on the papers invited and contributed, but on you all as enthusiastic participants, questioners, debaters and advocates for this field. We hope that you enjoy this IWCN, that you make many new friends here, and that you are inspired in your own research, by both the conference activity and the Lakeland setting.



# International Workshop on Computational Nanotechnology

## Programme

### Tuesday 6 June

**09:00** Welcome/Introduction to the Workshop

*Ullswater room - lecture theatre*

#### Session: Carbon Nanostructures

**Session chair:** Wolfgang Porod, University of Notre Dame, USA

**09:15** (Invited) From carbon nanostructures to 2D semiconductors beyond graphene

David Tománek, Michigan State University, USA

**09:45** Effect of disorder on the band gap of a graphene ribbon with an antidot lattice

Massimo Macucci, Università di Pisa, Italy

**10:00** Simulation of contact resistance in patterned graphene

Enrique Marin, Università di Pisa, Italy

**10:15** Transport properties and applications of disoriented graphene systems: twisted bilayers and grain boundaries

Philippe Dollfus, CNRS / C2N, France

**10:30** A hierarchical model for CNT and Cu-CNT composite interconnects: from density functional theory to circuit-level simulations

Jaehyun Lee, University of Glasgow, UK

**10:45** Refreshments and exhibition

*Gallery Lounge*

#### Session: Organic Semiconductor Devices/Soft Matter

**Session chair:** Sarah Harris

**11:15** (Invited) Charge and exciton dynamics in molecular aggregates: simple models from complicated ones

Alessandro Troisi, University of Liverpool, UK

**11:45** (Invited) Using nanopores to sequence DNA: what can we learn from molecular dynamics

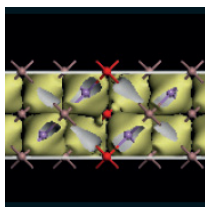
Syma Khalid, University of Southampton, UK

**12:15** Model parameter estimation and adaptive numerical simulation for organic thin-film transistors

Pasquale Africa, Politecnico di Milano, Italy

**12:30** A numerical study of fermi kinetics transport

Nicholas Miller, Michigan State University, USA



# International Workshop on Computational Nanotechnology

**13:00 Lunch and exhibition**

*Gallery Lounge*

**Session: Organic Semiconductor Devices/Soft Matter**

**Session chair:** Massimo Macucci, University of Pisa, Italy

**14:30 (Invited) Towards the understanding of the mechanism of ions permeation through graphene-based membranes**

Paola Carbone, The University of Manchester, UK

**15:00 Simulation of tunneling based biosensor considering ion transport and electron tunneling**

Kyoung Yeon Kim, Seoul National University, South Korea

**15:15 Theoretical study on the rectification mechanisms of molecular pn diodes**

Tatsuhiko Ohto, Osaka University, Japan

**15:30 Time-resolved carrier transfer at molecular junction interface**

Katawoura Beltako, Aix-Marseille University, France

**16:00 Refreshments and exhibition**

*Gallery Lounge*

**Session: NanoHub**

**16:30 NanoHub - Always “on” enabling global scientific knowledge transfer**

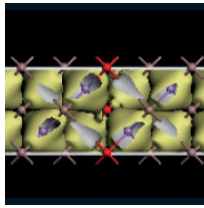
Gerhard Klimeck, Purdue University, USA

**17:30 Workshop poster session**

*Gallery Lounge*

**18:30 Exhibition BBQ**

*Restaurant lawns*



# International Workshop on Computational Nanotechnology

Wednesday 7 June

## Session: Quantum Transport

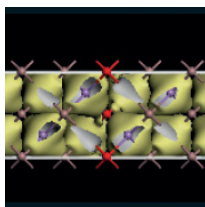
**Session chair:** Marc Bescond, CNRS, France

- 09:00 **(Invited) First principles calculations of electron transport in gated 2D nano-structures**  
Mads Brandbyge, Technical University of Denmark, Denmark
- 09:30 **Electron-phonon scattering from green's function transport combined with molecular dynamics: Applications to mobility predictions.**  
Daniele Stradi, QuantumWise A/S, Denmark
- 09:45 **Efficient quantum approach of electron-phonon scattering for nanoscale device simulations**  
Youseung Lee, Aix-Marseille University, France
- 10:00 **Transport through Si QDs in coulomb blockade regime: Theory and experiment**  
Aleksey Andreev, Hitachi Cambridge Laboratory, UK
- 10:15 **The role of the displacement current in quantifying the speed of ballistic nano devices: beyond the quasi-static approximation**  
Zhen Zhan, Universitat Autònoma de Barcelona, Spain
- 10:30 **Multiscale modeling of electrodynamic radiation from quantum monopole antenna**  
Timothy Philip, University of Illinois at Urbana-Champaign, USA
- 10:45 **Refreshments and exhibition**  
*Gallery Lounge*

## Session: Quantum Transport

**Session chair:** Philippe Dollfus, CNRS, France

- 11:00 **Non-local scattering with a new recursive nonequilibrium green's function method**  
James Charles, Purdue University, USA
- 11:15 **Plasmonic response of graphene nanoribbons**  
Irena Knezevic, University of Wisconsin-Madison, USA
- 11:30 **Nonequilibrium Green's function method: Performance prediction of band-to-band tunneling devices in electron-only representation**  
Prasad Sarangapani, Purdue University, USA
- 11:45 **Dissipative NEGF methodology to treat short range Coulomb interaction: Current through a 1D nanostructure**  
Antonio Martinez, Swansea University, UK
- 12:00 **Equivalent model representation in first-principle transport simulations of nanowire MOSFETs**  
Nobuya Mori, Osaka University, Japan



# International Workshop on Computational Nanotechnology

12:15 **First-principles based simulations of Si ultra-thin-body FETs with SiO<sub>2</sub> gate dielectric**  
Hyo-Eun Jung, Korea Advanced Institute of Science and Technology, South Korea

12:30 **Lunch and Muncaster Castle excursion**

## Thursday 8 June

### Session: 2D Semiconductors

**Session chair:** Michael Strosio, The University of Illinois at Chicago, USA

09:00 **(Invited) Transistors based on heterostructures of 2D materials**  
Giuseppe Iannaccone, Università di Pisa, Italy

09:30 **Monte Carlo study of high field transport in some transition metal di-chalcogenides**  
David Ferry, Arizona State University, USA

09:45 **Stark effect in the photoluminescence of transition metal dichalcogenide structures**  
James Charles, Purdue University, USA

10:00 **Theoretical study of charge transport in mono- and bi-layer phosphorene using full-band Monte Carlo simulations**  
Gautam Gaddemane, University of Texas at Dallas, USA

10:15 **Effects of uniaxial strain on phosphorene tunneling field-effect transistors**  
Junbeom Seo, Korea Advanced Institute of Science and Technology, South Korea

10:30 **Understanding resistive switching mechanism of interfacial phase change memory by topological super-lattice and topological phase of interface states**  
Hisao Nakamura, National Institute of Advanced Industrial Science and Technology (AIST), Japan

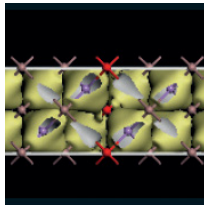
10:45 **Refreshments and exhibition**  
*Gallery Lounge*

### Session: Photonics/optoelectronics/plasmonics

**Session chair:** David Ferry, Arizona State University, USA

11:15 **(Invited) Multiscale modelling of the impact of intrinsic disorder and localisation effects on the optical and electronic properties of III-N LEDs**  
Eoin O'Reilly, Tyndall Institute, Ireland

11:45 **Unified numerical solver for modeling metastability and reliability of CdTe solar cells**  
Dragica Vasileska, Arizona State University, USA



# International Workshop on Computational Nanotechnology

12:00 **Systematic study of quantum dot laser emission controlled by coherent phonon wave packets**  
Daniel Wigger, Universität Münster, Germany

12:15 **Density matrix model for bound to continuum terahertz quantum cascade lasers**  
Aleksandar Demić, University of Leeds, UK

12:30 **Simulation of a midinfrared quantum cascade laser using a density-matrix formalism**  
Irena Knezevic, University of Wisconsin-Madison, USA

12:45 **Lunch**  
*Gallery Lounge*

## Session: Device Simulations

**Session chair:** William Vandenberghe, University of Texas at Dallas, USA

14:30 **(Invited) Transport modeling for plasma waves in THz devices**  
Christoph Jungemann, RWTH Aachen University, Germany

15:00 **Metal grain work-function variability in GAA Si nanowire via a fluctuation sensitivity map**  
Natalia Seoane-Iglesias, Universidade de Santiago de Compostela, Spain

15:15 **Variability-aware simulations of 5 nm vertically stacked lateral Si nanowires transistors**  
Talib Al-Ameri, University of Glasgow, UK

15:30 **Simulation of negative differential transconductance from devices fabricated using conventional CMOS technology**  
Pratik B Vyas, University of Texas at Dallas, USA

15:45 **Physically based diagonal treatment of polar optical phonons in III-V p-type double-gate transistors: comparison of InAs vs Ge and Si**  
Manel Moussavou, Aix Marseille Universite, France

16:00 **Refreshments**  
*Gallery Lounge*

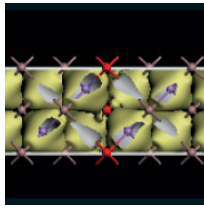
## Session: Device Simulations

**Session chair:** William Vandenberghe, University of Texas at Dallas, USA

16:30 **3D Monte Carlo simulations of strained Si GAA nanowire FETs with different channel orientations**  
Karol Kalna, Swansea University, UK

16:45 **Spin-dependent trap-assisted tunneling in magnetic tunnel junctions: A Monte Carlo study**  
Josef Weinbub, TU Wien, Austria

17:00 **Full band Monte Carlo simulation of high- field transport in Si nanowires**  
Stephen Goodnick, Arizona State Univesity, USA



# International Workshop on Computational Nanotechnology

18:15 **Private charter on Miss Lakeland followed by Conference dinner**

**Friday 9 June**

## Session: Phonon Properties and Thermal Transport

**Session chair:** Dragica Vasileska, Arizona State University, USA

09:00 **(Invited) Anderson-like localization of phonons in nano-structures**  
Yann Chalopin, Ecole CentraleSupélec, France

09:30 **Thermionic cooling devices based on AlGaAs/GaAs heterostructures**  
Marc Bescond, CNRS IM2NP, France

09:45 **DFT/NEGF study of discrete dopants in Si/GaAs 3D FETs including phonon scattering and self-heating**  
Antonio Martinez, Swansea University, UK

10:00 **Numerical techniques for the reduction of thermal conductivity measurements at nanoscale**  
Giovanni Pennelli, University of Pisa, Italy

10:15 **Thermal transport in III-V semiconductor materials and superlattices based on molecular dynamics with optimized Tersoff potentials**  
Irena Knezevic, University of Wisconsin-Madison, USA

10:30 **Electron momentum relaxation rates via Frohlich interaction with polar-optical-phonons in bulk wurtzite gallium nitride**  
Michael Strosio, , University of Illinois at Urbana-Champaign, USA

10:45 **Refreshments and exhibition**  
*Gallery Lounge*

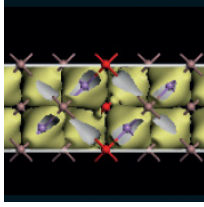
## Session: Electronic Structure/First Principles Calculations

**Session chair:** Gerhard Klimeck, Purdue University, USA

11:15 **(Invited) Structural diversity of silicene'**  
Tetsuya Morishita, National Institute of Advanced Industrial Science and Technology (AIST), Japan

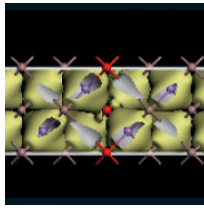
11:45 **General atomistic approach for modeling metal-semiconductor interfaces and surfaces**  
Umberto Martinez, QuantumWise, Denmark

12:00 **Non-equilibrium Green's function method: Band tail formation in non-local polar optical phonon scattering**  
Prasad Sarangapani, Purdue University, USA



## International Workshop on Computational Nanotechnology

- 12:15 **Electronic structure calculation of SiGeSn-C alloys – prospective direct gap materials**  
Zoran Ikonić, University of Leeds, UK
- 12:30 **Image charge models for accurate construction of the electrostatic self-energy of 3D layered nanostructure devices**  
John Barker, University of Glasgow, UK
- 12:45 **Lunch and Close**



# International Workshop on Computational Nanotechnology

## Posters

### **P:01 Using vacancy transport to unify memristor models**

Isaac Abraham, University of Washington, USA

### **P:02 Position dependent performance in 5 nm vertically stacked lateral Si nanowires transistors**

Talib Al-Ameri, University of Glasgow, UK

### **P:03 The impact of interface traps and self-heating in the degradation of the 4H-SiC VDMOSFET performance**

Brendan Ubochi, Swansea University, UK

### **P:04 TCAD analysis of discrete dopant effect on variability of tunnel field effect transistor**

Hidehiro Asai, National Institute of Advanced Industrial Science and Technology, Japan

### **P:05 Characterization of topological phase transitions in silicene and other 2D gapped Dirac materials**

Juan Carlos Bolívar Fernández, Instituto Carlos I de Física Teórica y Computacional, Spain

### **P:06 Study of ballistic transport in phosphorene-nanoribbon- FETs using empirical pseudopotentials**

William Vandenberghe, The University of Texas at Dallas, USA

### **P:07 Power dissipation and noise in spin-wave-based computing systems**

Wolfgang Porod, University of Notre Dame, USA

### **P:08 Quantization and analysis of acoustic modes in a rectangular microsound nanowaveguide fixed on a rigid substrate**

Michael Stroschio, University of Illinois at Chicago, USA

### **P:09 Effect of quantum confinement on lifetime of anharmonic decay of optical phonon in a confined GaAs structure**

Michael Stroschio, University of Illinois at Chicago, USA

### **P:10 Quantized acoustic-phonon modes in a non-piezoelectric nanowaveguide**

Michael Stroschio, University of Illinois at Chicago, USA

### **P:11 Quantized acoustic-phonon shear horizontal modes in a piezoelectric nanoresonator**

Michael Stroschio, University of Illinois at Chicago, USA

### **P:12 Exchange-coupled majority logic gate**

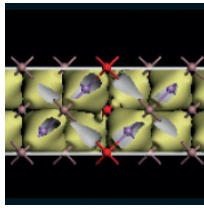
Wolfgang Porod, University of Notre Dame, USA

### **P:13 Multi-subband ensemble monte carlo simulator for 3D electron devices**

Luca Donetti, Universidad de Granada, Spain

### **P:14 Charge corrections from exact electrostatics for metal-oxide interfaces**

Thomas Durrant, University College London, UK



# International Workshop on Computational Nanotechnology

**P:15 Monte Carlo simulations of electron transport in bulk GaN**

Simon Forster, Swansea University, UK

**P:16 Scaling of Tunnel FETs**

Koichi Fukuda, National Institute of Advanced Industrial Science and Technology, Japan

**P:17 Monte Carlo analysis of impact ionization processes and band-to-band tunneling in In<sub>x</sub>Ga<sub>1-x</sub>As PIN ungated devices**

Beatriz García Vasallo, Universidad de Salamanca, Spain, Spain

**P:18 Multi-scale nonequilibrium green's function method for LEDs: Balance of thermalization and tunneling**

Gerhard Klimeck, Purdue University, USA

**P:19 Electron and hole mobility calculation in GeSn alloys**

Zoran Ikonić, University of Leeds, UK

**P:20 Transport modelling and design of GaN/AlN based unipolar (opto-)electronic devices, and interface quality effects**

Zoran Ikonić, University of Leeds, UK

**P:21 Investigation of hot-carrier effects using a backward Monte Carlo method and full bands**

Markus Kampl, TU Wien, Austria

**P:22 Lindblad-based Markov approach to spatiotemporal quantum dynamics of wave packets in nanostructures**

Frank Lengers, Universität Münster, Germany

**P:23 Impact of the gate and external insulator thickness on the static characteristics of ultra-scaled silicon nanowire FETs**

Demetrio Logoteta, Aix Marseille Université, France

**P:24 Towards a full self - consistently coupled drift diffusion and Monte Carlo simulator to model silicon heterojunction solar cells**

Dragica Vasileska, Arizona State University, USA

**P:25 Characterisation of a tunnel field-effect transistor using 2D TCAD simulations**

Daniel Nagy, University of Santiago de Compostela, Spain

**P:26 Impact of layer rotational misalignment on the transport properties of van der Waals tunnel field effect transistors**

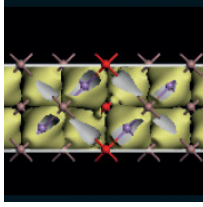
Marco Pala, Center for Nanoscience et Nanotechnology, France

**P:27 Do we really need the collapse law when modelling quantum transport in electron devices?**

Zhen Zhan, Universitat Autònoma de Barcelona, Spain

**P:28 Electric field modulation of phosphorene nanoribbons' electronic properties**

Irena Knezevic, University of Wisconsin-Madison, USA



# International Workshop on Computational Nanotechnology

**P:29 Hole Trapping in Amorphous HfO<sub>2</sub> and Al<sub>2</sub>O<sub>3</sub> as a source of positive charging**

Jack Strand, University College London, UK

**P:30 Electron transport in defective metallic and semiconducting carbon nanotubes: An improved RGF-based O(N) approach**

Fabian Teichert, TU Dresden, Germany

**P:31 A mobility model for TCAD simulation of current variation by random discrete dopant**

Ho In Yu, Seoul National University, South Korea

**P:32 Spin recovery in the 25 nm gate length InGaAs field effect transistor**

Ben Thorpe, Swansea University, UK

**P:33 Computing interfacial properties of polypyrrole on diamond nanoparticles for photovoltaic applications**

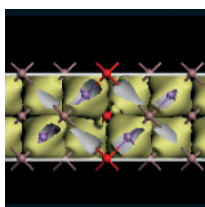
Petra Matunová, Institute of Physics of the Czech Academy of Sciences

**P:34 Wigner modelling of surface roughness in quantum wires**

Mihail Nedjalkov, TU Wien, Austria

**P:35 NEGF through finite-volume discretization**

Hans Kosina, TU Wien, Austria



# International Workshop on Computational Nanotechnology

## Session: Carbon Nanostructures

### (Invited) From carbon nanostructures to 2D semiconductors beyond graphene

D Tománek

Michigan State University, USA

If graphene had a band gap, it would probably be the optimum 2D system for electronics applications. While graphene research is still revealing intriguing properties of this unusual material, a new class of 2D semiconductors has been rapidly gaining attention, namely layered black phosphorus and related phosphorene monolayers [1]. These 2D systems display a tunable, direct fundamental band gap and thus are ideal candidates for optoelectronics applications. Recent Quantum Monte Carlo (QMC) calculations show that the inter-layer bonding, while weak, is not well described by dispersive van der Waals (vdW) interactions [2]. As seen in Fig. 1, QMC results differ qualitatively from vdW-enhanced DFT functionals and the common designation of similar systems as “van der Waals solids” is strictly incorrect. Also other group V systems including monolayers of  $\text{As}_x\text{P}_{1-x}$  [3], IV-VI compounds such as SiS [4] with the same average valence, and related 2D phosphorus carbide [5] share the same nonplanarity of their structure with phosphorene. These systems share another similarity with phosphorene, namely the dependence of the fundamental band gap on the number of layers and in-layer strain. A surprising twist on the story of group V semiconductors is the recent discovery of yet another phosphorus allotrope, namely a quasi-1D coil structure [6,7] that is the most stable phosphorus allotrope known to date. Predictive *ab initio* calculations provide here a useful guidance to experimental studies.

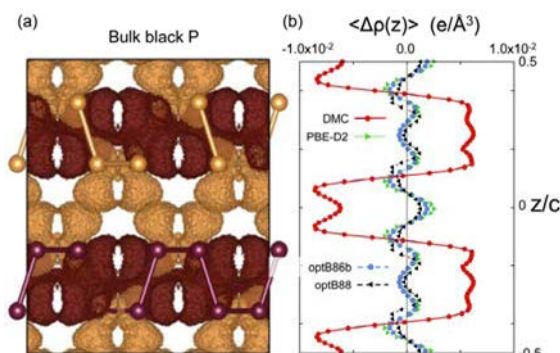
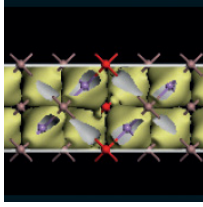


Figure 1. Calculated electron density difference  $\Delta\rho = \rho_{\text{tot}}(\text{bulk}) - \sum \rho_{\text{tot}}(\text{monolayers})$  representing the charge redistribution caused by assembling the bulk structure from isolated monolayers. (a) Diffusion Monte Carlo (DMC) isosurfaces bounding regions of excess electron density (dark brown) and electron deficiency (light brown), with respective values  $\pm 6.5 \times 10^{-3} \text{ e}/\text{\AA}^3$ . (b)  $\langle \Delta\rho(z) \rangle$  for DMC and selected DFT functionals averaged across the  $x$ - $y$  plane of the layers, with  $z/c$  indicating the relative position of the plane in the unit cell. (From Ref. [2]).

\* Partly supported by the NSF/AFOSR EFRI 2-DARE grant number #EFMA-1433459.

- [1] H. Liu *et al.* [ACS Nano 8, 4033 \(2014\)](#).
- [2] L. Shulenburger, A.D. Baczewski, Z. Zhu, J. Guan, and D. Tománek, [Nano Lett. 15, 8170 \(2015\)](#).
- [3] Zhen Zhu, Jie Guan, and David Tománek, [Nano Lett. 15, 6042 \(2015\)](#).
- [4] Zhen Zhu, Jie Guan, Dan Liu, and David Tománek, [ACS Nano 9, 8284 \(2015\)](#).
- [5] Jie Guan, Dan Liu, Zhen Zhu, and David Tománek, [Nano Lett. 16, 3247 \(2016\)](#).
- [6] Dan Liu, Jie Guan, Jingwei Jiang, and David Tománek, [Nano Lett. 16, 7865 \(2016\)](#).
- [7] Jinying Zhang *et al.* [Angew. Chem. Int. Ed. 56, 1850 \(2017\)](#).

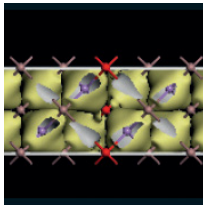


## Effect of disorder on the band gap of a graphene ribbon with an antidot lattice

P Marconcini and M Macucci

Università di Pisa, Italy

The absence of an energy gap represents the main obstacle to the application of graphene for the fabrication of digital electronic devices. The introduction of a regular lattice of holes (antidots) in addition to lateral confinement is among the methods that have been proposed to introduce an energy gap in graphene. We have studied the dependence of the energy gap of a graphene ribbon with an antidot lattice on geometrical parameters [1], adopting a numerical approach based on the solution of the envelope-function (Dirac) equation, where a nonzero mass term is used to emulate the presence of the antidots. We have solved the transport problem with a scattering matrix approach and, from the resulting behavior of the conductance as a function of energy, we have obtained the transport gap, defined as the energy interval around zero where the conductance is lower than a given threshold. This simplified approach has been shown to give good results, as far as no extended zigzag edges exist at the boundaries of the antidots. We have found that, when the geometry of the structure is such that the presence of the antidots introduces a gap larger than that generated by lateral confinement, the dependence of this gap  $E_g$  is analogous to that previously observed for unconfined graphene [2], i.e.  $E_g \propto \sqrt{N_{rem}/N_{tot}}$ , where  $N_{rem}$  and  $N_{tot}$  are the number of carbon atoms that have been removed from the unit cell of the antidot lattice to create the antidot itself, and the number of the atoms that were originally present in the unit cell, respectively. Envelope-function calculations indicate that the transport gap is preserved also when the regularity of the antidot lattice is broken by the presence of disorder, for example in the position of the antidots. Here we report the results for a ribbon with a hexagonal lattice of antidots, each with a hexagonal shape and armchair edges (Fig. 1). In Figs. 2 and 3 we show that the transport gap is enlarged by the presence of the antidots, for a 10.224 nm long and  $\sim 6$  nm wide ribbon with 47 and 48 dimer lines across its width, and thus with a metallic and semiconducting behaviour, respectively. A random longitudinal and transverse shift of the antidots from their ideal position by a quantity uniformly distributed in the range  $[-0.25 \text{ nm}, 0.25 \text{ nm}]$  leaves the transport gap unchanged (Fig. 2). In order to verify whether an actual energy gap exists in the presence of disorder, we have performed a nearest-neighbor tight-binding calculation of the dispersion relations, considering only the  $2p_z$  orbital for each carbon atom, with a transfer integral equal to  $-2.7 \text{ eV}$  and disregarding edge-bond relaxation effects (in order to make this tight-binding calculation feasible, here we have considered much narrower nanoribbons with respect to Ref. [1]). Since the calculation has to be performed also for the disordered structure, we have considered a unit cell with the same length as the entire ribbon, assuming to replicate it periodically in the longitudinal direction. The results for the metallic and semiconducting ribbons without the antidots are shown in Fig. 4, while in Figs. 5 and 6 we compare (for the metallic and semiconducting ribbon, respectively) the dispersion relations obtained in the absence and in the presence of disorder. We observe that the presence of disorder strongly decreases the energy gap. We conclude that the transport gap observed for the disordered case in Figs. 2 and 3 is not always a true energy gap (i.e. an energy interval without any available state), but instead a region where strong (Anderson) localization [3] plays a major role: as a consequence of disorder in the antidot position, the states in the structure become localized and transport through the ribbon is quenched, with a corresponding suppression of the device conductance.



# International Workshop on Computational Nanotechnology

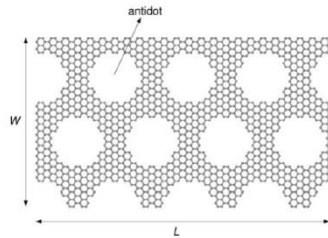


**Fig. 1.** Graphene ribbon with antidot lattice. The considered antidots have a hexagonal shape, with a 0.99 nm edge and a distance between the centers of neighboring antidots of 2.55 nm.

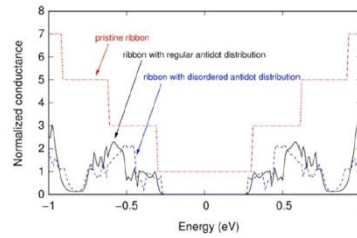


**Fig. 2.** Behavior of the conductance (normalized with respect to the conductance quantum) as a function of energy for the metallic ribbon, in its pristine form, with a regular antidot distribution, and with a disordered one.

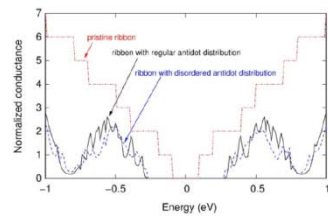


**Fig. 3.** Behavior of the normalized conductance as a function of energy for the semiconducting ribbon, in its pristine form, with a regular antidot distribution, and with a disordered one.

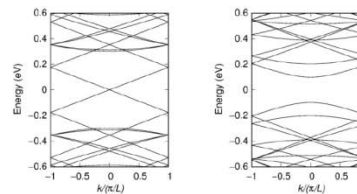


**Fig. 4.** Dispersion relations around zero energy for the metallic (left panel) and semiconducting (right panel) ribbon without antidots.

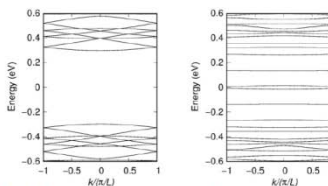


**Fig. 5.** Dispersion relations around zero energy for the metallic ribbon with a regular (left panel) and disordered (right panel) distribution of antidots.

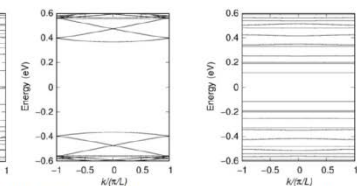
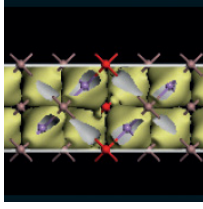


**Fig. 6.** Dispersion relations around zero energy for the semiconducting ribbon with a regular (left panel) and disordered (right panel) distribution of antidots.

- [1] P. Marconcini et al, IEEE Trans Nanotechnol (2016),DOI: 10.1109/TNANO.2016.2645663
- [2] T. G. Pedersen et al., Phys. Rev. Lett. 100, 136804 (2008)
- [3] P. W. Anderson, Phys. Rev. 109, 1492 (1958)



# International Workshop on Computational Nanotechnology

## Simulation of contact resistance in patterned graphene

E. G. Marin, T. Cusati, A. Fortunelli, G. Iannaccone, and G. Fiori

Università di Pisa, Italy

While trying to exploit graphene in Radio Frequency applications, the reduction of the contact resistance ( $R_c$ ) is probably one of the most challenging technological issues to be solved. Graphene patterning under the metal has been demonstrated to be a promising solution, leading to a reduction of  $R_c$  by up to a factor of 20 [1], probably due to an increased conductivity at the borders of the patterns of graphene [2]–[5]. This technology is still at the early stage and a complete understanding of the physical mechanisms at play is lacking. To this purpose we propose a multi-scale approach based on first-principle calculations, and the solution of the continuity equation to compute  $R_c$  in the considered patterned contacts.

The continuity equation in the graphene flake reads:

$$\nabla \cdot J_{2D}(y, z) = |J_{inj}(y, z)| \quad (1)$$

where  $J_{2D}$  is a in-plane current density (in A/m), and  $J_{inj}$  is the metal-to-graphene vertically injected current, (in A/m<sup>2</sup>). In particular,  $J_{2D} = \mu\rho\nabla\varphi + D\nabla\rho$ , where  $\mu, \rho, D$ , are the mobility, density, and diffusivity of carriers (either  $n$  or  $p$  depending on the metal exploited for the contact [6]) and  $\varphi$  is the electrostatic potential. Assuming quasi-equilibrium conditions and neglecting the diffusive term,  $J_{2D}$  reduces to  $J_{2D} \cong q\mu\rho\nabla\varphi$ . To model the vertical injected current from the overlapping metal, we assume an ohmic relationship i.e.,  $J_{inj} = G\varphi$  where  $G$  is a conductance per unit surface (in S/m<sup>2</sup>) estimated from atomistic simulations. As a consequence Eq. (1) eventually reads:

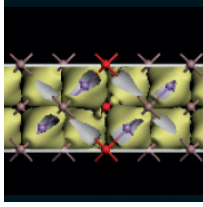
$$\nabla q\mu n n \nabla \varphi(y, z) = G\varphi(y, z) \quad (2)$$

Regarding the geometrical structure, we assume that the metal fills the graphene etched regions as in Fig. 1a. The metal-filled regions behave as equi-potential surfaces and can be modeled as Dirichlet conditions for the solution of the differential equation. For what concerns the graphene under the metal, we have considered two different sets of parameters ( $\rho, \mu, G$ ) depending if it is close to the edges of the pattern or far away. An estimation can be obtained from Density Functional Theory (DFT) calculations. Once  $\varphi$  is obtained, we can determine the component along the transport direction ( $y$ -direction) of the current density  $J_{2D, y} = q\mu n n \partial\varphi$  and  $R_c$  calculated (in  $\Omega$ ) as:

$$R_c = V_{m-g} / \int dz J_{2D, y}(y, z)|_{y=y_{max}} \quad (3)$$

where  $V_{m-g}$  is the metal-graphene bias and the integral accounts for the total current flowing at the contact end, i.e.,  $y=y_{max}$

In this work, inspired by recent experimental results [12], we have considered gold-graphene contacts with graphene patterned with square holes. Two hole sizes (with hole side  $l_h = 100$  nm and  $l_h = 200$  nm) and two different number of holes ( $n_h = 400$  and  $n_h = 160$ ) have been considered. The graphene region dimension has been set to  $12 \mu\text{m} \times 5 \mu\text{m}$ . We have performed DFT calculations using the Quantum Espresso package [7], with a gradient-corrected exchange correlation functional (Perdew-Burke-Ernzerhof (PBE)) [8], and ultrasoft pseudopotentials (US-PPs) [9] in scalar relativistic form. The simulated Au-graphene structure is depicted in Figure 1a. It consists of four continuous layers of Au and an interrupted layer of graphene. Dipole correction and the dispersion effects (Van der Waals corrections [10]) have been included in the simulations. The curve corresponding to the Dirac point energy on graphene in the interacting system has been extracted computing the difference of the local Fermi energies with respect to the vacuum levels and the local work function. The calculated  $\Delta E_f = E_d - E_f$  (where  $E_f$  is the Fermi level and  $E_d$  is the Dirac point) is:



# International Workshop on Computational Nanotechnology

0.32 eV and 0.25 eV, at the edges and the surface graphene respectively (Fig. 1b), resulting in electron concentrations of  $7.68 \times 10^{12} \text{ cm}^{-2}$  and  $4.75 \times 10^{12} \text{ cm}^{-2}$ . The electron mobility has been taken equal to  $3.5 \times 10^3 \text{ cm}^2/\text{Vs}$  as in [5]. The geometry of graphene and gold has been optimized keeping the upper two gold layers fixed and relaxing the position of the atoms. Au-graphene equilibrium distances are  $3.1 \text{ \AA}$  at the center and  $1.9$

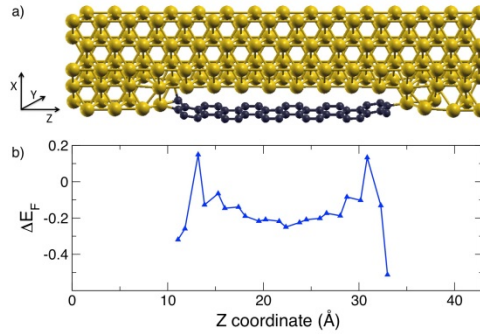
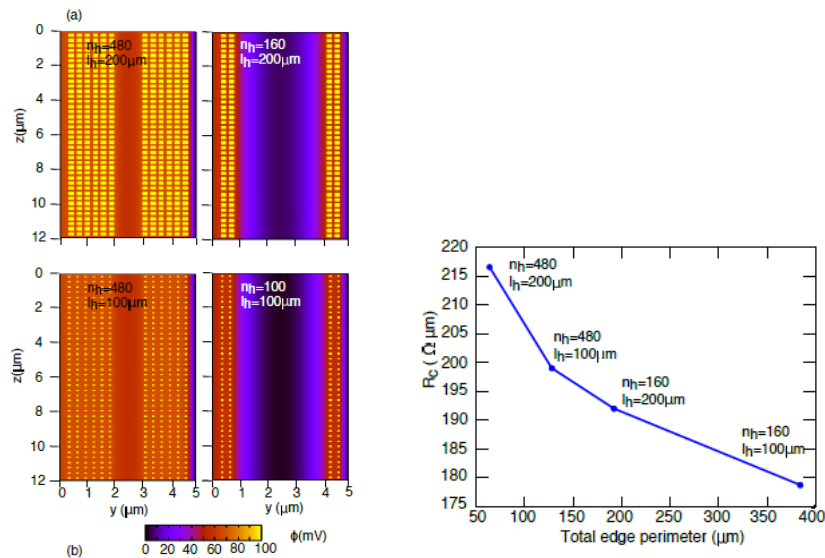
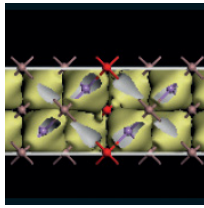


Fig. 1. (a) DFT Au-graphene structure and (b) Fermi energy shift with respect to the Dirac point ( $\Delta E_f$ ) obtained from the electrostatic potential analysis on carbon atoms.

$\text{\AA}$  at the edges. A tight-binding model of graphene has then been used to obtain the transmission coefficient. An electronic gap simulating the gold-graphene interlayer has been introduced by modifying the on-site energies of the graphene Hamiltonian. Using  $T$  and  $\Delta E_f$  we have determined the conductance from Landauer's formalism:  $G = \frac{q^2}{2h} \int dE \frac{\partial f}{\partial E} T T$  at the edges and the surface respectively. Eq. (2) has then been solved using NanoTCAD ViDES open-source code [11]. We imposed zero potential (as a reference) at the  $y = 5 \mu\text{m}$  end and set  $V_{m-g} = 0.1 \text{ V}$  (note that  $R_c$  is not dependent on this value). The solution of Eq. (2) for the four different considered configurations is depicted in Fig. 2a. In Fig. 2b we show  $R_c$  as a function of the total edge perimeter. As can be seen, as the patterning is increased  $R_c$  is reduced in accordance with experimental results. The contact resistance is nonetheless dependent also on the remaining graphene surface, and a large increase of the etched regions spoils the contact [5].



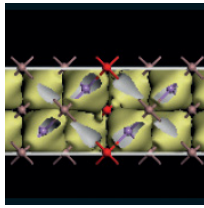


## International Workshop on Computational Nanotechnology

Fig. 2. (a) Potential distribution in the graphene flakes for hole sizes  $l_h = 200$  nm (top) and  $l_h = 100$  nm (bottom) and two number of holes:  $n_h = 480$  (left),  $n_h = 160$  (right). (b) Contact resistance as a function of the total edge perimeter.

A multi-scale approach based on DFT calculations and transport simulations has been proposed to calculate the resistance of metal/patterned graphene contacts. The model has been applied to several pattern configurations and manages to take into account the effects of the edges in reducing  $R_c$ . Such a model can be exploited to provide an optimization of the contact resistance and to guide and orient the experimental activity.

- [1] W. S. Leong et al. ACS Nano, 8, 994, 2014.
- [2] F. Xia et al. Nature Nanotech, 6, 179, 2011.
- [3] H-Y. Park et al. Adv Mat., 28 864, 2015.
- [4] S-M. Song et al., Appl. Phys. Lett, 104, 183506, 2014.
- [5] J. T. Smith et al. ACS Nano, 7, 3361, 2013.
- [6] G. Giovannetti et al. Phys. Rev. Lett., 101, 026803, 2008.
- [7] P. Giannozzi et al, J. Phys.: Condens. Matter, 21, 395502, 2009.
- [8] J. Perdew et al, Phys. Rev. Lett., 77, 3865, 1990.
- [9] D. Vanderbilt, Phys. Rev. B, 41, 7892(R), 1990.
- [10] D. Cheng et al, J. Phys. Chem C, 115, 10537, 2011.
- [11] NanoTCAD ViDES available at: <http://vides.nanotcad.com/>
- [12] V. Passi et al. ESSDERC'16 236, 2016



# International Workshop on Computational Nanotechnology

## Transport properties and applications of disoriented graphene systems: twisted bilayers and grain boundaries

V H Nguyen<sup>1</sup>, T X Hoang<sup>2</sup>, J Saint-Martin<sup>3</sup>, J-C Charlier<sup>1</sup> and P Dollfus<sup>3</sup>

<sup>1</sup>Université catholique de Louvain, Belgium, <sup>2</sup>Institute of Physics, Vietnam, <sup>3</sup>CNRS / C2N, France

To modulate the electronic and transport properties of graphene, a very attractive route consists in arranging properly two graphene sections of different orientation. One may think about twisted graphene bilayers [1] and grain boundaries separating two crystalline graphene domains [2]. Strain may be also used as an additional degree of freedom to tune differently the bandstructure of the two sections [3].

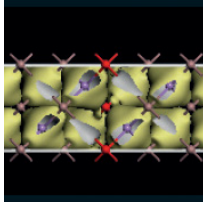
In the present work we investigate these different options and their possible applications, by means of atomistic calculations combining Green's functions (GF) and tight-binding (TB) formalisms, and including strain effects [4]. We show in particular the possibility to tune in a wide range the conductance gap, which allows improving the behavior of devices like tunnel diodes and transistors. In the case of polycrystalline graphene we show additionally the possibility to manipulate valley-polarized currents and the optical-like behavior of Dirac particles, even at room temperature.

We first investigated vertical structures made of two disoriented graphene layers that partially overlap each other, as schematized in Fig. 1. We considered both cases of commensurate and incommensurate systems [5]. To include the uniaxial strain effects, the hopping parameters of the TB model were adjusted as described in [6,7].

In commensurate systems, because of the different orientations of the two graphene lattices, their Dirac points can be displaced and separated in the k-space by the effects of strain (Fig.2). Hence, a finite gap of transmission (conduction gap) as large as a few hundred meV can be obtained in the device with a small strain of only a few percent. This gap is strongly dependent on the strain amplitude  $\sigma$ , the strain orientation ( $\theta$  angle) and the rotation angle  $\phi$  between the two layers. In incommensurate systems the misalignment of Dirac cones may appear even without strain and can be enhanced by strain (Fig. 3). Such conduction gap can be used to enhance the performance of graphene FET or the Seebeck coefficient [8].

Systems containing a single grain boundary (GB) separating two graphene domains of different orientations (Fig. 4) may offer similar properties [9]. It may be used for instance to enhance the negative differential conductance in PN tunnel diodes under the effect of uniform strain (Fig.4). A peak-to-valley ratio of 792 has been achieved for a strain of 4% at room temperature.

By looking carefully at the transmission in such GB systems, we can observe that it is modulated differently by strain in the two valleys of graphene D and D' [9]. Indeed the relationship between reflected and incident angles of de Broglie electron waves (see Fig.5) is valley-dependent. In devices as schematized in Fig. 6, this breaking of inversion symmetry may lead to directionally-separated and valley-polarized currents, even at room temperature (Fig. 7). In addition, the refraction index can be modulated electrically and take negative values. It makes it possible to control the valley filtering and the electronic optics properties of polycrystalline graphene.



# International Workshop on Computational Nanotechnology

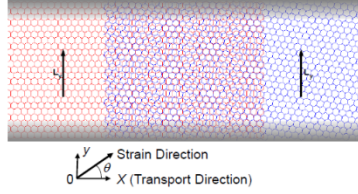


Fig. 1. Schematic of a device made of a vertical stack of misaligned graphene layers.

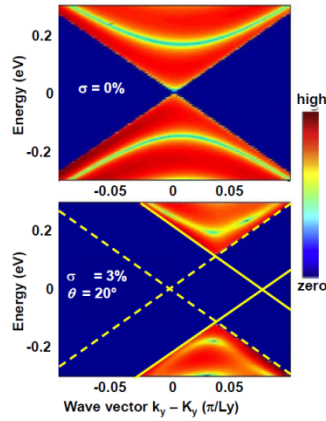


Fig. 2. (E-ky) maps of transmission probability in a particular bilayer structure for two strain configurations.

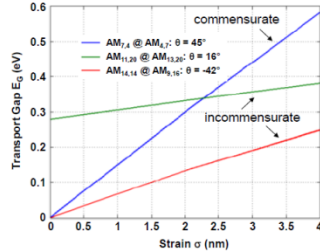


Fig. 3. Strain effects on the conductance gap in different devices with commensurate or incommensurate layers.

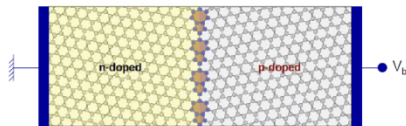


Figure 4. PN tunnel diode made of a grain boundary separating two crystalline graphene domains.

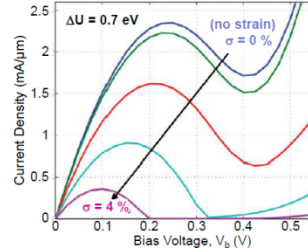


Fig. 4. I-V characteristics for different strain amplitudes  $\sigma$ , with strain direction  $\theta = 45^\circ$ ,  $T = 300$  K.

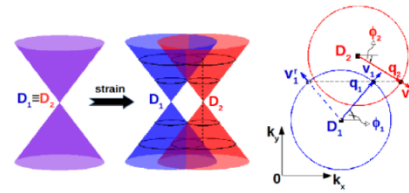


Fig. 5. Diagrams illustrating the strain effects on the band structure of graphene domains and the momentum conservation rule.

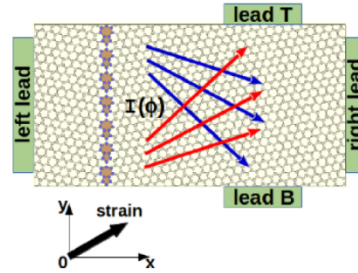


Fig. 6. Schematic view of a multiple electrode device made of a grain boundary system for measuring the directional polarized currents.

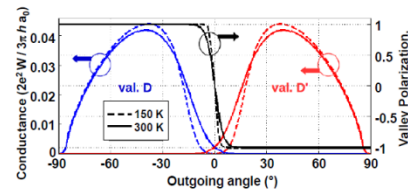
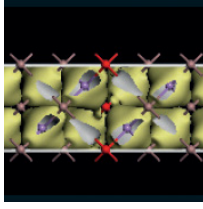


Fig. 6. Conductance (left axis) and valley polarization (right axis) as a function of outgoing angle  $\phi_2$  for a Fermi level  $E_F = 0.3$  eV and two temperatures.

- [1] J.M.B. Lopes dos Santos, N.M.R. Peres and A.H. Castro Neto, Phys. Rev. B 86, 155449 (2012).
- [2] P.Y. Huang et al., Nature 469, 389-393 (2011).
- [3] S. Bala Kumar and J. Guo, Nano Lett. 12, 1362-1366 (2012).
- [4] M.C. Nguyen et al., Semicond. Sci. Technol. 29, 115024 (2014).
- [5] V.H. Nguyen and P. Dollfus, J. Phys. D: Appl. Phys. 49, 045306 (2016).
- [6] Z. F. Wang, F. Liu and M.Y. Chou, NanoLett. 12, 3833 (2012).
- [7] V.M. Pereira, A.H. Castro Neto and N.M.R. Peres, Phys. Rev. B 80, 045401 (2009).
- [8] V.H. Nguyen et al., Nanoscale 8, 11658 (2016).
- [9] V.H. Nguyen et al., Phys. Rev. Lett. 117, 247702 (2016).



# International Workshop on Computational Nanotechnology

## A hierarchical model for CNT and Cu-CNT composite interconnects: from density functional theory to circuit-level simulations

J Lee<sup>1</sup>, T Sadi<sup>1</sup>, J Liang<sup>2</sup>, V P Georgiev<sup>1</sup>, A Todri-Saniai<sup>2</sup> and A Asenov<sup>1</sup>

<sup>1</sup>University of Glasgow, UK, <sup>2</sup>University of Montpellier, France

Metallic carbon nanotubes (CNTs) and Cu- CNT composites have been regarded for years as one of the promising candidates for the future interconnects to replace Cu. Due to CNTs' small effective mass and 1-D structure, and strong C-C bonding, they have a very high ampacity, a large mean free path ( $\lambda$ ), and excellent mechanical properties [1].

In this work, we have investigated the transport properties of CNT interconnects based on density functional theory (DFT) and compact model analysis. We also propose a hierarchical model to connect the DFT with circuit-level simulations.

We have used ATK [2] for DFT calculations involving the generalized gradient approximation (GGA). As the first step, a single-wall CNT (SWCNT) bundle as shown in Fig. 1 has been considered. In order to get optimal lattice constants, we have performed geometric optimization. All atoms are fully relaxed until the forces of any atom become less than 0.01 eV/Å. With the optimized atomistic structure, we have calculated the ballistic conductance ( $G_{bal}$ ) at 300 K using the non-equilibrium Green's function (NEGF) formalism.

Fig. 2 shows  $G_{bal}$  of SWCNT bundles and stand-alone SWCNTs. The difference between them, caused by the interaction with the adjacent SWCNTs, decreases as the diameter of CNTs ( $D_{CNT}$ ) increases.

Fig. 3 describes atomistic structures of iodine-doped SWCNT (24,0) and Cu- CNT(6,0) composite. In this work, the width ( $W$ ) and height ( $H$ ) of the local interconnect are assumed to be 8 and 16 nm, respectively, with reference to the ITRS node 2024 [3].

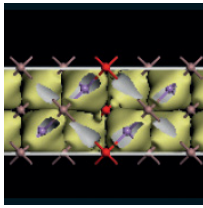
The resistance of the interconnect ( $R_w$ ) made of SWCNT bundles, the doped SWCNT, bulk Cu, and the Cu-CNT composite is plotted in Fig. 4. For bulk Cu, we do not consider the surface and grain boundary scattering effects. To calculate the diffusive conductance ( $G_{dif}$ ) from  $G_{bal}$ , we applied the mean free path approximation;  $G_{dif} = G_{bal}(1.0 + L/\lambda)^{-1}$ , where  $L$  is the interconnect length. As can be seen in this figure, bulk Cu has smaller  $R_w$  for short interconnects. Due to the large  $\lambda$  of CNT, however,  $R_w$  of the SWCNT(6,0) becomes better as  $L$  increases. It is noticeable that Cu-CNT composite is characterized by combining the advantage of both Cu and CNT.

To calculate the propagation time delay ( $t_d$ ), we have considered a driver-interconnect-load system, as shown in Fig. 5.  $R_s$ ,  $R_w$ , and  $C_L$  are assumed to be 35 kΩ, 7 aF, and 14 aF, respectively [3]. The capacitance of the interconnect ( $C_w$ ) is defined by  $C_w^{-1} = C_E^{-1} + C_Q^{-1}$ , where  $C_E$  and  $C_Q$  are the classical electrostatic and quantum capacitances, respectively.  $C_Q$  was extracted using the following relationship [4];

$$C_Q = \frac{e^2}{4KT} \int D(E) \text{sech}^2 \frac{E}{2KT} dE$$

where  $D(E)$  is the density-of-states obtained from DFT-GGA calculations. The calculated  $C_Q$  values are summarized in Table 1.

We have calculated  $t_d$  by using the Elmore formula;  $t_d = 0.69\{(C_s + C_w) + (R_w C_L + R_s C_w) + R_w C_w\}$ . Fig. 6 shows the dependence of  $t_d$  on  $L$  and  $C_E$ . In this calculation, we assumed that  $C_E$  does not rely on the interconnect material. As expected, long interconnects have large  $t_d$  due to large  $R_w$  and  $C_w$ . When  $C_E = 10^{-3}$  pF/μm, the SWCNT(6,0) bundle has the smallest  $t_d$  because of its small  $R_w$  (See Fig. 4). As  $C_E$  increases (the feature size decreases), however,  $t_d$  of the SWCNT(24,0) bundle becomes smaller than that of the SWCNT(6,0) bundle because of the small  $C_Q$  of SWCNT(24,0).



# International Workshop on Computational Nanotechnology

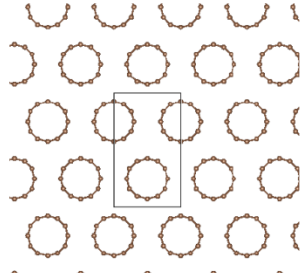


Fig 1. Atomic structure of the SWCNT(6,0) bundle. The black box indicates the primitive unit cell.

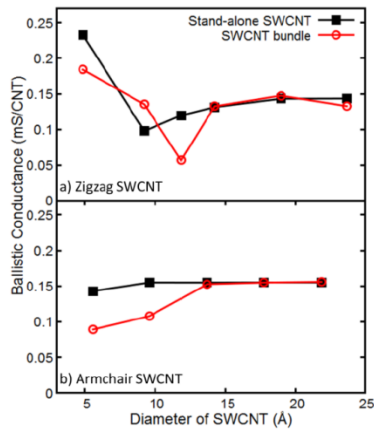


Fig 2. Dependence of  $G_{bal}$  on  $D_{CNT}$  of zigzag and armchair SWCNTs.

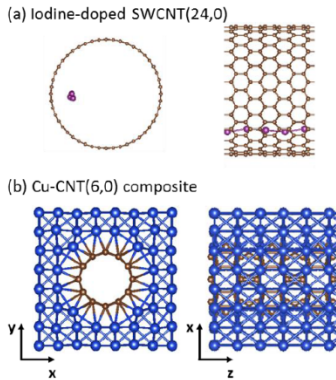


Fig. 3 Atomic structures of the iodine-doped SWCNT and the Cu-CNT composite.

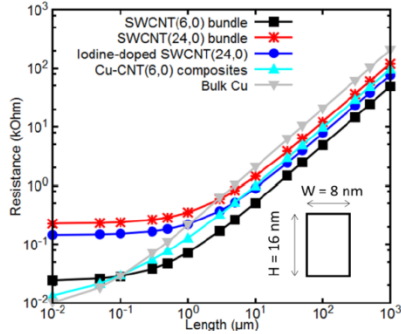


Fig. 4  $R_w$  vs  $L$  with  $W = 8$  nm and  $H = 16$  nm.

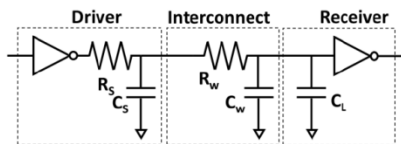


Fig. 5 Schematic representation of a typical interconnect.

Material	$C_Q$ (pF/μm)
SWCNT(6,0) bundle	0.3227
SWCNT(24,0) bundle	0.0146
Iodine-doped SWCNT(24,0)	0.0321
Cu-CNT(6,0)	0.7370
Bulk Cu	0.7821

Table 1.  $C_Q$  of the interconnect with  $W = 8$  nm and  $H = 16$  nm at 300 K.

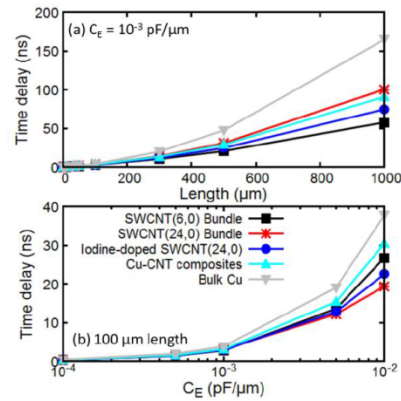
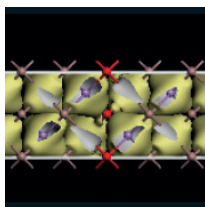


Fig. 6 Dependence of  $t_d$  on  $L$  and  $C_E$ .  $W$  and  $H$  of the interconnect are assumed to be 8 and 16 nm, respectively.

- [1] C. Subramaniam *et al.*, *Nat. Commu.* 4, 3202 (2013)
- [2] <http://quantumwise.com/>
- [3] A. Alizadeh and R. Sarvari, *IEEE Trans. VLSI Syst.* 24, 2, 803-807 (2016)
- [4] C. Zhan *et al.*, *J. Phys. Chem.* 119, 22297-22303 (2015)



# International Workshop on Computational Nanotechnology

Session: Organic Semiconductor Devices/Soft Matter

**(Invited) Charge and exciton dynamics in molecular aggregates: simple models from complicated ones**

A Troisi

University of Liverpool, UK

We systematically approach the study of quantum dynamics problems by “model reduction”, i.e. by determining a suitable model Hamiltonian from more accurate electronic structure calculations. Several examples of this procedure will be illustrated. A global map of all molecular semiconductors will be built by reducing to the essence charge transport models based on a large set of computational exploration. A similar procedure will be used to study the exciton dynamics in biological light harvesting complexes.

**(Invited) Using nanopores to sequence DNA: what can we learn from molecular dynamics**

S Khalid

University of Southampton, UK

Nanopores, whether synthetic or based on proteins have been used to sequence single stranded DNA by making use of the differential partial blocking of an electric current, of the four bases. A key goal of this technology now is to optimise these pores for improved performance. Understanding the translocation of ssDNA through the confined geometry of nano-scale pores, at the atomistic and molecular level is extremely difficult using experimental methods. Computational methods such as molecular dynamics simulations offer a route to exploring the details of DNA conformational dynamics and translocation through nanopores, under an applied electric field. I will present some of our results to date.

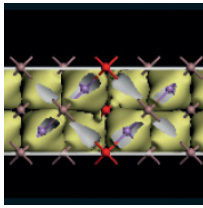
**Model parameter estimation and adaptive numerical simulation for organic thin film transistors**

P Africa<sup>1</sup>, C de Falco<sup>1</sup> and D Natali<sup>2</sup>

<sup>1</sup>Politecnico di Milano, Italy, <sup>2</sup>Istituto Italiano di Tecnologia, Italy

The accurate knowledge of relevant physical parameters is crucial to determine the predictive accuracy of numerical models for organic semiconductor devices. We present a step-by-step procedure enabling to determine critical model parameters - such as the density of states width, the carrier mobility and the injection barrier - by fitting experimental data from a sequence of relatively simple measurements to 2D numerical simulations under different regimes.

The current presentation extends the results of [1,2] where 1D models were used both for transient simulation of Metal-Insulator-Semiconductor (MIS) capacitors and for the estimating the DC transfer characteristics of Organic Thin-Film Transistors in the linear regime. The newly developed 2D simulator allows to account in a more natural way for a set of inherently two-dimensional phenomena, such as: the non-planarity of the semiconductor/insulator interface (due to the solution processing of materials); parasitic capacitances due to coupling between metal layers; the boundary condition at the semiconductor/substrate interface; contact resistance due to current-crowding effects. In order to deal with the increased complexity of numerical simulations in the new 2D setting efficient numerical methods based on a suitable a-posteriori error estimator and adaptive mesh refinement (see figure 1) have been implemented. The devices being considered in this study are shown in figure 2. Our approach is tested on a benchmark semiconducting



# International Workshop on Computational Nanotechnology

polymer: a very satisfactory fitting of experimental measurements is achieved and physically meaningful values for the extracted parameters are obtained, thus confirming the strategy effectiveness.

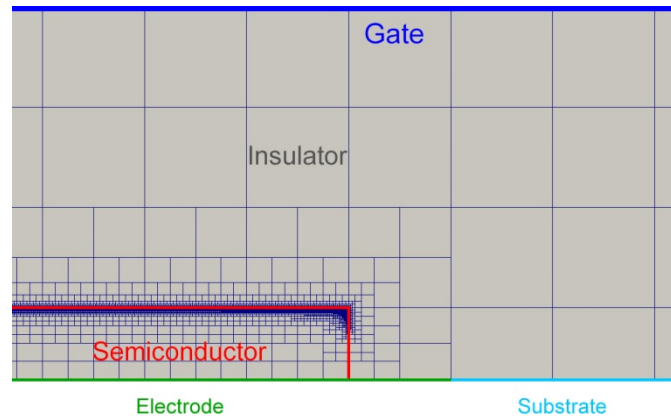


Figure 1 Example of an a-posteriori estimator driven mesh adaptation at the semiconductor/insulator interface in a benchmark MIS structure.

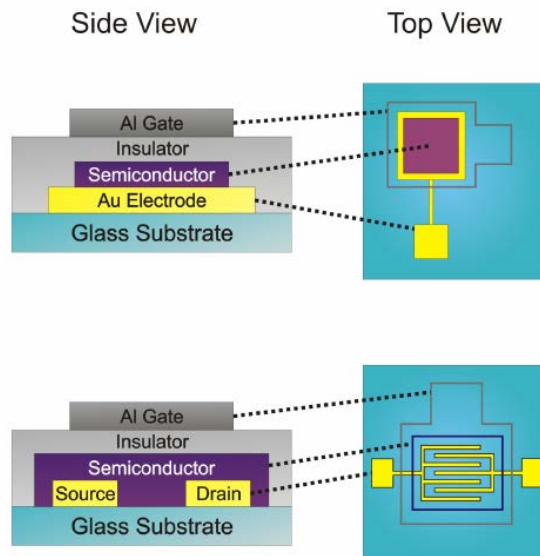
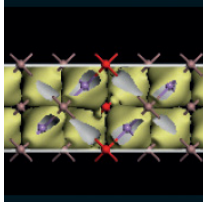


Figure 2 Top and side view of the devices used: the MIS capacitor at the top and the OTFT at the bottom. Reprinted with permission from Ref. [2]. Copyright Elsevier 2015.

- [1] P. C. Africa, F. Maddalena, C. de Falco, M. Caironi, D. Natali. Simultaneous Extraction of Density of States Width, Carrier Mobility and Injection Barriers in Organic Semiconductors. Submitted, 2016.
- [2] F. Maddalena, C. de Falco, M. Caironi, D. Natali. Assessing the width of Gaussian density of states in organic semiconductors. In *Organic Electronics*, 17, 304–318, 2015.



# International Workshop on Computational Nanotechnology

## A numerical study of fermi kinetics transport

N C Miller<sup>1</sup>, J D Albrecht<sup>1</sup>, D Smithe<sup>2</sup>, K Beckwith<sup>2</sup> and M Grupen<sup>3</sup>

<sup>1</sup>Michigan State University, USA, <sup>2</sup>Tech-X Corporation, USA, <sup>3</sup>Air Force Research Laboratory, USA

Numerical analyses of Fermi kinetics transport illustrate its convergence characteristics. Its adaptation of the Scharfetter-Gummel discretization scheme yields convergence between first and second-order.

Fermi kinetics transport (FKT) uses moments of the Boltzmann transport equation (BTE) to simulate charge transport in semiconductor devices. Its defining feature is electronic heat flow based on the thermodynamic identity and enforcing the second law of thermodynamics [1]. When combined with electronic band-structure and full-wave electromagnetics, it can accurately simulate electronic devices from DC up through mm-wave frequencies without adjustable calibration parameters [2], [3].

This abstract demonstrates FKT's numerical convergence characteristics. Analyses of semiconductor device simulations reveal convergence between first and second-order.

Convergence is quantified by evaluating the relative  $L^2$  error,

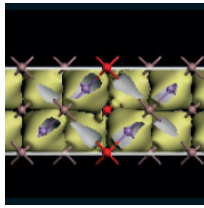
$$\epsilon_k = \sqrt{\frac{\sum_i [\tilde{u}_{i,k} - u_{i,k}]^2}{\sum_i u_{i,k}^2}} \quad (1)$$

on a series of meshes. Here,  $\tilde{u}_{i,k}$  and  $u_{i,k}$  are numerical and analytic solutions in the  $i^{\text{th}}$  element of the  $k^{\text{th}}$  mesh, respectively. First, discrete particle flux divergence is computed with an analytic solution variable profile. The numerical solution is  $\tilde{u}_{i,k} = \sum_j J_{n,ijk} / A_{ijk}$ , where  $J_{n,ijk}$  is the flux through the  $j^{\text{th}}$  surface with area  $A_{ijk}$  of the  $i^{\text{th}}$  Voronoi polyhedron [3] in the  $k^{\text{th}}$  mesh. The analytic solution is  $u_{i,k} = \sum_j (\nabla \cdot \vec{J}_n)_{ijk} \omega_{ijk} V_{ik}$  where  $\omega_{ijk}$  is the  $j^{\text{th}}$  quadrature weight inside the  $i^{\text{th}}$  Voronoi polyhedron with volume  $V_{ik}$  in the  $k^{\text{th}}$  mesh. Analytic flux divergence is calculated at the  $j^{\text{th}}$  quadrature point.

Order analyses for electronic device examples are determined in a similar way. The solution  $u_{i,k} = u_{i,k}^D \omega_i V_i$  at the  $i^{\text{th}}$  quadrature point in the  $k^{\text{th}}$  mesh is interpolated from the solution set  $u^D$  numerically calculated on a dense mesh. The numerical solutions  $\tilde{u}_{i,k} = u_{i,k}^k \omega_i V_i$  are interpolated from the  $k^{\text{th}}$  mesh solution set  $u^k$  to quadrature points generated in mesh tetrahedra. Errors are calculated with (1).

Figure 1 shows electric potentials and particle fluxes. Flux and flux divergence reconstruction errors in Figure 2 reveal first-order Scharfetter-Gummel discretization. Figures 3 and 5 show GaAs device solution variables with error convergences in Figures 4 and 6 varying between first and second order.

FKT is a deterministic BTE solver incorporating the second law of thermodynamics as its closure relation. Several results are presented which provide insights into the discretization techniques. Solving the discretized device equations shows convergence is first-order and higher.



# International Workshop on Computational Nanotechnology

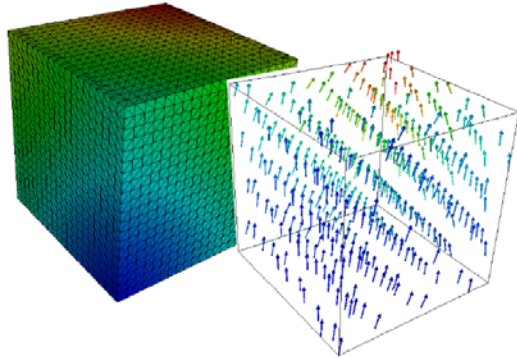


Fig. 1. 3D particle flux reconstruction on the DV mesh. (left) The electric potential profile and (right) the resulting particle flux.

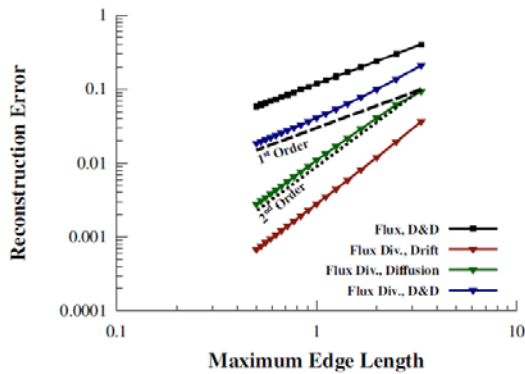


Fig. 2. Error analysis of the FKT flux and flux divergence reconstruction on a series of structured meshes. Here, D&D stands for drift and diffusion. Each mesh reconstruction was compared to an analytic flux and flux divergence as described in Section II.

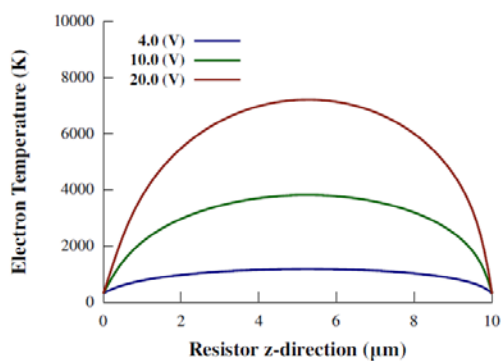


Fig. 3. The electron temperature profiles in the resistor example along the drift axis (the z-axis) for applied biases of 4 V (blue), 10 V (green), and 20 V (red).

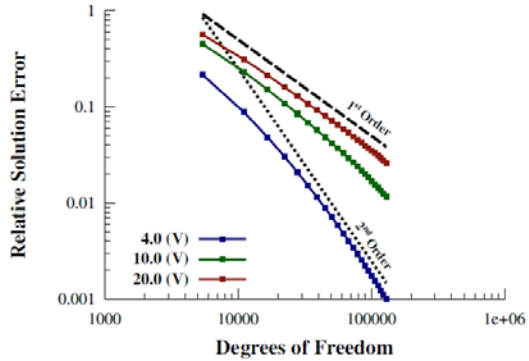


Fig. 4. Error analysis of the fully coupled nonlinear FKT system on a series of structured meshes. The device is a GaAs resistor with applied biases of 4 V (blue), 10 V (green), and 20 V (red). Each mesh solution set was compared to a numerical solution set calculated on a dense mesh.

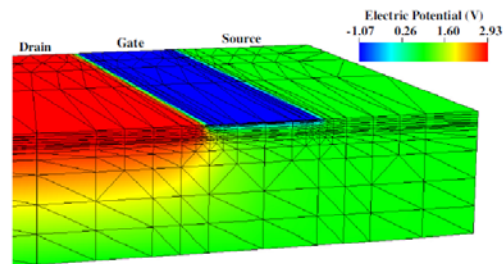


Fig. 5. The electric potential profile in the GaAs MESFET example with a gate bias of  $-1$  V and a drain-source bias of 2 V.

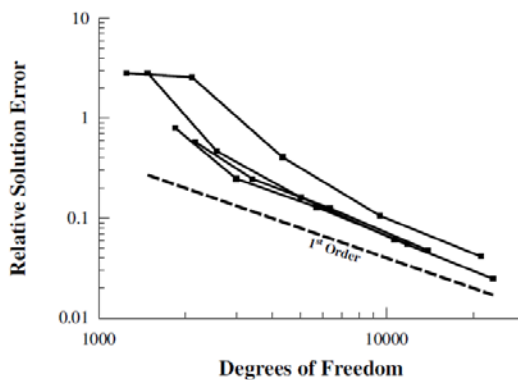
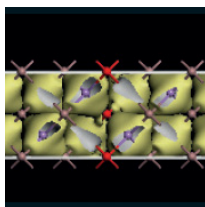


Fig. 6. Error analysis of the fully coupled nonlinear FKT system on a series of device meshes. The device is a GaAs MESFET with an applied gate bias of  $-1$  V and a drain-source bias of 2 V. The multiple error lines correspond to different mesh refinements. Each mesh solution set was compared to a numerical solution set calculated on a dense mesh.

- [1] M. Grupen, *Journal of Appl. Phys.* 106, 12, 123702, 2009.
- [2] M. Grupen, *IEEE Trans. on MTT*, 62, 12, 2868, 2014.
- [3] M. Grupen, *IEEE Trans. on Elect. Dev.*, 63, 8, 3096, 2016.



# International Workshop on Computational Nanotechnology

Session: Organic Semiconductor Devices/Soft Matter

## (Invited) Towards the understanding of the mechanism of ions permeation through graphene-based membranes

P Carbone

The University of Manchester, UK

Permeation through nanometer pores is important in the design of materials for filtration and separation techniques and because of unusual fundamental behaviour arising at the molecular scale. Membranes comprising or incorporating graphene or graphene oxide (GO) offer remarkable potential for selective uptake and transport of molecular or ionic species. [1, 4] This high selectivity makes these membrane perfect candidates for membrane filtration technology. For a rational design of such nanomaterial the mechanism of permeation through the graphene layers need to be however fully understood and explained. Simulations can help in guiding the design of these extraordinary materials. In this talk we will present some recent results on GO-membrane and the challenges that molecular models face in simulating the real device.

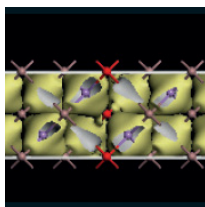
- [1] Nair *et al.*, *Science*, 2012, 335, 442
- [2] Joshi *et al.*, *Science*, 2014, 343, 6172
- [3] Abraham *et al.*, *Nat. Nano*, 2017, doi:10.1038/nnano.2017.21
- [4] Williams *et al.*, *J. Phys. Chem. Lett*, 2017, 8, 703

## Simulation of tunneling based biosensor considering ion transport and electron tunneling

K Y Kim<sup>1</sup>, W C Lee<sup>1</sup>, J Y Yun<sup>1</sup>, Y Lee<sup>1</sup>, S Jin<sup>2</sup> and Y J Park<sup>1</sup>

<sup>1</sup>Seoul National University, South Korea, <sup>2</sup>Samsung Semiconductor INC., USA

Our group developed a reference electrode-free biosensor device having concentric electrode structure. (see Fig. 1.) An island electrode, hereafter called the drain, acts as a driving electrode, and an enclosing electrode, called the source, as a grounded electrode. Since the source electrode is bigger than the drain electrode, the electric potential of electrolyte is close to the source electrode as shown in Fig. 2., which shows the self-gating effect [1]. Recently, we extended the structure to detect matrix metalloproteinase9 (MMP-9), which is known as a biomarker of cancer cells. We immobilize the peptide substrate conjugated with methylene blue (MB) specific to MMP-9. Electron tunneling occurs between the MB and the drain electrode. As the MMP-9 cleaves the peptide, tunneling current between the MB states and drain electrode decreases [2]. We explain the influence of the ion transport on tunneling effect in this sensor using an in-house simulator. MODEL The simulation includes the three parts; Poisson equation, ion transport in the electrolyte system and the tunneling between the MB states and the electrode.



# International Workshop on Computational Nanotechnology

## Theoretical study on the rectification mechanisms of molecular *pn* diodes

T. Ohto<sup>1</sup>, K. Minode<sup>1</sup>, K. Albrecht<sup>2</sup>, K. Yamamoto<sup>2</sup>, M. Handayani<sup>1,3</sup>, H. Tanaka<sup>4</sup>, S. Katayose<sup>1</sup>, R. Yamada<sup>1</sup>, T. Ogawa<sup>1</sup> and H. Tada<sup>1</sup>

<sup>1</sup>Osaka University, Japan, <sup>2</sup>Tokyo Institute of Technology, Japan, <sup>3</sup>Indonesian Institute of Science (LIPI), Indonesia, <sup>4</sup>Kyushu Institute of Technology, Japan

Molecular electronics aims at a utilization of single molecules as electronic device components such as wires, memories, and diodes. As an example, Aviram and Ratner (AR) proposed a molecular diode consisting of donor (D) and acceptor (A) molecular fragments separated by a spacer as shown in Fig. 1[1]. The proposed forward direction of the AR diode is the same as that of the bulk *pn* diode. However, the forward direction of the most D-A complexes, even including the AR diode [2], has been found to be opposite to the *pn* mechanism. This is because the positive bias voltage of the A→D (reverse bias) direction narrows the gap between the highest occupied molecular orbital (HOMO) of D and the lowest unoccupied MO (LUMO) of A.

Recently, we found two molecular diodes that show the same rectification direction to that of *pn* junctions. The molecular structures are given in Fig. 2. To investigate the relationship between molecular junction structures and the rectification mechanism, the non-equilibrium green's function method combined with density functional theory (NEGF-DFT) [3] was used. The molecular projected self-consistent Hamiltonian (MPSH) scheme was employed to analyze the response of MOs to applied bias. Electron transport in the carbazole oligomer is dominated by HOMO. The bias voltage affects its couplings to the left/right electrodes through the deformation of HOMO, which is the origin of the rectification. On the other hand, in the case of the Zn-porphyrin-imide complex, MOs are localized on either of porphyrin (L), imide (M), or benzene (R). The applied bias voltage modulates the energy level alignment of MOs and the resonance between those localized MOs causes the rectification behavior.

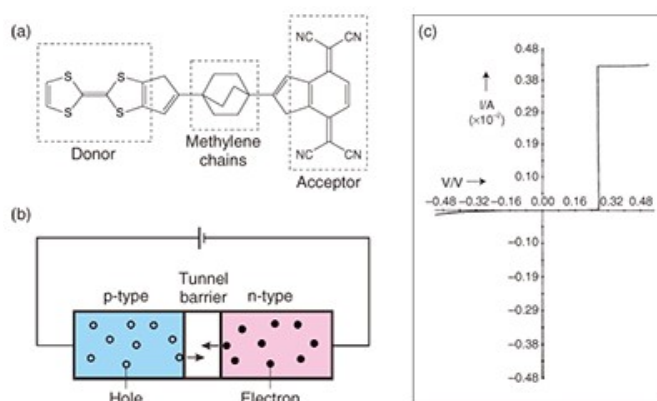
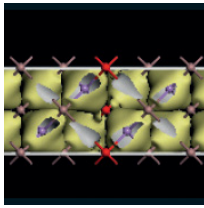


Figure 1: Aviram-Ratner diode. [1]



# International Workshop on Computational Nanotechnology

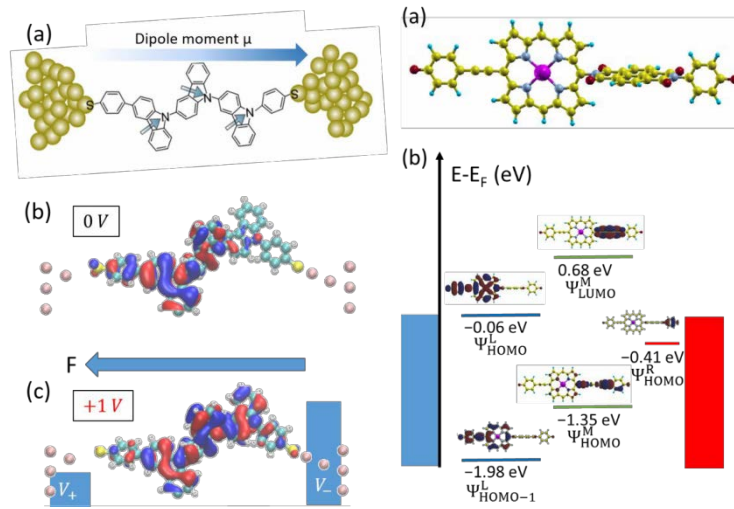
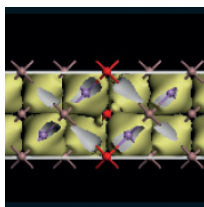


Figure 2: (Left) Carbazole oligomer diode. (a) Molecular structure and the distribution of HOMO under (b) 0 V and (c) 1 V. (Right) Zn-porphyrin-imide complex. (a) Molecular structure and (b) MO energy alignment.

- [1] A. Aviram and M. A. Ratner, Chem. Phys. Lett. 29, 277 (1974).
- [2] K. Stokbro et al., J. Am. Chem. Soc. 125, 3674 (2003).
- [3] A. R. Rocha et al., Phys. Rev. B 73, 085414 (2006).



# International Workshop on Computational Nanotechnology

## Time-resolved carrier transfer at molecular junction interface

K Beltako, N Cavassilas and F Michelini

Aix-Marseille University, France

Recent theoretical and experimental advances in electronic transport through molecular wires and junctions have generated interest for handling time-dependent regimes [1]. Molecular electronic devices are indeed a promising alternative to standard electronic switches due to their fast response on the pico-second time scale. Recently, wave function (WF) approach emerges as an alternative to Green's function formalism for the dynamical simulation of systems far from equilibrium without additional computational effort, at least within mean-field approximations [3]. In this work, the approach is used for the study of a molecular junction subjected to ultra-short excitation pulses. Numerical analysis enables us to correlate the time-dependent photocurrent to the underlying intramolecular dynamics.

Wave function approach is a technique based on the Keldysh formalism, in which one constructs wave functions instead of Green's functions. We use a tight-binding Hamiltonian  $(t) = \sum_{i,j} H_{i,j}(t) c_i^\dagger c_j$ . The model describes a two level donor-acceptor molecular junction (D-A) in contact with two leads as represented Fig. 1. We assume that the system is unperturbed in its far past ( $t < 0$ ). So that the problem is separated into a stationary part and a field-induced deviation throughout the hamiltonian and wave function partitions. Further detail could be found in [3].

In the case of a single ultrafast femtosecond pulse (1P), analysis of the dynamics of the intramolecular orbital populations (not shown) reveals that the pulse induces a HOMO-LUMO transition at the donor, followed by intramolecular tunneling oscillations between the donor and acceptor LUMO states. The electron decay is oscillating between the two leads, resulting in a left- to-right transient photocurrent within the relaxation time.

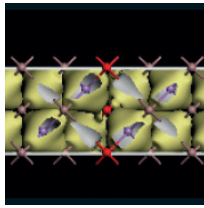
We show that an interplay between the pulse intensity and the molecular-metal coupling results in rearrangements of non-equilibrium molecular population between high- and low-conducting channels. This may lead to either enhancement or suppression of the 1P-photocurrent (see Fig.2,3). We notice from our investigation that the system shows up two characteristic frequencies: the field-induced frequency and an internal frequency which corresponds to the tunneling oscillation between the D- A LUMO states. In the *weak tunnel coupling regime*

( $\Gamma \ll A_1$ ), carrier life time  $\tau_v \sim h/\Gamma$  is long enough, so that even after the pulse is turned off, current is still flowing through the junction. The oscillation frequency of the photocurrent reveals internal tunnelling oscillations between the D-A LUMO states (Fig. 2) [4]. In contrast, in the *strong tunnel coupling regime* ( $\Gamma \gg A_1$ ), carriers have a short life time so that almost no current flows after the pulse off. During the pulse, the photocurrent follows the field amplitude with on top field-induced oscillations, as shown Fig. 3.

In the case of *two pulses* (2P), the second pulse occurs while the system has not reached a stationary configuration. Two limit cases are intuitive. For a delay between the two pulses  $\tau \ll \delta$  ( $\delta$  pulse width), the 2P-photocurrent signal is the same as the 1P-photocurrent generated by a single pulse of amplitude  $A_1 + A_2$  (see Fig. 4). In contrast, when  $\tau \gg \delta, \tau_v$  (relaxation time), the 2P-photocurrent is the result of the two independent 1P-responses.

In between, as the case shown Fig. 5, we investigate the direct photocurrent (integrated current) as a function of delay  $\tau$ , which confirms and generalizes the previous analysis (Fig.6).

Thanks to the accuracy of ultrafast spectroscopy with photocurrent detection scheme, this work opens avenues toward the possibility of controlling or analyzing the internal quantum properties of nanodevices with pump- probe photocurrent spectroscopy [2].



# International Workshop on Computational Nanotechnology

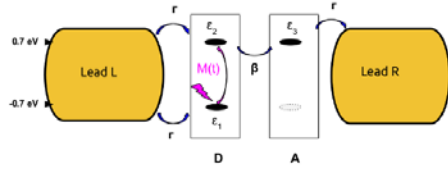


Fig. 1. Donor-acceptor (D-A) molecular junction.  $M(t)$  est  $A_1 \cos(\omega_0 t) \exp(-t^2/2\delta^2) + A_2 \cos(\omega_0(t-\tau)) \exp(-(t-\tau)^2/2\delta^2)$ .  $A_{1,2}$ ,  $\delta$  and  $\tau$  are respectively the pulse amplitude, width and delay.

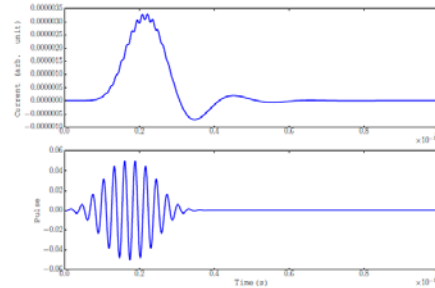


Fig. 4. D-A photocurrent for double pulse shows a single pulse response.  $A_1 = A_2 = 0.05 < \Gamma = 0.06$ ,  $\beta = 0.1$ ,  $\tau = 5 fs$ .

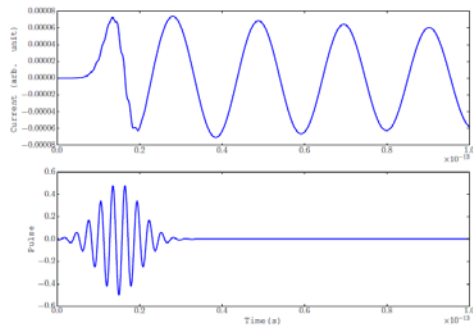


Fig. 2. Weak tunnel coupling  $A_1 = 0.5 > \Gamma = 0.02$ ,  $\beta = 0.1$ . D-A photocurrent for single pulse, shows long relaxation time.

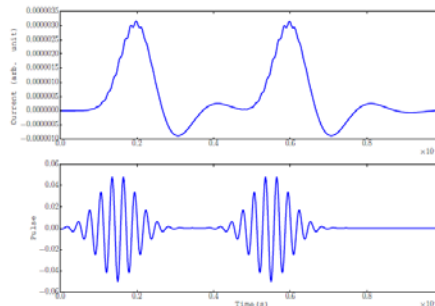


Fig. 5. D-A photocurrent for double pulse shows two independent single pulse response.  $A_1 = A_2 = 0.05 < \Gamma = 0.06$ ,  $\beta = 0.1$ ,  $\tau = 40 fs$ .

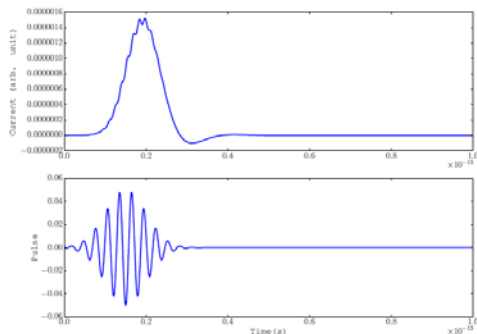


Fig. 3. Strong tunnel coupling  $A_1 = 0.05 < \Gamma = \beta = 0.1$ . D-A photocurrent for single pulse.

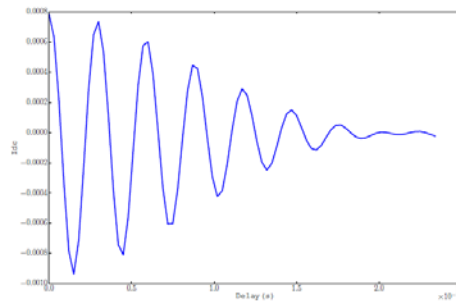
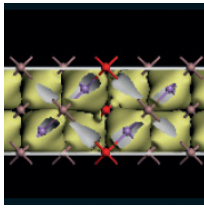


Fig. 6.  $I_{dc}$  the difference in the direct 2P-photocurrent and 2 times the direct 1P-photocurrent.  $A_1 = A_2 = 0.5 > \Gamma = \beta = 0.1$ .  $I_{dc}$  tend to zero as  $\tau \gg \delta, \tau_v$ , transient component is suppressed.

- [1] Artem A. Bakulin and al. *J. Phys. Chem. Lett.*, 7(2):250–258, 2016.
- [2] Tyler L. Cocker and al. *Nat. Photon*, 7(8):620–625, 2013.
- [3] B. Gaury, J. Weston, M. Santin, M. Houzet, C. Groth, and X. Waintal. *Phys Rep*, 534(1):1–37, 2014.
- [4] Yoram Selzer and Uri Peskin. *Phys Chem C*, 117(43):22369–22376, 2013.



# International Workshop on Computational Nanotechnology

Session: NanoHub

## NanoHUB.org – Always “on” enabling global scientific knowledge transfer

G Klimeck

Purdue University, USA

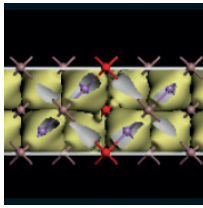
Gordon Moore’s 1965 prediction of continued semiconductor device down-scaling and circuit up-scaling has become a self-fulfilling prophecy in the past 50 years. Open source code development and sharing of the process modeling software SUPREM and the circuit modeling software SPICE were two critical technologies that enabled the down-scaling of semiconductor devices and up-scaling of circuit complexity. SPICE was originally a teaching tool that transitioned into a research tool, was disseminated by an inspired engineering professor via tapes, and improved by users who provided constructive feedback to a multidisciplinary group of electrical engineers, physicist, and numerical analysts. Ultimately SPICE and SUPREM transitioned into all electronic design software packages that power today’s 300 billion dollar semiconductor industry.

Can we duplicate such multi-disciplinary software development starting from teaching and research in a small research group leading to true economic impact? What are technologies that might advance such a process? How can we deliver such software to a broad audience? How can we teach the next generation engineers and scientists on the latest research software? What are critical user requirements? What are critical developer requirements? What are the incentives for faculty members to share their competitive advantages? Can real research be conducted in such a web portal? How do we know early on if such an infrastructure is successful? Can one really transfer knowledge from computational science to other areas or research and into education? This presentation will bust some of the myths and perceptions of what is possible and impossible.

By serving a community of over 1.4 million users in the past 12 months with an ever-growing collection of over 5,000 resources, including over 440 simulation tools, nanoHUB.org has established itself as “the world’s largest nanotechnology user facility” [1]. nanoHUB.org is driving significant knowledge transfer among researchers and speeding transfer from research to education, quantified with usage statistics, usage patterns, collaboration patterns, and citation data from the scientific literature. Over 1,800 nanoHUB citations in the literature resulting in over 19,700 secondary citations with h-index of 76 prove that high quality research by users outside of the pool of original tool developers can be enabled by nanoHUB processes. In addition to high-quality content, critical attributes of nanoHUB success are its open access, ease of use, utterly dependable operation, low-cost and rapid content adaptation and deployment, and open usage and assessment data. The open-source HUBzero software platform, built for nanoHUB and now powering many other hubs, is architected to deliver a user experience corresponding to these criteria.

Gerhard Klimeck is the Reilly Director of the Center for Predictive Materials and Devices (c-PRIMED) and the Network for Computational Nanotechnology (NCN) and a Professor of Electrical and Computer Engineering at Purdue University. He was previously with NASA/JPL and Texas Instruments leading the Nanoelectronic Modeling Tool development (NEMO). His work is documented in over 480 peer-reviewed journal and proceedings articles. He is a fellow of the IEEE, American Physical Society, and the Institute of Physics.

[1] Quote by Mikhail Roco, Senior Advisor for Nanotechnology, National Science Foundation.



# International Workshop on Computational Nanotechnology

## Session: Quantum Transport

### (Invited) First principles calculations of electron transport in gated 2D nano-structures

M Brandbyge

Technical University of Denmark, Denmark

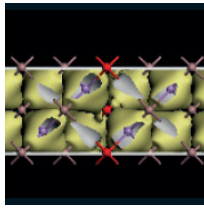
Devices based on stacked van der Waals heterostructures of two-dimensional (2D) materials are promising candidates for future atomically thin, flexible electronics with properties that can be tuned by the electrostatic and dielectric environment. One of the key advantages of two-dimensionality is that it allows very precise control of the carrier density and voltage drop[1] by a gate potential. However, the application of the gate potential may not only influence the transport via the carrier density in simple ways.

In this talk we present examples where we employ first principles transport calculations based on Density Functional Theory (DFT) which explicitly include the electrostatic gate potential and induced carriers. DFT is combined self-consistently with non-equilibrium Greens functions to study the effects of finite bias in devices[2], or as input to the Boltzmann equation to study bulk conductivity[3].

We consider the role of the gate geometry for the contact resistance in a stacked device where graphene is used as electrode to a MoS<sub>2</sub> channel[4]. We show how the contact resistance depends critically on the stacking configuration and establish a design rule for the stacking of devices based on 2D materials.

We also consider how the gate potential can induce a new flexural phonon scattering mechanism in a graphene device[5]. Gating can break the planar mirror symmetry activating one-phonon scattering from flexural phonons. Using the Boltzmann equation with parameters from DFT we calculate the mobility of graphene in a gate potential and find that this effect can have detrimental impact on the performance of a graphene device.

- [1] N. Papior, T. Gunst, D. Stradi, M. Brandbyge, *Phys. Chem. Chem. Phys.*, 18, 1025 (2016).
- [2] M. Brandbyge, J-L. Mozos, P. Ordejon, J. Taylor, K. Stokbro, *Phys. Rev. B* 65, 165401 (2002); N. R. Papior, N. Lorente, T. Frederiksen, A. Garcia, M. Brandbyge, *Comp. Phys. Comm.*, 212, 8, (2017).
- [3] T. Gunst, T. Markussen, K. Stokbro, M. Brandbyge, *Phys. Rev. B*, 93, 035414 (2016).
- [4] D. Stradi, N. R. Papior, O. Hansen, M. Brandbyge, *Nano Lett.* 17, 2660 (2017)
- [5] T. Gunst, K. Kaasbjerg, M. Brandbyge, *Phys. Rev. Lett.* 118, 046601 (2017).



# International Workshop on Computational Nanotechnology

## Electron-phonon scattering from green's function transport combined with molecular dynamics: Applications to mobility predictions

T Markussen<sup>1</sup>, M Palsgaard<sup>1,2</sup>, D Stradi<sup>1</sup>, T Gunst<sup>2</sup>, M Brandbyge<sup>2</sup> and K Stokbro<sup>1</sup>

<sup>1</sup>QuantumWise A/S, Denmark, <sup>2</sup>Technical University of Denmark, Denmark

The interaction between electrons and phonons is an important scattering effect limiting the mobility of carriers in nanoscale materials. Phonon-limited mobilities can be rigorously calculated at the atomistic level, using established electronic structure methods such as density functional theory (DFT) or tight-binding, coupled to either the Boltzmann transport equation (BTE) [1] in the case of bulk materials, or to Non-equilibrium Green's function (NEGF) theory [2,3,4] in the case of devices.

Nevertheless, in practical applications the evaluation of the electron-phonon coupling (EPC) matrix is numerically challenging, and approximations have to be applied. The most common one in both the BTE and the NEGF approaches is to treat the phonons within the harmonic approximation, thereby neglecting anharmonic effects, which might play an important role at finite-temperatures. Further approximations are also used in NEGF-based approaches to make the computation of the EPCs based on perturbation theory feasible [3,5,6].

In this contribution, we present an alternative approach combining NEGF theory and the Landauer approach with molecular dynamics (MD) [7] to calculate phonon-limited mobilities at the atomistic level [8]. In a device geometry with a central region coupled to two electrodes, we perform MD simulations for central regions of increasing length, and extract the resistivity and eventually the mobility from the slope of the resulting resistance vs. length curves. Compared to previous approaches for the phonon-limited mobility, the present method is conceptually simple, it naturally includes finite-temperature and anharmonic effects, and allows for simulations of mobilities in non-crystalline and defected materials. We validate our approach by comparing to mobilities and conductivities obtained using the BTE for different bulk and one-dimensional systems, and compare successfully against experimental values for bulk silicon and gold. All the calculations have been performed using the Atomistix ToolKit software [9].

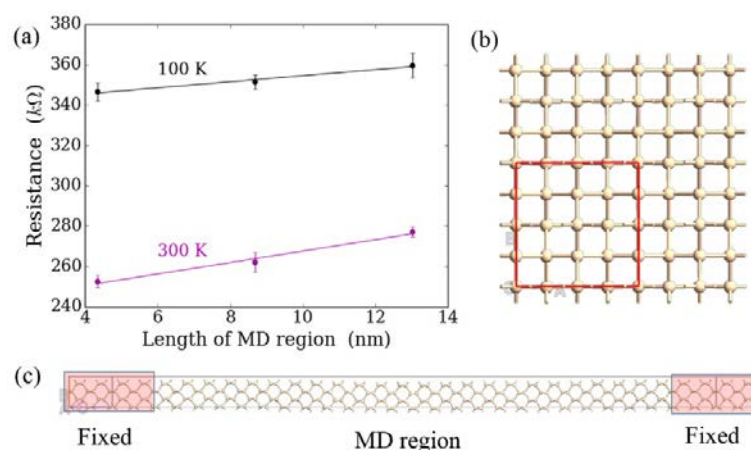
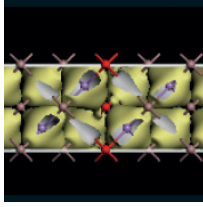


Figure: (a) Resistance vs. length curve for bulk silicon at temperatures  $T = 100$  K (upper curve) and  $T = 300$  K (lower curve). (b) Cross section of the simulation cell. (c) Scheme of the device configuration with a length of the central MD region of 13 nm.

[1] T. Gunst, T. Markussen, K. Stokbro and M. Brandbyge, Phys. Rev. B 93, 035414 (2016)

[2] M. Brandbyge, J.-L. Mozos, P. Ordejon, J. Taylor, and K. Stokbro, Phys. Rev. B 65, 165401 (2002)



# International Workshop on Computational Nanotechnology

- [3] M. Luisier, G. Klimeck, Phys. Rev. B 80, 155430 (2009)
- [4] K. Stokbro, D. E. Pedersen, S. Smidstrup, A. Blom, M. Ipsen, and K. Kaasbjerg, Phys. Rev B 82 075420 (2010)
- [5] T. Gunst, T. Markussen, K. Stokbro, and M. Brandbyge, Phys. Rev. B 93, 245415 (2016)
- [6] T. Frederiksen, M. Paulsson, M. Brandbyge, and A.-P. Jauho, Phys. Rev. B 75, 205413 (2007)
- [7] J. Schneider, J. Hamaekers, S. Smidstrup, J. Bulin, R. Thesen, A. Blom, and K. Stokbro, ArXiv:1701.02495
- [8] Atomistix ToolKit, version 2016.3, QuantumWise A/S [www.quantumwise.com](http://www.quantumwise.com)
- [9] T. Markussen, M. Paalsgaard, D. Stradi, T. Gunst, M. Brandbyge, and K. Stokbro, ArXiv:1701.02883

## Efficient quantum approach of electron-phonon scattering for nanoscale device simulations

Y Lee<sup>1</sup>, M Lannoo<sup>1</sup>, N Cavassilas<sup>1</sup>, M Luisier<sup>2</sup> and M Bescond<sup>1</sup>

<sup>1</sup>Aix-Marseille University, France, <sup>2</sup> ETH Zürich, Switzerland

In recent decades various transport approaches have been proposed to describe quantum effects occurring in nano-devices [1], [2]. Among them, Nonequilibrium Green's function formalism (NEGF) has been proved very suitable at treating inelastic interactions [3]. However, within this formalism the description of inelastic scattering is usually based on the computationally expensive self-consistent Born approximation (SCBA). As an alternative method to SCBA, we have proposed an efficient technique, the so-called Lowest Order Approximation (LOA) coupled with Padé approximants [4], [5]. In this work, we apply this approach to the treatment of phonon scattering in two 1D systems where phonon scattering is known to be important: the atomic linear chain and the nanowire transistor. In NEGF the interacting Green's function is calculated by combining an electron-phonon self-energy ( $\Sigma[G]$ ) with the Dyson equation [3]:

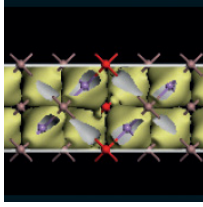
$$G = g_0 + g_0 \Sigma[G] G, \quad (1)$$

where  $g_0$  is the non-interacting Green's function. Since Dyson's equation (1) is non-linear, solving Eq. (1) is typically based on the iterative SCBA scheme. Alternatively, we define LOA Green's functions at a given order  $N$  in interaction as follows:

$$g_N = g_{N-1} + g_0 \sum_{n=0}^{N-1} \Sigma[\Delta g_{N-n-1}] \Delta g_n, \quad (2)$$

where  $\Delta g_n = g_n - g_{n-1}$  and  $\Delta g_0 = g_0$ . By using Eq. (2), we can calculate current series  $I_N = I(g_N)$  and carrier density series  $\rho_N = \rho(g_N)$  to  $N$ th order in interaction. According to the strength of the electron-phonon scattering, the LOA series can diverge. We then use Padé approximant technique to operate a convergent resummation. Note that the LOA series can be also coupled to Hyper geometric resummation technique [6].

We first apply our technique to the ideal 1D linear atomic chain (Fig. 1) where one optical phonon mode ( $\hbar\omega = 60$  meV) is coupled with electrons described by a two-band  $k$ - $p$  Hamiltonian (inset of Fig. 1). Figure 2 shows current-voltage characteristics in the ballistic regime, SCBA and with our LOA- Padé technique when electron-phonon coupling  $M$  is large. It is clearly shown that 3rd order LOA currents combined with Padé 1/2 successfully reproduce the SCBA values. Figure 3 shows that electron density along the device can also be reconstructed with the LOA- Padé approach even though it needs up to 5th order LOA (i.e. Padé 2/3). Moreover, the series of LOA physical quantities can be derived from the SCBA algorithm [7]. The approach can then be applied to the n-type 3D nanowire transistor (Fig. 4 (a)) where a full-band atomistic treatment for electrons (Fig. 4 (b)) and phonons (Fig. 4 (c)) is considered [8]. Figure 5 compares Id-Vg curves of



# International Workshop on Computational Nanotechnology

ballistic regime and SCBA with those obtained by Padé 1/2. We note that 3rd order LOA currents are enough to achieve high agreement with respect to SCBA (Fig. 6).

In conclusion, the results show the relevancy of our technique for efficient quantum transport modelling with high accuracy compared to SCBA.

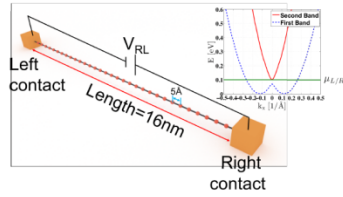


Fig. 1. Schematic view of a 1-D, 16 nm long atomic linear chain connected to left and right contacts at room temperature ( $T=300$  K). The applied voltage between left and right contacts is  $V_{RL}$ . (Inset) The electronic bandstructure is described by the two band  $k-p$  method. The Fermi levels of left and right contacts ( $\mu_{L/R}$ ) are located 0.1 eV above the bottom of the band.

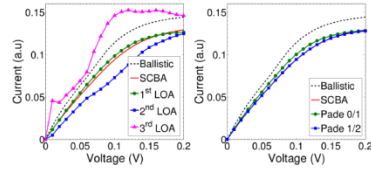


Fig. 2. I-V characteristics when electron-phonon coupling  $M$  is  $1.5 \times 10^{-3} \text{ eV}^2$  obtained (left) from ballistic, SCBA and first three LOA order and (right) from ballistic, SCBA, Padé 0/1 and Padé 1/2.

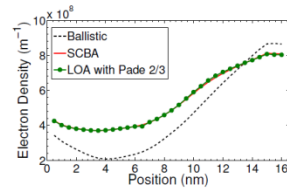


Fig. 3. Electron density profiles along the linear chain in ballistic regime and SCBA when electron-phonon coupling  $M$  is  $1.5 \times 10^{-3} \text{ eV}^2$ . Electron density profile reconstructed by Padé 2/3 with first five order LOA electron densities is also shown and fits perfectly with SCBA values.

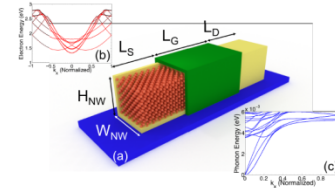


Fig. 4. (a) Schematic view of an n-type silicon 3D square cross-section nanowire transistor in (100) transport direction at room temperature ( $T=300$  K) with  $L_G = 13$  nm,  $L_{S/D} = 9$  nm and  $H_{NW} \times W_{NW} = 3 \times 3 \text{ nm}^2$ . The doping concentrations of donors in source and drain are  $10^{20} \text{ cm}^{-3}$ . (b) Electron bandstructure as produced by the full-band tight-binding  $sp^3d^5s^*$  model. (c) Phonon dispersion relation described by the valence-force-field method [8].

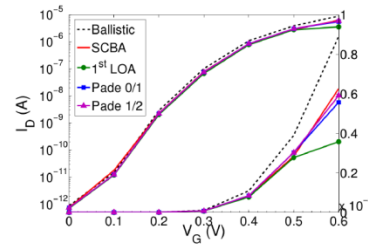


Fig. 5.  $I_D - V_G$  curves of the n-type 3D nanowire transistor for ballistic regime, SCBA, 1<sup>st</sup> order LOA, Padé 0/1 and Padé 1/2.

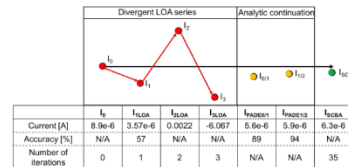
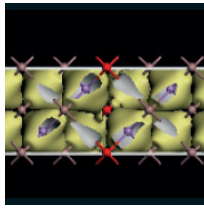


Fig. 6. Comparison of the ballistic current, first three order LOA currents, Padé 0/1 and Padé 1/2 with the SCBA current for the n-type 3D nanowire transistor at  $V_D = V_G = 0.6$  V. Accuracy with respect to the SCBA and number of iterations are reported in the table. Schematic diagram of the divergent LOA current series is also shown.

- [1] M. V. Fischetti, J. Appl. Phys. 83, 270 (1998).
- [2] J. Sellier et al., J. Comput. Phys. 280, 287 (2015).
- [3] G. D. Mahan, Many-Particle Physics (Plenum, New York, 1990).
- [4] H. Mera et al., Phys. Rev. B 88, 075147 (2013).
- [5] Y. Lee et al., Phys. Rev. B 93, 205411 (2016).
- [6] H. Mera et al., Phys. Rev. B 94, 165429 (2016).
- [7] Y. Lee et al., in preparation, (2017).
- [8] M. Luisier et al., Phys. Rev. B 80, 155430 (2009).



# International Workshop on Computational Nanotechnology

## Transport through Si QDs in coulomb blockade regime: Theory and experiment

A Andreev<sup>1</sup>, T-Y Yang<sup>1</sup>, M F Gonzalez-Zalba<sup>1</sup>, Yu Yamaoka<sup>2</sup>, T Ferrus<sup>1</sup>, S Oda<sup>3</sup>, T Kodera<sup>2</sup> and D A Williams<sup>1</sup>

<sup>1</sup>Hitachi Cambridge Laboratory, UK, <sup>2</sup>Tokyo Institute of Technology, Japan

The aim of this work is to develop a theory that can predict the transport through quantum dots (QDs) in the Coulomb blockade regime without any adjustable parameters, which will allow to use this model as a design tool for new structure with predefined properties for quantum computing applications. We present a detailed 3D modelling of transport through Si QD single electron transistor used for charge sensing in the devices for quantum information applications. For this reason we are only interested in the relative change of the current and not the absolute values. This means that we do not need to calculate the tunnelling rates and the relative change of the current (so-called stability diagrams – the current as a function of two gate voltages) can be calculated using the effective capacitance matrix approach that we have developed. The model includes several stages: 3D digitization of the real QD device (see Fig.1); electron wavefunction calculations in the QDs through the solution of the coupled Poisson's and Schroedinger-like equations; determination of the effective capacitance matrix of the device; transport calculations in the Coulomb blockade regime using the solution of the master equations. We apply the developed model to two types of the devices. The first type includes the structures [1] with trench-isolated double QDs and single electron transistors (formed as source, drain and side gates and the QD, see bottom of left image in Fig.1). The second type includes the structures with silicon nanowire field-effect transistors [2] with corner QDs formed by the electric field in the channel of the transistor. In both cases we have built a real 3D device and carried out the modelling of the transistor current to compare with the experiment [1,2]. It is important to note that the model does not contain any adjustable or fitting parameters – using the device structure and geometry we were able to predict qualitatively and quantitatively the current variations in both types of devices and reproduce stability diagrams showing charge movements in the QDs observed in experiment [1,2]. We conclude that the developed model can be used as a design and optimisation tool for new structures and predicting new phenomena for quantum information applications. This work is partly financially supported by Kakenhi Grants-in-Aid (Nos. 26709023 and 26249048) and JST-CREST, and by the European Community's Horizon 2020 Programme (Grant Agreement No. 688539).

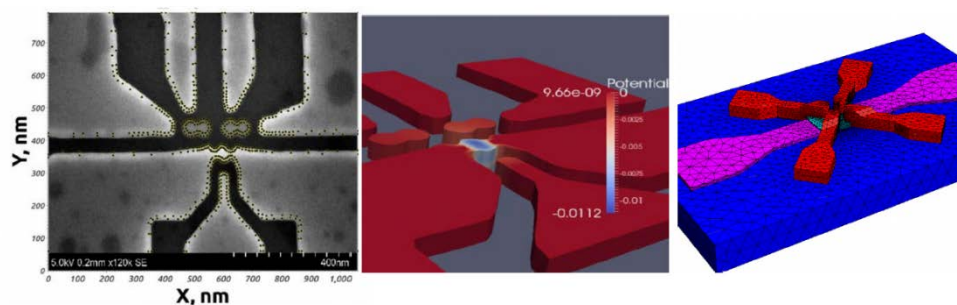
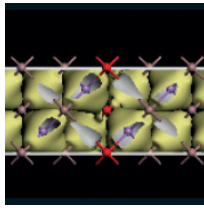


Fig.1 (left): SEM image of the structure with Si isolated double QDs and single electron transistor; the dots show the digitisation of the structure used for the modelling; (middle): calculated 3D distribution of electrical potential in the structure on the left as part of effective capacitance determination for Coulomb blockade transport modelling; (right): 3D model image of the structure with silicon nanowire field-effect transistor with 4 gates and QDs used for the modelling.

- [1] T.-Y. Yang, et.al., 2016 IEEE International Electron Devices Meeting (IEDM), (2016)
- [2] M.F. Gonzalez-Zalba, et.al. Nature Comm. 6, 6084 (2015)
- [2] M.F. Gonzalez-Zalba, et.al. Nature Comm. 6, 6084 (2015)



# International Workshop on Computational Nanotechnology

## The role of the displacement current in quantifying the speed of ballistic nano devices: beyond the quasi-static approximation

Z Zhan, E Colomés and X Oriols

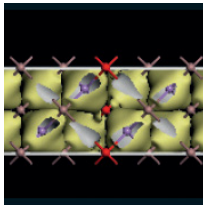
Universitat Autònoma de Barcelona, Spain

The development of faster electron devices is a constant demand from electronic industry and the ITRS roadmap envisions next future nano devices working at THz frequencies. For such devices, which are in the frontier between electronics and electromagnetism, the correct prediction of their performance enforces us to revisit the usual modelling of electron transport which only considers particle current (with drift and diffusion components) in semiconductors, and displacement current in dielectrics. In nano ballistic devices, since the dielectric relaxation time  $\tau_{Die}$  (the time needed for other electrons to screen the non-neutral electrical fields) is comparable to the electron transit time, an electron travelling through such active region generates a time-dependent electric field, which is detected as displacement current at the contacts when dealing with frequencies higher than  $1/\tau_{Die}$ . Therefore, for predictions of the ballistic nano device involving THz frequencies, the displacement current needs to be explicitly considered.

In particular, predictions on the speed of THz electron devices, either for analog or digital applications, are usually quantified in terms of the cut-off frequency,  $f_T$ , defined as the frequency where the current gain equals to one (0 dB). In this conference, we will show that the usual computation of  $f_T$  under the quasi-static approximation (which directly neglects the displacement current on the drain contact) is no longer valid for ballistic devices at THz frequencies. The value of  $f_T$ , for dual-gate 2D channel transistors plotted in Fig. 1(a), is estimated by a Fourier transform ( $Y$ -parameters) of the time-dependent currents computed from the BITLLES simulator [1-3]. From Figs. 3 and 6, we show that the displacement current is comparable to the particle (drift and diffusion) current. The quasi-static prediction of the device speed can be one order of magnitude faster than what these devices can really offer. Even in some design (not shown here), one can get  $f_T \rightarrow \infty$  when the drain phasor current is greater than the gate phasor current at all frequencies.

We propose to predict the speed of such nano devices working in the THz regime, from time-dependent simulations of the total (particle plus displacement) currents, i.e., from the intrinsic delay time  $\tau_d$  illustrated in Figs. 3 and 6 [4].

In conclusion, for ballistic nano devices, the electric field generated by electrons cannot be screened inside the device active region at frequencies higher than  $1/\tau_{die}$ . Then, the displacement current becomes as relevant as particle current and it has to be properly included in electron modelling. This conclusion is particularly critical for the speed predictions of nano devices which usually require quantum modelling. The proper quantum formulation of the displacement current faces important practical and conceptual issues. For example, the explicit simulations of the time-dependent displacement current requires a self-consistent simulation of the electric field along the device, which demand huge amount of computational resources to deal with the many-body problem. In this conference, the solutions proposed by the group of Dr. Oriols in terms of quantum trajectories, including electron-electron interaction beyond mean field for the direct computation of the particle and displacement currents, will also be presented [1-3]. These difficulties explain why most of the speed predictions for quantum devices are based on the quasi-static approximation that, as we have shown above, can provide quite exaggerated predictions.



# International Workshop on Computational Nanotechnology

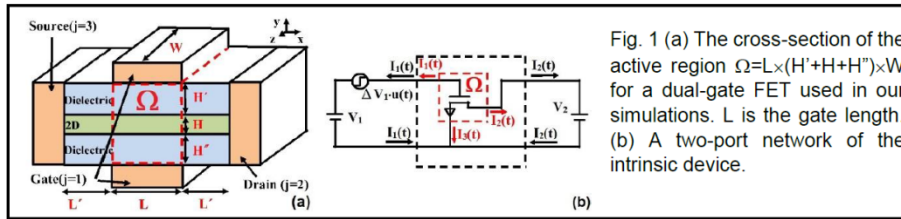


Fig. 1 (a) The cross-section of the active region  $\Omega=L \times (H'+H+H'') \times W$  for a dual-gate FET used in our simulations.  $L$  is the gate length. (b) A two-port network of the intrinsic device.

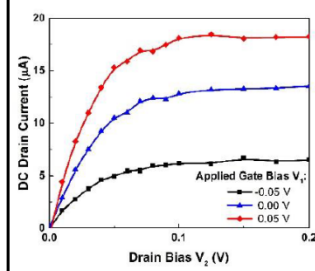
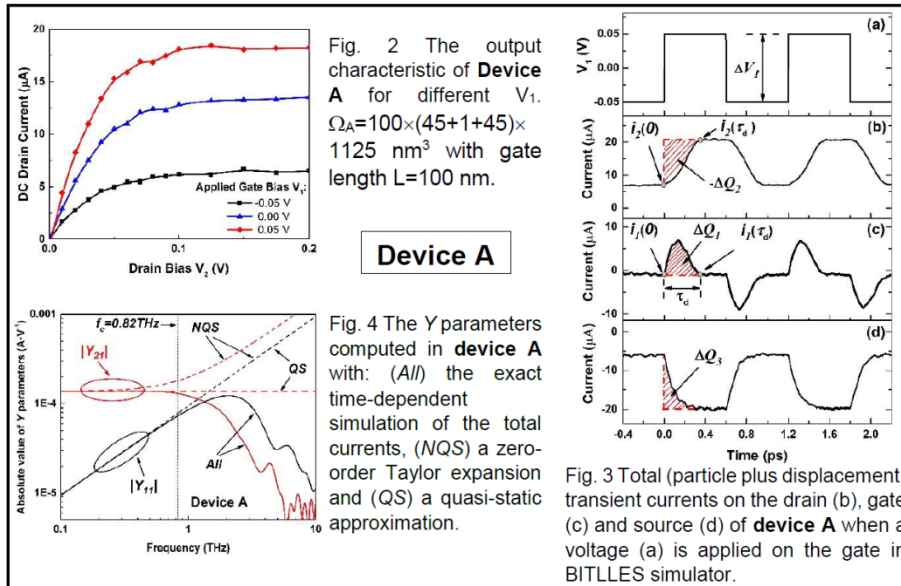


Fig. 2 The output characteristic of **Device A** for different  $V_1$ .  $\Omega_A=100 \times (45+1+45) \times 1125 \text{ nm}^3$  with gate length  $L=100 \text{ nm}$ .

## Device A

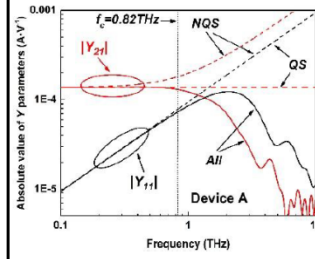


Fig. 4 The Y parameters computed in **device A** with: (All) the exact time-dependent simulation of the total currents, (NQS) a zero-order Taylor expansion and (QS) a quasi-static approximation.

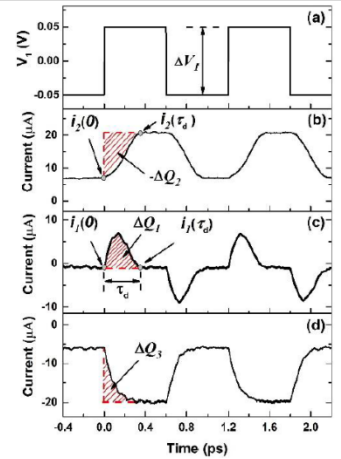


Fig. 3 Total (particle plus displacement) transient currents on the drain (b), gate (c) and source (d) of **device A** when a voltage (a) is applied on the gate in BITLLES simulator.

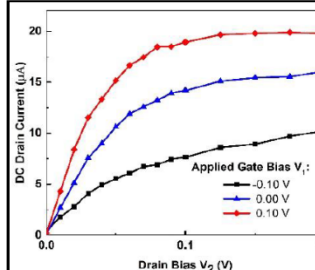
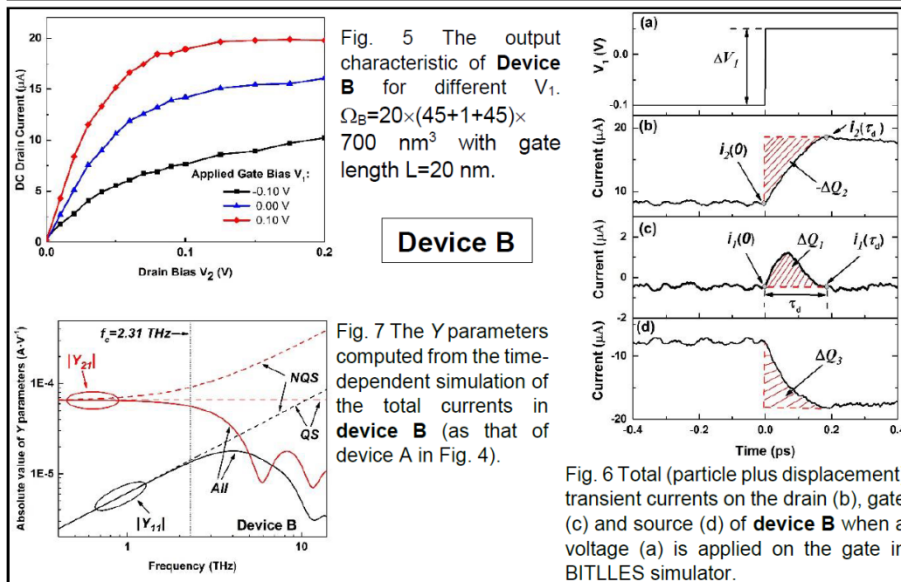


Fig. 5 The output characteristic of **Device B** for different  $V_1$ .  $\Omega_B=20 \times (45+1+45) \times 700 \text{ nm}^3$  with gate length  $L=20 \text{ nm}$ .

## Device B

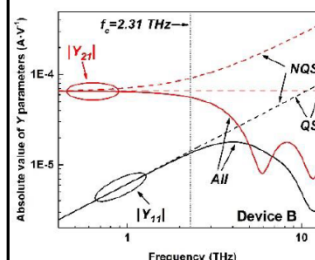


Fig. 7 The Y parameters computed from the time-dependent simulation of the total currents in **device B** (as that of device A in Fig. 4).

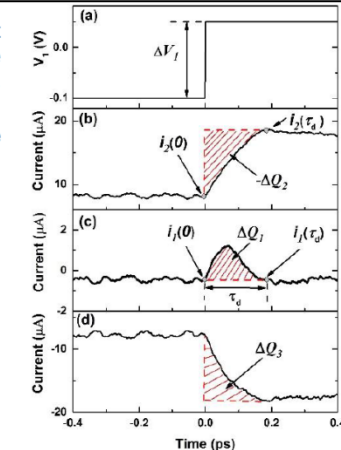
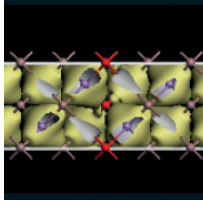


Fig. 6 Total (particle plus displacement) transient currents on the drain (b), gate (c) and source (d) of **device B** when a voltage (a) is applied on the gate in BITLLES simulator.

- [1] X. Oriols, PRL, 98 (2007) 066803.
- [2] D. Marian, N. Zanghì and X. Oriols, PRL, 116 (2016) 110404.
- [3] <http://europe.uab.es/bitlles>.
- [4] Z. Zhan, E. Colomés and X. Oriols, Submitted (2017).



# International Workshop on Computational Nanotechnology

## Multiscale modeling of electrodynamic radiation from quantum monopole antenna

T.M. Philip, B Basa, and M J Gilbert

University of Illinois at Urbana-Champaign, USA

The AC non-equilibrium Green function (NEGF) formalism provides a powerful tool to model the dynamic behavior of electrons in nanoscale devices [2]. Here, we present a novel simulation technique that couples the AC NEGF formulation with the full solution of Maxwell's equations to capture the electrodynamic coupling that is necessary to characterize the high-frequency operation of electron devices. We demonstrate the efficacy of the technique by simulating a quantum wire monopole antenna.

The total retarded Green function, that is, the impulse response of the system Hamiltonian, at energy  $E$  can be expressed as

$$G^r(E) = G_o^r(E) + G_w^r(E), \quad (1)$$

where  $G_o^r(E)$  is the DC retarded Green function and  $G_w^r(E)$  is first-order response due to an AC perturbation. The DC component is calculated via standard NEGF formalism [1].

The AC bias is introduced perturbatively resulting in a small-signal retarded AC Green function  $G_w^r(E)$  at frequency  $\omega$  that is expressed as a product of DC Green functions at energies  $E$  and  $E^+ = E + \hbar\omega$  [2]:

$$G_w^r(E) = G_o^R(E^+) [-eV + \Sigma_\omega^R(E)] G_o^r(E) \quad (2)$$

Here  $V$  is the AC potential profile and  $\Sigma_\omega^R$  is the AC contact self-energy, which is given by

$$\Sigma_\omega^\gamma(E) = \frac{e\pi V_{AC}}{\hbar\omega} [\Sigma_0^\gamma(E) - \Sigma_0^\gamma(E^+)], \quad (3)$$

where  $e$  is the electron charge,  $\gamma = r, <$ ,  $V_{AC}$  is the bias amplitude and  $\Sigma_0^r$  is the typical DC self-energy.

The retarded Green function must be convolved with the lesser self-energy  $\Sigma^<(E)$  to account for the application of the bias and the occupancy of the leads. The resulting AC lesser Green function is written as

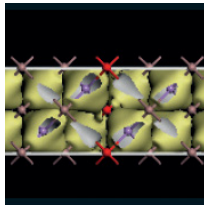
$$\begin{aligned} G_\omega^<(E) = & G_o^r(E^+) \Sigma_0^<(E^+) G_\omega^r(E) + \\ & + G_o^r(E^+) \Sigma_\omega^<(E) G_o^r(E) + \\ & + G_\omega^r(E) \Sigma_0^<(E) G_o^r(E) + \end{aligned} \quad (4)$$

The AC charge and current density is calculated in a similar fashion to DC NEGF by substituting the AC lesser Green function  $G_\omega^<(E)$  for the DC version  $G_0^<(E)$ .

The output charge density,  $\rho$ , and current density,  $\mathbf{J}$ , from AC NEGF is then input into the electrodynamics simulation. We solve directly for the scalar potential,  $V$ , and vector potential,  $\mathbf{A}$ , in the frequency domain using the Lorenz gauge, resulting in the following governing equations:

$$\left(\nabla^2 + \frac{\omega^2}{c^2}\right) V = -\frac{\rho}{\epsilon} \quad (5)$$

$$\left(\nabla^2 + \frac{\omega^2}{c^2}\right) \mathbf{A} = -\mu \mathbf{J} \quad (6)$$



# International Workshop on Computational Nanotechnology

Here,  $c$  is the speed of light,  $\epsilon$  is the electric permittivity,  $\mu$  is the magnetic permeability. Figure 1 illustrates the staggered Yee cell that the fields are solved on using the finite-difference frequency-domain (FDFD) formulation with absorbing boundary conditions [3]. The output scalar potential and vector potential are then reinserted into the Hamiltonian via an on-site energy and a Peierl's phase, respectively. Equations (2)-(6) are iterated in the process described by Fig. 2 until the change in  $V$  on successive iterations is less than  $1 \mu\text{V}$ , our criterion for self-consistency.

Figure 3 illustrates the quarter-wave monopole antenna system we simulate. The antenna is modeled using a 1D metal tight-binding Hamiltonian with hopping energy  $t_0 = 1.5 \text{ eV}$  placed on a perfect conductor in a larger 3D FDFD simulation domain. After self-consistency is achieved, the far-field radiation pattern is calculated using a near-to-far-field transformation. Figure 4 shows the far-field radiation pattern of the antenna operating at 100 GHz, which agrees well with typical quarter wave monopole radiation. The ability of this technique to capture the dynamic radiative fields of an antenna demonstrates its promise to model more complex dynamic light-matter interactions where the quasi-static approximation fails.

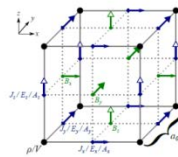


Fig. 1. The FDFD electromagnetic equations are solved on a Yee cell to solve directly for the scalar potential,  $V$ , and the vector potential components,  $A_i$ , generated by the charge density,  $\rho$ , and current density components,  $J_i$ , extracted from AC NEGF. The electric field components,  $E_i$ , and magnetic field components,  $B_i$ , are then computed from the potentials. The side length of the cell is the lattice constant  $a_0 = 37.5 \mu\text{m}$  of the Hamiltonian. This placement guarantees that the currents and charge density from NEGF align exactly with the Yee grid of the FDFD simulation.

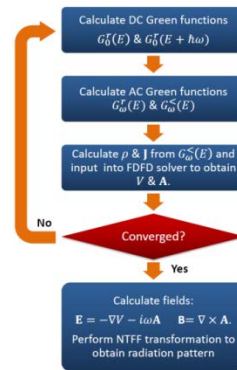


Fig. 2. Solution procedure to achieve self-consistent electrodynamic fields with AC NEGF.

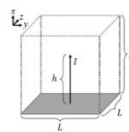


Fig. 3. Monopole radiation is simulated by using AC NEGF to simulate transport in a 1D metal wire with length  $h = 770 \mu\text{m}$  in an FDFD simulation of side length  $L = 1.73 \text{ mm}$ . Perfect electrical conductor electromagnetic boundary conditions are applied on  $y = z$  plane, shown as the solid gray cube face, while absorbing boundary conditions are applied to all other faces, illustrated as transparent faces with dashed edges.

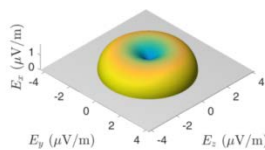
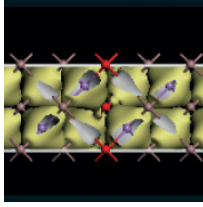


Fig. 4. The far-field radiation pattern at a distance  $r = 1 \text{ cm}$  obtained by performing a near-to-far-field transformation of the electric and magnetic fields outside the wire. We see that the antenna radiates as a quarter-wave monopole thereby demonstrating the ability of this method to capture radiative electrodynamic phenomena.

- [1] R. Lake, G. Klimeck, R. C. Bowen, and D. Jovanovic, "Single and multiband modeling of quantum electron transport through layered semiconductor devices," *J. Appl. Phys.*, vol. 81, no. 12, p. 7845, 1997.
- [2] Y. Wei and J. Wang, "Current conserving nonequilibrium ac transport theory," *Phys. Rev. B*, vol. 79, p. 195315, may 2009.
- [3] R. Luebbers, F. R. Hunsberger, K. S. Kunz, R. B. Standler, and M. Schneider, "A Frequency-Dependent Finite-Difference Time-Domain Formulation for Dispersive Materials," *IEEE Trans. Electro-magn. Compat.*, vol. 32, no. 3, pp. 222-227, 1990.



# International Workshop on Computational Nanotechnology

Session: Quantum Transport

## Non-local scattering with a new recursive nonequilibrium green's function method

J Charles, P Sarangapani, Y Chu, G Klimeck and T Kubis

Purdue University, USA

As modern nanodevice scales continue to shrink, sophisticated modeling methods that cover both coherent quantum mechanical effects and incoherent scattering on device imperfections (i.e. roughness, impurities and lattice vibrations) are needed. The non-equilibrium Green's function (NEGF) theory is widely accepted as one of the most consistent methods to model these phenomenon [1]. Solving the NEGF equations for atomistically resolved devices requires inverting large matrices that often do not fit into memory on modern computers. Efficient algorithms for solving only the relevant portions of the inversion have been developed [2]. In particular the so-called recursive Green's function algorithm (RGF) limits the inversion to the diagonals only. This is sufficient for observables such as charge current and density only when all considered scattering mechanisms are local. However many scattering mechanisms have significant non-local contributions and the state-of-the-art RGF is not appropriate then. This is particularly true for all scattering mechanisms involving the Coulomb interaction, such as scattering on phonons in polar materials and scattering on charged impurities [3]. This work extends the local RGF algorithm to nonlocal RGF which allows the solution of the NEGF equations including incoherent scattering up to an arbitrary number of off-diagonal elements of the Green's functions.

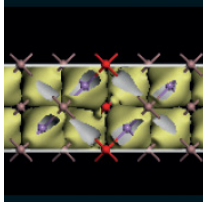
The nonlocal RGF (NL-RGF) method is presented for the first time in this work. It overcomes the constraint that is typically put on solving the NEGF equations in atomistic representations, i.e. the limitation of any scattering effect to the local range only. So far, the solution of the NEGF equations including incoherent scattering is numerically too expensive if solved without the RGF algorithm in local approximation. The so far very common truncation of scattering self-energy matrices to their local component only is typically justified with these numerical constrains only [4], [5]. The starting point for the NL-RGF derivation is the RGF method developed by Anantram and coworkers which is suitable for local scattering only [6]. The RGF method generally includes two main steps after decomposing the device into layers. The first step, the so-called "forward" step, is to solve the one-sided Dyson's equation for  $gR$  recursively through the layers starting with the first layer connected to the first lead. Once the last layer is reached and connected to the other lead, the last diagonal block is now solved exactly for  $GR$ . The other layer's diagonal

block  $GR$  are solved in the second step, the "backward" step. To include effects of scattering on the particle occupancy functions, the lesser Green's function,  $G<$ , is also solved recursively. The local RGF prescribed in Ref. [4] can be thought of as a special case of the  $LDLT$  decomposition method. The forward step for  $gR$  is equivalent to solving the decomposition  $LDLT$  [7].  $D$  and  $L$  are constructed with recursive generator functions. In the block tri-diagonal case,  $L$  is the coupling Hamiltonian between adjacent layers and does not need to be solved explicitly. Note that  $gR$  is the inverse of  $D$ . Once the forward step is done and  $gR$  is solved, the decomposition is used to solve the backward step and it can be shown that:

$$G^R = D^{-1} L^{-1} + (I - L^T) G^R \quad (1)$$

Similar equations can be found for forward  $g<$  and  $G<$  using the  $LDLT$  decomposition. From these decompositions, recursive relations have been determined in this work that are compatible with RGF and allow arbitrary number of off-diagonal blocks for non-local scattering to be solved.

Figure 1 compares the anti-diagonal of the retarded Green's function  $G^R$  for bulk silicon in  $sp3d5s^*$  tight-binding basis for the full inversion case and the non-local RGF when non-local RGF is used to solve for all



# International Workshop on Computational Nanotechnology

off-diagonal blocks. The two methods agree exactly even for far-offdiagonal elements. Figure 2 shows the timing for NL-RGF as a function of the non-locality in the transport direction for a 2 nm Silicon nanowire with a length of 20 nm in a 10 band atomistic tight-binding representation. A best polynomial fit of the simulation time gives a complexity of  $N^{2.4}$ , with  $N$  being the number of nonlocal blocks. Figure 3 shows the memory analysis. The increase in memory as a function of the non-locality in the transport direction is linear as expected, since the number of off-diagonal blocks stored is scaling linearly. This is much less than in the full inversion case, where the memory needed to store the full matrix is about 150 GB (the memory needed to store a complex double matrix with rank 97280). To confirm the non-locality in polar optical phonon scattering is treated correctly, the anti-diagonal of the retarded scattering self-energy for a bulk GaAs system is shown in Fig. 4. Figure 4, also compares the scattering self-energies solved in the new

NL-RGF method with the full inversion results. The fact the results are identical confirms the correctness of the presented method.

The Recursive Green's Function method was augmented to support non-local scattering self-energies. The timing and memory performance was demonstrated on a silicon nanowire in tight-binding with non-local scattering that previously could not be solved due to memory constraints. The correctness of the method was illustrated on polar optical phonon scattering self-energies in bulk GaAs. This algorithm is implemented into the NEGF framework of the nanodevice simulation software NEMO5 (academic open source).

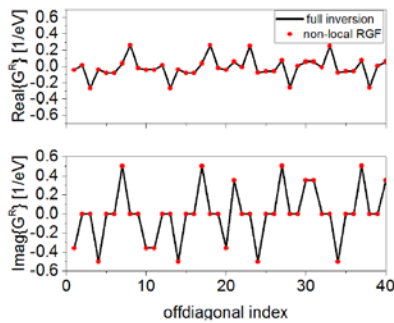


Fig. 1. Comparison of  $G^R$  for full inversion and non-local RGF for bulk silicon in  $sp^3d^5s^*$  tight-binding basis. Orbitals on the same atom are summed for clarity.

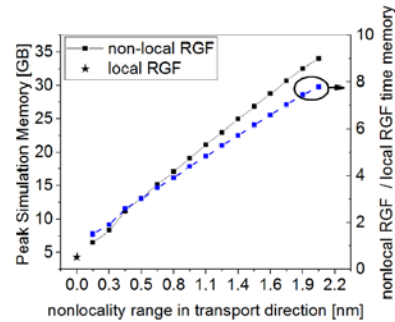


Fig. 3. Memory performance for non-local RGF as a function of non-locality in the transport direction.

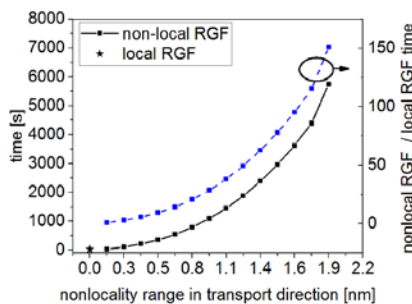


Fig. 2. Timing performance for non-local RGF as a function of non-locality in the transport direction.

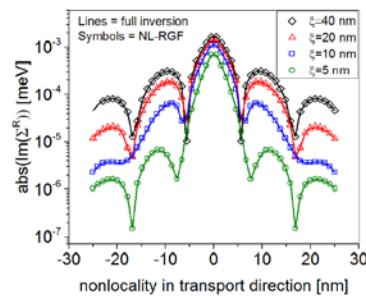
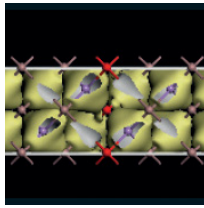


Fig. 4. Non-locality of the imaginary part of  $\Sigma^R$  at an energy  $k_B T$  above the bandedge for different screening lengths. For comparison, the non-locality solved using the NL-RGF method is also shown. Note that due to symmetries only the upper diagonal needs solved in the NL-RGF method.

- [1] S. Datta, Superlattices and Microstructures, vol. 28, no. 4, pp. 253-278, 2000.
- [2] R. Lake, G. Klimeck, R. C. Bowen, and D. Jovanovic, Journal of Applied Physics, vol. 81, no. 12, pp. 7845-7869, 1997.
- [3] T. Kubis, PhD thesis, Verein zur Förderung des Walter Schottky Instituts der Technischen Universität München e.V., Garching, 2009.



## International Workshop on Computational Nanotechnology

- [4] M. Luisier and G. Klimeck, *Journal of Applied Physics*, vol. 107, no.8, p. 084507, 2010.
- [5] M. Luisier and G. Klimeck, *Physical Review B*, vol. 80, no. 15 155430, 2009.
- [6] M. Anantram, M. S. Lundstrom, and D. E. Nikonov, *Proceedings of the IEEE*, vol. 96, no. 9, pp. 1511-1550, 2008.
- [7] Krishnamoorthy, A., Menon, D., *IEEE*, pp. 70-72, 2013.

### Plasmonic response of graphene nanoribbons

F Karimi and I Knezevic

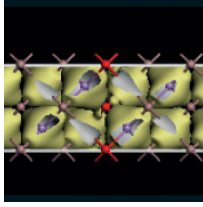
University of Wisconsin-Madison, USA

Plasmonics, as a promising way for shrinking the size of photonic and electronic circuits, has attracted a great interest [1], [2]. Plasmons are collective excitations of surface electrons in a good conductor and can confine the electromagnetic energy beyond the diffraction limit. Conventionally, metals like gold have been used as plasmonic materials; however, because of high dissipation in these materials, plasmons cannot propagate long distances. Graphene [3], [4], a two dimensional semimetallic allotrope of carbon, has high electron mobility and has been of a great interest as a novel plasmonic material [5], [6], [7], [8].

Graphene has a gapless electron band structure with Dirac cones; so, its plasmon dispersion is different from the plasmon dispersion in quasi- two-dimensional (quasi-2D) electron systems with a parabolic band structure. The plasmon resonances in graphene typically fall into the terahertz and mid-infrared range. Unlike in metals, the carrier density in graphene can be controlled by applying a gate voltage, which provides plasmon-resonance tunability. However, it has been shown that gaining tunability by putting graphene on substrate reduces the plasmon propagation length [7]. However, by lowering the system dimension and moving from graphene to graphene nanoribbons, one can decrease the electron scattering rates. Thus, supported graphene nanoribbons (GNRs) have higher electron mobility and offer the tunability feature, as well.

Here, we calculate the plasmon dispersion and plasmon propagation length in armchair graphene nanoribbons (aGNRs) and zigzag graphene nanoribbons (zGNRs) via self-consistent field and Markovian Master equation (SCF-MMEF) [7]. Electrons in supported GNRs, as in every open system, interact with a dissipative environment. SCF-MMEF is able to capture all the concurrent dissipative mechanisms, such as phonons, ionized impurities, surface optical (SO) phonons, the line-edge roughness. We derive the interaction Hamiltonian for electrons and SO phonons in GNRs, and quasi- one-dimensional (quasi-1D) systems in general. The SO phonon and electron interaction only requires the momentum conservation along the length of the ribbon. This means that a single electron transition can be mediated by a number of SO-phonon modes, unlike in the quasi-2D systems. As a result, in narrow GNRs, SO-phonon scattering is as important as ionized impurity scattering for electron transport.

By calculating the dielectric function via the SCF-MMEF, we calculate the loss function for GNRs on the  $\text{SiO}_2$  substrate. The loss function peaks at the plasmon resonances. The higher the peak, the farther the plasmons propagate. In zGNRs, because of heavy carriers (flat energy dispersions) and high scattering rates, plasmons are highly damped and the plasmon propagation length barely exceeds 100 nm. The same behavior happens in  $(3N)$ -aGNRs and  $(3N+1)$ -aGNRs, where  $N$  is an integer and  $3N$  and  $3N+1$  are the number of dimer lines. However, in  $(3N+2)$ -aGNRs, plasmons can propagate up to a micron. In Fig. 1, the loss function of three different  $(3N+2)$ -aGNRs on  $\text{SiO}_2$  is shown. The sheet electron density is  $n_s = 7 \times 10^{12} \text{ cm}^{-2}$ , and the impurity density is  $N_i = 4 \times 10^{11} \text{ cm}^{-2}$ . By increasing the width of the  $(3N+2)$ -



## International Workshop on Computational Nanotechnology

aGNRs, for the same sheet carrier density, the Fermi level increases; as a result, the loss-function peaks get higher and narrower (which equals longer plasmon propagation length). But, this trend stops when the Fermi level approaches the second conduction subband. This trend can be seen in Fig. 1. Also, in aGNRs, unlike in graphene, plasmons are not totally damped below the highest SO phonon mode.

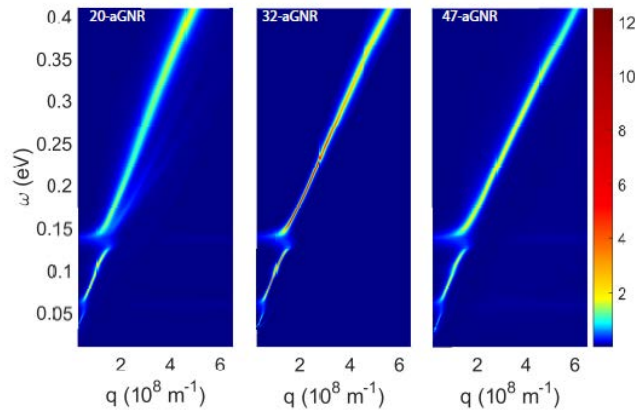
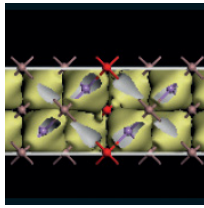


Fig. 1: The loss function of (left) 20-aGNR, (middle) 32-aGNR, (right) 47-aGNR as a function of the wave vector,  $q$ , and frequency,  $\omega$ . The sheet electron density is  $n_s = 7 \times 10^{12} \text{ cm}^{-2}$ , and the impurity density is  $N_i = 4 \times 10^{11} \text{ cm}^{-2}$ . All color bars have the same scale. The loss-function peaks are highest and narrowest in 32-aGNR (middle), which implies a long propagation length.

- [1] S. A. Maiera and H. A. Atwater, Plasmonics: Localization and guiding of electromagnetic energy in metal-dielectric structures, *Journal of Applied Physics* 98, 011101 (2005).
- [2] E. Ozbay, Plasmonics: Merging Photonics and Electronics at Nanoscale Dimensions, *Science* 311, 189 (2006).
- [3] K. S. Novoselov, A. K. Geim, S. V. Morozov, D. Jiang, Y. Zhang, S. V. Dubonos, I. V. Grigorieva, A. A. Firsov, Electric field effect in atomically thin carbon films, *Science* 306, 666 (2004).
- [4] A. K. Geim and K. S. Novoselov, The rise of graphene, *Nat. Mater.* 6, 183 (2007).
- [5] E. H. Hwang and S. Das Sarma, Dielectric function, screening, and plasmons in two-dimensional graphene, *Phys. Rev. B* 75, 205418 (2007).
- [6] M. Jablan, H. Buljan, and M. Soljačić, Plasmonics in graphene at infrared frequencies, *Phys. Rev. B* 80, 245435 (2009).
- [7] F. Karimi, A.H. Davoody, I. Knezevic, Dielectric function and plasmons in graphene: A self-consistent-field calculation within a Markovian master equation formalism, *Phys. Rev. B* 93, 205421 (2016).
- [8] H. Yan, T. Low, W. Zhu, Y. Wu, M. Freitag, X. Li, F. Guinea, P. Avouris, and F. Xia, Damping pathways of mid-infrared plasmons in graphene nanostructures, *Nature Photonics* 7, 394 (2013).



## International Workshop on Computational Nanotechnology

### Nonequilibrium Green's function method: Performance prediction of band-to-band tunneling devices in electron-only representation

Y Chu, P Sarangapani, J Charles, M Povolotskyi, G Klimeck and T Kubis

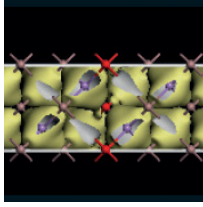
Purdue University, USA

Band-to-band tunneling field-effect transistors (TFETs) have gained great interest since their switching behavior is not affected by the 60mV/decade limit of traditional FETs. This fact makes them promising candidates for low power electronics. The quantitative prediction of TFET performances requires self-consistent solutions of charge distributions and transport equations. The nonequilibrium Green's Function (NEGF) method is widely accepted as a method of choice for this purpose [1]. It is common, however, to consider charge contributions of the conduction and valence band as electron and holes separately [2]. Although it is known to fail for band-to-band tunneling devices [3], this concept is still applied in many TFET studies [4]. In this work, a numerically efficient charge self-consistent model is developed where only electrons are considered throughout all bands – including the deepest lying valence band. Comparison of the common electron-hole picture with the new method shows agreement in standard FETs and systematic deviations in TFETs. Predictions of critical transistor benchmarks such as the transconductance are unreliable in the electron-hole picture.

In band-to-band tunneling valence band electrons tunnel across the semiconductor band gap to the conduction band. A direct implementation of charge self-consistent models of this process with the response of all other electrons requires a numerically expensive discretization of all valence band energies. In the NEGF method, however, the density of particles that are distributed in equilibrium can be solved by applying the residual theorem. With the Gaussian quadrature method, the numerical integration on the complex energy contour converges with only few tens of points [5]. The positive background ionic charge is calculated at equilibrium for every respective device structure. Electrons in nonequilibrium, i.e. those that face unequal lead distribution functions are still solved on the real energy axis. The free charge density of bulk silicon is illustrated in Fig. 1 when solved with the electron-only and the traditional electron-hole representation. It can be seen that the electron-only method matches well with the standard one in cases without pronounced band-to-band tunneling.

The impact of the electron-only charge self-consistent model is easy to see in the example of a silicon ultra-thin body double-gate transistor. The ballistic transfer characteristics  $I_d - V_{gs}$  at  $V_{ds} = 0.1V$  are presented in Fig. 2. The differences in the predicted performance of the traditional and new method can be understood in Fig. 3. The electron density in the bandgap (at positions around 10 nm) is considered as electrons only in the new method, whereas the traditional electron-hole method gives ambiguous charge prefactor assignments to it (indicated by the electron/hole delimiter line in Fig. 3). In consequence, the electrostatic potential around that position differs in the two methods which causes the transmission results (and with them the transfer characteristics) to differ as well (see Fig. 4).

We have developed a charge self-consistent model for quantum transport calculations in TFETs where standard charge self-consistent approaches that distinguish between electrons and holes fail. Although the new model enhances the predictive power of NEGF for band-to-band tunneling devices significantly, it keeps the numerical load virtually unaltered.



# International Workshop on Computational Nanotechnology

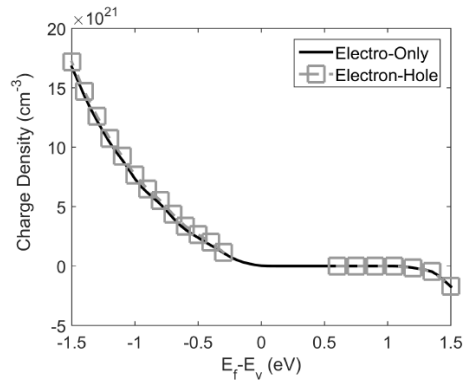


Fig. 1. The free charge density in bulk silicon is calculated in  $sp^3d^5s^*$  tight-binding basis in the new method (black) and the traditional approach (gray). The x-axis indicates the distance between the Fermi level and the top valence band.

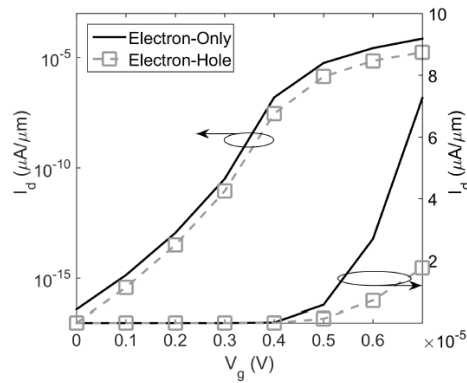


Fig. 2. Transfer characteristics  $I_d - V_{gs}$  at  $V_{ds} = 0.1V$  of a Si Ultra-thin body transistor with a double-gate contact of  $L_g=11$  nm and a thickness of 1.6 nm.

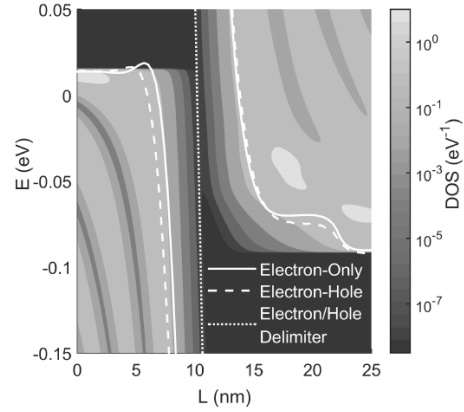


Fig. 3. Contour plot of the energy and position resolved density of states of the TFET simulated in Fig. 2 at  $\Gamma$  point with the new electron-only method. The band-edge of the electron-hole picture and the delimiter line of electron and hole states are represented in dashed and dotted lines. The solid line shows the band profile of the electron-only picture.

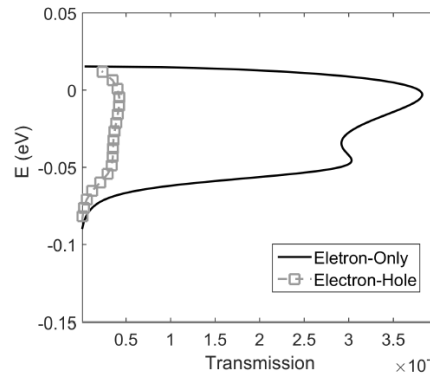
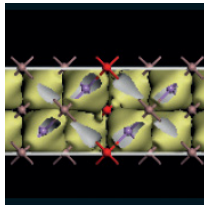


Fig. 4. Transmission at  $\Gamma$  point of the device simulated in Fig. 2.

- [1] S. Datta *Superlattices and Microstructures*, vol. 28, no. 4, pp. 253 - 278, 2000.
- [2] J. Charles and et al. vol. 15, no. 4, pp. 1123-1129, 2016.
- [3] T. Andlauer and et al. *Phys. Rev. B*, vol. 80, p. 035304, Jul 2009.
- [4] M. Luisier and et al. *IEEE Electron Device Letters*, vol. 30, pp. 602-604, June 2009.
- [5] M. Brandbyge and et al. *Phys. Rev. B*, vol. 65, p. 165401, Mar 2002.



## International Workshop on Computational Nanotechnology

### Dissipative NEGF methodology to treat short range Coulomb interaction: Current through a 1D nanostructure

A Martinez<sup>1</sup>, J R Barker<sup>2</sup> and R Di Pietro<sup>3</sup>

<sup>1</sup>Swansea University, UK, <sup>2</sup>University of Glasgow, UK, <sup>3</sup>Hitachi Cambridge Laboratory, UK

In this work a methodology describing Coulomb blockade within the Non Equilibrium Green Function formalism (NEGF) [1] is presented. The method incorporates the short-range coulomb interaction between two electrons [2] through the use of a two-particle Green's function (2pGF). Previous work [3] using the 2pGF in conjunction with NEGF has been carried out. However, the central region of the nanostructure or the quantum dot has no spatial resolution i.e. it is parameterized by the energy level and coupling constants of the dot. Our method intends to describe the effect of electron localization while maintaining an open boundary or extended wave function. It is of paramount importance that the methodology conserves the current through the nanostructure to ensure charge conservation.

The method developed here can be extended to describe recent results [4] on charge transport in polymer semiconductors, where the presence of crystalline and amorphous domains lead to a confinement of charge carriers in nanometer scale crystallites [5].

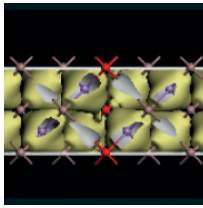
In standard NEGF, the potential energy of the electron is calculated in the mean field approximation. The 2pGF<sup>2</sup> incorporates the short-range electron-electron interaction<sup>3</sup>.

We have tested the methodology using a simple 1D nanostructure. Ballistic and dissipative (phonon scattering) current calculations have been carried out. A current increase is demonstrated when the 2pGF is incorporated. This is due to the shift and splitting of the energy levels caused by electron repulsion inside the structure. The increase of mobility [4] in polycrystalline polymers increases as electron occupation in the nanocrystalites increases. This has been associated with electron-electron coulomb interaction.

Fig. 1 shows the local density of states (LDOS) with and without considering the 2pGF. The short-range Coulomb energy [3] is 100 meV for a case of two electrons occupying the nanostructure. When the 2pGF is neglected, the ground state energy of the structure is lower than the source potential energy. In addition the next confined state energy is too high in energy to influence the current. In the upper panel the 2pGF is considered and as a consequence the ground state energy is lifted over the source potential and enters into the bias bandwidth. This substantially enhances the current by more than 100% as shown in Fig. 2. We have also studied the impact of inelastic phonon scattering. Phonon scattering reduces the current substantially when the 2pGF is included but the impact lessens when it is not included. As mentioned before our calculation conserves the current locally. This can be seen in figure 3 for inelastic electron phonon scattering.

Finally it is important to note that the LDOS show the two poles related to the 1 or 2 electron occupation, both poles are shown at an intermediate occupation number. Figures 4 and 5 show the LDOS for 0.01 eV<sup>2</sup> and 0.1 eV<sup>2</sup> electron-phonon couplings. Note the increase in broadening with increasing coupling.

This preliminary work demonstrates that coulomb blockade like effects can be integrated in a phenomenological way into the standard NEGF formalism. However, the issue of how to address the transition between localization and delocalization of electrons inside an open nanostructure is still unsolved as well as the self-consistent calculation of the local coulomb interaction in the nanostructure.



# International Workshop on Computational Nanotechnology

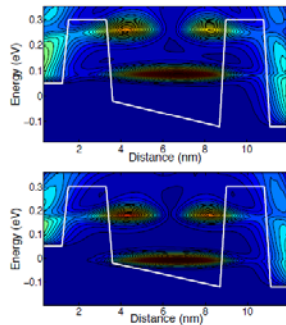


Fig.1 Upper panel: The LDOS including 2pGF. Lower panel: The LDOS without considering the 2pGF, when the electron occupation in the well is 2.

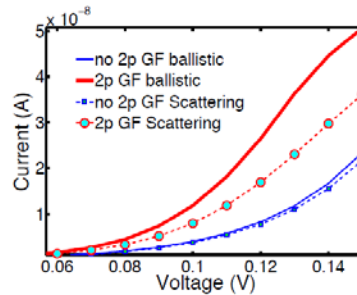


Fig.2 The current voltage characteristics for ballistic and scattering simulations. The simulations shown in red include the 2pGF and the blue neglects it.

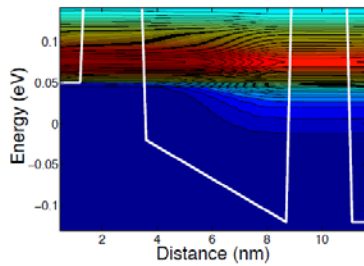


Fig.3. Current spectra through the nanostructure. The current is conserved as can be seen from the figure. The broadening of the distribution on the drain is due to inelastic phonon scattering.

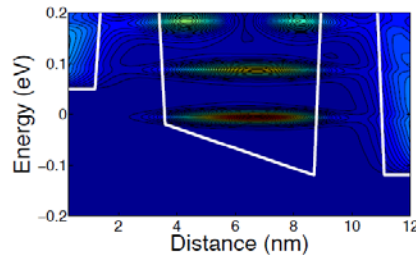


Fig. 4 LDOS for intermediate well occupation ( $0 < \text{occupation} < 2$ ). For an electron interaction coupling strength of  $0.01 \text{ eV}^2$ . The two poles of the LDOS are shown simultaneously in the  $G^R$  function.

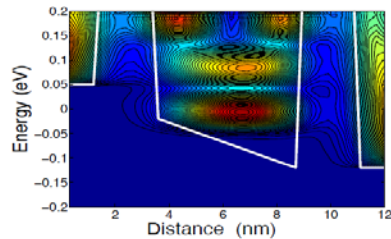
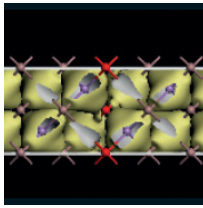


Fig. 5 LDOS for intermediate well occupation ( $0 < \text{occupation} < 2$ ). For an electron interaction coupling strength of  $0.1 \text{ eV}^2$ . The large broadening of the energy levels are a result of strong electron phonon coupling

- [1] A. Svizhenko et al, J. Appl. Phys. 91, 2343 (2002).
- [2] B. Song et al, Phys. Rev. B 76, 155430 (2007).
- [3] J. Hubbard, Proc.Roy.Soc. A 276, 238(1963).
- [4] Di Pietro et al, Adv. Funct. Mater. Accepted for publication (2016)
- [5] R. Noriega, et al, Nature Materials 12, 1038 (2013)



## International Workshop on Computational Nanotechnology

### Equivalent model representation in first-principle transport simulations of nanowire MOSFETs

G Mil'nikov<sup>1</sup>, N Mori<sup>1</sup>, J Iwata<sup>2</sup> and A Oshiyama<sup>2</sup>

<sup>1</sup>Osaka University, Japan, <sup>2</sup>The University of Tokyo, Japan

With continuing advances in semiconductor fabrication technology, it is predicted that the physical channel length in electronic devices will scale down to sub- 10 nm regime. Semiconductor nanowires (NWs) have been recently considered as promising novel devices to realize the scaling merit in the ultra-small scale. However, it is also anticipated that their practical implementation will face technical issues such as characteristics fluctuations. Theoretical study of the device performance of NW transistors requires detailed atomistic transport simulations based on first-principles modeling of semiconductor nanostructures.

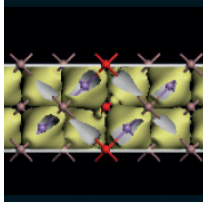
In this presentation, we report on our recent progress in developing a first-principle quantum transport simulator based on the real-space density functional theory (RSDFT) [1] and the Troullier-Martins pseudopotentials [2]. The RSDFT method has been shown to be applicable to large atomic clusters and nanowire structures which enables one to obtain an optimized nanostructure geometry and the Kohn-Sham Hamiltonian in the real-space representation. In this work, we utilize the  $R$ -matrix method [3] and perform RSDFT-based non-equilibrium Green's function (NEGF) transport simulations in ballistic regime

In scope of the  $R$ -matrix method, the computational domain is split into a set of fragments (i.e. small clusters of mesh points) and the  $R$ -matrix propagation algorithm is used for constructing the Green's function in the close device with no leads attached. The contact self-energies are computed independently at the end of calculation. This would generally involve a difficult numerical task of computing all the outgoing/decaying Bloch states in the leads. However, since the current is actually formed by mobile carriers in a few scattering states, one can make use of an appropriate low-dimension equivalent transport model (EM) to obtain the relevant physical solutions within a transport energy interval (Fig. 1). Small size of the EM representation greatly simplifies atomistic transport simulations [4].

We have developed a parallel computer code for constructing the EM representation within an arbitrary finite energy interval. The primary low-dimensional atomistic basis is extracted from a set of Bloch states computed at equidistant set of  $k$ -points in the Brillouin zone by the FEAST method [5]. Extra basis states are further constructed by minimizing the number of branches in the electronic band structure. Effective algorithms have been developed for optimizing parameters in the variational functional [4] and choice of the initial variational state.

The numerical tests in a thin SiNW with diameter of 1 nm have confirmed applicability of the method within a wide energy range in both conduction and valence bands. Figure 2 shows an example of the EM band structure within  $\sim 4$  eV energy window in the SiNW. For an ideal nanostructure, the EM provides an effective quantum chain model with equivalent transport characteristics. In general case, one can still make use of the EM in the lead area in order to compute the equilibrium states in the leads and obtain the contact self-energies in the NEGF formalism. The numerical tests confirm that such mixed EM-RSDFT representation causes no unphysical reflection at the contact interfaces (Fig. 3) and describes correctly the electron transport through the device channel.

Figure 4 presents an example of calculated IV characteristics in a [100] NW MOSFET with 10 nm gate length and 1 nm channel diameter. In these simulations, we have assumed a continuous dielectric layer in the insulator region and used the bulk parameters to account for polarization effects in the device electrostatics. More accurate analysis would require self-consistent calculation of the polarization charge distribution in the nanostructure which can also be greatly accelerated by implementing the EM representation.



# International Workshop on Computational Nanotechnology

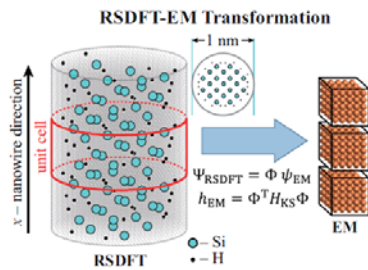


Fig. 1. EM transformation of the RSDFT Hamiltonian. The left panel shows mesh points (small gray dots) in three unit cells of a [100] Si nanowire with diameter of 1 nm. The rectangular  $N_{\text{RSDFT}} \times N_{\text{EM}}$  real-valued basis matrix  $\Phi$  is constructed in order to obtain a computationally inexpensive  $N_{\text{EM}}$ -dimensional model of a quantum chain with Hamiltonian  $h_{\text{EM}}$  which reproduces the scattering states  $\Psi_{\text{RSDFT}}$  within the transport energy interval.

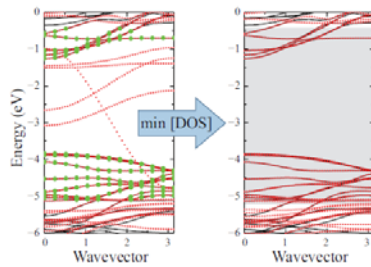


Fig. 2. Constructing the EM basis for RSDFT Hamiltonian in Fig. 1. The solid lines and small red points correspond to the exact RSDFT band structure and the EM approximation, respectively. The large green marks in the left panel represent the original set of atomic Bloch states in the EM model with extra unphysical branches. The right panel shows the final EM band structure obtained by minimizing the number of branches (number of red points) within the shaded area.

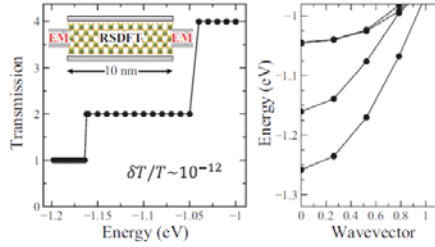


Fig. 3. Transmission function and the band structure in the SiNW in Fig. 1. The exact  $R$ -matrix is propagated through a central "device" area of 10 nm length. The EM representation is only used to compute the outgoing/decaying scattering states in the two leads and construct the contact self-energy. The computed transmission coefficient reproduces the exact (integer) values up to 12 significant digits, indicating the accuracy of the  $R$ -matrix propagation in the first-principle transport calculations.

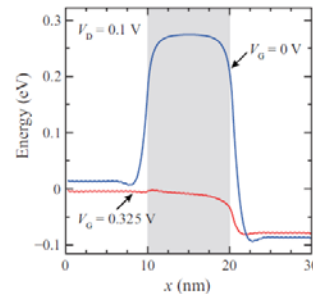
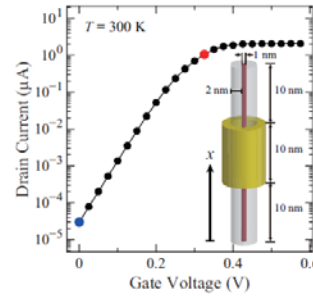
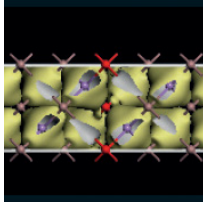


Fig. 4. Current-voltage characteristics and potential profiles in a n-SiNW MOSFET. The first-principle RSDFT method is only used in the silicon core region. The oxide layer in the gate region is treated as a continuous dielectric media, and the device electrostatics is calculated using the bulk parameters  $\epsilon_{\text{Si}} = 11.9$  and  $\epsilon_{\text{SiO}_2} = 3.8$ .

- [1] J.-I. Iwata, D. Takahashi, A. Oshiyama, B. Boku, K. Shiraishi, S. Okada, and K. Yabana, A massively-parallel electronic structure calculations based on real-space density functional theory, *Journal of Computational Physics* 229, 2339 (2010).
- [2] N. Troullier and J. L. Martins, Efficient pseudopotentials for plane-wave calculations, *Physical Review B* 43, 1993 (1991).
- [3] G. Mil'nikov, N. Mori, and Y. Kamakura, R-matrix method for quantum transport simulations in discrete systems, *Physical Review B* 79, 235337 (2009).
- [4] G. Mil'nikov, N. Mori, and Y. Kamakura, Equivalent transport models in atomistic quantum wires, *Physical Review B* 85, 035327 (2012).
- [5] E. Polizzi, Density-matrix-based algorithm for solving eigenvalue problems, *Physical Review B* 79, 115112 (2009).



# International Workshop on Computational Nanotechnology

## First-principles based simulations of si ultra-thin-body FETs with SiO<sub>2</sub> gate dielectric

M Shin and H-E Jung

Korea Advanced Institute of Science and Technology, South Korea

In ultra-thin-body (UTB) field effect transistors (FETs), the gate dielectric layer not only functions as a medium to deliver gate electric fields to the channel region but also gives significant influences on channel electrons. The band-offset between channel and dielectric materials affects the quantum confinement energy levels in the channel, and the charge distributions at the channel and dielectric interface may screen the gate electric fields considerably. However, in the empirical tight-binding method which is a state-of-the-art method to treat UTB FETs at the atomistic level, channel atoms are usually passivated by hydrogen atoms, thus enforcing the hard-wall boundary condition, and oxide atoms are virtual atoms that merely fill up the gate dielectric region. To address the above effects of the gate dielectric in UTB FETs, a first-principles based approach that treats the oxide atoms on an equal footing with the channel atoms is therefore called for.

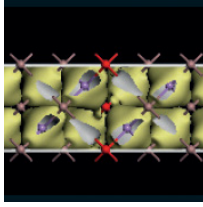
In this work, we have developed a first-principles, density functional theory (DFT) based non-equilibrium Green's function (NEGF) code to simulate Si UTB FETs, fully taking into account all the real SiO<sub>2</sub> atoms in the gate dielectric.

The schematic structure of the double-gate Si UTB FET that we simulate in this work is shown in Fig. 1. Simulations were done in the following three steps: In the first step, to realize the double gate structure at the atomistic level, SiO<sub>2</sub>/Si/SiO<sub>2</sub> unit cell was taken as shown in Fig. 3. Its atomic and electronic structure was obtained by using the openMX DFT package with GGA-PBE functional and a *s2p2d2* atomic orbitals basis set (18 orbitals per atom) for both Si and O atoms. For SiO<sub>2</sub>, crystalline  $\beta$ -cristobalite and  $\alpha$ -quartz phases were realized, and the bridge-oxygen model was adopted at the Si/SiO<sub>2</sub> interface. After full relaxation, the DFT Hamiltonian (H) and overlap (s) matrices of the unit cell were extracted.

In the second step, imported H and s matrices were reduced in size to greatly alleviate the computational burden but without loss of accuracy [1]. This is a crucial enabling step that makes the calculations possible. Stemmed from the periodic boundary condition along the width ( $y$ ) of the UTB device, 40  $k_y$  values uniformly distributed in the Brillouin zone were used in our calculations, and  $H(k_y)$  and  $s(k_y)$  for each  $k_y$  were constructed and transformed. For the unit cell having  $\alpha$ -quartz for the dielectric (Fig. 3(c)), the full Hamiltonian is reduced to around 60 x 60 from its original size of 3240 x 3240, but the band structure is accurately reproduced as seen in Fig. 4.

In the third step, the Hamiltonian matrices and atom coordinates were imported into our in-house NEGF transport simulator. All the Si and O atoms were involved in the charge density and electrostatic potential calculations. After convergence of NEGF and Poisson self-consistent calculations, ballistic current was calculated.

Fig. 5 shows the calculated current-voltage characteristics of the double-gate, n-type Si UTB FET of Fig.1. The device with gate dielectric of  $\beta$ -cristobalite SiO<sub>2</sub> and that of  $\alpha$ -quartz SiO<sub>2</sub> are compared to the device with simple H-passivated Si surfaces and virtual atoms. Our calculations show that the H-passivation results in overestimation of on-state current by 13 % and 33 %, compared to when the  $\beta$ -cristobalite and  $\alpha$ -quartz gate dielectrics, respectively, are put into place. The differences in the band structures and local density of states of the three cases as shown in Fig. 4 can account for the difference in the currents, as the group of subbands indicated by the arrow in the figure is lowered in energy for  $\beta$ -cristobalite and  $\alpha$ -quartz SiO<sub>2</sub>, increasing the density of states and hence lowering the Fermi energy.



# International Workshop on Computational Nanotechnology

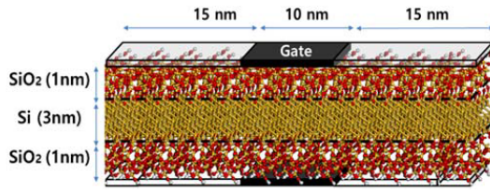


Fig.1 Schematic structure of double-gate Si UTB FET with SiO<sub>2</sub> gate dielectric used in the device simulation. The Si channel of 3 nm thickness is confined in the [001] direction and transport along the [110] direction. The source/drain extensions are 15 nm long with the doping density of 10<sup>20</sup> cm<sup>-3</sup> and the channel region is intrinsically doped.

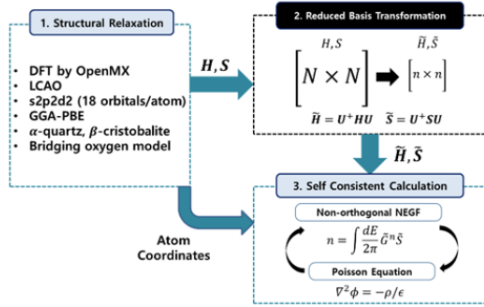


Fig.2 The simulations steps. From the fully relaxed structure, Hamiltonian ( $H$  and  $S$ ) is extracted and fed to the NEGF-Poisson self-consistent routines to compute the drain current. A reduced basis transformation is performed for  $H$  and  $S$  for efficient calculations but without loss of accuracy.

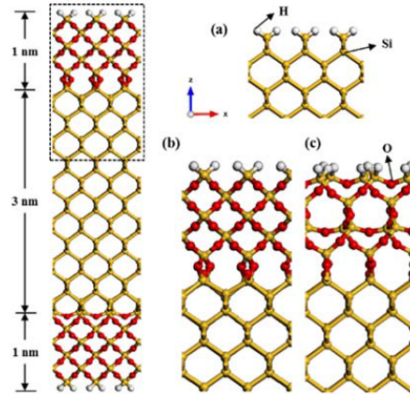


Fig. 3 Atomic models of SiO<sub>2</sub>/Si/SiO<sub>2</sub> super cell used in the DFT relaxation. The 3 nm thick Si region consists of 23 atomic layers grown in the [001] direction, with which 1 nm thick crystalline SiO<sub>2</sub> of (b)  $\beta$ -cristobalite or (c)  $\alpha$ -quartz phase is interfaced. The periodic boundary conditions are imposed in the  $x$  and  $y$  directions while vacuum layers with sufficient thickness are included in the  $z$  direction for the supercell calculation. Hydrogen passivated surfaces are shown in (a).

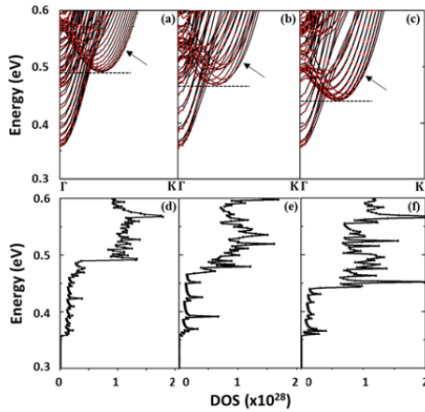


Fig. 4 The conduction band structures of the SiO<sub>2</sub>/Si/SiO<sub>2</sub> unit cells shown in Fig. 3 along the  $\Gamma$  to K direction, with (a) H passivated surface, (b)  $\beta$ -cristobalite SiO<sub>2</sub>, and (c)  $\alpha$ -quartz SiO<sub>2</sub>. Solid lines and dots represent the bands calculated by the original DFT and reduced-sized Hamiltonians, respectively. The conduction band edges are aligned for a comparison purpose. (d), (e), and (f) are the local density of states corresponding to (a), (b), and (c), respectively.

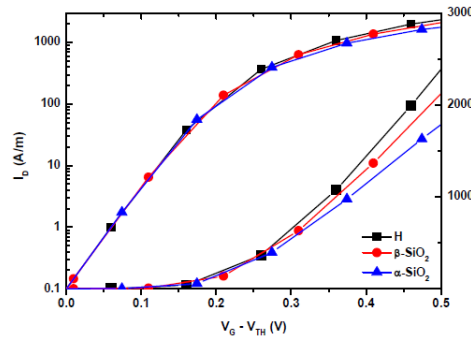
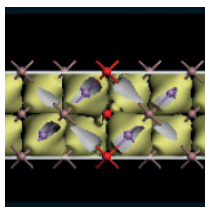


Fig. 5 The calculated current-voltage characteristics of the double-gate, n-type Si UTB FET of Fig.1. The devices with H-passivated surface,  $\beta$ -cristobalite SiO<sub>2</sub>, and  $\alpha$ -quartz SiO<sub>2</sub> are compared. The drain voltage of 0.5 V is applied and the off-current is set to 0.1  $\mu$ A/ $\mu$ m.

[1] M. Shin, W. J. Jeong, and J. Lee, J. Appl. Phys., vol. 119, no. 15, 154505, 2016.



# International Workshop on Computational Nanotechnology

## Session: 2D Semiconductors

### (Invited) Transistors based on heterostructures of 2D materials

G Iannaccone

Università di Pisa, Italy

Native graphene has a zero energy gap and it is therefore not suitable as a transistor channel material for digital electronics. However, recent advances based on materials engineering have demonstrated “*materials on demand*”, with tailored properties. *Vertical heterostructures* of graphene and 2D materials have been proven to be suitable for FETs and hot-electron transistors exhibiting large current modulation.

Inspired by recent progress in the growth of seamless *lateral 2D heterostructures*, lateral heterostructure (LH)-FETs have been proposed, exhibiting extremely promising switching behavior in terms of leakage current, propagation delay, and power-delay product.

We investigate the performance and the scaling perspectives of transistors based on heterostructures of two-dimensional materials against the requirements set by Semiconductor Industry Roadmaps for CMOS (first ITRS and then IRDS). We show that LH-FETs are very promising for high performance logic, down to the 3-5 nm gate length, depending on the types of materials. On the other hand, vertical heterostructure FETs exhibit intrinsic delay times higher by four orders of magnitude, due to large capacitance and poor electrostatics.

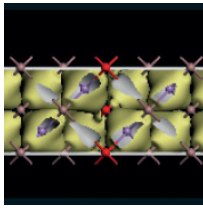
We also address some critical aspects related to the modeling of off-plane and in-plane transport in heterostructures of 2D materials.

### Monte Carlo study of high field transport in some transition metal di-chalcogenides

D K Ferry

Arizona State University Tempe, USA

In recent years, there has been a push to find new materials which may have application in the electronics industry. The monolayer compounds came to the forefront when single layers of graphene were isolated [1]. The success of graphene for some applications has led to the investigation of the monolayer transition-metal di-chalcogenides (TMDCs) [2,3,4]. Indeed, field-effect transistors have been created in some of these TMDCs [5]. Of interest in these materials for device applications are specifically the saturated value of the velocity at high electric fields and the possibility of impact ionization within the channel of the device [5,6]. Recently, we have reported the theoretical study of transport in MoS<sub>2</sub> at moderate to high electric fields [7]. Here, we report the studies of transport at higher electric fields in both MoS<sub>2</sub> and WS<sub>2</sub> with the use of the ensemble Monte Carlo technique. These materials are monolayers in which each layer is composed of Mo or W atoms at the center of the layer and S atoms displaced above and below this center. In bulk form, they have an indirect band gap, which becomes direct only in the monolayer limit. The band extrema are located at the K and K' points of the Brillouin zone, so that there are two minima for the conduction band. Subsidiary valleys of the conduction arise from the residual valleys of what was the indirect gap. These valleys, referred to as the T valleys [8], lie midway between  $\Gamma$  and K on the connecting line between these two points. The conduction band mass is approximately 0.45(0.32) $m_0$  in the K valleys and 0.57(0.52)  $m_0$  in the subsidiary valley for MoS<sub>2</sub>(WS<sub>2</sub>). These satellite valleys lie some 200(50) meV above the K valleys. These bands are non-parabolic, and this has to be taken into account for high field transport. We consider impact ionization initiated in both sets of conduction band valleys with a two-dimensional model based upon our



# International Workshop on Computational Nanotechnology

old work [9]. Scattering of carriers in the K valleys, and between them, is dominated by the acoustic phonons and the homopolar and LO optical phonons, which are scattered via the deformation potential interaction. These are the  $\Gamma$  (intravalley) and K (equivalent intervalley via the LO) phonons responsible for scattering in the K valleys. Scattering between the K valleys and the T valleys is via T point LO phonons. Similarly, the scattering between the various T valleys is by these same phonons. The coupling constants for the various phonon modes have been determined from DFT calculations by Kaasbjerg et al. [10], and we use these values in the computation. We include Coulomb scattering from remote ionized impurities connected with the  $\text{SiO}_2$  upon which the monolayer is deposited. A nominal density of  $0.3\text{--}1.0 \times 10^{12} \text{ cm}^{-2}$ , with a uniform distribution on the surface of the oxide, is assumed. In Fig. 1, the velocity at high fields is plotted for a carrier density of  $2 \times 10^{12} \text{ cm}^{-2}$ . We find that the apparently velocity is weakly dependent upon the carrier density, although it varies more significantly as the impurity density is varied. It is clear that saturation sets in a relatively modest values of the electric field and that there appears to be a slight negative differential conductance (NDC) at higher fields. This effect is not due to intervalley transfer, as most carriers are in the satellite valleys well before the onset of this behavior. It is more likely a result of increased scattering in the two dimensional material and streaming in the distribution function, as we will see below. In Fig. 2, the fraction of carriers that remain in the K and K' valleys is plotted, so that it is clear this is greatly reduced prior to the onset of the NDC. In Fig. 3, the distribution function at two different values of the field are shown for  $\text{WS}_2$ . At the higher field, the distribution is deviating from a thermal behavior and exhibiting streaming which can contribute to the NDC as the carriers move to higher energies and therefore more scattering in the non-parabolic bands. Finally, in Fig. 4, we plot the observed generation rate for impact ionization as a function of the inverse field. The linear behavior on this plot is a sign of this effect being due to quasi-ballistic carriers, the so-called “lucky electron” model [11].

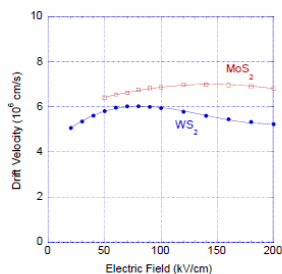


Fig. 1 Velocity as a function of the electric field.

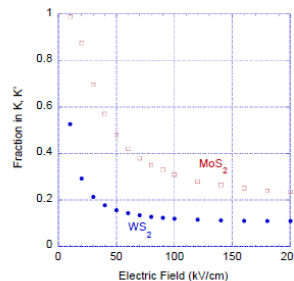


Fig. 2 Fraction of carriers that remain in the K and K' valleys.

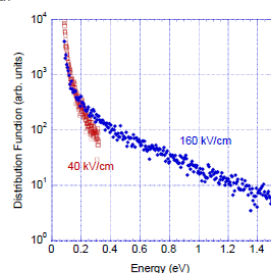


Fig. 3 Distribution function for two fields in  $\text{WS}_2$ .

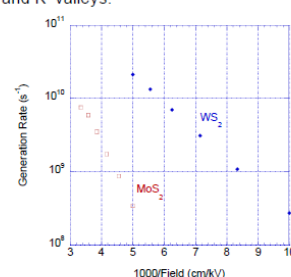
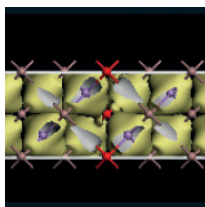


Fig. 4 Impact ionization generation rates as a function of the inverse field.

- [1] Castro Neto A H, Guinea F, Peres N M R, Novoselov K S and Geim A K 2009 *Rev. Mod. Phys.* 81 109.
- [2] Ayari A, Cobas E, Ogundadegbe O, and Fuhrer M S 2007 *J. Appl. Phys.* 101 014507
- [3] Lebègue S and Eriksson O 2009 *Phys. Rev. B* 79 115409
- [4] Carvalho A and Castro Neto A H 2014 *Phys. Rev. B* 89 081406



## International Workshop on Computational Nanotechnology

- [5] See, e.g. He G, Singiseti U, Ramamoorthy H, Somphonsane R, Bohra G, Matsunaga M, Higuchi A, Aoki N, Najmaei S, Gong Y, Zhang X, VAjtai R, Ajayan P M, and Bird J P 2015 *Nano Lett.* 15 5052, and references therein
- [6] Ferry D K 1975 *Phys. Rev. B* 12 2361
- [7] Ferry D K 2016 *Semicond. Sci. Technol.* 31 11LT01
- [8] The notation here is that of Slater J C 1965 *Quantum Theory of Molecules and Solids Vol. 2* (New York: McGraw-Hill) p 347 ff; others have used the notation Q for this point
- [9] Curby R C and Ferry D K 1973 *Phys. Stat. Sol. (a)* 15 319
- [10] Kaasbjerg K, Thygesen K S and Jacobsen K W 2012 *Phys. Rev. B* 85 115317
- [11] Ferry D K 1991 *Semiconductors* (New York: Macmillan) Sec. 11.1

### Stark effect in the photoluminescence of transition metal dichalcogenide structures

K-C Wang<sup>1</sup>, T K Stanev<sup>1</sup>, D Valencia<sup>1</sup>, J Charles<sup>1</sup>, P Sarangapani<sup>1</sup>, A Henning<sup>2</sup>, V K Sangwan<sup>2</sup>, A Lahiri<sup>1</sup>, M Povolotskyi<sup>1</sup>, A Afzalian<sup>3</sup>, G Klimeck<sup>1</sup>, M Lundstrom<sup>1</sup>, M C Hersam<sup>2</sup>, L J Lauhon<sup>2</sup>, N P Stern<sup>1</sup>, and T Kubis<sup>1</sup>

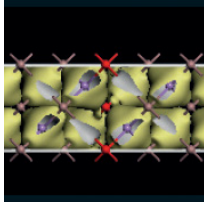
<sup>1</sup>Purdue University, USA, <sup>2</sup>Northwestern University, USA, <sup>4</sup>TSMC, Belgium

Transition metal dichalcogenides (TMDs) are promising material candidates for next generation nanodevices due to few-atom device thickness and best imaginable gate control. In contrast to e.g. graphene, TMD offers a finite band gap which makes it suitable for transistors [1]. Van der Waal bonded layers are interesting for thin and flexible photovoltaics [2]. To identify the interlayer coupling, the band structure variation with different layer thicknesses and its gate field dependence is assessed here.

The electronic Hamiltonian and basis functions of density functional theory simulations (GGA with PBE [3] using the VASP software [4]) are used (within the Wannier90 software [5]) to extract an electronic Hamiltonian of a TMD unit cell in MLWF representation. This unit cell Hamiltonian is repeated in the NEMO5 software [6] to generate a real-size device Hamiltonian and solve for electronic densities. For charge self-consistency, the Schrödinger equation is iteratively solved with the Poisson equation in sub-atomic resolution, simplifying the spatial shape of Wannier functions with Gaussian functions ( $\sigma = 0.6 \text{ \AA}$ ). All assessed structures are close to the experimental setups of Ref. [2] with the same oxide capacitance and gate voltage.

The equivalent oxide thickness is set to be 300nm. The channel consists of one to ten layers of MoS<sub>2</sub> with doping deducted from current measurement. On the gate side, a Dirichlet boundary condition is used to set the gate voltage value. The top side is exposed to vacuum and a Neumann boundary condition of flat band (zero electric field) is applied.

Using the relaxed lattice, MLWF-calculated bandstructures are found to agree with ab-initio calculations for any TMD layer thickness [7]. The conduction band minimum in 2D momentum space is shown in agreement with Ref.[9] Two inequivalent valleys exist with non-isotropic and layer dependent effective masses (in agreement with Ref.[9]), K and Q valley are the lowest for the conduction while K and  $\Gamma$  highest for the valence band. With increasing layer thickness, the band edge shifts from K to Q (K and  $\Gamma$ ) valley around 2 layer for the conduction(valence) bands as shown in Fig. 2. Fig. 3 compares the bandstructure of a 5-layer thick MoS<sub>2</sub> system with and without a finite gate bias applied. Without electric fields, the K-valley is 5-fold degenerate. The finite gate field lifts this degeneracy and reduces the energy separation between K and Q valleys. This indicates the wavefunction localization differs for different valleys and the bandgap is tunable with electric gate fields. This is observed in Fig. 4 with a red shift of the PL spectrum - in good agreement with experimental data.



# International Workshop on Computational Nanotechnology

The nanodevice simulation tool NEMO5 was altered to accurately describe TMD in MLWF representation with ab-initio accuracy. Distinct valleys are tunable with layer thickness and applied gate voltage. Localized wavefunction of the K valley can cause a stark effect measurable with PL.

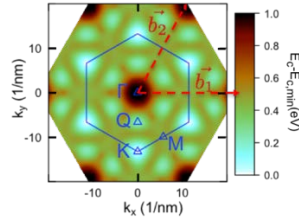


Fig. 1. Contour graph of the minimum of the conduction band for mono-layer MoS<sub>2</sub>. The red hexagon depicts the first Brillouin zone.

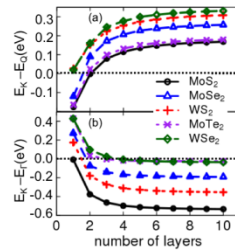


Fig. 2. Energy difference between the (a) K and Q valleys of the conduction band and (b) K and  $\Gamma$  for the valence band of different number of layer TMDs.

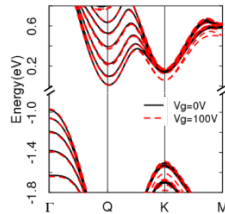


Fig. 3. Bandstructures of a 5-layer MoS<sub>2</sub> with and without finite gate voltage. The gate field lifts the degeneracy at the K valley while other valley unaltered.

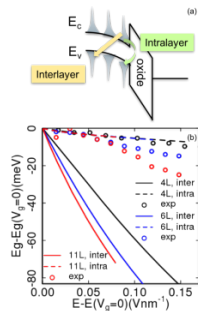
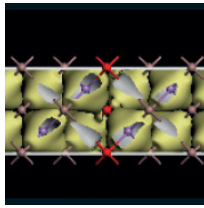


Fig. 2. (a) Schematic of the inter-layer and intra-layer bandgaps extraction. (b) The direct bandgap is biased via gate voltage. Both interlayer and intralayer bandgaps are extracted for 4,6, and 11 layers with different electric field at the oxide interface. Experimental bandgaps extracted from the PL measurement shows closer shifting to the intralayer bandgap.

[1] B. Radisavljevic, A. Radenovic, J. Brivio, V. Giacometti, and A. Kis, Nat. Nanotechnol. 6, 147 (2011).



## International Workshop on Computational Nanotechnology

- [2] S. L. Howell, D. Jariwala, C.-C. Wu, K.-S. Chen, V. K. Sangwan, J. Kang, T. J. Marks, M. C. Hersam, and L. J. Lauhon, *Nano Lett.* 15, 2278 (2015).
- [3] J. Perdew, K. Burke, and Y. Wang, *Phys. Rev. B* 54, 16533 (1996).
- [4] G. Kresse and J. Furthmüller, *Phys. Rev. B* 54, 11169 (1996).
- [5] N. Marzari and D. Vanderbilt, *Phys. Rev. B* 56, 12847 (1997).
- [6] S. Steiger, M. Povolotskyi, H. H. Park, T. Kubis, and G. Klimeck, *IEEE Trans. Nanotechnol.* 10, 1464 (2011).
- [7] Á. Szabó, R. Rhyner, and M. Luisier, *Phys. Rev. B* 92, 1 (2015).
- [8] F. Jellinek, G. Brauer, and H. Müller, *Nature* 185, 376 (1960).
- [9] H. Heo, J. H. Sung, S. Cha, B.-G. Jang, J.-Y. Kim, G. Jin, D. Lee, J.-H. Ahn, M.-J. Lee, J. H. Shim, H. Choi, and M.-H. Jo, *Nat. Commun.* 6, 7372 (2015).

### Theoretical study of charge transport in mono- and bi-layer phosphorene using full-band Monte Carlo simulations

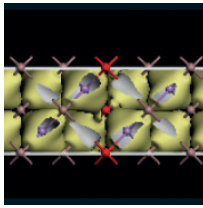
G Gaddemane, W G Vandenberghe, and M V Fischetti

The University of Texas at Dallas, USA

Phosphorene, single- or few-layer black phosphorous, has been recently added to the family of two-dimensional (2D) materials of interest for nanoelectronics applications. Indeed, phosphorene, like graphene and unlike buckled 2D materials, maintains horizontal ( $\sigma_h$ ) symmetry. Therefore, the coupling between electrons/holes and out-of-plane acoustic (ZA) phonons vanishes at first order [1], [2], thus suggesting good phonon-limited charge transport properties. However, reported theoretical estimates of the carrier mobility appear to be excessively optimistic. Indeed, the Bardeen-Shockley deformation potential theorem [3], used to evaluate the electron-phonon coupling, despite its success when applied to well-known materials, often ignores the anisotropy of the matrix elements and wavefunction overlap-integral. Using such a simplified form of the deformation potentials, and also considering only acoustic intravalley processes, mobilities in the range of 700-1100 (300-600)  $\text{cm}^2/\text{Vs}$  have been calculated for electrons (holes) in mono-layers [4], [5]. On the contrary, calculations performed by employing the full matrix elements yield significantly less satisfactory results,  $\approx 172 \text{ cm}^2/\text{Vs}$  for both electrons and holes [6]. Here, by implementing full *ab initio*-based electron/hole-phonon scattering on an extremely fine grid and using the Monte Carlo method, we calculate the phonon-limited mobility and high-field characteristics for mono-layer and bilayer phosphorene.

*Electron and phonon dispersion.* In our study, we obtain the band-structure (Fig. 1) from the density-functional theory (DFT) Vienna *Ab initio* Simulation Package (VASP) [7] and phonon spectra (Fig. 2) from the PHONOPY computer program [8]. The relaxed lattice constants obtained are  $4.62 \text{ \AA}$  and  $3.30 \text{ \AA}$  for mono-layer and  $4.52 \text{ \AA}$  and  $3.30 \text{ \AA}$  for bi-layer phosphorene. The estimated band gaps are 0.90 eV and 0.50 eV for mono- and bi-layers, respectively. For the bi-layer, the Van der Waals gap obtained is  $3.50 \text{ \AA}$ . We find low energy optical modes in bi-layer which are inter-layer modes. Two  $k$ -space grids, fine and coarse ( $0.004 \text{ \AA}^{-1}$  and  $0.013 \text{ \AA}^{-1}$ ) for the electronic band structure and  $0.013 \text{ \AA}^{-1}$  for the phonons) created on the Brillouin Zone, has been used to calculate and tabulate the electronic and phonon dispersions.

*Calculation of electron-phonon scattering rates.* The scattering rates are calculated numerically using Fermi's Golden rule. The deformation potentials are calculated by full *ab initio* calculations [9] on two grids, fine and coarse, with a size of  $0.04 \text{ \AA}^{-1}$  and  $0.16 \text{ \AA}^{-1}$  respectively. The density of states is computed using



# International Workshop on Computational Nanotechnology

the 2D version of the Gilat- Raubenheimer algorithm [10]. The scattering rates calculated as a function of carrier kinetic energy, having performed an angular average, are shown in Fig. 3 and Fig. 4.

*Charge transport.* The Boltzmann transport equation is solved numerically using the full- band ensemble Monte Carlo algorithm to obtain the velocity-field and energy-field characteristics. The evaluation of the carrier mobility has been performed by evaluating the diffusion constant  $D$ , a procedure that is less affected by stochastic noise [11]. The mobility can then be extracted from  $D$  using the Einstein relation.

The velocity-field and energy-field characteristics for transport along the armchair direction for mono- and bi-layer phosphorene are shown in Figs. 5 and 6.

The 300K mobilities for mono-layer and bi-layer are 146 (55)  $\text{cm}^2/\text{Vs}$  and 175 (12)  $\text{cm}^2/\text{Vs}$  for electrons (holes) along the armchair direction and 20 (5)  $\text{cm}^2/\text{Vs}$  and 20 (2)  $\text{cm}^2/\text{Vs}$  for electrons (holes) along the zigzag direction. For monolayers these values are in agreement with Ref. [6] but are much lower than those calculated in Refs. [4] and [5] using isotropic deformation potentials. Note in Figs. 5 and 6 the negative differential mobility resulting from  $\Gamma - Q$  intervalley scattering, more noticeable in bilayers because of the smaller energetic separation of these valleys (see Fig.1). Compared to monolayer phosphorene, the higher scattering rate with optical phonons is due to the presence of low-energy inter- layer optical modes. In conclusion, the results obtained do not seem encouraging for the potential use of phosphorene as FETs.

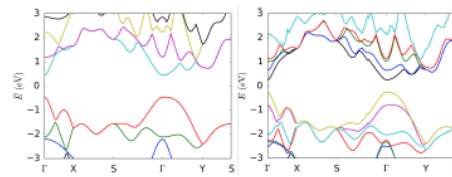


Fig. 1: Electronic band structure of monolayer (left) and bilayer (right) phosphorene obtained using the DFT package VASP[7]

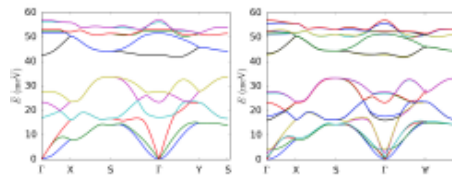


Fig. 2: Phonon dispersion in monolayer (left) and bilayer (right) phosphorene obtained using the PHONOPY program[8]

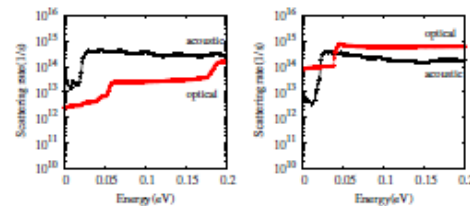


Fig. 3: Electron-phonon (left) and hole-phonon (right) scattering rates at 300 K for monolayer phosphorene.

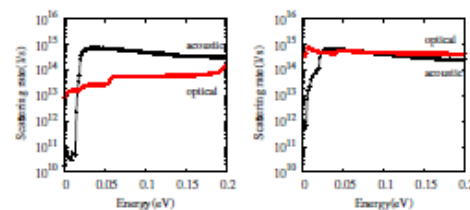
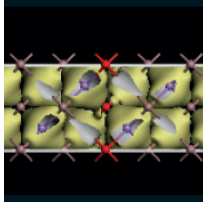


Fig. 4: As in Fig. 3, but for bilayer phosphorene.



# International Workshop on Computational Nanotechnology

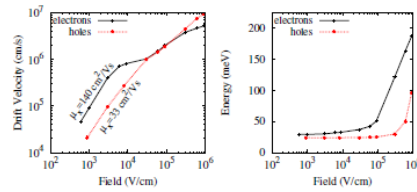


Fig. 5: Drift velocity (left) and average kinetic energy (right) in monolayer phosphorene at 300 K as a function of electric field. Note the negative differential mobility due to strong  $\Gamma-Q$  intervalley scattering.

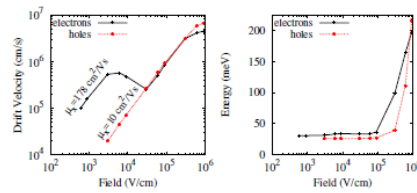
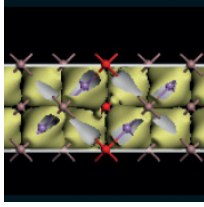


Fig. 6: As in Fig. 5, but for bilayer phosphorene. The negative differential mobility is even more noticeable.

- [1] N. D. Mermin and H. Wagner, Phys. Rev. Lett. 17, 1133 (1966); P. C. Hohenberg, Phys. Rev. 158, 383,(1967).
- [2] M. V. Fischetti and W. G. Vandenberghe, Phys. Rev.B 93, 155413 (2016).
- [3] J. Bardeen and W. Shockley, Phys. Rev. B 80, 72 (1950).
- [4] J. Qiuo, X. Kong, Z.-X. Hu, F. Yang, and W. Ji, Nat. Comm. 5, 4475 (2014).
- [5] A. N. Rudenko, S. Brener, and M. I. Katsnelson, Phys. Rev. Lett., 116, 246401 (2016).
- [6] B. Liao, J. Zhou, B. Qiu, M. Dresselhaus, and G. Chen, Phys. Rev. B 91, 235419 (2015).
- [7] G. Kresse and J. Hafner, Phys. Rev. B 47, RC558 (1993); G. Kresse and J. Furthmüller, Comput. Mat. Sci. 6, 15 (1996); G. Kresse and J. Furthmüller, Phys. Rev. B 54, 11169 (1996)
- [8] A. Togo, I. Tanaka, Scr. Mater. 108, 1 (2015).
- [9] W. G. Vandenberghe and M. V. Fischetti, Appl. Phys. Lett. 106, 013505 (2015).
- [10] G. Gilat and L. J. Raubenheimer, Phys. Rev. 144, 390 (1966).
- [11] C. Jacoboni and L. Reggiani, Rev. Mod. Phys. 55, 645 (1983).



# International Workshop on Computational Nanotechnology

## Effects of uniaxial strain on phosphorene tunneling field-effect transistors

J Seo, S Jung, and M Shin

Korea Advanced Institute of Science and Technology, South Korea

Black phosphorus (BP) field-effect transistors (FETs) show high on/off current ratio and high mobility, thus making BP a promising candidate for future FETs. Theoretical studies predict that single layer BP (phosphorene) tunneling FETs (TFETs) exhibit steep subthreshold swing (SS) and high on-current ( $I_{ON}$ ). In this work, we perform a first-principles-based quantum transport simulation to investigate the effects of uniaxial strain on phosphorene TFETs.

Phosphorene has a puckered honeycomb structure as shown in Fig. 1(a). We calculate the band structure of strained phosphorene by employing density functional theory (DFT) with the openMX code [1]. The uniaxial strain is imposed along the zigzag direction.

For quantum transport simulation of phosphorene TFETs (Fig.1(c)), the non-orthogonal DFT Hamiltonians are extracted for each strained structure of phosphorene.

The DFT Hamiltonians are reduced in size by the approach in [2] to alleviate the computational cost but without the loss of the accuracy. The Hamiltonians are imported into our in-house quantum transport simulator based on the non-equilibrium Green's function method [2].

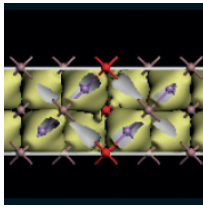
The anisotropic band structures of phosphorene are shown in Fig. 2. The unstrained phosphorene has a direct band gap of 0.92 eV. The band gap and effective masses of electron ( $m_e^*$ ) and hole ( $m_h^*$ ) are altered by the strain as shown in Fig. 2 and Fig. 3. Especially, it is found that ( $m_e^*$ ) of both armchair direction (AD) and zigzag direction (ZD) is dramatically changed at the strain of 4%, where the band switching between the first and second conduction bands occurs. Over 8% tensile strain, the band gap at the  $\chi$  point, which is located between  $\Gamma$  and X points (see Fig. 1(b)), becomes comparable to that at  $\Gamma$  point.

The compressive strain enhances the current of both AD and ZD TFETs due to the band gap narrowing as shown in Fig. 4(a). However, it is difficult for AD and ZD TFETs to be used as low power devices under the compressive strain, because AD TFETs cannot satisfy off-current ( $I_{OFF}$ ) requirement of  $10^{-5}$   $\mu\text{A}/\mu\text{m}$  for low standby power (LSTP) application and ZD TFETs still show low current level due to heavy  $m_e^*$  and  $m_h^*$ .

Fig. 4(b) shows the transfer curves of phosphorene TFETs under the tensile strain. Unlike the case of the compressive strain, the band gap increases with the tensile strain of up to 4%, thus deteriorating the current levels of both AD and ZD TFETs. However, over the tensile strain of 4%, the performances of ZD FETs become similar to those of AD TFETs. This is because the band switching drastically reduces  $m_e^*$  along ZD but increases  $m_e^*$  along AD, changing the tunneling probability.

Fig. 5 shows  $I_{ON}/I_{OFF}$  ratio as a function of  $I_{OFF}$  for different tensile strain. Under the tensile strain, both AD and ZD TFETs meet  $I_{OFF}$  requirement of LSTP devices. Moreover, over 8% strain, they can be operated as high performance (HP) devices with  $I_{OFF}$  of 0.1  $\mu\text{A}/\mu\text{m}$ , albeit with low  $I_{ON}/I_{OFF}$  ratio. This is because the  $\chi$  point contributes to the current (see Fig. 2). Nevertheless, Fig. 6 shows that SS is kept below 40 mV/dec under the tensile strain.

In summary, the uniaxial strained phosphorene TFETs are investigated by DFT-based NEGF calculations. We found that as the tensile strain is applied over 4%, the performance of ZD TFETs reaches that of AD TFETs due to the band switching.



# International Workshop on Computational Nanotechnology

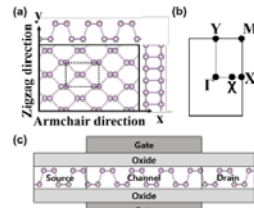


Figure 1. (a) Atomic structure and (b) the first Brillouin zone of phosphorene. Dotted box represents a primitive unit cell of phosphorene. (c) Schematic structure of phosphorene TFET. Channel length and equivalent oxide thickness are 10 and 0.5 nm, respectively. Drain voltage is set to 0.5 V.

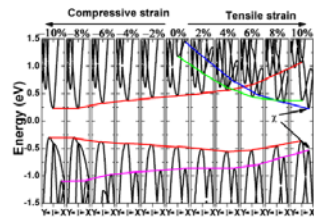


Figure 2. Band structures of phosphorene under uniaxial strain. The band gap decreases with increasing compressive strain, but increases with tensile strain of up to 4%. The band switching between the first and second conduction bands is observed at 4%, after which the band gap decreases. Over 8% tensile strain, the direct band gap at the  $\gamma$  point, which is located on  $\Gamma$ -X valley (see Fig. 1(b)), becomes comparable to that at the  $\Gamma$  point.

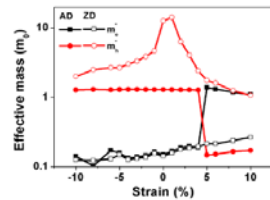


Figure 3. Effective masses of electron ( $m_e^*$ ) and hole ( $m_h^*$ ) as a function of strain.  $m_e^*$  is dramatically changed at 4% tensile strain due to the band switching (see Fig. 2).

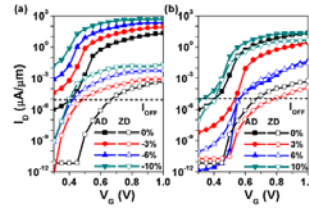


Figure 4. Transfer characteristics of phosphorene TFETs under compressive strain.  $I_{OFF}$  is  $10^{-5}$   $\mu\text{A}/\mu\text{m}$  for LSTP devices. The current levels of AD and ZD TFETs increase with the compressive strain. Below 4% strain, the current levels of AD and ZD TFETs decrease with increasing tensile strain. Over 4% strain, the current levels of ZD TFETs become comparable to those of AD TFETs.

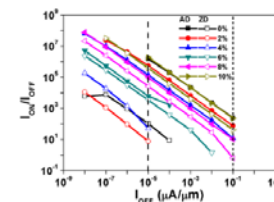


Figure 5.  $I_{ON}/I_{OFF}$  as function of  $I_{OFF}$  for different tensile strain. Dashed and short-dashed lines represent LSTP and HP applications, respectively.

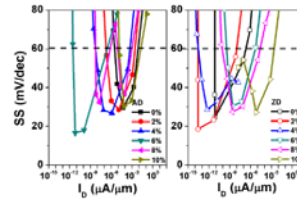
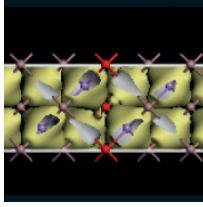


Figure 6. SS versus  $I_D$ . Under the tensile strain, SS is kept lower than 40 mV/dec.

- [1] T. Ozaki *et al.*, *Phys. Rev. B*, 72, 045121 (2005).
- [2] M. Shin *et al.*, *J. Appl. Phys.*, 119, 154505, (2016).



# International Workshop on Computational Nanotechnology

## Understanding resistive switching mechanism of interfacial phase change memory by topological super-lattice and topological phase of interface states

H Nakamura

National Institute of Advanced Industrial Science and Technology (AIST), Japan

We performed first principles electric transport simulation of nano-scale interfacial phase change memory (iPCM) device, which consists of Ge, Sb and Te super-lattice (GST-SL) as resistive switching layer (RSL). GST-SL consists of the ordered layers of  $Sb_2Te_3$  quintuple layers (QLs) and GeTe layers. Since phase change of iPCM is crystalline-crystalline transition, loss of enthalpy is quite small during SET/RESET processes. However, the High and Low Resistance State (HRS/LRS) is still under debates. To argue the HRS/LRS, we examined first-principles nonequilibrium Green's function theory (NEGF). In the present study, we adopted the device model of  $W/[(QL)_m(GeTe)_n]/(QL)_2/W$ , where (m,n) is (2,2) and / is set to 3 and 9 to check device-scale dependence of resistance. Though strong interlayer mixing is reported in some of recent studies, it is convinced that structural transition is within GeTe layer for iPCM when m and n is sufficiently small. We took three phases, inverted-Petrov, Ferro-GeTe, and Petrov, respectively, as shown in Figure 1. By analyzing calculated IV characteristics, we found that spin-orbit interaction is important to the ratio of high and low resistances in low bias regime, in particular, if resistive switch is triggered by field-driven bipolar mode.

It is also known that GST-SL is 3D strong topological insulator (TI). Furthermore, GST-SL is multilayer of TI (=QL) and normal insulator (=GeTe) layers: thus the 2D interface state confined in the RSL can be also topologically non-trivial. We construct simple effective Hamiltonian and calculates topological phase diagram of RSL as shown in Fig. 2. Comparing with our first-principles data, we discuss an alternative new device function using topological phase transition, not structure transition.

Figure 1. The detail structures of GST-SL of each structural phase.

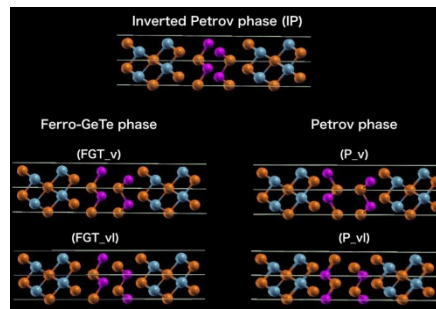
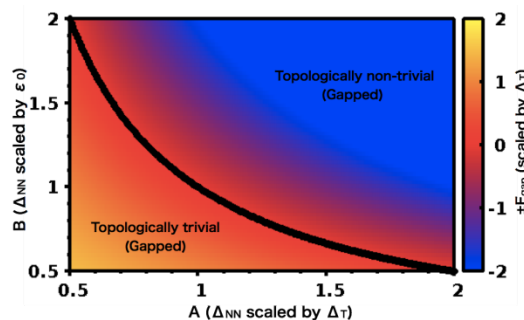
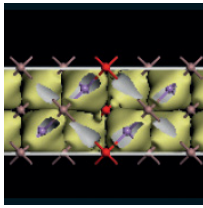


Figure 2. The phase diagram of the topological phase of 3D TI/NI multilayer model as a functions of the scaled transfer integral between the nearest neighboring TI and NI layers.





# International Workshop on Computational Nanotechnology

Session: Photonics/optoelectronics/plasmonics

## Multiscale modelling of the impact of intrinsic disorder and localisation effects on the optical and electronic properties of III-N LEDs

S Schulz<sup>1</sup>, M Caro<sup>3</sup>, D I Tanner<sup>1,2</sup>, C Coughlan<sup>1,2</sup> and E P O'Reilly<sup>1,2</sup>

<sup>1</sup>Tyndall National Institute, Ireland, <sup>2</sup>University College Cork, Ireland, <sup>3</sup>Aalto University, Finland

Over the last twenty years, research into nitride-based semiconductor materials (InN, GaN, AlN, and their respective alloys) has gathered pace. This stems from their potential to emit light over a wide spectral range. Despite very high defect densities, blue emitting InGaN-based devices exhibit high quantum efficiencies. The widely accepted explanation for this is that the carriers are spatially localized due to alloy fluctuations and are thus prevented from diffusing to defects. It is important to note that in wurtzite InGaN systems the effect of these fluctuations is much more severe compared to that found, e.g., in zinc-blende InGaAs alloys. This originates from the very different physical properties (e.g., band gap and lattice spacing) of the binary constituents (InN and GaN). A further complication is that InGaN/GaN quantum wells (QWs), compared with InGaAs/GaAs wells, exhibit much stronger electrostatic built-in fields, arising in part from the strain dependent piezoelectric response (Fig. 1). Thus even random alloy fluctuations in InGaN/GaN QWs affect the electronic structure through a complicated interplay of local alloy, strain, and built-in field fluctuations.

To date, most simulation of the optoelectronic properties of III-N heterostructures and devices has been based on using  $\mathbf{k}\cdot\mathbf{p}$  and effective mass models to describe the carrier states, as illustrated in Fig. 1. However there is a growing realisation that further device development and optimisation requires accurate understanding, control and exploitation of material properties. We first show here that calculations using density functional theory (DFT) provide clear evidence for the importance of random alloy effects in III-N alloys. Detailed treatment of the electronic structure then requires an empirical atomistic model capable to treat large-scale (100,000 atom) structures. We have developed a  $sp^3$  tight-binding Hamiltonian which gives an excellent description of the electronic and optical properties of III-N alloys and nanostructures. Preliminary non-equilibrium Green's function (NEGF) calculations show that inclusion of alloy disorder effects are also important for an accurate treatment of carrier transport in III-N heterostructures. There are still however many challenges to apply NEGF calculations to a full LED device. We discuss how modified drift-diffusion approaches can include alloy disorder effects and the consequences of disorder on transport and recombination properties.

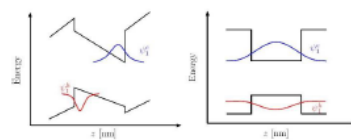


Fig. 1: Idealised variation of band-edge potential along growth direction in a c-axis quantum well structure, with spatial separation of electron (blue) and hole (red) wavefunctions (left), compared with strong overlap in absence of polarization potential (right).

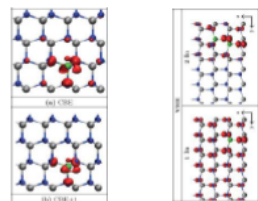
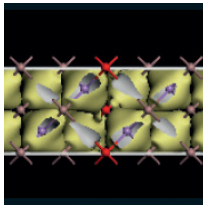


Fig. 2: Left: calculated LDA charge densities for (a) lowest conduction and (b) second conduction state in an  $\text{In}_1\text{Al}_{799}\text{N}_{800}$  supercell. Right: Highest valence state in a 1600 atom InAlN supercell with (a) one In (b) In pair.

The left hand panel in Fig. 2 shows the charge density calculated using the local density approximation (LDA) in DFT for the lowest (CBE) and the second (CBE+1) conduction state in an  $\text{In}_1\text{Al}_{799}\text{N}_{800}$  supercell. It can be seen that the second state in this calculation is a resonant state, localised on the indium (In) site, with the lowest state also showing large probability density at the In site [1]. In the valence band (RHS, Fig. 2), the highest valence state remains delocalised in an  $\text{In}_1\text{Al}_{799}\text{N}_{800}$  supercell (lower panel), but evidence of



## International Workshop on Computational Nanotechnology

localisation can be observed when a pair of In atoms are considered in the supercell. These results highlight the importance of including detailed atomistic effects in III-N alloy calculations. We have developed a  $sp^3$  tight-binding model and benchmarked it against DFT calculations and experiment, in order to treat the large supercell structures required for accurate modelling of heterostructures.

Figure 3 shows the ground state electron and hole charge densities in an exemplary  $\text{In}_{0.25}\text{Ga}_{0.75}\text{N}/\text{GaN}$   $c$ -plane QW structure, using the  $sp^3$  model, and including the effects of well width fluctuation, local alloy composition, strain and built-in field fluctuations as well as Coulomb effects [2]. This and related calculations show that while the electron states are mainly localized by well-width fluctuations, the holes states are already localized by random alloy fluctuations. These localization effects dominate the QW optical properties, leading to strong inhomogeneous broadening of the lowest interband transition energy. Even when including Coulomb interactions, the electron and hole states remain separated along the  $c$ -axis in Fig. 3, due to the built-in polarisation potential.

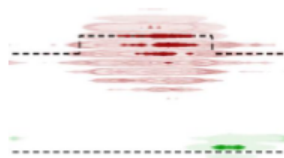


Fig. 3: Ground-state electron (red) and hole (green) charge densities with Coulomb interaction for an exemplar  $\text{In}_{0.25}\text{Ga}_{0.75}\text{N}/\text{GaN}$  QW. Dashed lines indicate the QW interfaces.

The built-in polarisation potential can be eliminated by growing on non-polar substrates. This allows improved electron-hole overlap and increased exciton binding compared to growth on  $c$ -plane substrates. We have made a detailed theoretical and experimental comparison of the electronic structure and optical properties of a (non-polar)  $m$ -plane  $\text{InGaN}/\text{GaN}$  QW structure [3]. Our microscopic theoretical description again reveals strong hole wave function localization effects due to random alloy fluctuations, resulting in strong variations in ground state energies and consequently the corresponding transition energies (Fig. 4). This is consistent with the experimentally observed broad photoluminescence (PL) peak. Likewise, the calculations find strong exciton localization effects which explain the form of the PL decay transients. Additionally, the theoretical results confirm the experimentally observed high degree of optical linear polarization. Overall, the theoretical data highlight the strong impact of the microscopic alloy structure on the optoelectronic properties of these systems.

Given the strong impact of localization effects on the electronic states and optical properties, it can be expected that they will also strongly impact carrier transport in III-N heterostructures. We present preliminary calculations that confirm this expectation and conclude by discussing the importance of linking different scale models to ensure an accurate description and analysis of III-N LEDs and related devices.

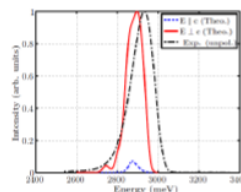
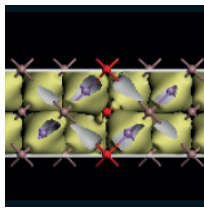


Fig. 4: Calculated excitonic ground state emission spectrum with light polarization vectors parallel and perpendicular to the  $c$  axis. The dashed-dotted line shows the experimental (unpolarized) PL spectrum

- [1] S. Schulz, M. A. Caro and E. P. O'Reilly, *Appl. Phys. Lett.* 104, 172102 (2014)
- [2] S. Schulz, M. A. Caro, C. Coughlan and E. P. O'Reilly, *Phys. Rev. B* 91, 035439 (2015)
- [3] S. Schulz *et al.*, *Phys. Rev. B* 92, 235419 (2015).



# International Workshop on Computational Nanotechnology

## Unified numerical solver for modeling metastability and reliability of CdTe solar cells

D Vasileska<sup>1</sup>, A Shaik<sup>1</sup>, D Guo<sup>1</sup>, C Ringhofer<sup>1</sup>, D Brinkman<sup>2</sup>, D Krasikov<sup>3</sup> and I Sankin<sup>3</sup>

<sup>1</sup>Arizona State University, USA, <sup>2</sup>San Jose State University, USA, <sup>3</sup>First Solar, USA

CdTe is the most successful thin-film PV (TFPV) technology in the market to date. Recent advances in CdTe TFPVs have boosted module efficiency from 12% to beyond 18% and these results were achieved on the basis of costly empirical research and development that was only weakly supported by theoretical guidance. There are two primary directions of improvement for this technology: (1) *improvements in efficiency*, primarily the open-circuit voltage (Voc), and (2) *reduction of metastabilities and long-term degradation rates*. The remaining challenges are: (1) understanding of *doping formation*, which is clouded by the presence of self-compensation and a multitude of defects, (2) understanding of *recombination*, which is challenged by the presence of external and internal (GB) interfaces, and (3) understanding of *degradation* that is influenced by the fact that all of the above can change under field conditions. In parallel, the empirical evolution to cell efficiencies above 21% was enabled through the increased use of band-gap grading in the absorber structures, which further complicates the defect physics of the material and makes our ability to predict performance or stability ever more challenging. *The above mentioned problems must be treated to the degree that they can become predictive to polycrystalline device behaviour and replace empirical “trial and error” with an “engineering by design” approach.* Therefore, the need for the Unified Numerical Solver depicted in Figure 1 which bridges physics across multiple length and time scales. Species under investigation are described by sets of low-level parameters that include (depending on the model level) formation energy, ionization energies and diffusion coefficients for different charged states, solubility limits, grain boundary segregation parameters, etc. System evolution for a given set of stressors (temperature, light, and bias) is calculated based on provided initial conditions (distributions). The solver outputs the distributions of charged and neutral dopants and recombination states. Given device geometry and band structure of semiconductors, the solver uses these distributions to simulate IV, CV, and QE trends that could be confirmed experimentally on real device structures.

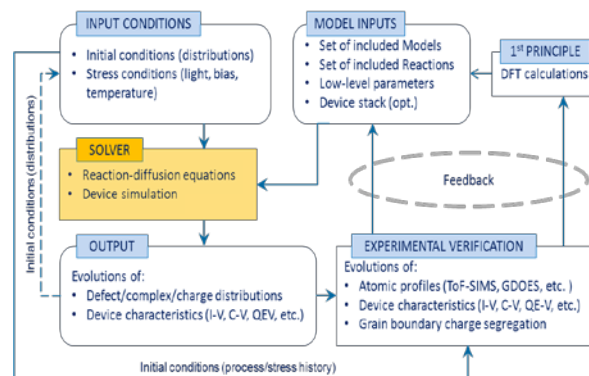
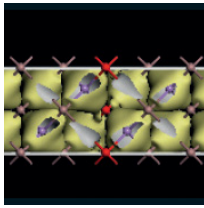


Figure 1: Schematic block-diagram illustrates the use of the solver to tune the model and study CdTe device metastability.

We have demonstrated functional prototypes of 1D and 2D Unified Numerical solvers that have already provided unique insight into physical processes behind doping formation and metastabilities observed in thin-film CdTe devices. In particular, we have explained the long-standing mystery of “Cu solubility limits” in CdTe by the difference in the formation energies of Cu-related defects in the CdTe absorber and the Cu source layer. Thus we were able to accurately simulate atomic Cu profiles obtained in as-fabricated devices for different annealing/quenching conditions. We have also determined the role of donor-acceptor pairs (DAP) in the diffusion of Cu, when the dissociation energy of Cu(i)-Cu(Cd) complex was found to dominate



# International Workshop on Computational Nanotechnology

Cu migration in CdTe. When simulating Cu diffusion profiles obtained at different annealing conditions, we found pronounced discrepancy between fitted and DFT-calculated values of Cu diffusion barrier (0.7eV vs. 0.46eV, correspondingly). To explain this contradiction, we have analyzed the energy path for dissociation of Cu complex and found exact match to effective Cu diffusion barrier fitted by the Unified Solver. Experimental data overlaid with simulation curves and DFT analysis are shown in Fig.2. Yet another interesting discovery we have made, that shed some light on the nature of metastabilities in CdTe absorbers, is illustrated in Fig. 3. Experiment performed on Colorado State University samples suggested that under zero bias, atomic concentration of Cu in CdTe absorber can drop by 50% over several weeks at field temperature (e.g., 65°C). At the same time, total net acceptor concentration in the bulk remains positive showing changes in the range of  $< 1 \times 10^{15} \text{cm}^{-3}$ , which means bulk regions lose both Cu donors and Cu acceptors. Since only interstitial Cu donor ions can diffuse at such low temperatures, this observation has led to conclusion that in the presence of Cd(i), Cu/Cd exchange reactions happen at high rate already at 65°C. DFT calculations performed to explain observed phenomena have confirmed this hypothesis.

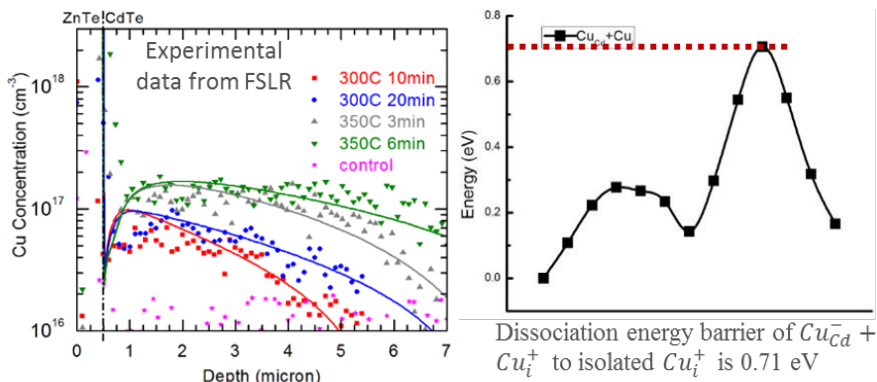


Figure 2: DFT-calculated dissociation energy barrier of Cu(i)-Cu(Cd) is 0.71eV (right plot) that corresponds to effective diffusion barrier fitted from experimental data (left plot). Note that DFT-calculated diffusion barrier for the Cu(i) is only 0.46eV.

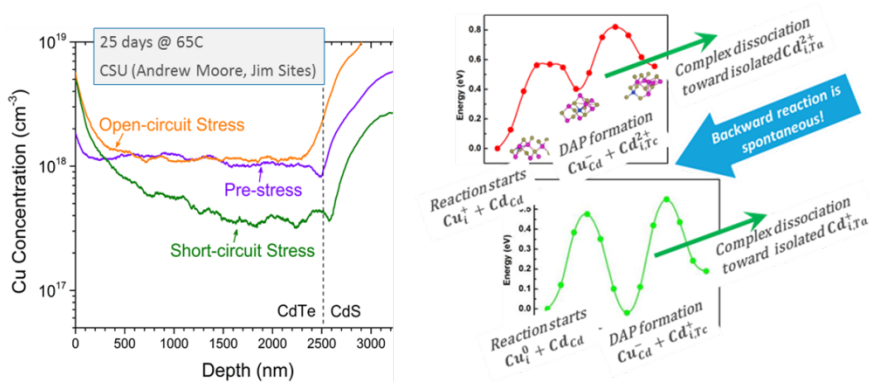
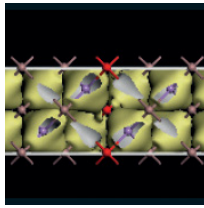


Figure 3: Results of DFT calculations (right plot) in our previous work using Unified Numerical Solver explain observed instability of Cu doping (left plot) in the presence of interstitial Cd.

We consider the presented Unified Numerical Solver as the best scientific approach to study formation and evolution of defects responsible for the performance of TFPV device as it accounts for all the components depicted in Fig. 1.



# International Workshop on Computational Nanotechnology

## Systematic study of quantum dot laser emission controlled by coherent phonon wave packets

D Wigger<sup>1</sup>, T Czerniuk<sup>2</sup>, D E Reiter<sup>1</sup>, A V Akimov<sup>3</sup>, M Bayer<sup>2</sup> and T Kuhn<sup>1</sup>

<sup>1</sup>Universität Münster, Germany, <sup>2</sup>Technische Universität Dortmund, Germany, <sup>3</sup>University of Nottingham, UK

Light emission from semiconductor nanostructures can be greatly modified by coherent phonons because the strain associated with the phonons shifts the electronic transitions of a laser medium with respect to the cavity mode. This can lead to significant enhancement and attenuation of the emission intensity, making phonons attractive for the control of light-matter interaction on the picosecond time scale. We consider an ensemble of quantum dots (QDs) as active medium for which such a control of the light emission has recently been demonstrated experimentally [1]. The same method has already been successfully extended to other nanostructures [2,3]. Two basic mechanisms have been identified, which affect the laser intensity: (i) The *shaking effect*, which dynamically brings highly occupied excitons into resonance with the cavity mode and therefore increases the output. (ii) The *adiabatic shift* of the ensemble, which varies the absolute number of QDs in resonance with the laser mode. We develop a semiclassical laser model that is schematically shown in Fig.1(a) to analyze these mechanisms in detail. The model combines the three nonlinearly coupled subsystems: excitons, photons and phonons. By choosing special ensemble distributions and intuitive strain dynamics it is possible to distinguish between the two effects [4]. In the experiment, which is schematically shown in Fig. 1 (b), the phonons are injected into the system by intense laser pulses hitting an aluminum surface on the back side of the sample. Due to nonlinear propagation and multi-scattering processes when passing through the distributed Bragg reflector (DBR), the shape of the acoustic field hitting the QDs [given in Fig.1(c)] is quite involved. Using these strain dynamics as input in the simulations we can directly compare the laser emission properties of experiment and theory [5]. By choosing different initial detunings between the QD ensemble and the cavity mode and excitation powers close to the lasing threshold we extend the original experiment [1]. We find an excellent agreement between experiment and theory, as is exemplarily shown in Fig.1(d) and (e). Our combined approach helps to distinguish between the shaking effect and the adiabatic shift that both simultaneously affect the laser output in the experiment. This also allows us to propose new system designs to further tailor the interplay between phonons, excitons and photons.

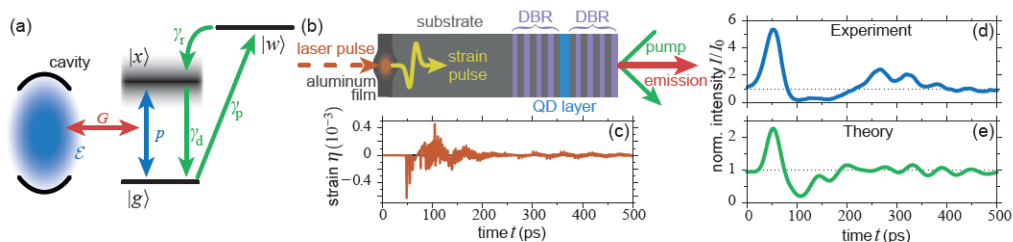
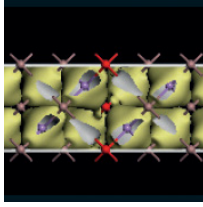


Figure 1: (a) Sketch of the theoretical model. (b) Scheme of the experiment. (c) Strain in the experiment. (d,e) Measured and calculated laser intensity.

- [1] C. Brüggemann et al., Nature Photon. 6, 30 (2012).
- [2] T. Czerniuk et al., Nature Comm. 5,4038 (2014).
- [3] T. Czerniuk et al., Appl. Phys. Lett. 106, 41103 (2015).
- [4] D. Wigger et al., arXiv:1701.04209 (2017).
- [5] T. Czerniuk et al., arXiv:1701.03707 (2017).



# International Workshop on Computational Nanotechnology

## Density matrix model for bound to continuum terahertz quantum cascade lasers

A Demić<sup>1</sup>, A Grier<sup>2</sup>, Z Ikonić<sup>1</sup>, A Valavanis<sup>1</sup>, R Mohandas<sup>1</sup>, L Li<sup>1</sup>, E Linfield<sup>1</sup>, A G Davies<sup>1</sup> and D Indjin<sup>1</sup>

<sup>1</sup>University of Leeds, UK, <sup>2</sup> Seagate Technology, UK

Terahertz-frequency quantum cascade lasers (THz QCLs) require very small energy difference between the lasing states ( $\sim 10$  meV), and modelling of these devices can be challenging. Furthermore, thermal excitation of carriers can rapidly degrade device performance and THz QCLs must operate at cryogenic temperatures. A variety of materials and approaches are being employed in order to improve the thermal performance of QCLs [1], and this must be underpinned by a good understanding of carrier transport within these devices. Various models for transport in QCLs exist [2]; most commonly employing semi-classical approaches such as self-consistent rate-equation (RE) modelling, which considers non-radiative transitions of carriers due to various scattering mechanisms, including interactions of electrons with phonons (LO), alloy disorder (AD), interface roughness (IRF), ionised impurities (II) and other electrons (CC). These models are semi-classical because they consider transitions of discrete electrons between energy levels and neglect coherence effects and quantum mechanical dephasing. Although RE models are usually computationally efficient, and provide insight into the scattering behaviour, they are unable to correctly describe transport between adjacent periods of a QCL structure [3] because they do not take injection barrier thickness into account in transport calculations. This leads to the prediction of instantaneous transport between the periods, whereas the actual transport that occurs is based on resonant tunnelling.

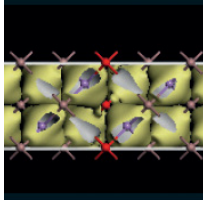
Alternative approaches, based on density matrix (DM) modelling include quantum transport effects and are able to overcome known shortcomings of RE models, while keeping reasonable computational complexity. DM models include a finite dephasing time through the barrier as well as Rabi oscillations at the frequency  $\Delta ij' / \hbar$ , where  $\Delta ij'$  is the anticrossing energy between state  $i$  and  $j'$  where  $j'$  is the state from the adjacent period which is aligned with state  $i$  due to the external bias.

RE models can be successfully applied to mid infra-red (MIR) structures [4] which have much larger photon energies and due to the thin injection barriers anticrossing gaps are large (which causes fast oscillations through the barrier). However, THz QCLs strongly depend on the coherent transport and an appropriate model needs to be used.

DM models are frequently applied to approximate QCL bandstructure, containing just 2 or 3 states per period [5]. Although this approach reduces the computational complexity, it results in a cumbersome set of analytic expressions, which is inconvenient for bound-to-continuum (BTC) THz QCLs, since these have a large number of states per module.

In this work, we present a new DM approach that extends the model presented in [6], applicable for arbitrary number of states per module. This model has proved successful for a variety of QCL simulations, including BTC structures [7], quantum dot QCLs [8], non-linear effects [9] and self-mixing interferometry [10].

The time evolution of the density matrix is described by the Liouville equation. We consider QCL structure with infinite number of periods, which implies infinite-sized matrices, but due to the nearest neighbour approximation and symmetry of QCL structure Liouville equation folds into the following system of  $N \times N$  block equations (where  $N$  is the number of states in the module):



# International Workshop on Computational Nanotechnology

$$\begin{aligned}\frac{d\rho_1}{dt} &= -\frac{i}{\hbar}([H_1, \rho_1] + [H_3, \rho_2] + [H_2, \rho_3]) - \frac{\rho_1}{\tau} - \frac{\rho_1}{\tau_{||}} \\ \frac{d\rho_2}{dt} &= -\frac{i}{\hbar}([H_2, \rho_1] + [H_1, \rho_2] + KL_P\rho_2) - \frac{\rho_2}{\tau_{||}} \\ \frac{d\rho_3}{dt} &= -\frac{i}{\hbar}([H_3, \rho_1] + [H_1, \rho_3] - KL_P\rho_3) - \frac{\rho_3}{\tau_{||}}\end{aligned}$$

The Hamiltonian block  $H_1$  describes the central period and is composed of tight-binding energies (on the main diagonal) and optical coupling terms of the form  $H_{ij} = ez_{ij} A_{inc}$  where  $z_{ij}$  are dipole matrix elements, and  $A_{inc}$  is the electric field of the incident light. In this work, we use the non-rotating-wave approximation (NRWA) presented in [6] and assume that optical field has the form  $A_{inc} = A_0(e^{i\omega t} + e^{-i\omega t})$  and therefore refer to the main diagonal of  $H_1$  as  $H^{dc}$ , while the remaining ac terms have equal amplitudes which represent  $H^{ac}$ , (where  $H_{ij}^{ac} = e_{zij} A_0$ ).

Hamiltonian blocks  $H_2$  and  $H_3$  only have dc terms which implies that  $H_2 = H_3$ . The elements in  $H_2$  and  $H_3$  contain Rabi coupling terms (half the anticrossing energy over  $\hbar$ ), and formally these blocks are obtained by  $\langle i | H_{TB} - H_{EXT} | j \rangle$ , where  $H_{TB}$  EXT for Rabi coupling terms from [11], [12].

Transport terms  $\tau$  and  $\tau_{||}$  correspond to intraperiod and interperiod transport respectively and account to pure dephasing as well. Term  $\tau$  is obtained by semi-classical Fermi's golden rule, while  $\tau_{||}$  describes interperiod transport in coherent manner. This is the main difference between the RE and DM approaches: RE uses Fermi's golden rule for interperiod transport as well, while in DM we assume that resonant tunnelling will occur at the Rabi frequency through the injection barrier, which is described by the Hamiltonian blocks  $H_2$  and  $H_3$ , and that states additionally change their phase during the interperiod transport. Output of the system (current density and gain) are calculated as:

$$\begin{aligned}j &= \frac{ien_2D}{\hbar L_P} \text{Tr} \left( \rho_1[H_1, Z] + \rho_2[H_3, Z] + \rho_3[H_2, Z] + L_P(H_2\rho_3 - \rho_2H_3) \right) \\ g &= -\frac{we n_2D}{\epsilon_0 A_0 n_r c \hbar} \text{Tr} (\rho_1^{AC} Z)\end{aligned}$$

We apply the model to the structure similar to one in [13]. The structure is designed for emission at 2.06 THz at 20K. The current-voltage I-V characteristic of the device can be calculated by sweeping the applied electric field (terminal voltage).

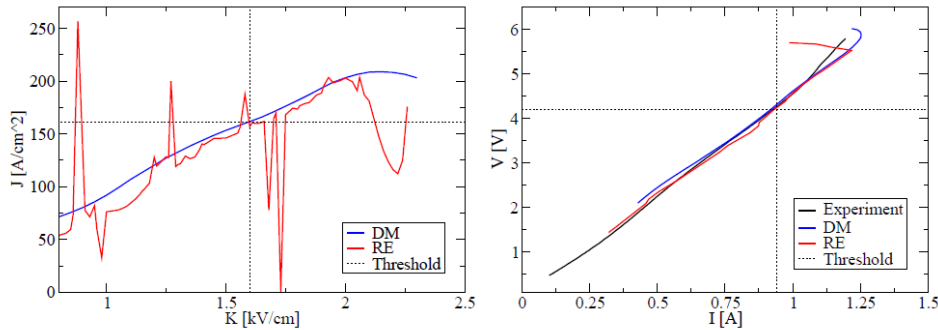
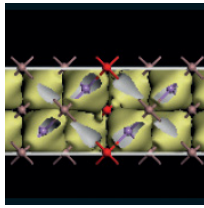


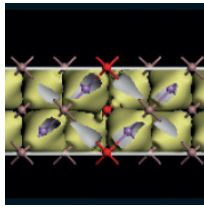
Fig. 1. a) Current density versus electric field from RE (red) and DM model (blue). Results were fitted to threshold point at  $(K_t, J_t) = (1.6 \text{ kV/cm}, 161.5 \text{ A/cm}^2)$  and b) I-V characteristic of the BTC device at 20K. RE model fit (red) needed  $2.72 \Omega$  of contact resistance, while DM model fit (blue) need  $2.25 \Omega$  of contact resistance, both results were fitted to experimental threshold at  $(I_t, V_t) = (0.94 \text{ A}, 4.2 \text{ V})$ .



## International Workshop on Computational Nanotechnology

Density matrix results show a smooth dependence in Fig. 1, while RE model exhibits non-physical spikes. In order to obtain comparison with experimental current-voltage ( $I-V$ ) characteristics, the axes in Fig. 1 b) need to be scaled by the corresponding device dimensions, but an additional fitting parameter is also required. In order to fit theoretical data to the experiment, non-zero contact resistance needs to be included in the model, this resistance is usually not known from the experimental setup, but it is reasonable to assume the values of several Ohms. Figure 1 b) shows how RE and DM model compare to the experimental output, note that here we manually removed the spikes that occurred in Fig. 1 a) while this is not necessary for the DM model, this property shows promise for application in QCL devices optimisation.

- [1] S. Kumar, "Recent Progress in Terahertz Quantum Cascade Lasers," IEEE Journal of Selected Topics in Quantum Electronics, vol. 17, no. 1, pp. 38-47, 2011.
- [2] C. Jirauschek and T. Kubis, "Modeling techniques for quantum cascade lasers," Applied Physics Reviews, vol. 1, no. 1, p. 011307, 2014.
- [3] H. Callebaut and Q. Hu, "Importance of coherence for electron transport in terahertz quantum cascade lasers," Journal of Applied Physics, vol. 98, no. 10, p. 104505, 2005.
- [4] D. Indjin, P. Harrison, R. W. Kelsall, and Z. Ikonić, "Self-consistent scattering model of carrier dynamics in GaAs-AlGaAs terahertz quantum-cascade lasers," IEEE Photonics Technology Letters, vol. 15, no. 1, pp. 15-17, 2003.
- [5] R. W. Boyd, Nonlinear Optics. Academic Press, 2008.
- [6] T. V. Dinh, A. Valavanis, L. J. M. Lever, Z. Ikonić, and R. W. Kelsall, "Extended density-matrix model applied to silicon-based terahertz quantum cascade lasers," Phys. Rev. B, vol. 85, no. 23, p. 235427, 2012.
- [7] A. Grier, Modelling the optical and electronic transport properties of AlGaAs and AlGaN intersubband devices and optimisation of quantum cascade laser active regions. Phd, University of Leeds, 2015.
- [8] B. A. Burnett and B. S. Williams, "Density matrix model for polarons in a terahertz quantum dot cascade laser," Phys. Rev. B, vol. 90, no. 15, p. 155309, 2014.
- [9] B. A. Burnett and B. S. Williams, "Origins of Terahertz Difference Frequency Susceptibility in Midinfrared Quantum Cascade Lasers," Phys. Rev. Applied, vol. 5, no. 3, p. 034013, 2016.
- [10] A. Grier, P. Dean, A. Valavanis, J. Keeley, I. Kundu, J. D. Cooper, G. Agnew, T. Taimre, Y. L. Lim, K. Bertling, A. D. Rakić, L. H. Li, P. Harrison, E. H. Linfield, Z. Ikonić, A. G. Davies, and D. Indjin, "Origin of terminal voltage variations due to self-mixing in terahertz frequency quantum cascade lasers," Opt. Express, vol. 24, no. 19, pp. 21948-21956, 2016.
- [11] A. Yariv, C. Lindsey, and U. Sivan, "Approximate analytic solution for electronic wave functions and energies in coupled quantum wells," Journal of Applied Physics, vol. 58, no. 9, pp. 3669-3672, 1985.3
- [12] G. Bastard, Wave Mechanics Applied to Semiconductor Heterostructures. EDP SCIENCES, 1988.
- [13] J. R. Freeman, O. Marshall, H. E. Beere, and D. A. Ritchie, "Improved wall plug efficiency of a 1.9 thz quantum cascade laser by an automated design approach," Applied Physics Letters, vol. 93, no. 19, p. 191119, 2008.



# International Workshop on Computational Nanotechnology

## Simulation of a midinfrared quantum cascade laser using a density-matrix formalism

O Jonasson and I Knezevic

University of Wisconsin-Madison, USA

Quantum cascade lasers (QCLs) are intra-subband light-emitting sources in the midinfrared and THz parts of the electromagnetic spectrum. The core of the QCL (the gain medium) is a vertically grown semiconductor heterostructure consisting of an alternating arrangement of quantum wells and barriers with a typical layer width of a few nanometers [1]. In this work, we propose a computationally efficient density-matrix model capable of describing quantum transport in QCLs. The model is based on a Markovian master equation for the single-electron density matrix that conserves the positivity of the density matrix and includes full in-plane dynamics.

Existing simulation methods for electron transport in QCLs include semiclassical methods (rate equations [2] and Monte Carlo [3]) and quantum techniques (density matrix [4], [5], [6] and nonequilibrium Green's functions (NEGF) [7], [8]). Semiclassical methods are advantageous because of their low computational cost, but can fail when off-diagonal density-matrix (DM) elements (coherences) are similar in size to the diagonal ones [9]. While NEGF simulation can capture quantum transport in QCLs, they are computationally intensive, especially for short-wavelength devices, where a large range of energies are involved. Density-matrix models offer a compromise, as they can describe coherent-transport features with lower computational overhead than NEGF.

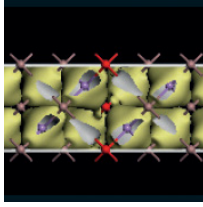
Previously proposed density-matrix models have drawbacks that are avoided in this work. One drawback is the assumption of thermalized subbands with electron temperature as an input parameter [6], [10]. This approximation is not warranted far from equilibrium, when the in-plane energy distribution deviates far from a heated thermal distribution. A second drawback with existing DM models is the phenomenological treatment of dephasing across thick potential barriers, where transport is

treated semiclassically within a subregion of a QCL (typically a single stage) and coupling between stages is treated using phenomenological dephasing times [6], [10]. We present a computationally tractable density-matrix model that makes neither of the aforementioned simplification.

In order to verify our model, we simulated QCL based on the InGaAs/InAlAs material system emitting around  $8.5 \mu\text{m}$  [11]. We chose this specific device because it has previously been successfully modeled using the NEGF formalism [10], enabling us to compare our results to both experimental and theory. Figure 1 shows the bandstructure at a field strength of  $52 \text{ kV/cm}$ , which is slightly above threshold. The bandstructure is calculated using a 3-band  $\mathbf{k} \cdot \mathbf{p}$  model that includes the conduction band, light-hole band and the spin split-off band. The upper (lower) lasing level is labeled as 8 (7) and the lowest-energy injector state is 1.

Figure 2 shows the current density vs electric field calculated using our density-matrix model, along with comparison with experiment and theoretical results using the NEGF formalism. Our results are in excellent agreement with NEGF for all considered fields. Our results are also in good agreement with experiment up to threshold (denoted by vertical dashed lines). Note that our model does not include the laser electromagnetic field, so we do not expect to reproduce current density far above threshold.

Figure 3 shows our theoretical results for the peak optical gain, as well as a comparison with NEGF [10]. The estimated threshold gain from experiment E1 is denoted by a horizontal dashed line. We see that our results are in fairly good agreement with NEGF for fields up to  $60 \text{ kV/cm}$ , while for higher fields, we predict higher gain. From



# International Workshop on Computational Nanotechnology

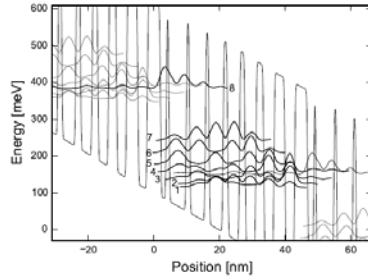


Fig. 1. Conduction-band edge (thin black curve) and probability densities for the 8 eigenstates used in calculations (bold curves). States belonging to neighboring periods are denoted by thin gray curves. States are numbered in increasing order of energy, starting with the ground state in the injector. The length of one period is 44.9 nm, with a layer structure (in nanometers), starting with the injector barrier (centered at the origin) **4.0/1.8/0.8/5.3/1.0/4.8/1.1/4.3/1.4/3.6/1.7/3.3/2.4/3.1/3.4/2.9**, with barriers denoted bold. Underlined layers are doped to  $1.2 \times 10^{17} \text{ cm}^{-3}$ .

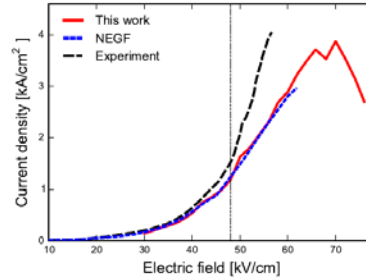


Fig. 2. Current density vs electric field. Shown are theoretical results based on this work, as well as results based on NEGF [10]. Experimental results from Ref. [11] are also shown. Experimentally determined threshold field of 48 kV/cm is denoted by the dashed vertical line.

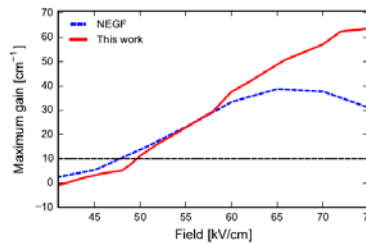


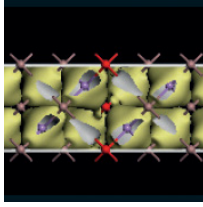
Fig. 3. Peak gain vs electric field, based on this work (solid red) and NEGF (dashed blue). The dashed horizontal line denotes the estimated threshold gain of  $10 \text{ cm}^{-1}$ .

the data presented in Figs. 2 and 3 we get a threshold field of  $E_{th} = 49.5 \text{ kV/cm}$  and threshold current density of  $J_{th} = 1.53 \text{ kA/cm}^2$ , which is close to the experimentally determined values of  $E_{th} = 48.0 \text{ kV/cm}$  and  $J_{th} = 1.50 \text{ kA/cm}^2$ . The results are also in fairly good agreement with the NEGF results ( $E_{th} = 47.6 \text{ kV/cm}$  and  $J_{th} = 1.20 \text{ kA/cm}^2$ ).

In conclusion, we have proposed a density-matrix model based on a Markovian master equation that preserves positivity and includes full in-plane dynamics. We compared our results with experiment, as well as a theoretical results based on the more computationally demanding NEGF formalism. We obtained excellent agreement with experiment and NEGF for the current density and fair agreement with the calculated optical gain.

This work was supported by the U.S. Department of Energy, Office of Basic Energy Sciences, Division of Materials Sciences and Engineering, award DE-SC0008712.

- [1] J. Faist. *Quantum cascade lasers*. Oxford University Press (2013).
- [2] D. Indjin, *et al.* *J. Appl. Phys.*, 91, 11, 9019 (2002).
- [3] X. Gao, D. Botez, and I. Knezevic. *J. Appl. Phys.*, 101,6, 063101 (2007).
- [4] C. Weber, A. Wacker, and A. Knorr. *Phys. Rev. B*, 79,165322 (2009).
- [5] S. Kumar and Q. Hu. *Phys. Rev. B*, 80, 245316 (2009).
- [6] R. Terazzi and J. Faist. *New J. Phys.*, 12, 3, 033045 (2010).
- [7] S.-C. Lee and A. Wacker. *Phys. Rev. B*, 66, 245314 (2002).
- [8] M. Bugajski, *et al.* *Phys. Status Solidi B*, 251 (2014).
- [9] H. Callebaut and Q. Hu. *J. Appl. Phys.*, 98, 10, 104505 (2005).
- [10] M. Lindskog, *et al.* *Appl. Phys. Lett.*, 105, 10, 103106 (2014).
- [11] A. Bismuto, *et al.* *Appl. Phys. Lett.*, 96, 14, 141105 (2010).



# International Workshop on Computational Nanotechnology

## Session: Device Simulations

### (Invited) Transport modeling for plasma waves in THz devices

Z Kargar, T Linn, D Ruić and C Jungemann

RWTH Aachen University, Germany

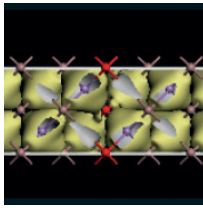
The plasma wave instability in a field effect transistor can be used to generate THz waves [1]. The analytical models which are used to investigate the behavior of the two dimensional electron gas in such devices are usually based on the first two moments of the semi-classical Boltzmann Transport Equation (BTE) which are the Euler and continuity equations [2] and we will call them the Semiconductor Equations (SE) [3]. The derivation of these equations requires many approximations and their accuracy compared to the BTE is limited. In this paper the accuracy of SE will be investigated by comparison with the results of the BTE.

The accuracy of the SE is assessed by comparing its small signal mobility with the one of the BTE. In this step no dispersion relation between the wave number and frequency is imposed by the Poisson Equation (PE) and therefore we can compare the transport models for arbitrary frequencies and wave numbers [3]. The stationary electric field is chosen such that both models yield the same stationary drift velocity.

In Fig. 1 the real and imaginary part of the small signal mobility is shown when the wave number is set to zero. The SE model fails even at low frequencies, because the analytical modeling does not contain velocity saturation. The absolute value of the small signal mobility for a constant frequency of 1THz is shown for positive and negative wave numbers in Fig. 2. For small wave numbers the product of frequency and relaxation time is much larger than one and the transport is ballistic. Therefore in this area the SE model and the BTE results agree well. In the case of larger wave numbers the SE model fails and the resonant behavior of the SE model is far too strong and two resonance peaks are found for negative wave numbers.

In order to obtain the plasma dispersion, the SE or BTE are solved together with the PE for the quasi-static potential as a general eigenvalue problem. Calculation of the plasma dispersion relation is exemplified for a simple double gate structure which is homogeneous in the transport direction and the thickness of the GaAs quantum well is assumed to be negligible compared to the oxide thickness. In Fig. 3 the Vlasov plasma modes for nonzero electric field are plotted for the SE and BTE. Again we can see that the SE fails in most cases.

We consider a device with a 60 nm long channel and asymmetric boundary conditions, to simulate the plasma instability by the Dyakonov and Shur approach [1]. Fig. 4 shows the growth rate (increment) of the oscillation versus drift velocity and its frequency. The drift velocity depends on the applied drain/source bias and for large voltages velocity saturation occurs leading to strong dissipation and damping of the plasma waves. Since velocity saturation is neglected in the SE, their results are far too optimistic.



# International Workshop on Computational Nanotechnology

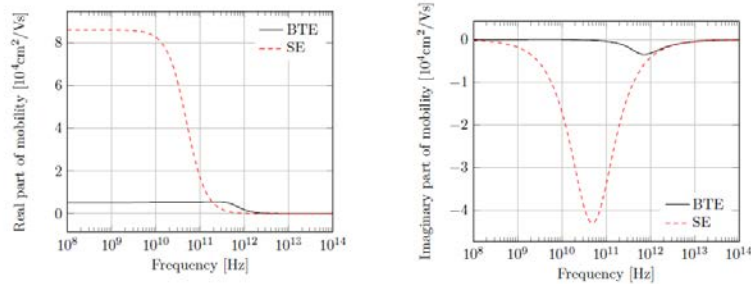


Figure 1: The real (left) and imaginary (right) parts of the small signal electron mobility for the GaAs quantum well at 77K and zero wave number for a drift velocity of  $-2 \cdot 10^7$  cm/s

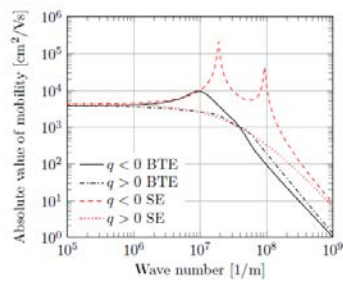


Figure 2: Absolute value of the small signal mobility for 1THz in the GaAs quantum well for a drift velocity of  $-2 \cdot 10^7$  cm/s at 77K

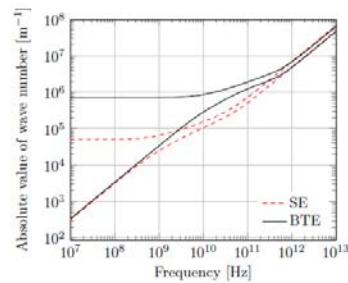


Figure 3: The two Vlasov plasma modes for a drift velocity of  $-2 \cdot 10^7$  cm/s at 77K.

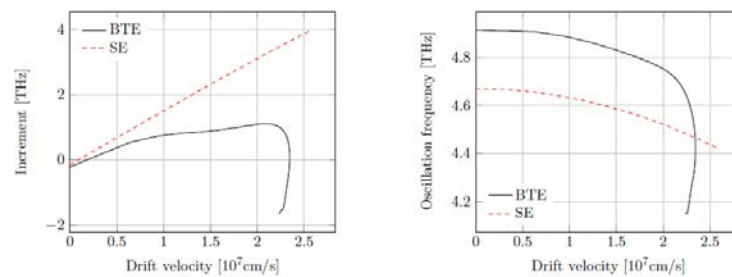
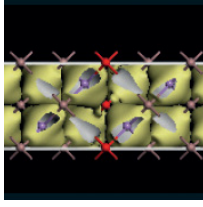


Figure 4: Increment (left) and oscillation frequency (right) of plasma waves versus drift velocity at 77K for a 60nm device.

- [1] M. Dyakonov and M. Shur, *Phys. Rev. Lett.*, vol. 71, pp. 2465–2468, Oct 1993. [Online]. Available: <http://link.aps.org/doi/10.1103/PhysRevLett.71.2465>
- [2] S.-M. Hong and J.-H. Jang, *Electron Devices, IEEE Transactions on*, vol. 62, pp. 4192–4198, Dec 2015.
- [3] Z. Kargar *et al.*, *IEEE Transactions on Electron Devices*, vol. 63, pp. 4402–4408, Nov 2016.



# International Workshop on Computational Nanotechnology

## Metal grain work-function variability in GAA Si nanowire via a fluctuation sensitivity map

N Seoane-Iglesias<sup>1</sup>, G Indalecio<sup>1</sup>, D Nagy<sup>1</sup>, M Elmessary<sup>2</sup>, K Kalna<sup>2</sup> and A J García-Loureiro<sup>1</sup>

<sup>1</sup>Universidade de Santiago de Compostela, Spain, <sup>2</sup>Swansea University, UK

One of the main burdens of a TCAD variability study of semiconductor devices is its high computational cost. There is a direct relation between the accuracy of results and the time needed to obtain them leading to substantial economic expenses. In this work, we present a technique to substantially reduce the computational costs when studying the impact of metal grain work-function variability (MGWV) on devices. The technique is based on a construction of a matrix, the fluctuation sensitivity map (FSM), with  $M \times N$  elements ( $FSM_{i,j}$ ), related to mesh points ( $u, v$ ) on a metal gate. The FSM represents how sensitive  $V_T$  (or any other figure-of-merit) is to a work-function (WF),  $WF(u, v)$ , at that position in the gate. The construction of the FSM requires simulations of an ensemble of  $P$  device configurations. For the  $k$ -th device, a local sensitivity is:

$$FSM_{i,j}^k = \frac{\partial V_T^k}{\partial WF^k(f(i,j))} \quad (1)$$

The residual of this equation is minimised by fitting coefficients  $a$  and  $b$  for each ( $i, j$ ) node using the relation:

$$V_T^k - (a(i,j) + b(i,j) \cdot WF^k(f(i,j))) = 0 \quad \forall k \in [1, P]$$

The value of each element of the matrix  $FSM_{i,j}$  is equal to  $b(i,j)$ . The FSM can be used to predict the behaviour of a device for different grain sizes (GSs) using: i) a FSM for the device generated using a particular GS, ii) an ensemble of  $P$  realistic gate WF profiles, and iii) the standard deviation of the  $V_T$  ( $\sigma V_T Real$ ) obtained after simulations of that ensemble of profiles.  $V_T$  can be estimated via the FSM ( $V_T^k FSM$ ) as:

$$V_T^k FSM = \frac{1}{M \times N} \sum_{i,j}^{M,N} FSM_{ij} \times WF_{ij}^k \quad (2)$$

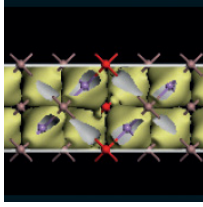
There is a mismatch ( $\alpha$ ) between standard deviations of the real ( $\sigma V_T Real$ ) and the FSM generated ( $\sigma V_T FSM$ ) results, which is independent of the GS. Therefore:

$$\sigma(V_T Predic) = \alpha \times \sigma(V_T FSM) \simeq \sigma(V_T Real) \quad (3)$$

As a test device, we investigate a 22 nm gate length Si

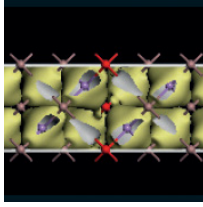
gate-all-around (GAA) nanowire (NW) FET that has been modelled from and calibrated to an experimental device [1], [2]. A schematic of the device can be seen in Fig. 1, and the calibration results in Fig. 2. A 3D density-gradient quantum-corrected drift-diffusion (DD-DG) simulator [3] is used while the TiN MGWV is modelled via the Voronoi approach [4].

Fig. 3 shows examples of work-function profiles that are wrapped around the gate, for four different grain sizes. Figs. 4 and 5 show 2D threshold voltage ( $V_T$ ) fluctuation sensitivity maps (FSM) for the GAA NW FET generated from Voronoi gate WF profiles (with either 7 or 10 nm GS) at low and high drain biases, respectively. The aggregated gate sensitivity (AGS) (shown at the bottom of the images) for a particular  $X$  coordinate is computed as a normalised sum of all the  $V_T$  values that form the column of the FSM associated to that coordinate. The largest sensitivity is found in the middle of the gate ( $X=0$ ) when the drain bias is low



## International Workshop on Computational Nanotechnology

(0.05 V). At a high drain bias, the maximum slightly shifts towards the source end ( $\lambda = -1.4$  nm). However, the method used to calculate the FSM is affected by the GS. The larger the grain size, the less number of samples are needed to accurately capture the sensitivity of the gate region to the MGW variations. The lower the GS, the more affected the results will be by statistical noise. Once the ensemble of devices is simulated for a GS 10 nm (or any other chosen grain size) and the FSM is generated, it can be used to predict the  $I/V$  variability for other GS, without further simulations saving a large amount of computational time. Fig. 6 shows scatter plots comparing the FSM generated  $I/V$  distribution against the real one (from full simulations) for four different grain sizes. The predicted and full results are highly correlated (with Pearson correlation coefficients ( $r$ ) equal to 0.93 or higher). Table I shows a comparison between  $\sigma V_T$  due to the MGWV obtained from either full DD-DG simulations or the prediction by the FSM. Note that the % in the error of the prediction is lower than 7% in all the analysed GS. The execution time (Intel one-core i5-2500 processor at 3.3 GHz) is around 6 hr. Since we study 300 different configurations, the time to estimate  $\sigma_{Real}$  for the 4 analysed GS is  $\sim 7200$  hr. However, in the evaluation of  $\sigma_{P predic}$ , we only need to simulate the ensemble of devices for the larger GS reducing the cost by a factor of 4, since the time needed to generate the FSM and to estimate the prediction is negligible (around 2 min).



# International Workshop on Computational Nanotechnology

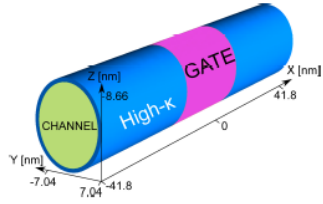


Fig. 1. Schematic of the 22 nm gate length Si GAA NW FET.

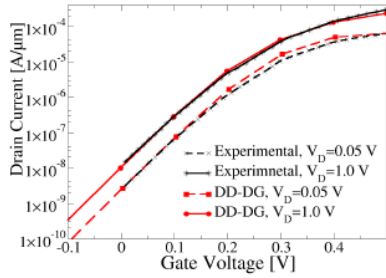


Fig. 2.  $I_D$ - $V_G$  for the 22 nm gate length Si GAA NW FET comparing experimental data against DD-DG results.

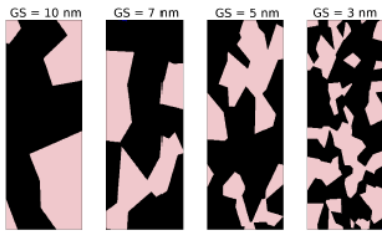


Fig. 3. Examples of TiN metal gate WF profiles generated using the Voronoi approach for four different GSs. The pink and black colours correspond to WFs of 4.4 and 4.6 eV, respectively.

TABLE I  
THE  $V_T$  MGWV FOR THE 22 NM GATE LENGTH Si GAA NANOWIRE FET USING EITHER SIMULATION RESULTS ( $\sigma_{Real}$ ) OR THE FSM MATRIX GENERATED FROM VORONOI PATCHES ( $\sigma_{Predic}$ ) WITH A 10 NM GS. THE VALUE OF THE FITTING PARAMETER ( $\alpha$ ) AND THE PERCENTAGE OF ERROR OF THE FSM-BASED ESTIMATION ARE ALSO SHOWN.

$\alpha$	GS (nm)	$V_T$ (mV)		Error %
		$\sigma_{Real}$	$\sigma_{Predic}$	
9.6	10	36.70	36.70	0.0
	7	25.71	24.13	6.1
	5	18.41	17.99	2.2
	3	11.78	11.25	4.5

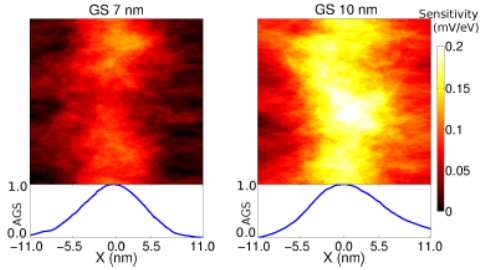


Fig. 4. 2D  $V_T$  FSMs for the 22 nm gate length Si GAA NW FET obtained via Voronoi gate WF profiles (top) and 1D AGS along the transport direction (bottom) at a drain bias of 0.05 V.

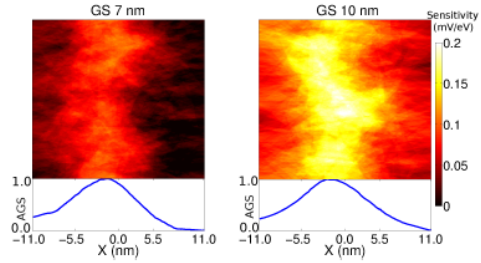


Fig. 5. 2D  $V_T$  FSMs for the 22 nm gate length Si GAA NW FET obtained via Voronoi gate WF profiles (top) and 1D AGS along the transport direction (bottom) at a drain bias of 1.0 V.

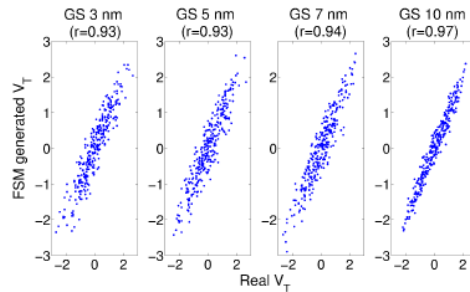
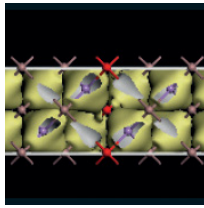


Fig. 6. Scatter plot of the predicted  $V_T$  distribution vs. the real one for four GSs at a drain bias of 1.0 V. The predicted values were obtained from a FSM generated from 300 Voronoi profiles with a 10 nm average GS and their corresponding  $V_T$  simulation values.  $V_T$  values were normalized to the mean value (set at 0) and the standard deviation (set at 1). The correlation coefficient ( $r$ ) is shown for reference.

- [1] S. Bangsaruntip et al., IEDM Tech. Dig., p. 526, 2013.
- [2] M. A. Elmessary et al., Solid-State Electronics, 128, p. 17, 2017.
- [3] A. J. Garcia-Loureiro et al., IEEE Trans. CAD., 30, no. 6, p. 841, 2011.
- [4] G. Indalecio et al., Semicond. Sci. Technol., 29, p. 045005, 2014.



# International Workshop on Computational Nanotechnology

## Variability-aware simulations of 5 nm vertically stacked lateral Si nanowires transistors

T Al-Ameri, V P Georgiev, F Adamu-Lema, T Sadi and A Asenov

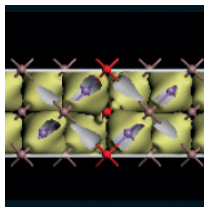
University of Glasgow, UK

In this work, we present a simulation study of vertically stacked lateral nanowires transistors (NWTs) considering various sources of statistical variability. Our simulation approach is based on various simulations techniques in order to capture the complexity in such ultra- scaled device.

Gate all around nanowire transistors (GAA NWTs) promise an improved transistor's electrostatics, offering better performance at lower supply voltages and significantly reducing the short channel effects. Arranging multiple GAA NWTs in vertically stacked lateral (VSL) configuration is a promising structure to increase the drive current for 7nm CMOS technology and beyond [1]. Also in current technology nodes, the variability is becoming important in nanoscale transistors due to process deviation and intrinsic properties of materials and interfaces. There are numerous sources of statistical variability (SV) such as Random Discrete Dopants (RDD), Wire Edge Roughness (WER) and Metal Gate Granularity (MGG), which dominate the NWT behaviour. Due to the inherited SV related to doping and gate patterning, it is very important to include SV information in process design kits (PDKs). Accurate statistical reliability (SR) information is crucial in defining the reliability criteria, and for supporting reliability-aware statistical design. For example, NBTI and PBTI degradations are associated with injection and trapping of carriers in defect states in the gate stack during device operation [2].

In this work, we study the SV of Si n-channel GAA NWTs with an elliptical cross-section of 7 nm x 5 nm. The device has a 0.4nm interfacial SiO<sub>2</sub> and 0.8nm HfO<sub>2</sub> (High-k) layers as shown in Fig. 1. The doping concentrations are as follows: channel - 10<sup>14</sup>/cm<sup>3</sup>, source/drain extensions - 10<sup>20</sup>/cm<sup>3</sup>, and source/drain contacts - 4x10<sup>20</sup>/cm<sup>3</sup>. In our recently published work [3] we investigated the performance of vertically stacked lateral (VSL) NWTs. In this work, we examined the effects of SV and SR on the performance of VSL configured NWT. For this work two computational methods have been used: a Poisson-Schrödinger model (PS) coupled with Monte Carlo (MC) technique and quantum corrected drift-diffusion model. The flowchart in Fig. 2, illustrates the overall simulation methodology. The quantum corrections obtained from the Poisson-Schrödinger solution is used in the MC simulations to deliver predictive simulation results. Then the drift-diffusion simulator is calibrated against the MC result and used for efficient SV and SR simulations. An ensemble of 1000 devices has been simulated for the statistical analysis.

The simulated statistical ID-VG characteristics are shown in Fig 3(top). The correlation between different FOM as a function of trap density is shown in Fig. 4. The simulation data presented in Fig.5 include the main sources of SV and the interplay between interface traps and the FOM correlation. For example, the anti-correlation coefficient is lower (-0.95) between I<sub>on</sub> and V<sub>T</sub> compared to when SV is not considered (-1) for VSL NWT with the double channels. Moreover, the distribution of I<sub>ON</sub> and I<sub>off</sub> also shows more variability when both interface traps and sources of SV are considered as shown in Fig 5. Fig. 6 (top left) shows DIBL distribution for 1000 devices at five different scenarios. The average of the distribution is almost the same for all devices that include sources of SV (blue, red and black curves). The standard deviation is also very similar for those three cases and does not follow entirely the Gaussian distribution the two cases. When we consider only interface traps in the uniformly doped device, the DIBL has a lower value than in the other three scenarios where variability sources are included. Also for all cases the average value increases with increasing trap density in the oxide. Similarly, the distribution does not follow an entirely Gaussian distribution. Fig. 6 (bottom) present the I<sub>on</sub> and I<sub>OFF</sub> current distribution for the ensemble of 1000 devices with and without sources of statistical variability and traps in the oxide, correspondingly. Like before the average value of both I<sub>on</sub> and I<sub>off</sub> is shifted to higher values. Moreover, for all devices with included statistical variability, values of I<sub>on</sub> and I<sub>off</sub> follow a Gaussian distribution. For the devices with interface traps



# International Workshop on Computational Nanotechnology

only and no variability sources the distribution is very similar in both cases. Fig. 6 (bottom right) reveals the threshold voltage distribution for all five scenarios. As expected when only the devices with statistical variability are considered, the average value of the distribution increases because of increasing the charge trapping but the standard deviation is almost identical in all cases. Like the data presented above the uniformly doped devices with just charge trapping in the oxide shows different behavior than the other three cases. In those two cases the average value of  $V_T$  also moves to higher values when the trap concentration is increased. Fig. 7 shows the distributions of threshold voltage subject to a combination of VS and ITC for both two & three VSL NWTs.

Detailed simulation of SV and SR study of 5 nm NWT-based CMOS technology at 5nm is presented. Local variability sources including RDD, GER, WER and MGG are considered in this studying in addition to ITC. The presence of SV sources in the simulations affects dramatically the SR results.

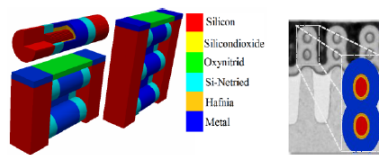


Fig. 1 (right) 3D schematic view of a Si nanowire transistor (NTW) and material information for the two channel Si NWT(left). Cross-section TEM [1] image of two channel Si NWT.

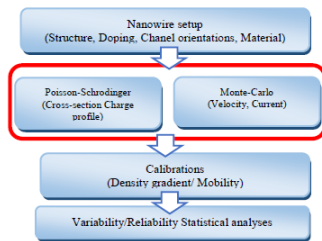


Fig. 2: The simulation tool calibration flow chart

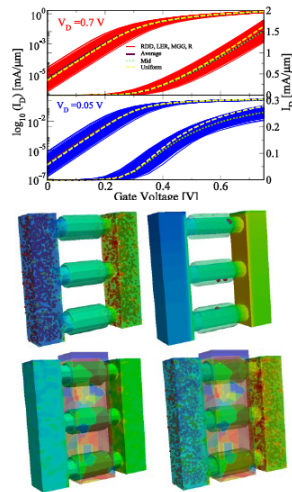


Fig. 3(top) Linear transfer characteristics for the ensemble with RDD, LER and MGG for double channel Si NWT at  $L_g=12$  nm calibrated DD methods. (Bottom) 3D schematic of effects of SV and SR on the potential

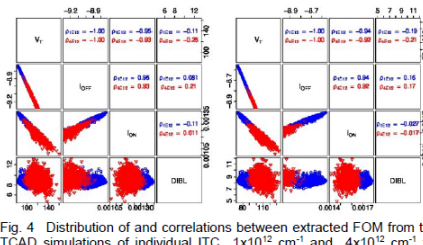


Fig. 4 Distribution of and correlations between extracted FOM from the TCAD simulations of individual ITC  $1 \times 10^{12} \text{ cm}^{-1}$  and  $4 \times 10^{12} \text{ cm}^{-1}$  for double NWT (left) and triple NWT (right).

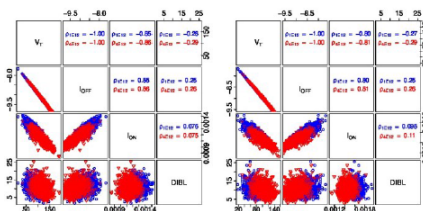


Fig. 5 Correlations between extracted FOM from the TCAD simulations for both ITC and VS effect (RDD, WER, MGG and R) for double NWT (left) and triple NWT (right).

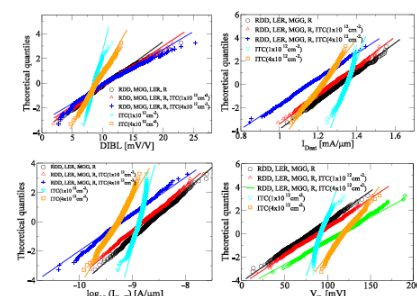


Fig. 6 Normal probability QQ-plot of DIBL,  $I_{sat}$ ,  $I_{off}$ , and  $V_T$  distributions due to individual VS effect of (RDD, LER, MGG, and R), and in their combination with  $1 \times 10^{12} \text{ cm}^{-1}$  and  $1 \times 10^{12} \text{ cm}^{-1}$  ITC.

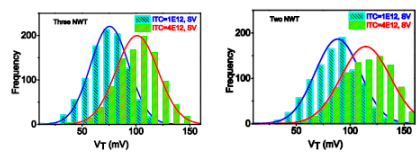
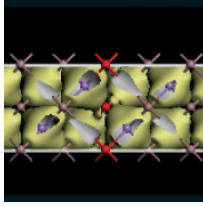


Fig. 7 Distributions of threshold voltage subject to VS effect of (RDD, LER, MGG, and R), and in their combination with  $1 \times 10^{12} \text{ cm}^{-1}$  and  $1 \times 10^{12} \text{ cm}^{-1}$  ITC for three VSL NWTs(left), and Two VSL NWT (right)



## International Workshop on Computational Nanotechnology

- [1] H. Mertens et al., IEEE Symposium on VLSI Technology, 2016.
- [2] A. Asenov et al, IEEE International Symposium on Quality Electronic Design (ISQED), 2016.
- [3] T. Al-Ameri et al, IEEE Nanotechnology Materials and Devices Conference (NMDC). 2016.

### Simulation of negative differential transconductance from devices fabricated using conventional CMOS technology

P B Vyas<sup>1</sup>, C Naquin<sup>2</sup>, M Lee<sup>2</sup>, W. G. Vandenberghe<sup>1</sup> and M V Fischetti<sup>1</sup>

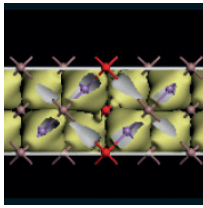
<sup>1</sup>The University of Texas at Dallas, USA, <sup>2</sup>Texas Instruments Inc., USA

Negative differential transconductance (NDT) has been recently observed in Si CMOS devices using lateral quantum wells defined by ion implantation[1]. Here, we present a theoretical study[2] of these unique type of devices, emphasizing the limitations of their practical realization as well of our understanding of the basic physical processes involved. At the same time, we also indicate possible future promising paths that can help to achieve and optimize the observed quantum behavior at room temperature.

The aforementioned CMOS (nMOS) devices have a lateral quantum well (QW) built into the surface channel, formed by reversing the dopant polarity of the shallow source/drain (S/D) extensions (pSDE) from the standard n-type (for an nMOS transistor) to p-type, as sketched in Fig. 1. A two-dimensional (2-D) QW is formed when the gate-to-source voltage  $V_{GS}$  is large enough to invert the channel. Electrons injected into the channel at energies equal to the bound states, created by the 2-D confinement, undergo resonant or sequential tunneling. At certain gate biases, when the energy of the bound states will coincide with the Fermi energy of the electrons in the source, the source-to-drain current,  $I_{DS}$ , should exhibit sharp peaks. This observation of NDT in the  $I_{DS} - V_{GS}$  characteristics is the motivation behind our investigation.

The simulation of the device characteristics[2] is done in 2 steps. First, we solve the 2-D single electron 'effective mass' Luttinger-Kohn (Schrödinger) equation under *closed* boundary condition self-consistently with the Poisson equation[3] with a source-to-drain bias  $V_{DS} = 0$  and for several values of  $V_{GS}$ . As a second step, ballistic electron transport via tunneling through the confined states is studied by solving the Schrödinger equation with *open* boundary conditions (Quantum Transmitting Boundary Method)[4] using the self-consistent potential distribution obtained from the previous step. This allows us to calculate the current-voltage characteristics.

Figs. 2 and 3 show that the lateral QW nMOS devices exhibit the desired NDT at low temperatures ( $\sim 10$  K) and for gate lengths of the order of 20 nm and smaller. The strong dependence of  $I_{DS}$  on temperature indicate a significant presence of thermionic emission over the pSDE barriers. Punch-through current is also observed in these devices. The energy spacing between the quasi bound states (Fig. 4) suggest that devices with a gate length of 10 nm and lower should exhibit a sharp NDT signature even at room temperature, provided an optimal design can be found that minimizes thermionic emission (requiring high pSDE barriers) and punch-through (that meets the opposite requirement of potential-barriers low enough to favor the tunneling current). The former plays a crucial role in suppressing the NDT, the latter is favored over the tunneling current for high pSDE barriers. We are currently looking into silicon-on-insulator (SOI) devices with high pSDE barriers that can meet the requirements to exhibit NDT at room temperature.



# International Workshop on Computational Nanotechnology

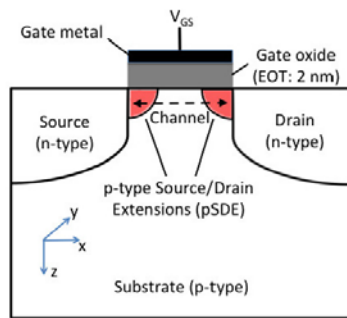


Fig. 1. Schematic cross-section of the lateral QW nMOSFET.

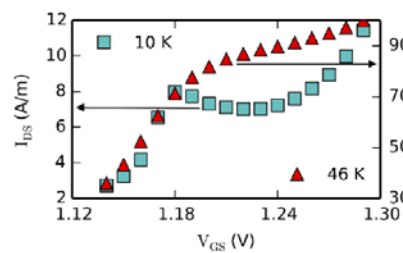


Fig. 2. Calculated  $I_{DS} - V_{GS}$  characteristics at 46 K (black triangles) and 10 K (cyan circles) for the 10 nm device with  $V_{DS} = 10$  mV.

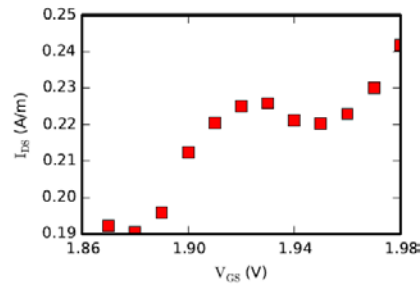


Fig. 3. Calculated  $I_{DS} - V_{GS}$  characteristics for the 20 nm device at 10 K.  $V_{DS} = 1$  mV.

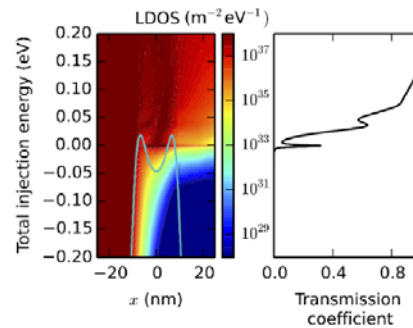
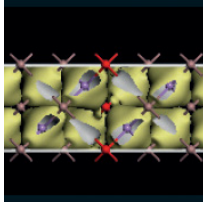


Fig. 4. Left: Average local density-of-states (LDOS) in the channel of the 10 nm device at 10 K. The cyan colored lines represent the potential-energy profile at the semiconductor/gate-insulator interface in each device. The energies are measured with respect to the Fermi energy in the source contact. Right: Transmission coefficient vs. injection energy for a particular traveling mode with energy -0.83 eV in the 10 nm device.  $V_{GS} = 1.18$  V. The peaks in the transmission coefficient and the dark colored regions in the LDOS correspond to the quasi bound states in the channel.

- [1] C. Naquin, M. Lee, H. Edwards, G. Mathur, T. Chatterjee, K. Maggio, J. Appl. Phys. 118, 124505 (2015).
- [2] P. B. Vyas et al., J. Appl. Phys. 121, 044501 (2017).
- [3] F. Stern, Phys. Rev. B 5, 4891 (1972).
- [4] C. S. Lent and D. J. Kirkner, J. Appl. Phys. 67, 6353 (1990).



## International Workshop on Computational Nanotechnology

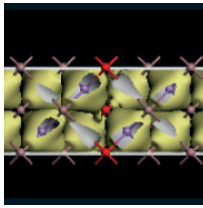
### Physically based diagonal treatment of polar optical phonons in III-V p-type double-gate transistors: comparison of InAs vs Ge and Si

M Moussavou, M Bescond, D Logoteta, L Raymond, N Cavassilas and M Lannoo

Aix Marseille Universite, France

III-V materials are considered to be a promising solution for the next generation of Complementary Metal Oxide Semiconductor (CMOS) technology [1]. It is then a central issue to predict the performances of III-V based devices through realistic quantum modeling [2]. Non-Equilibrium Green's Function (NEGF) is one of the most established technique to treat quantum transport in nano-devices. For numerical convenience carrier-phonon scattering is usually treated in NEGF within a local approximation through the concept of self-energy [3]. However III-V compound semiconductors are subject to long range polar optical (PO) interactions of the Frohlich type [4]. The difficulty with these PO interactions is that the corresponding self-energy decays very slowly in real space, like a Coulomb potential. Furthermore they should be affected by the confinement. Previous studies have attempted to model them with diagonal self-energies multiplied by a scaling factor estimated to be of order 10 in some cases [5] but there is no general prescription. In this work we developed an original method to determine the scaling factor taking into account the confinement and the effective masses. We first use the electron-phonon PO coupling derived by Mori and Ando [6] for heterostructures. From this we determine the analytic form of the equilibrium self-energy which we average over the confined zone and compare it to its local approximation to get the scaling factor. This procedure is well defined and should at least be valid for small departures from equilibrium in the spirit of the quantum Boltzmann equation [7].

Based on a  $8 \times 8$  k.p Hamiltonian, we then use this model for a performance benchmarking of Ge and Si with respect to the principal III-V materials (InAs, InSb, GaSb) considering 15 nm gate length (LG) double-gate pMOSFETs under uniaxial strain (Fig.1). Among the various strains and III-V material configurations which have been investigated, InAs  $\langle 110 \rangle$ -compression presents the best ION vs IOFF ratio in the ballistic regime (Fig 2). Figure 2 also shows the impact of phonon scattering for three current coordinates in InAs, Ge and Si. We can see that ON-current decreases by 70% in InAs device. PO phonons represent the major contribution to this reduction since reduction with acoustic and non polar optical phonons is 26%. As a comparison the ON-current decrease in Ge and Si devices is equal to 30% and 50% respectively. The impact of phonon scattering in the different materials is illustrated *via* the spectral current in Figures 3, 4 and 5. The influence of phonon scattering is also shown in Fig. 6, which presents the broadening of DOS in the valence band. It has a gradual impact from Ge, Si and InAs. These results are in agreement with the trend in experimental bulk mobilities and effective masses shown in TABLE I. Indeed with the same values of effective masses, bulk InAs is found to have a very small mobility compared to Ge, pointing that phonon scattering is higher in InAs. When compared with Si (same hole mobilities but different effective masses), the InAs phonon scattering strength is also higher. This work then emphasizes the large impact of PO phonons on III-V double gate nanotransistor characteristics. This scattering must be correctly included to assess the real performances of such devices.



# International Workshop on Computational Nanotechnology

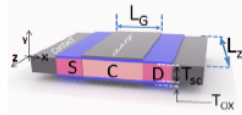


Fig. 1. Top view of the considered Double-Gate p-type MOSFETs. For all devices  $T_{SC}=2$  nm,  $T_{OX}=1$  nm, Source and Drain doping is  $8 \cdot 10^{19} \text{ cm}^{-3}$ ,  $L_G$  equal to 15 nm and  $V_{DS}=-0.6$  V.

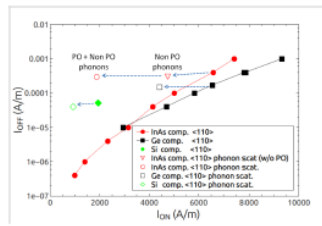


Fig. 2.  $I_{ON}$  vs  $I_{OFF}$  curves of  $\langle 110 \rangle$ -compression III-V material based devices and Ge in the ballistic regime. Empty symbols represent current coordinates calculated with phonon scattering. Value of InAs with only acoustic non polar optical is also indicated (empty circle).

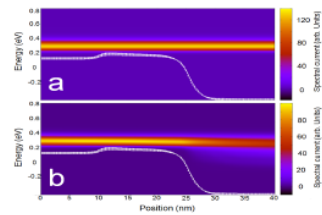


Fig. 3. Current spectrum (arb. units) of  $\langle 110 \rangle$ -compressive Ge along the device (a) in the ballistic regime and (b) with phonon scattering calculated with the bulk deformation potentials. Phonon scattering is weaker than in Si (Fig. 4) and InAs (Fig. 5).

	Ge	InAs	Si
Hole mobility ( $\text{cm}^2/\text{Vs}$ )	1900	500	430
Hole Effective mass ( $/m_0$ )	0.35 0.043	0.37 0.043	0.53 0.16
$m_{HH}$   $m_{LH}$			

TABLE I  
BULK HOLE MOBILITY AND EFFECTIVE MASS VALUES FOR Ge, InAs AND Si.

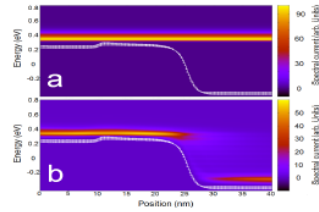


Fig. 4. Current spectrum (arb. units) of  $\langle 110 \rangle$ -compressive Si along the device (a) in the ballistic regime and (b) with phonon scattering calculated with the bulk deformation potentials.

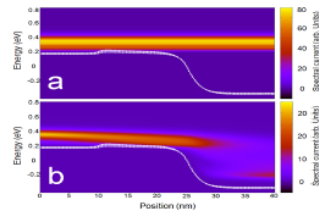


Fig. 5. Current spectrum (arb. units) of  $\langle 110 \rangle$ -compressive InAs along the device (a) in the ballistic regime and (b) with phonon scattering. All phonon interactions are included (acoustic, non polar optical and polar optical).

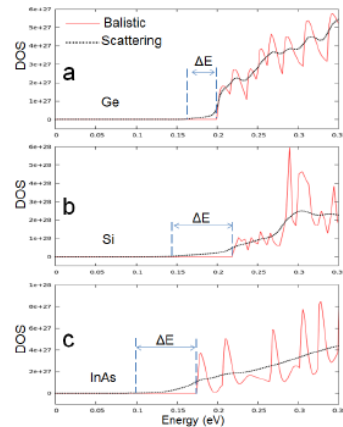
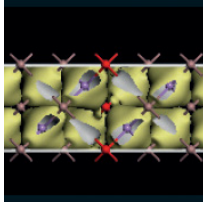


Fig. 6. Density of states (DOS) at the device source side for (a) Ge, (b) Si and (c) InAs, showing the broadening of states  $\Delta E$  in the valence band due to phonon interactions.  $\Delta E = 4$  meV for Ge  $\Delta E = 8$  meV for InAs and  $\Delta E = 9$  meV for Si.

[1] K. Kuhn *IEEE Trans. Electron Devices*, vol. 59, p. 1813, (2012).  
 [2] N. Cavassilas *et al. App. Phys. Lett.*, vol. 96, p. 102102, (2010).  
 [3] M. Luisier *et al. Phys. Rev. B.*, vol. 80, p. 155430, (2009).  
 [4] H. Frohlich in *Proc. R. Soc. London, Ser. A*, p. 230, (1937).  
 [5] G. Klimeck *et al.*, "Numerical approximations for polar optical phonon scattering in resonant tunneling diodes," in *Proc. Quantum Devices and Circuits. Imperial Press, London*, p. 154, (1996).  
 [6] N. Mori and T. Ando *Phys. Rev. B*, vol. 40, p. 6175, (1989). [7] M. Moussavou *et al. under preparation*, (2017).



# International Workshop on Computational Nanotechnology

## 3D Monte Carlo simulations of strained Si GAA nanowire FETs with different channel orientations

M A Elmessary<sup>1,2</sup>, D Nagy<sup>3</sup>, M Aldegunde<sup>4</sup>, A J García-Loureiro<sup>3</sup> and K Kalna<sup>1</sup>

<sup>1</sup>Swansea University, UK, <sup>2</sup>Mansoura University, Egypt, <sup>3</sup>Universidade de Santiago de Compostela, Spain, <sup>4</sup>University of Notre Dame, USA

GAA NW FETs are considered to be the most promising candidates for sub-10 nm digital technology suitable for future CMOS integration due to their superior electrostatics, immunity to short channel effects and large on-current [1]. Strain technology can enhance the drain current [2] but the effectiveness of strain can be reduced due to the pre-existing quantum confinement induced valley splitting [3].

In this work, we study the effects of uniaxial tensile strain in nanoscale Si GAA NW FETs affected by surface and channel orientation with our in-house 3D Finite Element (FE) Monte Carlo (MC) toolbox which uses the calibration-free Schrödinger Equation based Quantum Corrections (SEQC) [4-6] allowing to account for exact nanoscale geometry and thus confinement. The 3D FE mesh contains predefined 2D planes perpendicular to transport direction to solve 2D Schrödinger Eq. separately for the three/six  $\Delta$  valleys:

$$-\frac{\hbar^2}{2} \nabla_{\perp} \cdot [(\mathbf{m}^*)^{-1} \cdot \nabla_{\perp} \psi(y, z)] + U(y, z) \psi(y, z) = E \psi(y, z),$$

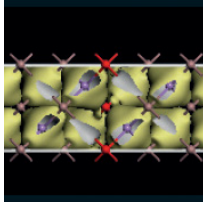
where  $(\mathbf{m}^*)^{-1}$  is the inverse effective mass tensor listed in Table 1,  $U(y, z) = -[qV(y, z) + \chi(y, z)]$  is the potential energy,  $\chi(y, z)$  is the electron affinity,  $\psi(y, z)$  is the wavefunction penetrating into oxide, and  $E$  is the energy [5].

Fig. 1 shows 6 Si  $\Delta$  valleys within confinement cross-section along the transport direction. The strain is modeled by shifting the Si valley by  $\Delta E_C$  according to the strain type and strength (Table 2) [8]. For the uniaxial  $\langle 110 \rangle$  strain, the transverse effective masses in  $\Delta 3$  valley split due to a band-structure warping resulting in a lighter  $m_t^{transport}$  and a heavier  $m_t^{perpendicular}$  [8].

The GAA NW FET has an elliptical cross-section ( $R=5.7/7.17$  nm) and a gate length of 10 nm with EOT=0.8 nm (Fig. 2). We simulate  $\langle 100 \rangle$  and  $\langle 110 \rangle$  channel orientations and two types of tensile strain: uniaxial  $\langle 100 \rangle$  and uniaxial  $\langle 110 \rangle$  with strengths of 0.5%, 0.7% and 1.0%. To show the effect of confinement on strain, the 10 nm gate NW is compared to a bigger device with an elliptical cross-section ( $R=11.3/14.22$  nm) and a gate length of 22 nm with EOT=1.5 nm [1]. The MC toolbox was verified against experimental data for the 22 nm GAA NW with excellent agreement [1, 7].

Fig. 3 shows ID-VG characteristics at  $V_D=0.7$  V for the 10 nm gate length NW in the  $\langle 100 \rangle$  channel orientation under three uniaxial  $\langle 100 \rangle$  strengths of strain delivering increase in the drive-current by 6%, 6.9% and 7.3%, respectively. The sub-threshold slope exhibits a small deterioration under the increasing strain strength. Fig. 4 plots the 3  $\Delta$  valleys contributions to the current in the  $\langle 100 \rangle$  device under uniaxial  $\langle 100 \rangle$  strain with indicated strengths. In this case,  $\Delta 1$  valley is shifted up reducing its contribution to the drain current because it has the largest effective transport mass ( $m_t$ ) (see Table 2).  $\Delta 2$  and  $\Delta 3$  valleys (Table 2) are shifted down increasing their contributions to the drain current because of a smaller effective transport mass ( $m_t$ ).

Since a larger confinement (perpendicular-to-transport) mass results in a lower bound state, the  $\Delta 3$  with a larger confinement effective mass ( $m_t$ ) contributes more to the current than  $\Delta 2$ . The reduction in the strain effectiveness caused by the quantum confinement due to the pre-existing valley splitting is seen in the less confined 22 nm device (Fig. 5). The 0.5/0.7/1.0% uniaxial  $\langle 100 \rangle$  strain increases the drive current (at



# International Workshop on Computational Nanotechnology

$V_{DD}=1.3$  V) in the 22 nm gate length NW FET by 16.6/19.3/21.4% compared to only 6/6.9/7.3% for the 10 nm gate length device.

Fig. 6 shows  $I_D-V_G$  characteristics for the 10 nm gate length NW FET with a  $\langle 100 \rangle$  channel orientation at  $V_D=0.7$  V under uniaxial  $\langle 100 \rangle$  strain. In the  $\langle 100 \rangle$  orientation, a transformation of coordinates is performed since the ellipsoid principal axes are not aligned with the device coordinate system [4, 9]. Without applying any strain, the  $\langle 100 \rangle$  channel device delivers more current (20.4%) than the  $\langle 110 \rangle$  channel device due to enhanced mobility (lighter effective transport mass). When applying uniaxial  $\langle 100 \rangle$  strain, the drive-current at  $V_{DD}=1.0$  V increases by 4.2%, 4.8%, and 3.3% at increasing strain strengths, respectively. The drive-current drop at 1.0% strain is due to the swap of valley contributions to the current with increasing strain. Although  $\Delta 3$  contributes more to the current than  $\Delta 1$  and  $\Delta 2$ , it has smaller increment from 1.0% strain than 0.7% strain while the  $\Delta 1$  and  $\Delta 2$  valleys reduce the current more at the 1.0% strain (see Fig. 7). For the  $\langle 110 \rangle$  side-walls, the  $\Delta 3$  has a smaller confinement mass ( $0.19m_0$ ) than that of  $\Delta 1$  and  $\Delta 2$  ( $0.315m_0$ ). However, the  $\Delta 1$  and  $\Delta 2$  have a larger confinement mass resulting in a confinement of carriers to appear closer to the interface charge. To see the effect of confinement, Fig. 8 shows a comparison for the less-confined 22 nm gate length NW in which the 0.5/0.7/1.0% uniaxial  $\langle 110 \rangle$  strain increases the drive current (at  $V_{DD}=1.0$  V) by 11.6/12.7/7.6% compared to only 4.2/4.8/3.3% in the 10 nm gate device.

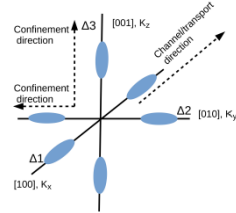


Fig. 1: Schematic of six Si valleys along a confinement plane. The transport direction is along the x-axis.

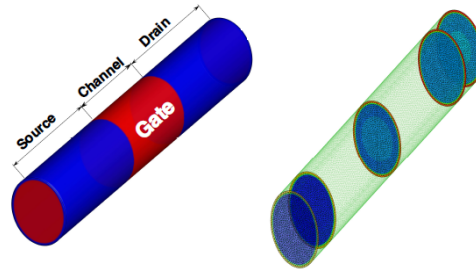


Fig. 2: Schematic of the investigated  $n$ -channel Si GAA nanowire FET (left) and the device mesh with sample of the 2D slices for the Schrödinger solver (right).

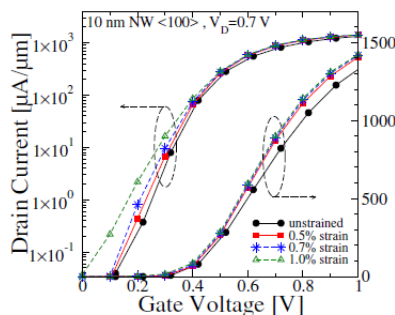


Fig. 3:  $I_D-V_G$  characteristics at  $V_D=0.7$  V for the 10 nm gate length GAA-NW with  $\langle 100 \rangle$  channel orientation under different uniaxial  $\langle 100 \rangle$  strain strengths.

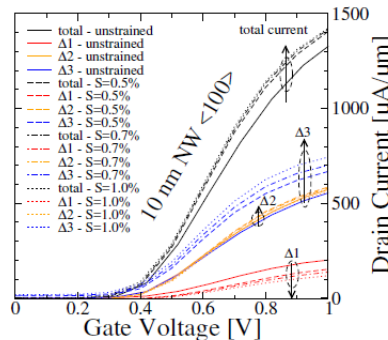


Fig. 4: Valley contributions to the current at  $V_D=0.7$  V for the 10 nm gate length GAA-NW with  $\langle 100 \rangle$  channel orientation under different uniaxial  $\langle 100 \rangle$  strain strengths.

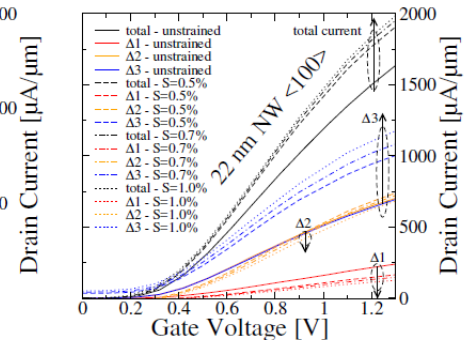
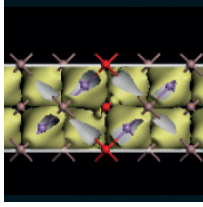


Fig. 5: Valley contributions to the current at  $V_D=1.0$  V for the 22 nm gate length GAA-NW with  $\langle 100 \rangle$  channel orientation under different uniaxial  $\langle 100 \rangle$  strain strengths.



# International Workshop on Computational Nanotechnology

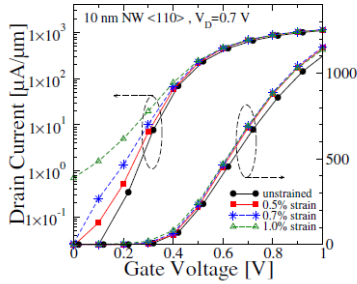


Fig. 6:  $I_D$ - $V_G$  characteristics at  $V_D=0.7$  V for the 10 nm gate length GAA-NW with  $\langle 110 \rangle$  channel orientation under different uniaxial  $\langle 110 \rangle$  strain strengths.

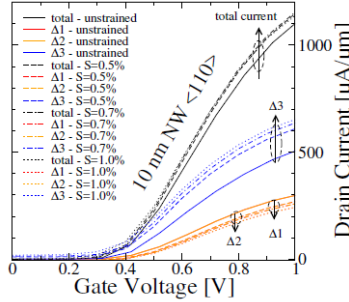


Fig. 7: Valley contributions to the current at  $V_D=0.7$  V for the 10 nm gate length GAA-NW with  $\langle 110 \rangle$  channel orientation under different uniaxial  $\langle 110 \rangle$  strain strengths.

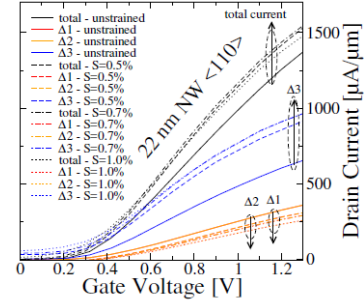


Fig. 8: Valley contributions to the current at  $V_D=1.0$  V for the 22 nm gate length GAA-NW with  $\langle 110 \rangle$  channel orientation under different uniaxial  $\langle 110 \rangle$  strain strengths.

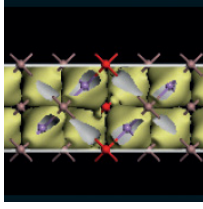
Orientation	Valley	$1/m_{xy}^*$	$1/m_{zz}^*$	$m_{\Gamma}^*$
$\langle 100 \rangle$	$\Delta 1$	$1/m_t$	$1/m_t$	$m_t$
$\langle 100 \rangle$	$\Delta 2$	$1/m_t$	$1/m_t$	$m_t$
$\langle 100 \rangle$	$\Delta 3$	$1/m_t$	$1/m_t$	$m_t$
$\langle 110 \rangle$	$\Delta 1$	$(m_t + m_l)/(2m_t m_l)$	$1/m_t$	$(m_t + m_l)/2$
$\langle 110 \rangle$	$\Delta 2$	$(m_t + m_l)/(2m_t m_l)$	$1/m_t$	$(m_t + m_l)/2$
$\langle 110 \rangle$	$\Delta 3$	$1/m_t$	$1/m_l$	$m_t$

Table 1: Effective-mass tensor and effective transport mass of  $\Delta$  valleys for  $\langle 100 \rangle$  and  $\langle 110 \rangle$  channel orientations where  $1/m_{yz}^*=0$  and degeneracy = 2.

Strain type strain strength	Uniaxial $\langle 100 \rangle$ strain			Uniaxial $\langle 110 \rangle$ strain		
	0.5%	0.7%	1.0%	0.5%	0.7%	1.0%
$\Delta 1$	+0.03eV	+0.042eV	+0.06eV	-0.01eV	-0.014eV	-0.02eV
$\Delta 2$	-0.045eV	-0.063eV	-0.09eV	-0.01eV	-0.014eV	-0.02eV
$\Delta 3$	-0.045eV	-0.063eV	-0.09eV	-0.065eV	-0.091eV	-0.13eV

Table 2: Valley-edge shifts for each valley with different types and strengths of tensile strain [8].

- [1] S. Bangsaruntip et al., *IEDM Tech. Dig.*, pp. 526-529, 2013.
- [2] Keng-Ming Liu et al., *IEEE TED*, vol. 58, no. 10, 2011.
- [3] M. V. Fischetti et al., *J. Appl. Phys.*, vol. 92, no. 12, pp. 7320-7324, 2002.
- [4] M. A. Elmessary et al., *IEEE TED*, vol. 63, no. 3, pp. 933-939, 2016.
- [5] J. Lindberg et al., *IEEE TED*, pp. 423-429, 2014.
- [6] M. Aldegunde et al., *IEEE TED*, pp. 1561-1567, 2013.
- [7] M. A. Elmessary et al., *Solid-St. Electron.*, vol. 128, pp. 17-24, 2017.
- [8] K. Uchida et al., *IEDM Tech. Dig.*, pp. 129-132, 2005.
- [9] A. Rahman et al., *J. Appl. Phys.*, vol. 97, no. 5, pp. 053702, 2005.



# International Workshop on Computational Nanotechnology

## Spin-dependent trap-assisted tunneling in magnetic tunnel junctions: A Monte Carlo study

V Sverdlov, J Weinbub, and S Selberherr

TU Wien, Austria

Spin-dependent resonant tunneling is responsible for the large resistance modulation with magnetic fields observed in three-terminal spin accumulation experiments [1]; however, the expression for the magnetoresistance dependence was questioned [2]. To resolve the controversy, we developed a numerical Monte Carlo approach for the trap-assisted spin tunneling in tunnel junctions. In contrast to spin-independent tunneling [3,4], the transition rates depend on the magnetic field  $\mathbf{B}$  and the magnetization  $\mathbf{M}$  direction of the electrodes. In the case, when an electron can jump from a normal electrode to the trap with the rate  $\Gamma_N$  and from the trap to the ferromagnetic electrode (characterized by the polarization vector  $\mathbf{p} = \frac{\Gamma_+ - \Gamma_-}{2\Gamma_F} \frac{\mathbf{M}}{|\mathbf{M}|}$ ) with the rates  $\Gamma_{\pm} = \Gamma_F(1 \pm |\mathbf{p}|)$  for the spin parallel (anti-parallel) to  $\mathbf{M}$  (Fig.1), the trap occupation  $n$  depends on the electron spin  $\mathbf{s}$  [5]:

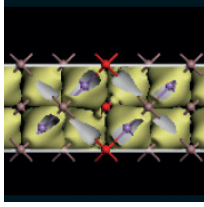
$$\frac{d}{dt}n = \Gamma_N(1 - n) - \Gamma_F n - \Gamma_F \mathbf{p} \mathbf{s}, \quad \frac{d}{dt}\mathbf{s} = -\Gamma_F \mathbf{s} - \mathbf{p} \Gamma_F n + [\mathbf{s} \times \boldsymbol{\omega}_L].$$

Here  $\boldsymbol{\omega}_L = \frac{e\mathbf{B}}{mc}$  is the Larmor frequency vector pointing along the magnetic field  $\mathbf{B}$ . The escape probability  $P(t) = 1 - n(t)$  from the trap is determined by the matrix differential equation (1) (Fig.2). Since the electrons tunnel to the trap from the normal spin-unpolarized electrode, the initial conditions for Eq.1 are  $n(t=0)=1$  and  $\mathbf{s}(t=0)=0$ .

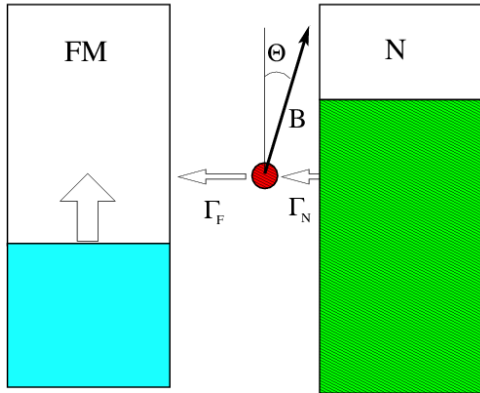
Fig.3 shows the typical probability distributions for escape times from the trap. In contrast to spin-independent tunneling, the probability is not determined by a single exponential and has a more complex behavior. For further calculations the probabilities are stored to evaluate the escape times later.

The charge transport consists of a series of repeated cycles: An electron jumps from the normal electrode to the trap with the rate  $\Gamma_N$ , followed by the electron hop from the trap to the ferromagnetic electrode with the probability  $P(t)$ . Double occupancy of the trap is prohibited by the Coulomb repulsion. One electron charge is transferred at each cycle during the time  $T=T_1+T_2$ . The fluctuating time  $T_1$  is evaluated by a direct Monte Carlo technique according to the distribution probability  $P_1(t) = \exp(-t/\Gamma_N)$ . The time  $T_2$  is distributed according to  $P_2(t) = n(t)$  and is evaluated with the rejection technique. The total current  $I$  is computed as  $I = eN / \sum_{i=1}^N (T_1 + T_2)_i$ , where  $N$  is a large number of cycles  $i$ .

Current simulation results are shown in Fig.4. They are in good agreement with the results from [1]. The current values from [2] are too large for all the directions of the magnetic field except the one, when  $\mathbf{B}$  is parallel to  $\mathbf{p}$ . This implies that escape times used in [2] are shorter. The escape time distribution probability in [2] is determined by the two tunneling rates from each of the Zeeman levels renormalized by coupling to the ferromagnetic contact (Fig.5, dashed lines). This approximation [2] is appropriate only in the case, when the magnetic field is aligned with the magnetization. Fig.6 shows the error reduction for a shorter time while solving the matrix equation (Fig.2) for this case. The consideration based on the matrix equation (Fig.2) is necessary to reproduce the correct transition probabilities and currents.



# International Workshop on Computational Nanotechnology



$$\frac{d}{dt} \begin{pmatrix} n \\ S_x \\ S_y \\ S_z \end{pmatrix} = A \begin{pmatrix} n \\ S_x \\ S_y \\ S_z \end{pmatrix}, \quad (1)$$

$$A = \begin{pmatrix} -\Gamma_F & -|\mathbf{p}|\Gamma_F \sin(\theta) & 0 & -|\mathbf{p}|\Gamma_F \cos(\theta) \\ -|\mathbf{p}|\Gamma_F \sin(\theta) & -\Gamma_F & -\omega_L & 0 \\ 0 & \omega_L & -\Gamma_F & 0 \\ -|\mathbf{p}|\Gamma_F \cos(\theta) & 0 & 0 & -\Gamma_F \end{pmatrix}$$

Fig.1 Electrons tunnel from the normal electrode to the trap with the rate  $\Gamma_N$  and from the trap to the ferromagnetic electrode with the rates  $\Gamma_+$  ( $\Gamma_-$ ) for the spin parallel (anti-parallel) to  $\mathbf{M}$ .

Fig.2 Matrix equation which describes the trap occupation and the spin. To find the escape rates the equation is solved numerically with the initial conditions  $n(t=0)=1$  and  $\mathbf{s}(t=0)=0$ .

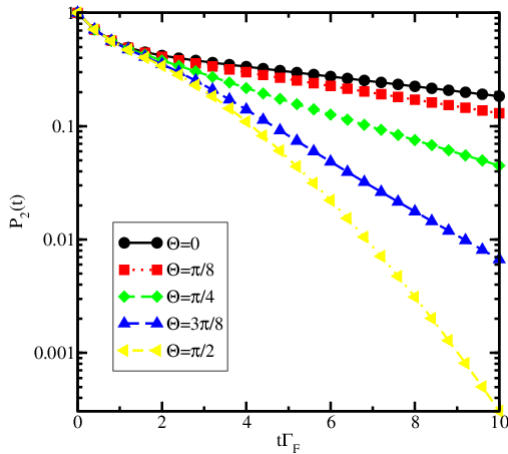


Fig.3 Probability distribution of escape times for  $\Gamma_F = \omega_L$  and  $|\mathbf{p}|=0.9$ .

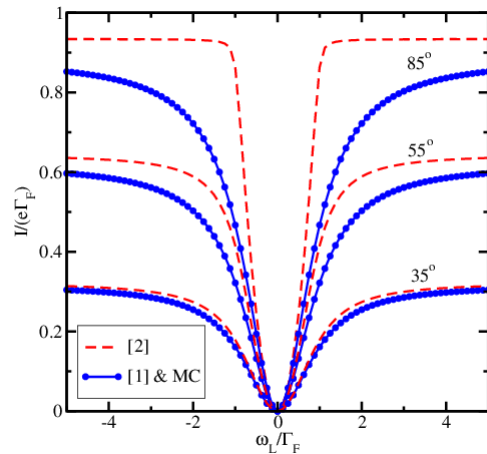


Fig.4 Comparison of Monte Carlo results (symbols) with the results from [1] and [2].

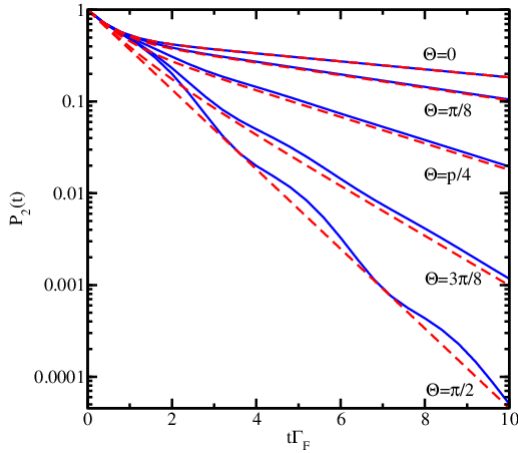
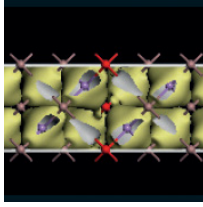


Fig.5 Probability distribution of escape times for  $\omega_L=2\Gamma_F$ ,  $|\mathbf{p}|=0.9$  compared to those computed with the method from [2].

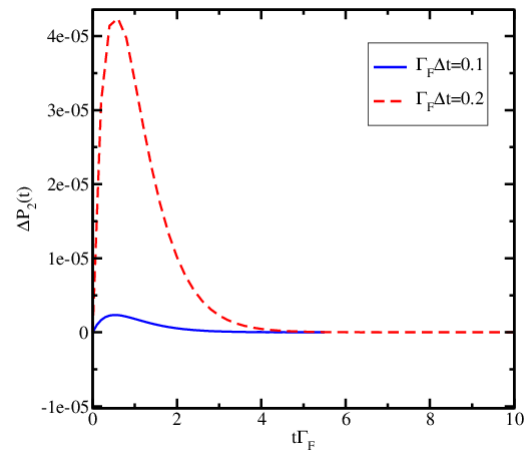


Fig.6 Validation of the numerical rates for two different time steps by comparing with the analytical results from [2] for  $\Theta = 0$ .

- [1] Y.Song and H.Dery, Phys.Rev.Lett. 113, 047205 (2014).
- [2] Z.Yue et al., Phys.Rev.B 91, 195316 (2015).
- [3] C.Wasshuber, H.Kosina, and S.Selberherr, IEEE Trans.on CAD of Int.Circuits and Systems 16, 937 (1997).
- [4] A.N.Korotkov and K.K.Likharev, Phys.Rev.B 61, 15975 (2000).
- [5] V.Sverdlov and S.Selberherr, EUROSOI-ULIS, p.202 (2016).

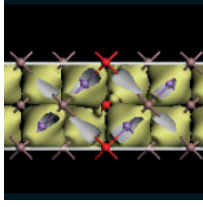
## Full band Monte Carlo simulation of high-field transport in si nanowires

R Hathwar, M Saraniti, and S M Goodnick

Arizona State University, USA

The effect of collision broadening on the number of impact events has previously been studied in bulk materials. It was shown that incorporating collision broadening increases the number of impact events in the bulk [1]. In this paper, we study the effect of collision broadening in nanowires, where it is expected to have more significance due to the 1D nature of the density of states. In this initial study, a simple Lorentzian broadening is employed and its effects on the velocity field and impact ionization events are studied. A full band impact ionization rate for nanowires is also presented for the first time within the tight binding scheme.

The band structure of the Si nanowires along the [100] direction is calculated according to the empirical tight binding method (TB) [2]. The deformation potential scattering rates are calculated using Fermi's golden rule from the TB coefficients using the method outlined in [3]. At high electric fields multiband tunneling during the free-flight process becomes important [4]. This is taken into account by solving the Krieger and lafrate equations using the Magnus expansion method [5]. The impact ionization rate is derived for nanowires within the TB scheme and is given by eqn. (1)  $k_{1,n}$  represents the high energy electron/hole impacting with a valence band electron/conduction band hole,  $k_{4,m}$  creating two new electrons/holes,  $k_{2,n'}$  and  $k_{3,m'}$ .



## International Workshop on Computational Nanotechnology

$$W_{II}(k_{1,n}, \Delta k_{2,n'}) = \frac{e^4}{\varepsilon^2 (2\pi)^3 \hbar} \times \int_{E_{\min}}^{E_{\max}} \sum_{k_3, m'} \left| F_{n,n'}(k_1, k_2, k_3, k_4) \right|^2 \times [JDOS_{m,m'}(k_4, k_3)] DOS_{n'}(k_2) dE_{n'}(k_2) \quad (1)$$

where the overlap integral is given by

$$F_{n,n'}(k_1, k_2, k_3, k_4) = \sum_{\mu, \nu} e^{iq_x |\tau_\mu - \tau_\nu|} \int \frac{J_0(q_t a_{diff})}{q_x^2 + q_t^2} \times C_{n,\mu}(k_1) C_{n',\mu}^*(k_2) C_{m,\nu}(k_4) C_{m',\nu}^*(k_3) q_t dq_t \quad (2)$$

and the joint density of states is

$$JDOS_{m,m'}(k_a, k_b) = \frac{1}{\left| \frac{\partial E_m(k_a)}{\partial k_b} - \frac{\partial E_{m'}(k_b)}{\partial k_b} \right|} \quad (3)$$

$$q_x = (k_1 - k_2) \quad , \quad \tau_\mu \quad \text{is the atom position,} \quad a_{diff} = \sqrt{(\tau_{\mu,y} - \tau_{\mu',y})^2 + (\tau_{\mu,z} - \tau_{\mu',z})^2}$$

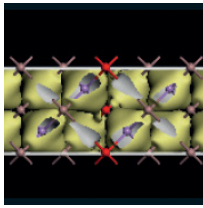
and  $C_{i,j}(k)$  are the tight binding coefficients.

The calculation of the overlap integral given by eqn. (2) is computationally very expensive. It can be replaced with a constant overlap integral which greatly reduces the number of computations while still being fairly accurate as shown in Fig.1 and Fig.2, though the effect of the approximation on the anisotropy of the impact ionization rates is unclear.

As an initial study of the effect of collision broadening on the high field properties of Si nanowires, the final energy after a scattering event is governed by a Lorentzian distribution rather than a delta function. The width of the Lorentzian distribution is given by the total scattering rate at that energy [6].

The nanowires considered in this study are 2nm x 2nm rectangular Si nanowires along the [100] direction. The effect of adding the simple collision broadening on the velocity- field curves is shown in Fig.3. The addition of collision broadening reduces the mobility and the peak velocity. In Fig.4 the energy distribution of electrons at an electric field of 750 kV/cm after they have reached steady state is shown. When collision broadening is included, the electrons are able to reach much higher energies as shown in the figure.

This increase in the energy distribution leads to a significant increase in the number of impact events occurring as shown in Fig. 5. Therefore the correct treatment of collision broadening is important to properly understand the role of impact ionization at high electric fields in nanowires.



# International Workshop on Computational Nanotechnology

ionization rate and the rate calculate with a fixed overlap integral of  $10^{-8}$ .

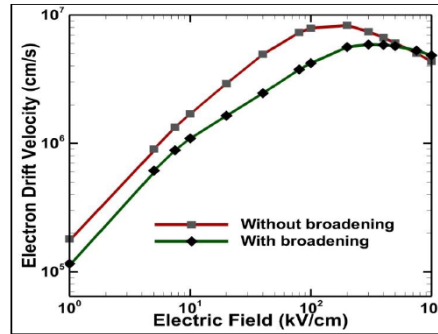


Fig. 3. Velocity field curves for electrons in a 2nm x 2nm Si nanowire with and without Lorentzian broadening.

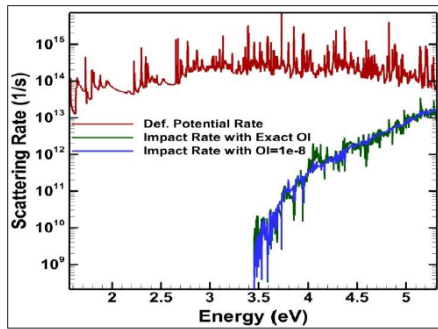


Fig. 1. Scattering rates for electrons in a 2nm x 2nm Si nanowire. Comparison between the exact impact ionization rate and the rate calculate with a fixed overlap integral of  $10^{-8}$ .

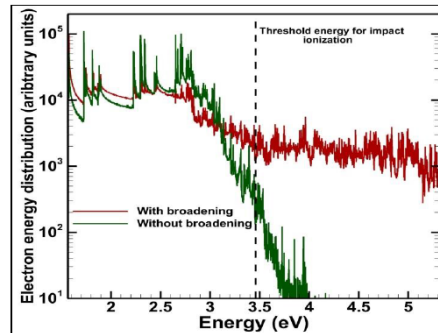


Fig. 4. Electron energy distributions for electrons in a 2nm x 2nm Si nanowire at 750 kV/cm with and without Lorentzian broadening.

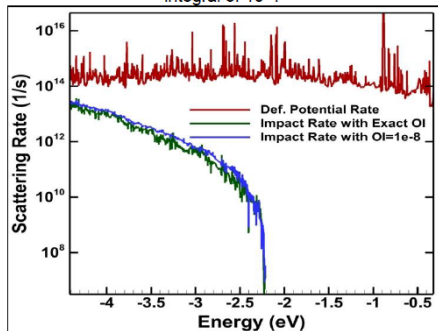


Fig. 2. Scattering rates for holes in a 2nm x 2nm Si nanowire. Comparison between the exact impact

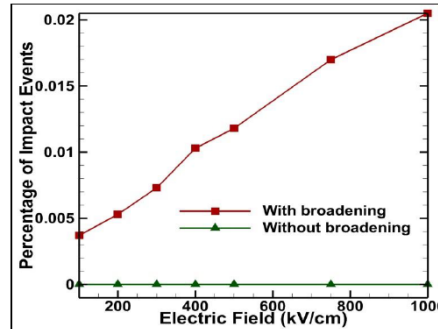
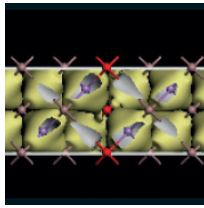


Fig. 5. Percentage impact events during a single free-flight duration of electrons in a 2nm x 2nm Si nanowire with and without Lorentzian broadening.

- [1] Y.Chang, D. Ting, J. Tang, K. Hess, Applied Physics Letters, 42, 76 (1983).
- [2] S. Lee, F. Oyafuso, P. Allmen, G. Klimeck, Physical Review B, 69, 045316 (2004).
- [3] A.K. Buin, A. Verma, and M. P. Anantram, J. Appl. Phys. 104, 053716 (2008).
- [4] H-E. Nilsson, A. Martinez, E. Ghillino, U. Sannemo, E. Bellotti and M. Goano, Journal of Applied Physics, 90,6 (2001).
- [5] R. Hathwar, M. Saraniti, S.M. Goodnick, Journal of Applied Physics, 120, 044307 (2016)
- [6] L. Reggiani, P. Lugli, and A. Jauho, Journal of Applied Physics, 34, 3072 (1988).



# International Workshop on Computational Nanotechnology

## Session: Phonon Properties and Thermal Transport

### (Invited) Anderson-like localization of phonon in nano-structures

Y Chalopin<sup>1</sup>, S Mayboroda<sup>2</sup> and M Filoche<sup>3</sup>

<sup>1</sup>Ecole CentraleSupelec, France, <sup>2</sup>University of Minnesota, USA, <sup>3</sup>Ecole Polytechnique, France

Based on a recent theory of wave localization and the development of a mathematical tool (the localization landscape) we propose an approach that predicts the localization of thermal phonons in disordered lattices. An analogy between the Schrödinger equation and the classical equation of motion is introduced to demonstrate that localization of thermal energy in phonon systems arises from atomic disorder through which the localization landscape can be revealed. This approach, illustrated on disordered graphene, provides a powerful framework for engineering heat conduction in nanostructures using wave effects.

### Thermionic cooling devices based on AlGaAs/GaAs heterostructures

M Bescond<sup>1</sup>, D Logoteta<sup>1</sup>, N Cavassilas<sup>1</sup>, A Yangui<sup>2</sup>, K Hirakawa<sup>2</sup> and M Lannoo<sup>1</sup>

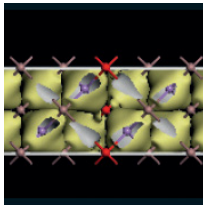
<sup>1</sup> CNRS IM2NP, France, <sup>2</sup>University of Tokyo, Japan

Efficient cooling devices in nanoelectronics and optoelectronics is a matter of urgency. For instance, it is well-recognized that self-heating of microprocessors is one of the fundamental limit to system performance [1]. Recently, nanostructured devices have attracted broad interest since they have enhanced thermoelectric effects with respect to their bulk counterparts [2]. The present work theoretically investigates thermionic cooling devices based on AlGaAs/GaAs heterostructures. To do so, we couple self-consistently the non-equilibrium Green's function (NEGF) equations for electrons with 1D-Poisson equation for electrostatic and 1D-heat equation [3], [4]. Phonon scattering in the electron transport is described *via* the concept of self-energy in the self-consistent Born approximation (SCBA). It includes interactions with acoustic and non-polar optical phonons as well as long range polar optical interactions of the Frohlich type treated within a diagonal (*i.e.* local) approach [5].

Figure 1 represents the studied semiconductor heterostructure refrigerator (SHR) initially proposed in Ref.[6] which couples tunneling injection with thermionic extraction. The cold electrons are injected into the active region by resonant tunneling through a potential barrier, while the hot electrons are removed from the active region by thermionic emission over a thicker barrier that serves as a thermal wall to reduce the heat backflow. Since the left access region cools while the right one heats up, the central region acts then as an energy-selective filter [7].

Figure 2 shows the current characteristics obtained for three different temperatures enforced at the contacts without (empty symbols) and with (solid symbols) the treatment of the heat equation. We can see that the self-heating inside the active region has almost no influence on the current even at higher temperatures. However, the two physical phenomena described in Figure 1, namely the resonant tunneling and the thermionic emission above the thick barrier are clearly visible in the current spectrum (Fig.3). In particular we see in Figure 4 that the current injected from the left part of the active region corresponds to the energy of the resonant state in the central GaAs quantum well.

Moreover, as shown in Figure 5, the electronic heat power density (*i.e.* the power transferred locally between the electrons and the lattice) is negative in the left region (the lattice is cooled by the electron current) and peaked at the position of the resonant level.



# International Workshop on Computational Nanotechnology

Acoustic phonons having a higher group velocity than their optical counterparts they are responsible of heat transport. Figure 6 shows the acoustic phonon temperature along the device. As expected it decreases in the left region while it increases in the right side. The considered SHR actually acts as a thermionic cooling device. This work quantifies the heat removal by the electric current due to the resonant-tunneling thermionic process. A numerical analysis will be performed in order to optimize the performances of the device and to reach the highest thermionic cooling efficiency.

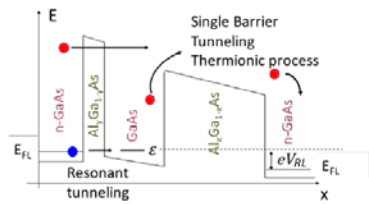


Fig. 1. Schematic representation of the heterostructure. The thicknesses of the left and right n-GaAs regions are equal to 150 nm and 60 nm respectively with a doping of  $10^{18} \text{cm}^{-3}$ . The AlGaAs barriers have a thickness of 2.4 nm and 150 nm respectively. The Al mole fractions are  $y = 0.2$  and  $x = 0.1$ . The GaAs quantum well thickness is 4.8 nm.

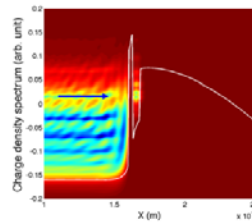


Fig. 4. Charge density spectrum corresponding to the current of Fig. 3. The current injected from the left contact clearly aligns with the resonant level of the central GaAs quantum well.

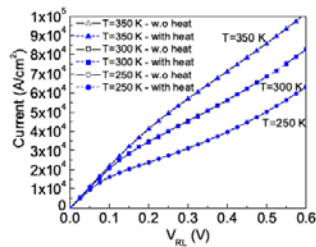


Fig. 2. Current characteristics for three temperatures:  $T = 350 \text{ K}$  (triangles),  $300 \text{ K}$  (squares), and  $250 \text{ K}$  (circles). Empty symbols corresponds to the results obtained without including the coupling with the heat equation while the solid symbols are obtained with the effect of heat equation.

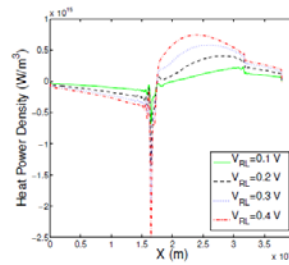


Fig. 5. Heat power density along the structure obtained at  $T = 350 \text{ K}$  for various biases  $V_{RL}$ . Positive and negative components are well separated spatially by the resonant level.

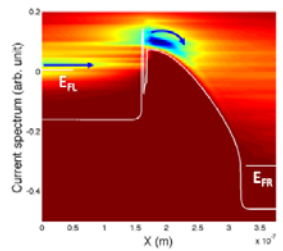


Fig. 3. Current spectrum obtained at  $T = 350 \text{ K}$  and  $V_{RL} = 0.3 \text{ V}$ . Fermi levels of left and right contacts are also represented. Arrows indicate the main current flux in the left access region and above the barrier, highlighting the physical processes represented in Figure 1.

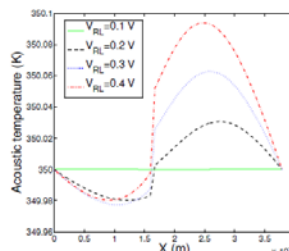
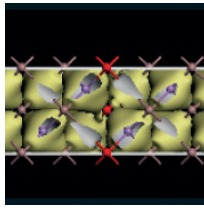


Fig. 6. Acoustic phonon temperature profiles corresponding to the heat power density of Fig. 5. The temperature cools by 20 mK in the left side and increases by almost 90 mK in the right side.

- [1] R. Rhyner *et al.*, *Nano Lett.* 16, 1022 (2016).
- [2] J.T. Muhonen *et al.*, *Rep. Prog. Phys.* 75, 046501 (2012).



## International Workshop on Computational Nanotechnology

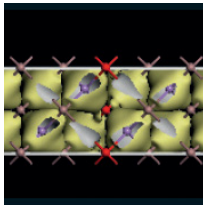
- [3] R. Kim *et al.*, *J. Appl. Phys.* 110, 03451 (2011).
- [4] M. Pala *et al.*, *J. Appl. Phys.* 117, 084313 (2015).
- [5] M. Moussavou, M. Bescond *et al.*, under preparation (2017).
- [6] K. A. Chao *et al.*, *Appl. Phys. Lett.* 87, 022103 (2005).
- [7] T. E. Humphrey *et al.*, *Phys. Rev. Lett.* 89, 116801 (2002).

### DFT/NEGF study of discrete dopants in Si/GaAs 3D FETs including phonon scattering and self-heating

L Wilson<sup>1</sup>, A Martinez<sup>1</sup>, A Price<sup>1</sup> and R Rurali<sup>2</sup>

<sup>1</sup>Swansea University, UK, <sup>2</sup>Institut de Ciència de Materials de Barcelona, Spain

Si FinFET nanowire transistors have been in production since 2010 and exhibit the promise of superior electrostatic and better performance than the planar MOSFET counterpart. As the size of the active regions of devices continues to be scaled down to nanometre dimensions, the number and location of a few impurities dramatically affect device performance. Tunnelling and confinement combined by strong local electrostatic potential invalidate the use of semi-classical models such as the drift-diffusion and Monte Carlo methods. The lack of validity of these methodologies to sub 10 nanometre dimensions is a direct consequence of the wave nature of the electron. Substantial work on discrete dopants has been carried out using a discrete point charge model in the NEGF formalism [1]. The density produced by this point model is mostly spherically symmetric or slightly deformed by the effective mass tensor. However, the wavefunction of the electron/hole occupying the dopant atom exhibits a tetrahedral symmetry and a shape dictated by the atomistic distribution of the surrounding. This can be seen in Fig. 1 and 2, which shows the absolute value of the wavefunction corresponding to an impurity embedded in Si and GaAs atom supercells. In the case of silicon, the dopant atom is Phosphorus and in the GaAs the dopant atom is Silicon. There is a concern of how reliable this point charge model is and what are the differences of using a more accurate description of the dopant and how much the I-V characteristic is changed by the use of this model. In this work, using non-equilibrium Greens Function (NEGF) formalism, we calculated the transfer characteristics of Si and GaAs nanowire transistors with a dopant in the middle of the channel [2]. The device has a 2.2 nm<sup>2</sup> cross-section and a 6 nm channel length. The self-consistent electrostatic energy is shown in Fig. 4. We model the dopant atoms as a point charge, see Fig. 4, and also as a charge which reflects the DFT electron density. Scattering and self-heating are included. The calculation of the DFT dopant wavefunction is carried out with the Siesta code [3], using a supercell of 512 atoms. The ID-VG characteristics for the Si and GaAs devices are shown in Fig. 3, all simulations are done at VD = 0.4 V. In general, the current difference between the two dopant models is small. However, the difference is large in the case of GaAs. This difference can be attributed to the slight decrease in the source drain barrier height induced by the point charge. This effect can be observed by comparing the subbands in Fig. 5 and Fig. 6. These figures show the current spectrum and the first subbands for the 3 lowest Valleys of GaAs. Fig. 7 and 8 show the current spectra for the Si Device with DFT distributed charge at low and high drain. At low gate, the electron system heats up in the source and cools down at the drain, however at high gate bias the electron system is more efficient to dissipate the energy as the cooling of the electron system starts at the source-channel interface. It should be noted that for these devices there is a substantial amount of source to drain tunnelling. This can be observed in all the figures showing the current spectrum.



# International Workshop on Computational Nanotechnology

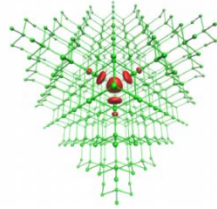


Fig. 1 Electron density of the LUMO in the 511 Si atoms supercell. The LUMO is centered in the P atom

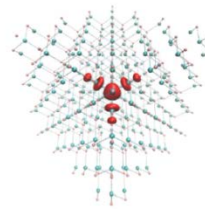


Fig. 2 Electron density of the LUMO in the 511 GaAs atoms supercell. The LUMO is centered in the Si atom

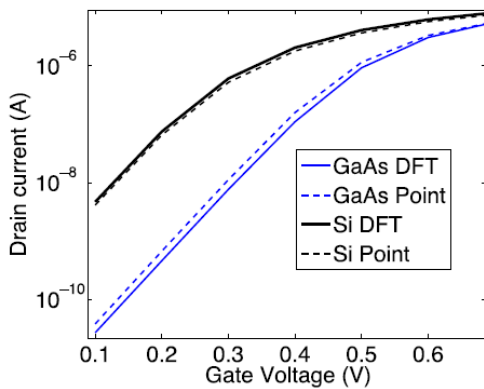


Fig. 3  $I_D$ - $V_G$  characteristic of Si and GaAs GAA nanowires with point/DFT charge density

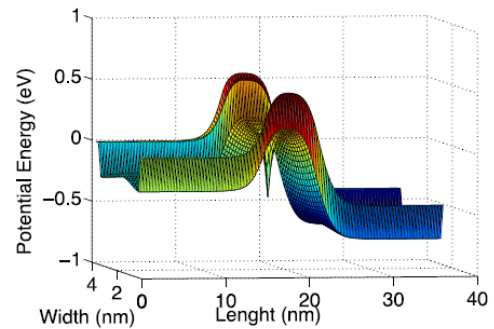


Fig. 4 Potential Energy along the channel and the one of the width for the point charge impurity.

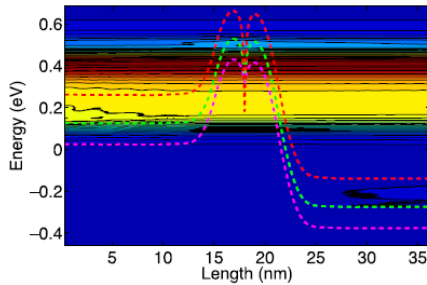


Fig. 5 Current spectrum for the GaAs device with a point charge. The subbands corresponding to the 3 lowest energy valleys are also shown. The point charge lower the energy barrier at the middle of the channel,  $V_g = 0.1$  V

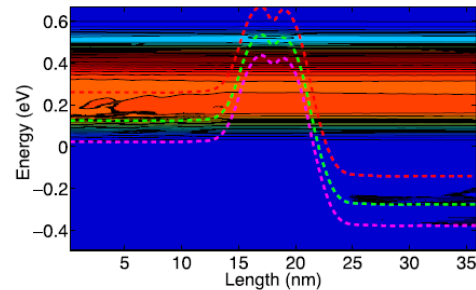


Fig. 6 Current spectrum for the GaAs device with a DFT distributed charge. The subbands of the three lowest valleys of GaAs are also shown,  $V_g = 0.1$  V

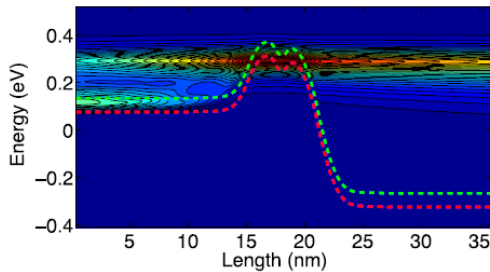


Fig. 7 Current spectrum for the Si device with a DFT distributed charge at  $V_g = 0.1$  V

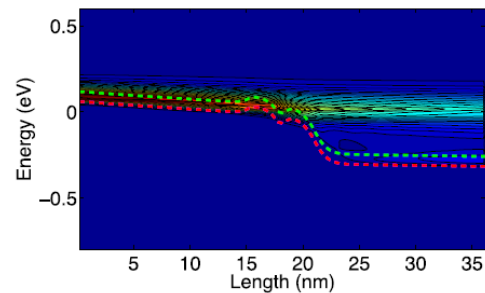
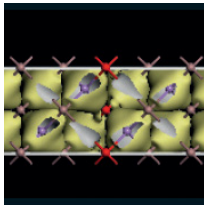


Fig. 8 Current spectrum for the Si device with DFT distributed charge at  $V_g = 0.7$  V



# International Workshop on Computational Nanotechnology

- [1] Valin, R. et al.: Non-equilibrium Green's functions study of discrete dopants variability on an ultra-scaled FinFET. *Journal of Applied Physics* 117(16) (2015).
- [2] Price, A. et al.: Investigation on phonon scattering in a GaAs nanowire field effect transistor using the non-equilibrium Green's function formalism. *Journal of Applied Physics* 117(16) (2015).
- [3] Soler, J.M. et al.: The SIESTA method for ab initio order-N materials simulation. *Journal of Physics-Condensed Matter* 14(11), 2745-2779 (2002).

## Numerical techniques for the reduction of thermal conductivity measurements at nanoscale

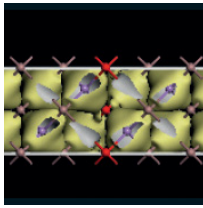
G Pennelli<sup>1</sup>, E Dimaggio<sup>1</sup>, D Narducci<sup>2</sup> and M Macucci<sup>1</sup>

<sup>1</sup>Università di Pisa, Italy, <sup>2</sup> University of Milan-Bicocca, Italy

Nanostructuring offers the opportunity to increase the figure of merit of materials for thermoelectric applications, through the reduction of their thermal conductivity. The development of innovative nanostructured materials for thermoelectric applications requires the improvement of techniques and procedures for the reliable measurement of the thermal conductivity on a nanometric scale. Techniques for the measurement of thermal conductivity require heaters and temperature sensors (thermistors or thermocouples) whose width cannot be very small with respect to that of the nanostructures to be characterized. Conventional data analysis assumes that they are negligible, and can thus lead to misleading results. We propose to analyse the experimental measurements by means of finite element (FEM) modelling, taking into account the thermal and electrical transport both in the heaters/sensors and in the material to be characterized.

We present a numerical method for the characterization of thermal conductivity at the nanoscale with the  $3\omega$  technique [1]. This method has been applied to the analysis of experimental data for a device based on silicon nanomembranes, whose SEM image is shown in Fig. 1: a metal strip is fabricated on the suspended silicon structure, and is biased with a sinusoidal current; the amplitude and phase of the third harmonic of the voltage drop is measured in a four-probe configuration, through a lock-in amplifier. The key challenge of the  $3\omega$  technique is to develop suitable models for relating this third harmonic amplitude with the thermal conductivity of the structures under test. Analytical models have been developed in the past [2], assuming that: 1) the room temperature value of the heater resistance can be used for calculating the dissipated power; 2) the width of the heater is negligible with respect to the size of the structure to be measured; 3) the nanostructures are good electrical insulators. All these assumptions can lead to misleading results at the nanoscale. Our numerical technique consists in detecting the exact size both of the nanostructures and of the metal strip (heater) from SEM images; the thickness of the Si structures and of the metal heater is estimated from AFM images. This information is used to define a 3D model of the whole device (nanostructures and heater), for which we generate a discretization grid (see Fig. 2). Then, the electrical and thermal transport is simulated (within this 3D model) by means of the finite-element (FEM) technique, considering the thermal conductivity as a fitting parameter (see Fig. 3). An excellent fitting of the data can be obtained, overcoming the limits of conventional modelling (see Fig. 4). An automated procedure (Python code) for SEM photo survey, grid generation, and FEM simulation has been developed to achieve an acceptable throughput in the processing of experimental data.

We applied this method also to material deposited on top of suspended  $\text{Si}_3\text{N}_4$  membranes (see Fig. 5). A metal heater has been considered in the middle of the nanomembrane, and the thermoelectric transport equations have been numerically solved for the thermal characterization of the material. Comparison with analytical models [1] will be reported.



# International Workshop on Computational Nanotechnology

Some materials cannot be deposited on suspended nanomembranes, but need to be supported on a semi-insulating substrate. In this case, conventional thermal conductivity techniques can be easily applied only to the measurement of the thermal conductivity in the perpendicular direction with respect to the film plane. Our numerical method can be applied also for the measurement of the thermal conductivity in the film plane, parallel to the supporting substrate. To this end, two metal strips, deposited on the supported film, must be considered. The distance, width and thickness of the two metal strips can be designed so that the thermal conductivity in the film plane is prevalent. Our FEM fitting procedure allows reliable data analysis for the thermal characterization of films deposited on a supporting semi-insulating substrate.

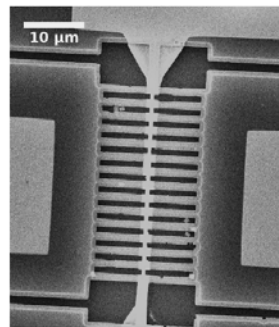


Fig. 1. SEM image of a device based on suspended Si nanomembranes, with a metal track (heater) fabricated in the middle



Fig. 2. A 3D model of the device of Fig. 1. Lengths and widths have been determined from the SEM photo, thicknesses have been determined by means of AFM imaging.

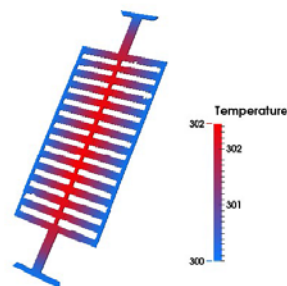


Fig. 3. Thermoelectric transport equations are solved by means of the Finite Element technique, considering the 3D model of the device (see Fig. 2). A current is imposed in the metal heater.

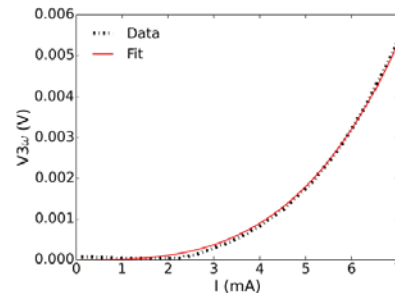


Fig. 4. The thermal conductivity is obtained by fitting the experimental data.

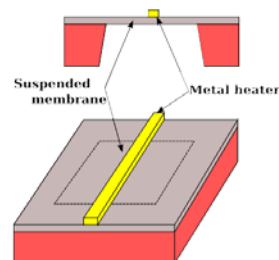


Fig. 5. The same technique can be applied to thin suspended nanomembranes, with a metal heater fabricated in the middle

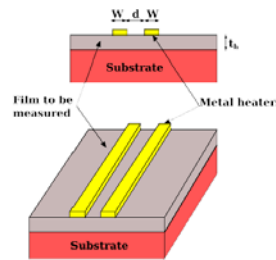
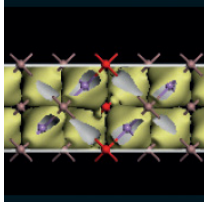


Fig. 6. Two heaters allow the characterization of the thermal properties of films on substrates. The width the separation of the metal tracks must be made small enough to guarantee that thermal transport through the substrate will be negligible.

- [1] D. G. Cahill, Rev. Sci. Instrum 61, 802, 1990.
- [2] A.Jain, K.E.Goodson, Journal of Heat Transfer 130, 102402, 2008.



# International Workshop on Computational Nanotechnology

## Thermal transport in III-V semiconductor materials and superlattices based on molecular dynamics with optimized tersoff potentials

S Mei and [I Knezevic](#)

University of Wisconsin-Madison, USA

III-V compound semiconductor materials are widely used in high-speed electronic and optoelectronics devices. III-V superlattices (SLs) make the active core of quantum cascade lasers (QCLs). Despite the wide popularity of III-V materials and III-V SLs, phonon transport in such materials and nanostructures, especially those involving ternary alloys, is still poorly understood.

The dominant scattering mechanism in III-V ternary alloys is mass-difference scattering. In previous efforts to describe the thermal conductivity of bulk III-V ternary alloys, the virtual crystal approximation (VCA) together with the Klemens-Callaway model was often employed [1]. However, the cation masses in III-V ternary alloys can differ a great deal (e.g.,  $m_{\text{Al}}=26.98$  au,  $m_{\text{In}}=114.82$  au). As a result, a simple first-order perturbation model like the VCA cannot accurately capture the influence that mass-difference scattering has on thermal conductivity in these systems. Molecular dynamics (MD) simulations treat atoms as classical particles following Newton's law of motion and explicitly consider the mass of each atom. Therefore, mass-difference scattering in III-V ternary alloys can be fully captured in MD simulations. In addition, all orders of the anharmonic phonon-phonon interactions are implicitly included in MD simulations, which is impossible in many other models.

To simulate III-V ternary alloys using MD, we adopt Tersoff-type nearest-neighbor potentials for III-V binaries [2]. Most reported potentials are parameterized to best capture the mechanical properties of these materials [3]-[5]. We further optimize these potentials to achieve agreement with acoustic-phonon dispersions, which ensures they are better suited for the calculation of thermal properties. We use equilibrium MD (EMD) simulations together with the Green-Kubo method to calculate the thermal conductivity of both binary crystals and ternary alloys. In ternary alloys, we simulate multiple random alloy structures and take the average to obtain the bulk thermal conductivity.

Furthermore, to study III-V SLs, the morphology of the interfaces can naturally be explicitly captured in MD, leading to an accurate description of interfacial transport. Nonequilibrium MD (NEMD) can provide insight into thermal transport across interfaces, and we will employ it to calculate the anisotropic thermal conductivity tensor in III-V SLs.

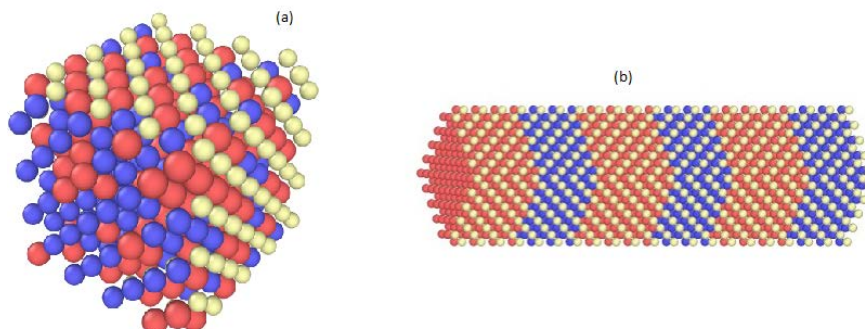
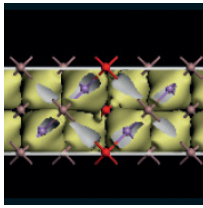


Figure 3. Sample simulation cells for (a) an InGaAs bulk alloy and (b) a InAs/GaAs superlattice. Red atoms represent Ga, blue atoms represent In, and yellow atoms represent As.



# International Workshop on Computational Nanotechnology

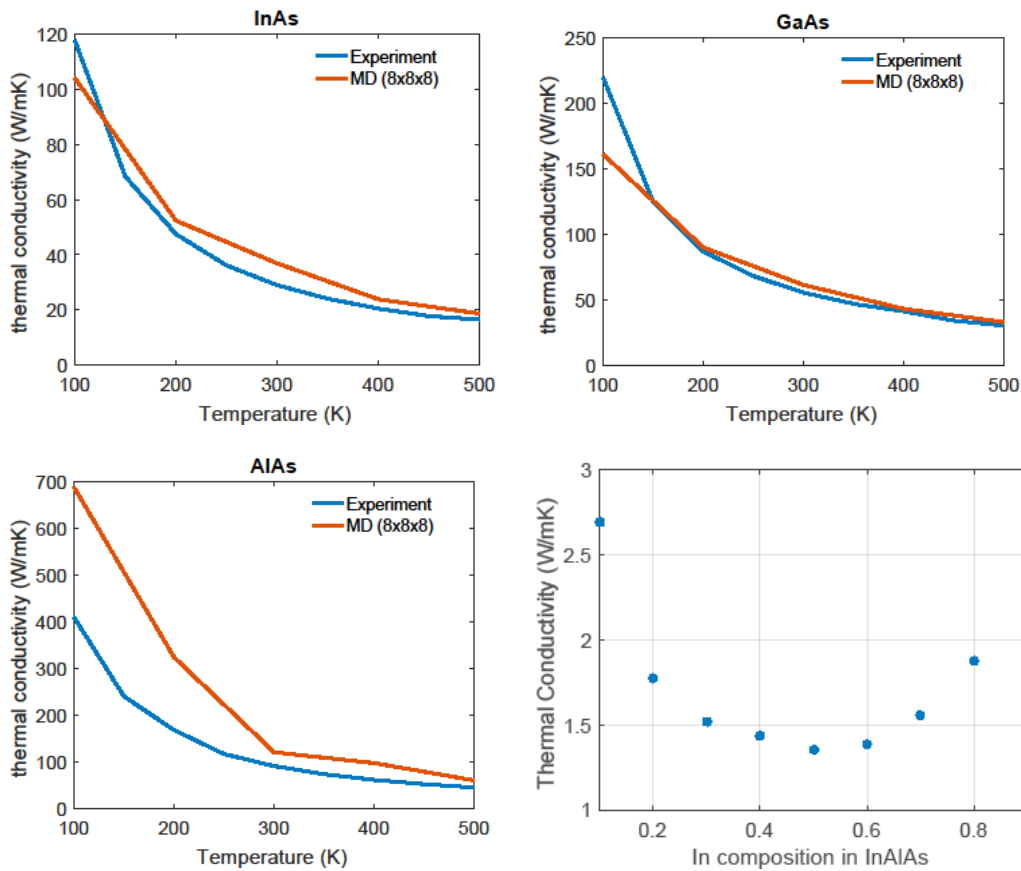
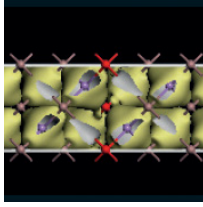


Figure 2 : Preliminary calculations of the thermal conductivity from EMD, for binary InAs (top left), GaAs (top right), and AlAs (bottom left) as a function of temperature (EMD is technically accurate only above the Debye temperature). (Bottom right) The room-temperature thermal conductivity versus In content in ternary InAlAs.

- [1] B. Abeles, "Lattice Thermal Conductivity of Disordered Semiconductor Alloys at High Temperatures," Phys. Rev. 131, 1906 (1963).
- [2] J. Tersoff, "Modeling solid-state chemistry: Interatomic potentials for multicomponent systems," Phys. Rev. B 39, 5566 (1989).
- [3] M. Sayed, J.H. Jefferson, A.B. Walker, and A.G. Cullis, "Molecular dynamics simulations of implantation damage and recovery in semiconductors," Nucl. Instr. Meth. Phys. Res. B 102, 218 (1995).
- [4] D. Powell, M. A. Migliorato, and A. G. Cullis, "Optimized Tersoff potential parameters for tetrahedrally bonded III-V semiconductors," Phys. Rev. B 75, 115202 (2007).
- [5] T. Hammerschmidt, P. Kratzer, and M. Scheffler, "Analytic many-body potential for InAs/GaAs surfaces and nanostructures: Formation energy of InAs quantum dots," Phys. Rev. B 77, 235303 (2008).



# International Workshop on Computational Nanotechnology

## Electron momentum relaxation rates via Frohlich interaction with polar-optical-phonons in bulk wurtzite gallium nitride

K Park, M A Stroschio and C Bayram

University of Illinois at Urbana-Champaign, USA

Here, we present a formalism for calculating electron scattering rates and momentum relaxation rates due to interaction with polar-optical-phonons in bulk wurtzite gallium nitrides. The formalism is established based on the dielectric continuum model and the uniaxial model. Relaxation rates are calculated as a function of electron incident angle and initial energy. We report that the total momentum relaxation rates as well as the scattering rates are mostly determined by the longitudinal optical phonon modes. Electron incident angle variation shows almost no effect on interaction with longitudinal-optical-like phonon modes. In contrast, for transverse-optical-like phonon modes, both scattering rates and momentum relaxation rates show up to a factor of 1.8 difference near the emission threshold energy, as the angle varies from 0 to  $\pi/2$  from the  $c$  axis.

Gallium nitride (GaN) based heterostructure high electron mobility transistors (HEMTs) are ideal for high-power and high-frequency applications due to the excellent material properties of GaN such as high breakdown field (3.3 MV/cm), high saturation velocity ( $2.5 \times 10^7$  cm/s), high thermal and chemical stability. Studies have shown that up to  $40 \text{ W/mm}^2$  power output is achievable with the development of GaN-based power transistors. Despite of these advantages, recent works show that these devices are thermally limited. For example, mismatch of the coefficient of thermal expansion (CTE) and temperature limited mobility are reasons suspected for the GaN-based HEMT current characteristics degradation at high voltages. As optical-phonon emission is known as the principal energy relaxation process of hot electrons in gallium nitride, the investigation of the interaction between electrons and polar-optical-phonons is critical in understanding this problem.

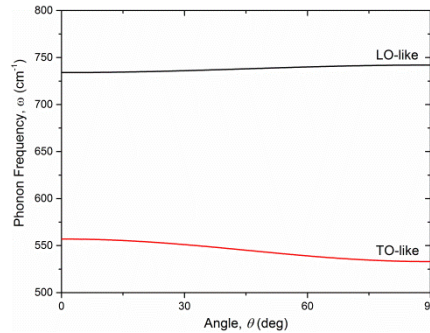


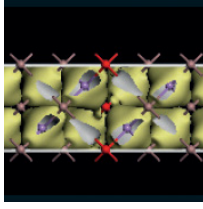
Figure 4. The longitudinal optical (LO) like and transverse optical (TO) like phonon frequencies as a function of angle between the phonon wave vector  $\mathbf{q}$  and  $c$  axis in bulk wurtzite GaN.

In this paper, we provide a formalism for the calculation of the incident angle and energy dependent electron scattering, momentum relaxation and present results obtained by numerical calculation.

We start from the solution of Loudon's model for frequencies of extraordinary phonons in uniaxial polar crystals<sup>2</sup>:

$$\omega_{LO}^2 = \omega_{zL}^2 \cos^2 \theta + \omega_{pL}^2 \sin^2 \theta,$$

$$\omega_{TO}^2 = \omega_z^2 \sin^2 \theta + \omega_p^2 \cos^2 \theta$$



## International Workshop on Computational Nanotechnology

where  $\theta$  is the angle between the phonon wave vector  $\mathbf{q}$  and the  $c$  axis, and the subscripts  $z$  and  $\rho$  indicate directions parallel and perpendicular to the  $c$  axis, respectively. The phonon frequencies used in the numerical calculations are taken from experimental results<sup>3</sup>:  $\omega_{zL} = 734 \text{ cm}^{-1}$  and  $\omega_z = 533 \text{ cm}^{-1}$  for  $A_1$  LO and TO phonons,  $\omega_{\rho L} = 742 \text{ cm}^{-1}$  and  $\omega_\rho = 557 \text{ cm}^{-1}$  for  $E_1$  LO and TO phonons, respectively. Figure 1 shows the angular variation of the LO-like and TO-like phonon frequencies. The normalized electron-optical-phonon Hamiltonian for uniaxial material is given as<sup>4</sup>

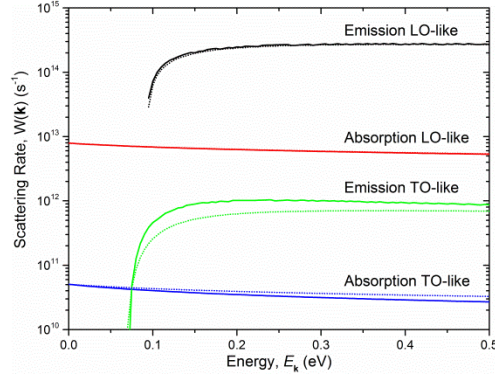


Figure 5. The electron energy variation of scattering rates with LO-like and TO-like phonon modes. Three different electron incident angles,  $\theta_k$  is 0 (solid line) and  $\pi/2$  (dotted line), are shown together.

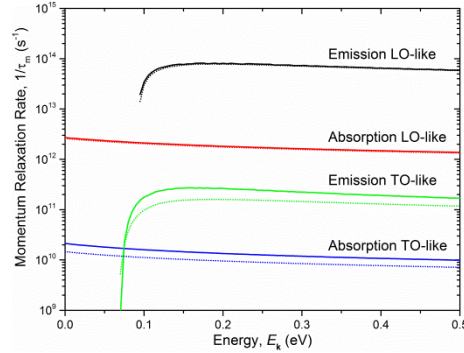
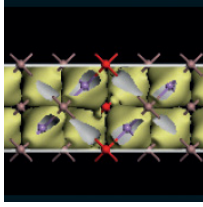


Figure 6. The electron energy variation of momentum relaxation rates for LO-like and TO-like phonon mode scattering.

$$\Omega^{-1}(\theta) = \frac{(\epsilon_{\perp}^0 - \epsilon_{\perp}^{\infty})\omega_{\perp}^2 \sin^2 \theta}{(\omega_{\perp}^2 - \omega^2)^2} + \frac{(\epsilon_z^0 - \epsilon_z^{\infty})\omega_z^2 \cos^2 \theta}{(\omega_z^2 - \omega^2)^2}$$

The electron scattering rate due to Frohlich interaction is obtained by the Fermi golden rule as

$$W(\mathbf{k}) = \frac{e^2 \sqrt{m^*}}{2\sqrt{2}\pi\hbar} \int_0^{2\pi} d\phi \int_0^{\pi} \sin\theta d\theta \left( n_{ph} + \frac{1}{2} \pm \frac{1}{2} \right) \\ \times \frac{\Omega(\theta)}{\omega} \frac{\sigma \sqrt{E_{\mathbf{k}} \cos^2 \phi' \mp \hbar\omega}}{\left( \sqrt{E_{\mathbf{k}} \cos^2 \phi' \mp \hbar\omega} + q_0 \right)^2}$$



## International Workshop on Computational Nanotechnology

where  $\phi'$  is the angle between the phonon wave vector  $\mathbf{q}$  and the initial electron wave vector  $\mathbf{k}$ . For the case of emission (upper signs),  $\sigma$  is equal to 2 when  $E_{\mathbf{k}} \cos^2 \phi' > \hbar\omega$ , and for the case of absorption (lower signs)  $\sigma=1$ . Here, we have included a screening factor of  $q_0 = 8 \times 10^{-12}$  to facilitate efficient numerical integration in the case of emission when  $E_{\mathbf{k}} \cos^2 \phi' \approx \hbar\omega$ . Figure 2 shows the electron scattering rates as a function of electron incident energy. LO-like phonon mode scattering shows no  $\theta_{\mathbf{k}}$  angle dependence whereas TO-like scattering shows up to a factor of 1.8 difference near the emission threshold energy.

The momentum relaxation of electrons is expressed as

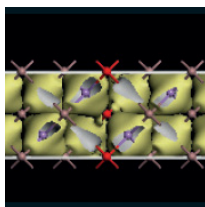
$$\frac{1}{\tau_m^e} = -\frac{e^2 \sqrt{m^*}}{\sqrt{2\pi\hbar}} \int_0^{2\pi} d\phi \int_0^{\pi} \sin\theta d\theta (n_{ph} + 1) \times \frac{\Omega(\theta) \cos^2 \phi' \sqrt{E_{\mathbf{k}} \cos^2 \phi' - \hbar\omega}}{\omega \left( \sqrt{E_{\mathbf{k}} \cos^2 \phi' - \hbar\omega} + q_0 \right)^2}$$

$$\frac{1}{\tau_m^a} = \frac{e^2 \sqrt{m^*}}{2\sqrt{2\pi\hbar}} \int_0^{2\pi} d\phi \int_0^{\pi} \sin\theta d\theta (n_{ph}) \times \frac{\Omega(\theta) \cos^2 \phi' \sqrt{E_{\mathbf{k}} \cos^2 \phi' + \hbar\omega}}{\omega \sqrt{E_{\mathbf{k}} \cos^2 \phi' + \hbar\omega}}$$

where the superscript  $a$  and  $e$  indicate the relaxation rates due to phonon absorption and emission, respectively. We have also included the screening factor  $q_0$  for the case of phonon emission. Figure 3 shows the numerically calculated momentum relaxation rates as a function of electron initial energy due to LO-like and TO-like phonons. Note that the absolute values are taken for the emission rates. Similar to the scattering rates, small anisotropy is shown near the electron emission threshold energy.

Electron-optical-phonon scattering rates and momentum relaxation rates were calculated numerically as a function of incident angle and electron energy. LO-like phonon scattering shows no dependency on electron incident angle whereas TO-like phonon scattering exhibits a maximum of 80% anisotropy near  $E_{\mathbf{k}} = \hbar\omega_{TO}$ .

- [1] Y.-F. Wu, et al., in *Proceedings of 2006 64th Device Research Conference*, June 2006, pp. 151-152.
- [2] R. Loudon, *Adv. Phys.* 13, 423 (1964).
- [3] V. Y. Davydov, et al., *Phys. Rev. B*, 65, 125203 (2002).
- [4] M. A. Stroscio and M. Dutta, *Phonons in Nano-structures*, Cambridge University Press (2001).



# International Workshop on Computational Nanotechnology

Session: Electronic Structure/First Principles Calculations

## (Invited) Structural diversity of silicene

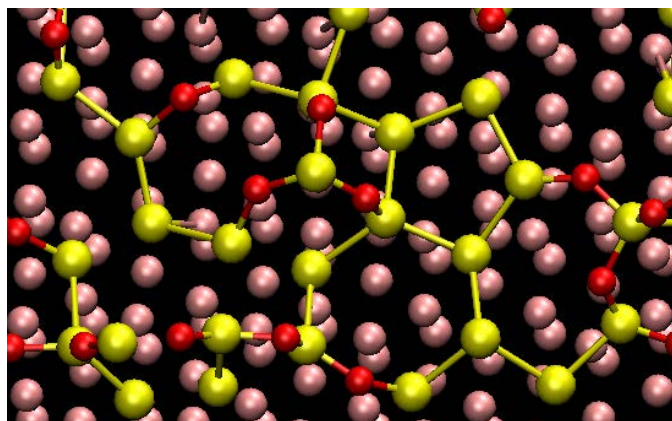
T Morishita

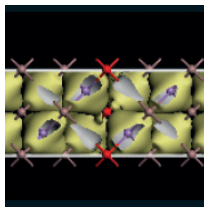
National Institute of Advanced Industrial Science and Technology (AIST), Japan

A silicon (Si) monolayer, which is a graphene analogue and is called silicene, has recently been successfully formed on metallic substrates. Silicene possesses a similar honeycomb structure to that of graphene though it is corrugated due to its  $sp^3$  hybridisation. The two-dimensional nature of silicene and the fact that Si forms the basis for most semiconducting devices today make it a promising material for use in future nanoscale electronic devices. However, in contrast to graphene, free-standing pristine silicene has never been synthesised thus far, partly because its structural stability is degraded by unsaturated  $sp^3$  bonds. It is thus highly demanded to elucidate how the two-dimensional honeycomb silicene behaves (with or without a substrate) under various conditions. We have thus carried out a series of first-principles molecular-dynamics simulations to investigate the stability of the silicene structure.

In the first part of my talk, I will discuss the atomistic mechanism of the oxidation process of the silicene overlayer on the Ag(111) surface [1] when exposed to highly dense oxygen gas. I will demonstrate that there exist barrier-less oxygen chemisorption pathways around the outer Si atoms of the silicene overlayer, indicating that oxygen can easily react with a Si atom to form an Si-O-Si configuration. In the reaction process involving multiple  $O_2$  molecules, a synergistic effect between the molecular dissociation and subsequent structural rearrangements was found to accelerate the oxidation process. This effect enhances self-organized formation of  $sp^3$ -like tetrahedral 3D configurations (consisting of Si and O atoms), which results in collapse of the two-dimensional silicene structure and its exfoliation from the substrate, thus indicating that silicene is highly unstable upon exposure to air.

This theoretical investigation suggests that capping the unsaturated  $sp^3$  bonds (dangling bonds) is a key to stabilising the silicene structure. In the latter part of my talk, I will talk on a bilayer silicene covered by atomistic walls [2,3] and on a organommodified monolayer silicene [4,5]. In both cases, we found that saturating the dangling bonds strongly affects the structural stability and the electronic properties. In particular, the structure of bilayer silicene can be controlled by tuning the degree of the saturation of the dangling bonds. I will also demonstrate that these modified silicene have non-zero band gap, being able to work as a semiconducting material, which is in stark contrast to graphene.





## International Workshop on Computational Nanotechnology

Figure 1: A snapshot from the first-principles MD simulation of the oxidation process of silicene (Si; yellow, O; red, Ag; pink).

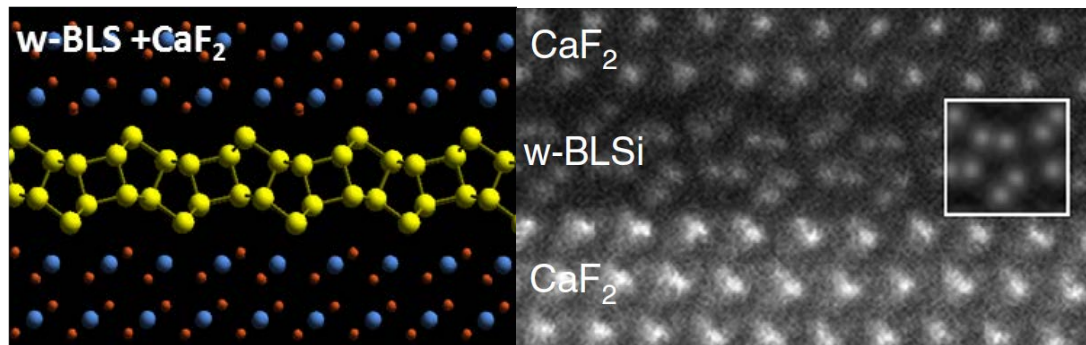


Figure 2: A bilayer silicene formed in a slit pore sandwiched by  $\text{CaF}_2$  layers (left: theoretical prediction, right: experimental synthesis).

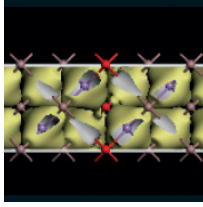
- [1] T. Morishita and M. J. S. Spencer, *Sci. Rep.* 5, 17570 (2015).
- [2] T. Morishita *et al.*, *Phys. Rev. B* 77, 081401(R) (2008); *Phys. Rev. B* 82, 045419 (2010).
- [3] R. Yaokawa, T. Ohsuna, T. Morishita, Y. Hayasaka, M.J.S. Spencer, H. Nakano, *Nat. Comm.* 7, 10657 (2016).
- [4] M.J.S. Spencer, T. Morishita, M. Mikami, I.K. Snook, Y. Sugiyama, and H. Nakano, *PCCP* 13, 15418 (2011).
- [5] M.R. Bassett, T. Morishita, H.F. Wilson, A.S. Barnard, and M.J.S. Spencer, *J. Phys. Chem. C* 120, 6762 (2016).

### General atomistic approach for modeling metal-semiconductor interfaces and surfaces

D Stradi<sup>1</sup>, U Martinez<sup>1</sup>, A Blom<sup>1</sup>, M Brandbyge<sup>2</sup>, S Smidstrup<sup>1</sup> and K Stokbro<sup>1</sup>

<sup>1</sup>QuantumWise A/S, Denmark, <sup>2</sup>Technical University of Denmark, Denmark

Metal-semiconductor (M-SC) contacts play a pivotal role in a broad range of technologically relevant devices. Still, their characterization at the atomic-scale remains a delicate issue. One of the reasons is that the present understanding relies either on simplified analytical models often parametrized using experimental data [1], or on electronic structure simulations describing the interface using simple slab calculations [2]. Here we propose a general strategy to model realistic M-SC interfaces by using density functional theory (DFT) in combination with the non-equilibrium Green's function (NEGF) method as implemented in the Atomistix ToolKit (ATK) simulation software [3]. An accurate description of both sides of the interface is achieved by using a meta-GGA functional [4] optimally tuned to reproduce the SC measured band-gap, and a spatially dependent effective scheme to account for the presence of doping in the SC side. Compared to previous computational methods [2], the present approach has the important advantages of (i) treating the system using the appropriate boundary conditions and (ii) allowing for a direct comparison between theory and experiments by simulating the I-V characteristics of the interface. We apply this methodology to an Ag/Si interface relevant for solar cell applications, and test the reliability of traditional strategies [1,2] to describe its properties [5]. Finally, we will describe a novel surface Green's function (SGF) method where the surface is described as a true semi-infinite system and present a number of examples to



# International Workshop on Computational Nanotechnology

illustrate how the SGF method gives a number of benefits compared to the slab approach as well as enables new type of studies.

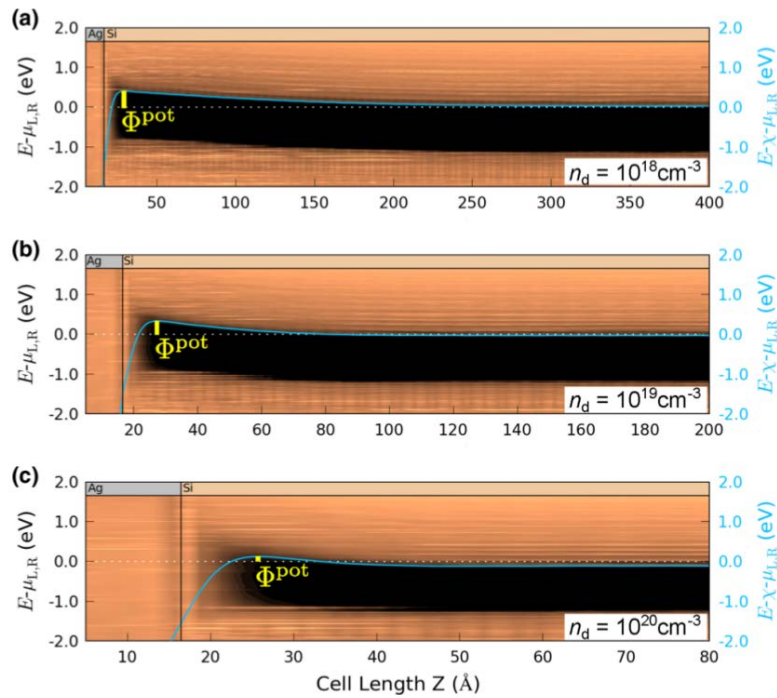
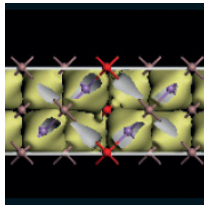


Figure 1. Local density of states (LDOS) of the two-probe setup at equilibrium for doping densities of  $10^{18}$   $\text{cm}^{-3}$  (a),  $10^{19}$   $\text{cm}^{-3}$  (b), and  $10^{20}$   $\text{cm}^{-3}$  (c). The energy on the vertical axis is relative to the system chemical potentials. Regions of low (high) LDOS are shown in dark (bright) color.

- [1] S. M. Sze and K. N. Kwok, Physics of Semiconductor Devices: 3rd edition (Wiley, 2006)
- [2] C. G. van de Walle and R. M. Martin, Phys. Rev. B 35, 8154 (1987)
- [3] "Atomistix ToolKit version 2016.3", QuantumWise A/S ([www.quantumwise.com](http://www.quantumwise.com))
- [4] F. Tran and P. Blaha, Phys. Rev. Lett. 102, 226401 (2009)
- [5] D. Stradi et al. Phys. Rev. B 93, 155302 (2016)



# International Workshop on Computational Nanotechnology

## Non-equilibrium Green's function method: Band tail formation in non-local polar optical phonon scattering

P Sarangapani, Y Chu, J Charles, G Klimeck, and T Kubis

Purdue University, USA

Polar materials with their unique properties offer a wide variety of applications in electronics and optoelectronics. III-V materials such as InGaAs, GaSb and InAs are being considered as potential candidates to replace Si technology due to their low effective mass [1], [2]. Transition metal dichalcogenides (TMDCs) based 2D materials have found applications as FETs and TFETs and are promising candidates for future electronics [3],[4]. Polar optical phonon scattering (POP) is one of the dominant scattering mechanisms in these materials and is necessary for quantitative and qualitative prediction of device performance. Previous works on POP scattering within Non-equilibrium Green's function (NEGF) formalism are either confined to bulk systems [5], [6] or apply diagonal approximations [7] which is known to underestimate scattering.

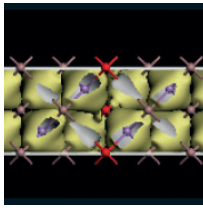
In this work, a physically consistent model to treat POP scattering with full non-locality through selfenergies has been developed for bulk, ultra thin body (UTB) and nanowire devices. Through this approach, reliable scattering rates are computed and compared against FGR. Presence of band tails is demonstrated and the extracted Urbach parameter is shown to agree well with available experimental data. Local approximation of scattering is shown to underestimate both scattering rate and Urbach parameter.

NEGF is widely accepted formalism for nanoscale electronic, thermal and optoelectronic simulations [8], [9], [10]. Within the NEGF formalism, scattering is treated through the self-consistent Born approximation where the scattering self-energy is solved iteratively with the Green's function until convergence. Scattering selfenergy formulas for POP have been derived assuming that the bulk phonons are in equilibrium. Fröhlich coupling is used to model the electron-phonon interaction potential. Electrostatic screening is calculated through the Debye approximation. This method has been implemented within the multipurpose nanodevice simulation tool, NEMO5 [11]. All POP scattering mechanisms are available in all electronic models of NEMO5 (e.g. effective mass, tight binding, Wannier function representation etc.). The scattering self-energies are verified by comparing the scattering rates from NEGF against FGR. Fig. 1 shows comparison of scattering rates obtained for bulk and nanowire GaAs indicating the validity of self-energy expressions.

High doping in semiconductors is associated with band tails (known as Urbach tails) that drop exponentially below the band gap. At room temperature, the band gap narrowing is in the order of few kBT. This can strongly alter performance of devices such as TFET and LEDs where band gaps play an important role in device behaviour. Through POP scattering simulation, one can directly observe such Urbach tails and extract the Urbach parameter. Fig. 2 shows band tails observed for GaAs nanowire. Fig. 3 shows comparison of Urbach parameter for undoped GaAs with experimental data [12]. Simulation results show good agreement with experimental observation confirming the accuracy of the model.

POP scattering is inherently a non-local scattering process. This results in dense self-energy matrices which increase computational time considerably. Often, local approximations are made to speed up simulation. From Fig. 3, one can observe that local approximations severely underestimate the Urbach parameter of GaAs. Fig. 1a shows the scattering rate with and without local approximation where the rate is underestimated by a factor of 2. Therefore, to get meaningful results, nonlocality must be an essential component of the simulation and cannot be neglected.

POP scattering covering full non-locality within the NEGF formalism has been shown and is verified by comparing it against FGR. Presence of Urbach band tails is demonstrated and the extracted Urbach parameter is found to be in agreement with experimental results. Local approximation for such scattering is shown to underestimate physical quantities such as Urbach parameter and scattering rates requiring a non-local simulation approach.



# International Workshop on Computational Nanotechnology

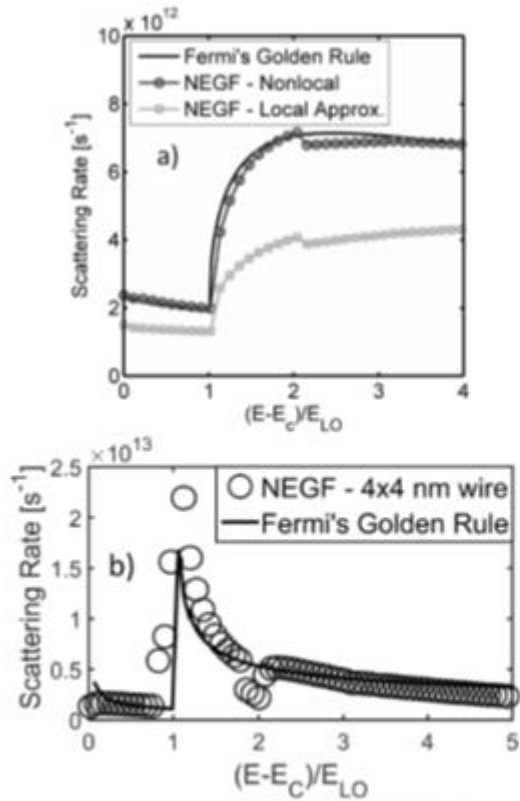


Fig. 1: a) Scattering rate comparison with FGR for bulk GaAs with and without local approximation. b) Scattering rate comparison with FGR for GaAs nanowire.

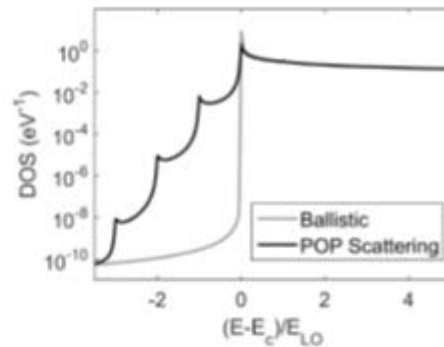


Fig. 2: Presence of band tails with POP scattering for GaAs nanowire. Peaks correspond to LO phonon sidebands.

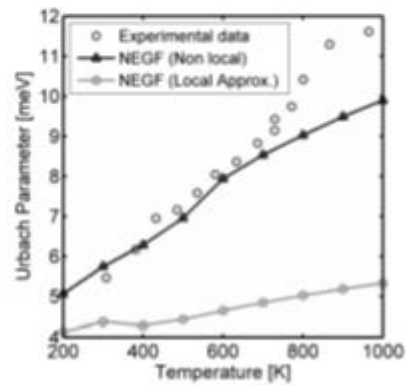
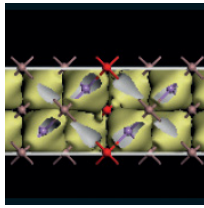


Fig. 3: Comparison of variation of Urbach parameter with temperature for undoped GaAs with experimental data [12]. Local approximation of scattering severely underestimates the Urbach parameter.

- [1] P. Ye et al., Applied Physics Letters, vol. 84, no. 3, pp. 434-436, 2004.
- [2] B. M. Borg et al., Nano letters, vol. 10, no. 10, pp. 4080-4085, 2010.
- [3] B. Radisavljevic et al., Nature nanotechnology, vol. 6, no. 3, pp. 147-150, 2011.
- [4] S. Das et al., Nano letters, vol. 13, no. 1, pp. 100-105, 2012.
- [5] R. Lake et al., Journal of Applied Physics, vol. 81, no. 12, pp. 7845-7869, 1997.
- [6] T. Kubis et al., physica status solidi (c), vol. 5, no. 1, pp. 232-235, 2008.
- [7] M. Luisier et al., Journal of Applied Physics, vol. 107, no. 8, p. 084507, 2010.
- [8] S. Datta, Superlattices and microstructures, vol. 28, no. 4, pp. 253-278, 2000.
- [9] J. Taylor et al., Physical Review B, vol. 63, no. 24, p. 245407, 2001.
- [10] S. Sadasivam et al., Ann. Rev. Heat Transfer, vol. 17, pp. 89-145, 2014.
- [11] S. Steiger et al., "Nemo5: A parallel multiscale nanoelectronics modeling tool," 2011.
- [12] M. Beaudoin et al., Applied physics letters, vol. 70, no. 26, pp. 3540-3542, 1997.



# International Workshop on Computational Nanotechnology

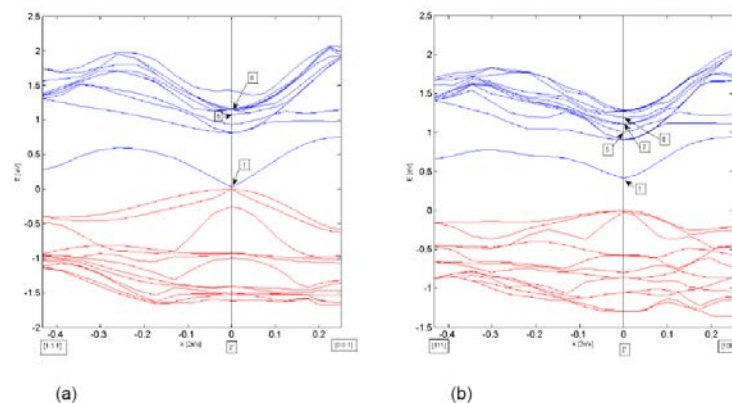
## Electronic structure calculation of SiGeSn-C alloys – prospective direct gap materials

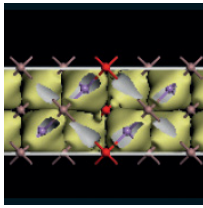
Z Ikonić<sup>1</sup> and D Buca<sup>2</sup>

<sup>1</sup>University of Leeds, UK, <sup>2</sup>Peter Grünberg Institute (PGI 9) and JARA-Fundamentals of Future Information Technologies, Germany

In the recent period large advances have been made in group-IV photonics (and also electronics), targeting the integration of group-IV alloy based (opto)electronic components on silicon substrate, with all the benefits coming from mature and cost-effective fabrication. This progress requires a reliable knowledge of the electronic band structure of CSiGeSn alloys, including their ternary and binary subsets. The directness of the band-gap is very important for optoelectronic devices – primarily lasers, as has been recently demonstrated [1], and also LEDs, photodetectors and modulators – very much improving the device performance. Along with the composition, the values of the direct and indirect gaps can be controlled by strain. The binary GeSn, and also the ternary SiGeSn alloys, which offer the direct band gap, have been studied in considerable detail, both experimentally and theoretically. An alternative way of achieving direct band gap in group-IV materials is in using dilute carbon alloys with other group IV's, which have been studied to some extent [2-6], with different predictions of the effects of C addition. This system is very different from the SiGeSn alloys, because C atom has a much larger electronegativity than the host, a very different lattice constant, the C-C bonds are stronger than C-Ge bonds, and such alloys normally have large density of C clusters and various defects which form trap states in the band gap, and do not lead to a high-quality direct gap material. However, recent successes in highly substitutional incorporation of C in very dilute Ge-C alloy, by using a suitable C source, have revived interest in this system.

Here we consider the band structure of Ge-C, and more generally SiGeSn-C alloys. The empirical pseudopotential method (EPM) is employed within the supercell approach (because the virtual crystal approximation is not applicable for C-containing alloys), with the formfactors made so to reproduce the workfunctions of all the alloy constituents, along with their band structure. This was done by using constrained cubic spline interpolation between the fixed formfactors, the method which avoids artificial over/under-shoots between the fitting points. Calculations were made with 32-, 64- and 128-atom supercells, followed by unfolding procedure. Also calculated is the optical activity at the unfolded direct gap of various alloys (v.b.-c.b. optical matrix element, compared to that in Ge). Examples of the band structure are given in Fig.1(a,b,c). The sensitivity of direct and indirect band gaps to carbon content is also extracted for SiGe-C alloy system, Fig.1d (both decreasing with the C content, in contrast to what VCA would suggest, but gap at  $\Gamma$  doing so at a faster rate than indirect gaps at L and X). The Ge-C is predicted to become a direct gap material at  $\sim 0.2\%C$ , still somewhat larger than contents which enable good quality substitutional alloy, however there are prospects of achieving direct gap in this system, with various possible applications.





# International Workshop on Computational Nanotechnology

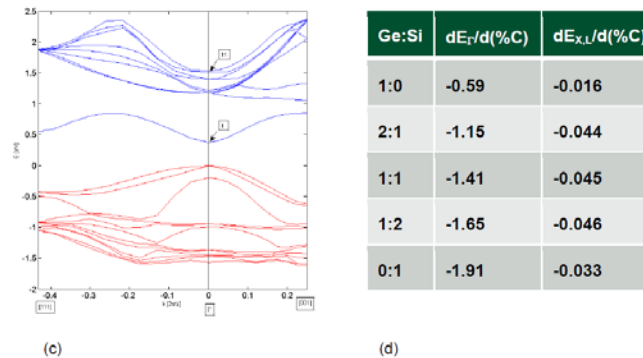
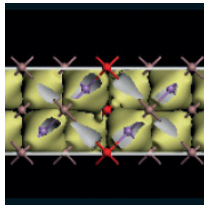


Fig. 1. Band structure of (a)  $C_1Ge_{63}$ , (b)  $C_1Ge_{127}$ , (c)  $C_1Ge_{41}Si_{22}$ , and (d) bandgaps sensitivity of different SiGe compositions to C content.

- [1] S. Wirths, R. Geiger, N. von den Driesch, G. Mussler, T. Stoica, S. Mantl, Z. Ikonc, M. Luysberg, S. Chiussi, J. M. Hartmann, H. Sigg, J. Faist, D. Buca, D. Grutzmacher, "Lasing in direct bandgap GeSn alloy grown on Si (001)", *Nature Photonics*, 9, 88 (2015).
- [2] R. Soref, "Direct-bandgap compositions of the CSiGeSn group-IV alloy," *Optical Materials Express*, 4, 836 (2014).
- [3] J. Kolodzey, P. R. Berger, B. A. Ormer, D. Hits, F. Chen, A. Khan, X. Shao, M. M. Waite, S. Ismat Shah, C. P. Swann, K. M. Unruh, "Optical and electronic properties of SiGeC alloys grown on Si substrates", *J. Crystal Growth*, 157, 386 (1995).
- [4] M. Rezki, A. Tadjer, H. Abid, and H. Aourag, "Electronic structure of  $Si_{1-x}C_xGe_y$ ", *Materials Science and Engineering B*, 55, 157 (1998).
- [5] T. Yamaha, K. Terasawa, H. Oda, M. Kurosawa, W. Takeuchi, N. Taoka, O. Nakatsuka, and S. Zaima, "Formation, crystalline structure, and optical properties of  $Ge_{1-x}Sn_xC_y$  ternary alloy layers", *Japanese J. Appl. Phys.*, 54, 04DH08 (2015).
- [6] C. A. Stephenson, W. A. O'Brien, M. W. Penninger, W. F. Schneider, M. Gillett-Kunnath, J. Zajicek, K. M. Yu, R. Kudrawiec, R. A. Stillwell, M. A. Wistey, "Band structure of germanium carbides for direct bandgap silicon photonics", *J. Appl. Phys.*, 120, 053102 (2016).



## International Workshop on Computational Nanotechnology

### Image charge models for accurate construction of the electrostatic self-energy of 3D layered nanostructure devices

J.R. Barker<sup>1</sup> and A. Martinez<sup>2</sup>

<sup>1</sup>University of Glasgow, UK, <sup>2</sup>Swansea University, UK

Efficient analytical image charge models are derived for the full spatial variation of the electrostatic self-energy [1] of electrons in semiconductor nanostructures arising from dielectric confinement using semi-classical analysis. The effect of the electrostatic self-energy on the  $I_b$ - $V_g$  characteristics of gate-all-around nanowire silicon transistors for different oxide thickness is subsequently studied numerically using the non-equilibrium Green's function formalism.

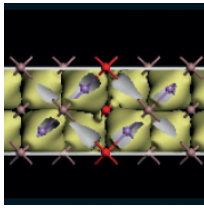
The semi-classical electrostatic self-energy due to a charge  $Q$  at location  $\mathbf{x}$  within a region with dielectric constant  $\epsilon$  that is embedded in a dielectric heterostructure is:

$$\Sigma(\mathbf{x}; \epsilon) = \lim_{\mathbf{x} \rightarrow \mathbf{x}_1} \frac{Q^2}{8\pi\epsilon} (g[\mathbf{x}, \mathbf{x}_1] - g_0[\mathbf{x}, \mathbf{x}_1])$$

Here,  $g_0[\mathbf{x}, \mathbf{x}']$  is the classical Green function of the Laplace equation for a homogeneous *bulk* region with dielectric constant  $\epsilon$ .  $g[\mathbf{x}, \mathbf{x}']$  is the corresponding Green function for the dielectric heterostructure. Although the electrostatic self-energy may be pre-computed along with a tight-binding evaluation of nanostructure energy band structure [2] there are considerable advantages in deploying accurate compact analytical models for the self-energy: it aids understanding of the key physical processes and the scope of effective device design is considerably strengthened without complex NIC.

Our approach utilises rigorous analytical solutions [3] for the electrostatic self-energy in cylindrical and rectangular 3D geometries for wrap-round gate nanowire FETs (Figures 1, 2) in semiconductor dielectric structures (with obvious extensions to carbon based structures). The exact formulations involve infinite sums and integrations over the relevant special function combinations appropriate to the geometry (assumed to have a high degree of symmetry about the channel direction). These rigorous results are used to extract and validate very much simpler compact models based on image charge concepts (both point charge and line charge) for long channels and finite channels plus source-drain extensions. The summation over image charges is well known [4] to have convergence problems because the resultant series are *asymptotic*. However, provided a position independent contribution to the self-energy is correctly identified, we have determined that low-order truncation in image charge sequences can deliver very accurate approximations for the self-energy. This result follows from taking the local limit of the classical Green function and the subtraction of the Coulomb divergence. It should be noted that our methodology does not use an *ad hoc* construction (such as an Ewald sum) of the image sequences but uses a convergent deconstruction based on exact convergent integral representations of the Green function.

The strategy may be exemplified by considering the electrostatic self-energy for a charge  $Q$  embedded in the channel of an infinite planar double gate structure sketched in Figure 3. In Figure 4, curve A is numerically computed from the exact formulation; curve B is computed using just two image charges. More complex structures require of the order of  $kN$  images where  $N$  is the number of interfaces and  $k$  is related to the number of vertices. For cylindrical geometries we encounter *line image charges* that often take *limaçon* forms (Figure 5). Figure 6 shows schematically the location of leading image charges required to model the self-energy near an extension between source and drain. With heterostructures, the resultant image charges are re-normalised via parameters depending on the dielectric mismatches.



# International Workshop on Computational Nanotechnology

Finally, the formalism is applied to the Non-Equilibrium Green Function modelling [5] of wrap-round gate nanowire FETs based on silicon technology. Generally, the effect is to modulate the channel confinement potential [3] and to lower the barrier potential.

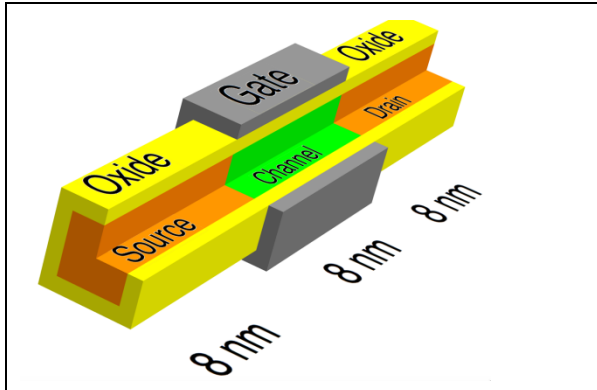


Figure 1: schematics of a wrap round gate nanowire FET: rectangular geometry

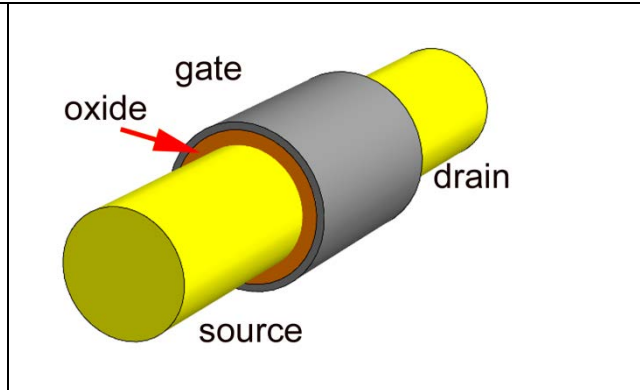
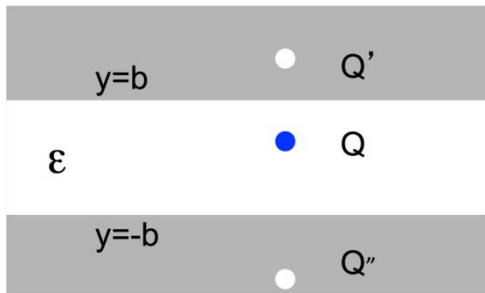


Figure 2: schematics of a wrap round gate nanowire FET: cylindrical geometry



$$\Sigma(\mathbf{x}, \epsilon) = \frac{-Q^2}{16\pi\epsilon} \left( \frac{1}{b-y} - \frac{1}{2b} + \frac{1}{b+y} \right)$$

Figure 3: a planar double gate structure showing point charge  $Q$ , and leading image charges  $Q'$ ,  $Q''$

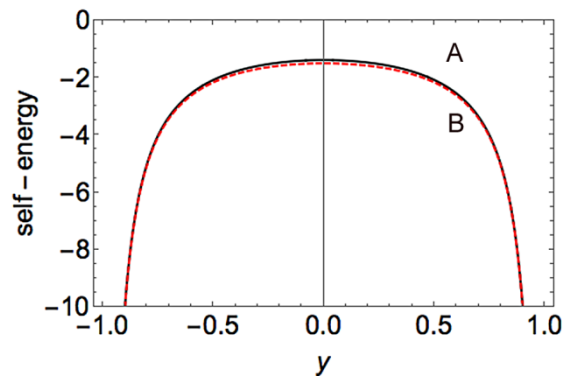
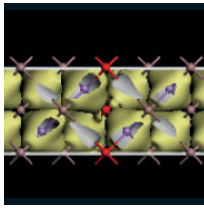


Figure 4: exact electrostatic self-energy (A) compared with (B) a two image model for the structure in Fig. 3. Interfaces at  $y = b = \pm 1.0$ .



# International Workshop on Computational Nanotechnology

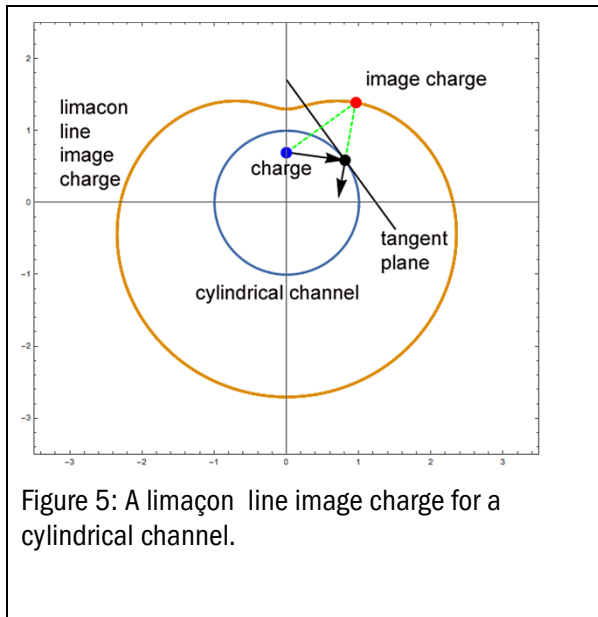


Figure 5: A limaçon line image charge for a cylindrical channel.

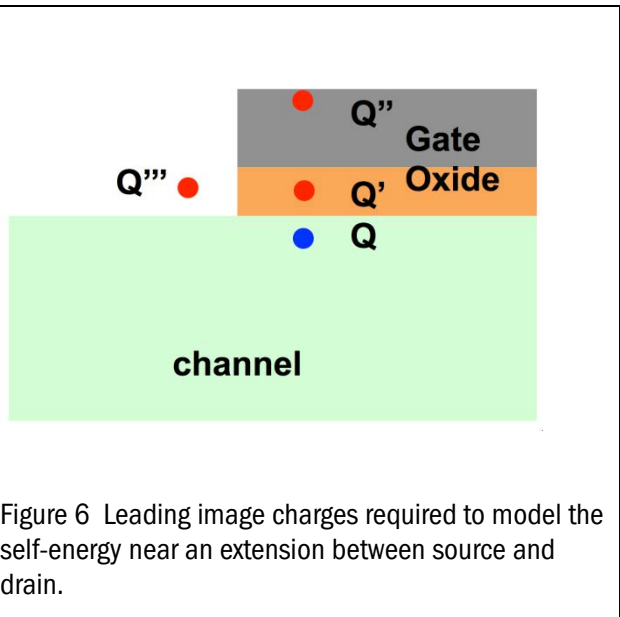
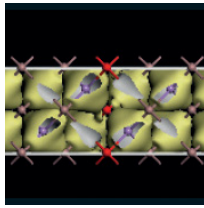


Figure 6: Leading image charges required to model the self-energy near an extension between source and drain.

- [1] C. Li, M. Bescond and M. Lannoo, Phys.Rev. B 80, 195318 (2009)
- [2] Y. M. Niquet et al, Phys.Rev. B 73, 165319 (2006)
- [3] A. Martinez, J.R.Barker and M. Aldegunde, IWCE 16, (ed N. Mori and S. Selberherr, 2013) Society for Micro-and Nanoelectronics, Technische Univeritat Wien:ISBN 978-3-901578-26-7) 50 (2013)
- [4] W. Cai, "Computational methods for electromagnetic phenomena", CUP 2013.
- [5] A. Martinez et al, J. Comp. Electronics 15, 1130 (2016).



# International Workshop on Computational Nanotechnology

## Posters

### P:01 Using vacancy transport to unify memristor models

I Abraham

University of Washington, USA

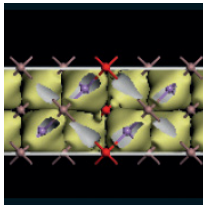
This research demonstrates how simple closed form and numerical solutions for memristive characteristics can be generated from the transport equation.

The memristor has hidden in plain view for over two centuries [1]. Contemporary models continue to be built around  $V, I$  relationships [2], [3]. An early attempt to inherently model nonlinearity without arbitrary window functions is by Lu [4]. A numerical model adds depth but is unable to generate an insightful abstraction [5]. This research demonstrates that vacancy transport can bind the various models, while bridging vacancy and circuit abstractions.

#### The Modeling Methodology

The transport partial differential equation (PDE) is proposed as the governing equation for the vacancy migration memristor. In its general form the transport PDE contains diffusion and generation-recombination (G-R) terms as in Table 1 equation (1).  $\vartheta$  is the normalized vacancy concentration,  $\vartheta$  is evolution velocity in  $(x, t)$ ,  $\mathcal{D}$  is diffusion constant and  $\tau_{GR}$  is the G-R coefficient. A symbolic solution of the form (2) is demonstrable when second order diffusion and G-R effects are ignored. The solution is inherently nonlinear, without window functions. (1) can be numerically solved with initial and boundary conditions generated from (2). Fig. 1 compares the symbolic and numeric solutions showing good correlation. Manipulating with methods from electrochemistry results in the closed form resistance formula (3). Variable  $\varnothing$  is the time-integral of voltage. Computing with (3) reveals the memristor as a two terminal device composed of two series complex resistors (4) that contain the phase information observed by Chua [6]. Numerically the imaginary parts in the two resistors cancel, leaving behind the ubiquitous (but in this case, improved) HP's dual variable resistor model (HP DVR) [3]. The larger of  $a, c$  in (4) takes on the positive sign, resulting in an always positive  $R(\varnothing)$ . Key result in Fig. 2(a) locates the vacancy accumulation boundary. Fig. 2(b) confirms vacancy conservation w.r.t. time. Fig. 2(c) shows current voltage I-V curve, the device progressively entering higher resistance. Fig. 2(d) shows that the model produces comparable symbolic (no diffusion or G-R) and numerical (diffusion and G-R) solution for resistance. Fig. 3 demonstrates reduced switching resistance range for increasing temperature. The memristor is ohmic in the ON region ( $R \propto T$ ) and semiconducting in the OFF region ( $R \propto T^{-1}$ ) [7]. This research introduces an improved nonlinear vacancy accumulation boundary similar to in [3], a new concept of symmetry boundary which is always a location  $0 \leq x_s(t) \leq d$  [8], where  $d$  is device length. The  $x_s(t)$  information can be used to confine the model to compute exclusively between a low and high resistance. The symbolic (and equivalent numeric) modeling can compute the switching time (5), energy (6) and a nonlinear vacancy evolution velocity (Fig. 4). With  $u_t + Du_{xx} = 0$  we can compute vacancy evolution (un-programming) on the shelf. Fig. 5 is the solution stack generated from a single PDE.

This research uniquely unifies memristor modeling under the umbrella of vacancy transport.



# International Workshop on Computational Nanotechnology

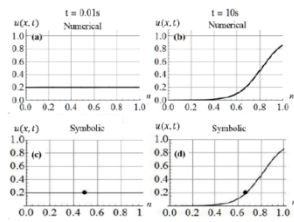


Fig. 1. (a), (b) show numerical results for vacancy evolution with  $D = \tau_{GR}^{-1} = 0$  while (c), (d) show matching results from using symbolic formula.

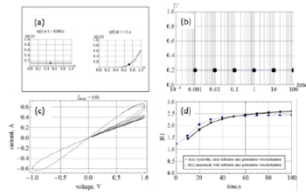


Fig. 2. Collage of results. (a) Evolution of  $u(x, t)$ . (b) Conservation of vacancies (c) Current-Voltage (I-V) curve and (d) symbolic, numeric overlay.

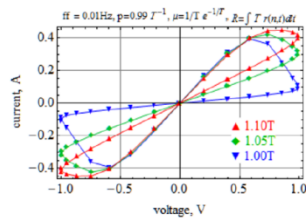


Fig. 3. Temperature dependence of I-V.

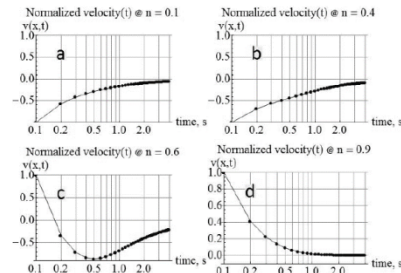


Fig. 4. Normalized  $u(x, t)$  evolution velocity  $\theta(x, t)$ .

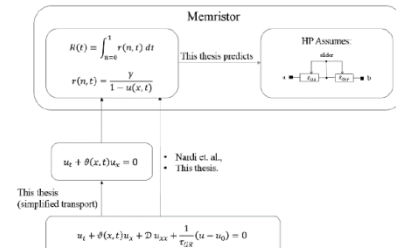
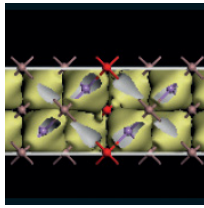


Fig. 5. Solution stack from this research.

**Table 1. Equations.**

$u_t + \theta u_x + D u_{xx} + \tau_{GR}^{-1}(u - u_0) = 0$	(1)
$u(x, t) = (1 + a e^{-g(x)} f(x,t) h(t))^{-1}$	(2)
$R(\theta) = \sum_{n=1}^3 C_n f_n(\theta)$	(3)
$R(\theta) = (\pm a \mp i b) + (\mp c \pm i b)$	(4)
$\tau = f(\theta) \ln(\alpha)$	(5)
$E = \int_{t=0}^{\tau} \frac{V^2}{R(t)} dt$	(6)

- [1] T. Prodromakis, C. Toumazou and L. Chua, "Two centuries of memristors," *Nature Mat*, pp. 478-481, 2012.
- [2] D. Bielek, Z. Bielek and V. Biolkova, "Differential Equations of Ideal Memristors," *Radio Engineering*, vol. 24, no. 2, pp. 369-377, 2015.
- [3] D. B. Strukov, G. S. Snider, D. R. Stewart and R. S. Williams, "The missing memristor found," *Nature*, vol. 453, pp. 80-83, 2008.
- [4] W. Lu, K.-H. Kim, T. Chang and S. Gaba, "Two-Terminal Resistive Switches (Memristors)," pp.217-223.
- [5] F. Nardi, S. Larentis, S. Balatti, D. Gilmer and D. Ielmini, "Resistive Switching by Voltage-Driven Ion Migration in Bipolar RRAM Part I/II," *IEEE Trans. Electron Devices*, vol. 59, no. 9, pp. 2461-2475, 2012.
- [6] L. Chua, "Resistance switching memories are memristors," *Appl Phys A*, pp. 765-783, 2011.
- [7] C. Walczyk, D. Walczyk, T. Schroeder, T. Bertaud, M. Sowinska, M. Lukosius, M. Frascchke, D. Wolansky, D. Tillack, E. Miranda and C. Wenger, "Impact of Temperature on the Resistive Switching Behavior of HfO<sub>2</sub>-Based RRAM Devices," *IEEE Trans. Electron Devices*, vol. 58, no. 9, pp. 3124-3131, 2011.
- [8] I. Abraham, "An Advection-Diffusion Model for the Vacancy Migration Memristor," *IEEE Access*, vol. 4, no. 99, pp. 7747-7757, 2016.



## International Workshop on Computational Nanotechnology

### P:02 Position dependent performance in 5 nm vertically stacked lateral Si nanowires transistors

T Al-Ameri, V P Georgiev, F Adamu-Lema and A Asenov

University of Glasgow, UK

In this work, we investigated the performance of vertically stacked lateral nanowires transistors (NWTs) considering the effects of series resistance. Also, we consider the vertical positions of the lateral nanowires in and diameter variation of the NWTs stack as new sources of statistical variability.

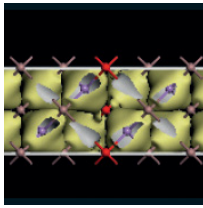
Vertically stacked lateral nanowire transistors (VSL - NWTs) called also gate-all-around (GAA) nanowire transistors can enable the next generation 5nm CMOS technology and beyond [1]. However, the performance of these is affected by the nanowire stack position dependence of the drain current in addition to the complexity of controlling the diameters of lateral NWTs in the stack. In our recent publication [2], we investigated the performance VSL - NWTs. Our results show a noticeable position-dependent current density degradation through the identically sized lateral NWTs in the vertical stack. Hence, the upper lateral nanowires closer to the source/drain contacts carry more current than that ones that are farther away (middle, bottom) due to the series resistance related voltage drop.

Also, the variability of NWTs position has a significant effect on ION and in combination with other sources of statistical variability (SV) such as Random Discrete Dopants (RDD), Wire Edge Roughness (WER) and Metal Gate Granularity (MGG) determines the NWT behavior. The variability of diameters of lateral NWTs in the same stack will enhance the SV and affects the electrostatic confinement. In addition to all sources of SV the reliability which also plays an important role. It is possible that the nearest NWT to the S/D contacts may become weak point suffering extensive aging. One possible solution is to increase the diameter of lower nanowires with respect to the upper nanowires in the stack. However, although the drain current is increasing with increasing of NWT cross-sectional area, the voltage drop will increase across the highly doped S/D regions. The idea of decreasing the doping concentrations near the top lateral NWT and increasing it gradually near the middle and the bottom lateral NWTs, would decrease the total Ion. Such solutions are unsatisfactory.

The simulated device has a three lateral Si NWTs with an elliptical cross-sectional shape (5nmx7nm) and (7nmx5nm) with 110 channel orientation as shown in Fig1. In this work we use the Poisson-Schrödinger (PS) quantum corrections coupled with Monte Carlo (MC) module of GARAND [2] as a reference point. We calibrate the GARAND drift-diffusion simulations to this reference MC simulations.

In this work, test the idea of slicing the S/D contact. The slice up is from the top of contact and the second slice up to the middle of the stack as shown in Fig 4. Also, we have tested position dependent performance 500 and SV of diameters of 729 (VSL NWTs) devices.

The simulated  $I_D-V_G$  characteristics of single NWTs with channel orientation 110 shown in Fig 2. The (5nmx7nm) has more quantum charge than (7nmx5nm) NWT, while (7nmx5nm) has less footprint than (5nmx7nm). Fig (3) shows the current density of stack NW with three lateral NWTs with the flowing dimensions: top NWT has 7nmx5nm, 7.4nmx5nm for the middle, and 8.0nmx5nm for the bottom. The upscaling diameter of lower nanowires with respect to the upper nanowires in the stack is not satisfactory to balance the current density in the stack. Fig 3 (B, C, D) shows that even if we use single NWT the position of NWT in the stack directly affects the current. Fig 4 shows that slicing the S/D contact, can satisfactory balance the current distribution in the stack. Fig 5 shows the distributions of ION subject to lateral NWT position along the vertical stack considering +/- 3nm deviation from the initial position. Fig. 5 shows the correlations between extracted device performance and cross-section profile for both 5nmx7nm and 7nmx5nm stacks, considering 730 atomistic devices.



# International Workshop on Computational Nanotechnology

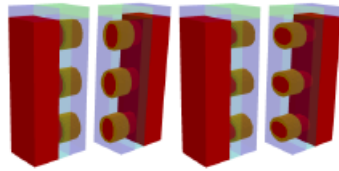


Fig. 1 3D schematic view a Si nanowire transistor (NTW). (Left) 7x5 nm and the (right) one in 5x7nm.

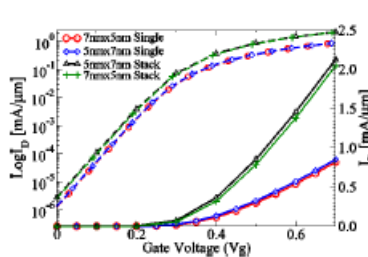
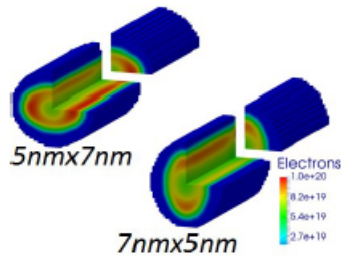


Fig. 2 (Top) Quantum charge distributions of a 5nmx7nm, and 7nmx5nm (NTW) (channels only) with effective gate length  $L_g=12\text{nm}$ . (Bottom)  $I_d - V_g$  curves for single and stack NWTs.

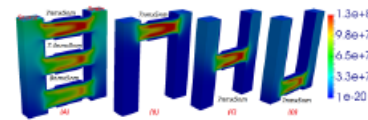


Fig. 3 (A) the current density of stack with three lateral NWTs: top 5nmx7nm, 5nmx8.8nm (middle), and 5nmx9.4nm bottom. (B, C, D) the current density of single (5nmx7nm) NWT in the top, middle, the bottom of the stack.

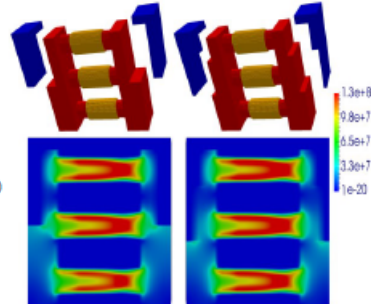


Fig. 4 (Bottom) Slicing the S/D contact, the up slice is from the top of contact and the second slice up to the middle of the stack. (Top) The current density of longitudinal cross section.

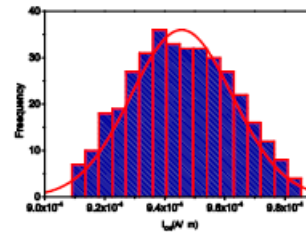


Fig. 5 The distributions of  $I_{ON}$  subject to lateral NWT position in the stack.

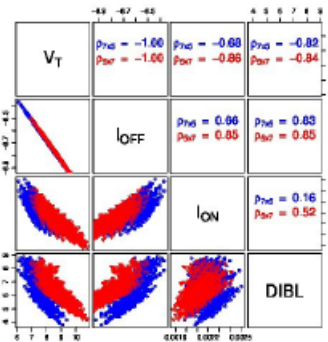
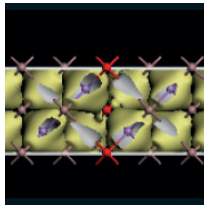


Fig. 6 Correlations between extracted Figure of Merit from the TCAD simulations for both 5nmx7nm and 7nmx5nm stacks with s diameter SV of 729 devices.

- [1] H. Mertens et al., IEEE Symposium on VLSI Technology, 2016.
- [2] T. Al-Ameri et al, IEEE Nanotechnology Materials and Devices Conference (NMDC). 2016
- [3] A. Asenov et al, IEEE International Symposium on Quality Electronic Design (ISQED), 2016.



## International Workshop on Computational Nanotechnology

### P:03 The impact of interface traps and self-heating in the degradation of the 4H-SiC VDMOSFET performance

M H Alqaysi, A Martinez, K Ahmeda and B Ubochi

Swansea University, UK

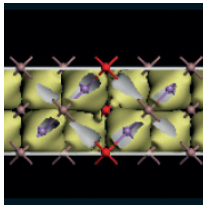
Silicon carbide (SiC) material is an ideal candidate to replace silicon (Si) for high temperature, high power device applications. This is due to its excellent physical and electronic properties such as a large band gap, high critical electric field, high thermal conductivity and high saturation velocity. SiC devices are ideal as high power switches and rectifiers for both low and high frequency applications [1]. Although there has been substantial improvements in the material technology, the quality of the oxide interface represents an issue for the reliability of these devices. The presence of unwanted traps at the interface degrades the device performance.

In this work, we study the impact of interface traps in the device performance. We also explore the interplay between traps and the self-heating effects.

The effect of self-heating is studied by comparing with the measured  $I$ - $V$  curves of a commercial device, C2M1000170D 1.7KV 4H-SiC vertical DMOSFET half-cell for study [2].

We have done electrical characterisation and subsequently extracted the device doping, dimension and physical parameters. The donor concentration of P-epi region is  $N_D = 3 \times 10^{15} \text{ cm}^{-3}$ . The gate oxide thickness was set to around 90nm and the channel length is 3.5 $\mu\text{m}$ . The layout and dimension of the device half cell is shown in Fig. 1.

Device simulations were carried out using a commercial TCAD software package Atlas by Silvaco [3]. Drift-diffusion transport model were used in all simulations. Physics-based models were included to account for carrier mobility, carrier generation and recombination, impact ionization and lattice heating. The electrothermal simulations allows us to localize the hot spot for self-heating. Electro-thermal simulations including interface traps with a density of  $10^{12} \text{ cm}^{-2}$  were performed. The simulated current-voltage characteristics are in good agreement with the experimental one in a wide range of bias as shown in Fig. 2. In addition, the simulated characteristics which includes a model for self-heating produces a better agreement with the experimental results. In Fig. 3, we see a shift in the threshold voltage by about 2V when the effect of interface traps are taken into account while self-heating leads to a decline in the transfer characteristic for the case with and without interface traps. We observe an increase in the on-resistance when the interface traps and self-heating effect are incorporated (see Fig. 4). Note that the combined effects of interface traps and self-heating is not linear, i.e the decrease in the current is not a simple addition of the two mechanisms and this can be seen in Fig. 4. Notice the collapse of the drain current by 12.9% for self-heating only, 17.6% for interface traps only and 51.4% when the combined effects of self-heating and interface traps are considered. By comparing Figs. 5 and 6, the observed increase in the local temperature is reduced by the presence of interface traps as the current is small when the interface traps are considered. The region with very high temperature is correlated to the region where high electric fields are experienced. In conclusion, we have carried out electrothermal simulations of n-type 4H-SiC VDMOSFET. We have shown that self-heating substantially reduces the on-current whereas the presence of interface traps leads to a reduction in the maximum lattice temperature, the on-current and a shift in the threshold voltage.



# International Workshop on Computational Nanotechnology

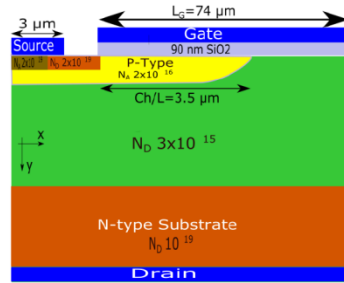


Figure 1: Structure of the SiC VDMOSFET

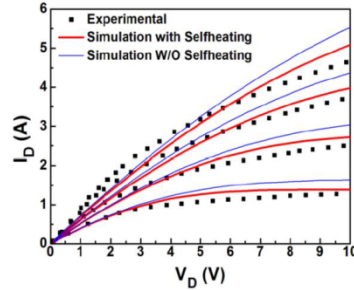


Figure 2:  $I_D$ - $V_D$  Characteristics with and without self-heating

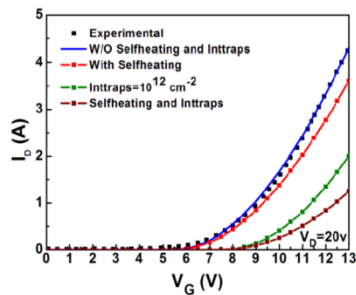


Figure 3:  $I_D$ - $V_G$  characteristics with and without Interface traps and self-heating

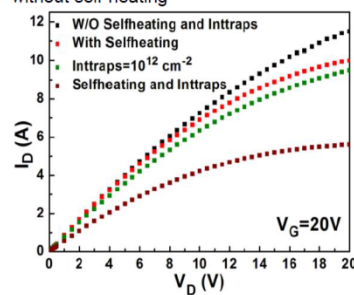


Figure 4:  $I_D$ - $V_D$  at  $V_G=20V$  with and without interface traps and self-heating

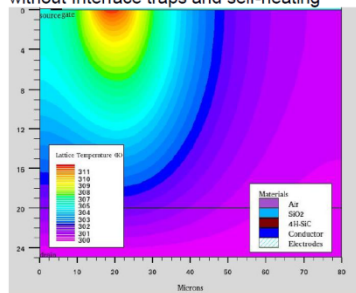


Figure 5: Lattice temperature assuming only self-heating in the device at  $V_G=20V$

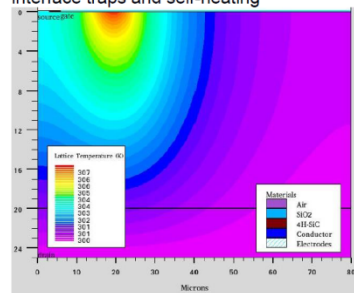
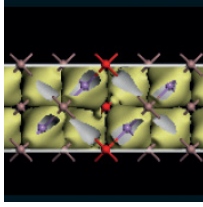


Figure 6: Lattice Temperature assuming both self-heating and Interface traps at  $V_G=20V$

- [1] M. Bhatnagar and B.J. Baliga, IEEE Trans. Electron Devices 40, 645, 1993.
- [2] CREE model C2M1000170D [online available: <http://www.cree.com/~media/Files/Cree/Power/Data%20Sheets/C2M1000170D.PDF>]
- [3] Silvaco, Atlas User 's Manual, Santa Clara, CA:Silvaco Inc., 2016.



## International Workshop on Computational Nanotechnology

### P:04 TCAD analysis of discrete dopant effect on variability of tunnel field effect transistor

H Asai<sup>1</sup>, K Fukuda<sup>1</sup>, J Hattori<sup>1</sup>, and N Sano<sup>2</sup>

<sup>1</sup>National Institute of Advanced Industrial Science and Technology, Japan, <sup>2</sup>University of Tsukuba, Japan

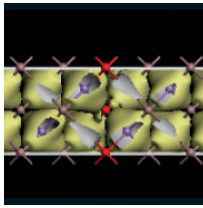
Tunnel field-effect transistor (TFET) is a one of steep slope transistors that have gated p-i-n diode structures. The gate voltage switches the band-to-band tunneling (BTBT) current between the source and the channel. The abrupt increase of BTBT current by the gate electrostatic control results in lower  $SS$  values than 60 mV/dec [1], and thus, TFET is expected to be a commercialized logic device in next generation. Recently, toward the circuit application of TFETs, the variability of TFETs has been investigated [2]. The analysis of the mechanisms of variability is crucial for the suppression of the variability.

In this work, we numerically investigate the variability of the TFETs in the presence of random fluctuation of discrete dopant using TCAD simulation. We find the variation in the drain current of TFETs is suppressed by increase of the device width. Interestingly, we also find that the TFETs with discrete dopant distribution tend to show higher drain current compared to the TFETs with homogeneous dopant distribution. Although the discreteness of the dopants causes the variability, it can also amplify the operation current.

We considered silicon-on-insulator (SOI) p-TFETs with discrete dopant distributions. Figure 1 indicates a schematic figure of the TFET, and dimensions of the TFET are given in the right side of the figure. To reduce computational cost, we considered discrete dopant distribution only in the red shaded area beneath a gate as shown in Fig. 1, where the strong BTBT occurs.

In this work, the device simulations based on the drift diffusion approximation were performed by the three dimensional simulator HyENEXSS [3]. We implemented the generation/recombination model arising from BTBT based on WKB approximation [4] into the simulator, which can treat non-uniform barrier potential along the tunneling path.

First, we calculated  $I_D$ - $V_{GS}$  curves for 100p-TFETs that have different discrete dopant distributions each other. Figure 2 indicates 100  $I_D$ - $V_{GS}$  curves for source doping density,  $N_S = 1e20 \text{ cm}^{-3}$ . The average of the current  $I_{AVE}$  and the relative standard deviation  $I_{DEV}$  at 1 V are shown in this figure. The  $I_D$ - $V_{GS}$  curve for homogeneous dopant model is also calculated as a reference. We calculated similar  $I_D$ - $V_{GS}$  curves for various device width,  $W_g = 6 \sim 30 \text{ nm}$ , and plotted  $DEV$  as a function of  $W_g$  in Fig. 3. As shown in this figure,  $I_{DEV}$  decrease with the increase of  $W_g$ . Of particular note is that the average current  $I_{AVE}$  is higher than that of continuum dopant model, as shown in Fig. 2. In order to clarify the mechanism of this enhancement, we investigated the effect of "localization" of the dopant density profile. We considered non-uniform density profile along the width direction ( $y$  axis) as shown in Fig. 4 (a) and calculated  $I_D$ . Figure 4 (b) shows the  $I_D$  as a function of localization strength,  $r$ . This figure indicates the localization enhances the current even though the average dopant density is equivalent. Figure 5 (a) and (b) show the intensity of electric field  $E_x$  along the tunneling direction ( $x$  axis) at the source edge ( $x = 0.057 \mu\text{m}$ ). As can be seen from this figure, the electric field locally increases owing to the local increase of the dopant density. According to the Kane's BTBT theory [5], BTBT rate exponentially increases with respect to electric field applied to the tunneling carries. Therefore, the appearance of high dopant density region due to the discreteness of the dopant causes the local enhancement of the electric field, and the exponential increase of the current in such region results in the enhancement of the total current. Based on this analysis, we investigated the relation between  $I_D$  and strength of the localization in 100 samples. From the calculation results, we estimated the region where BTBT rate is high, and plotted  $I_D$  and the maximum dopant density in this region. As expected from the aforementioned analysis, we see a strong correlation between  $I_D$  and local increase of the dopant density.



# International Workshop on Computational Nanotechnology

In this paper, we have numerically investigated the variability of TFETs by using TCAD simulation. The variability of drain currents is suppressed by increase of the device width. We have also found that TFETs with discrete dopant distribution tend to show high drain currents compared to the current calculated from homogeneous dopant model.

We clarified that this current enhancement originates from the local increase of the electric field around discrete dopant position.

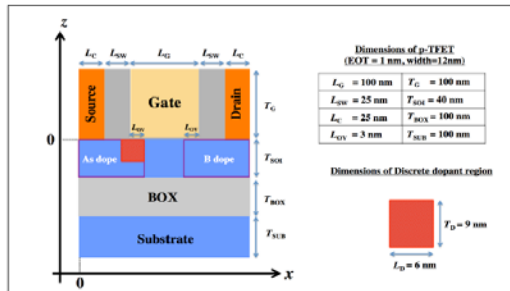


Fig. 1. Schematic figure of TFET with discrete dopant distribution (shaded area).

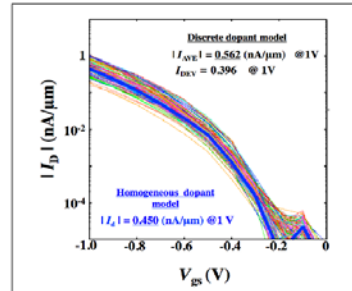


Fig. 2.  $I_D - V_{GS}$  curves for 100 TFETs with discrete dopant distributions.

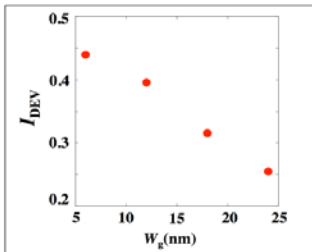


Fig. 3. Relative standard deviations of drain currents  $I_{DEV}$  as a function of device width  $W_g$ .

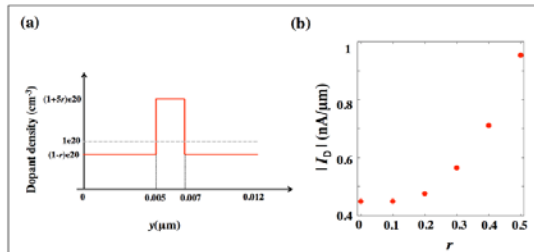


Fig. 4. (a) Non-uniform dopant density distribution with localization strength  $r$ , and (b) drain current  $I_D$  as a function of  $r$ .

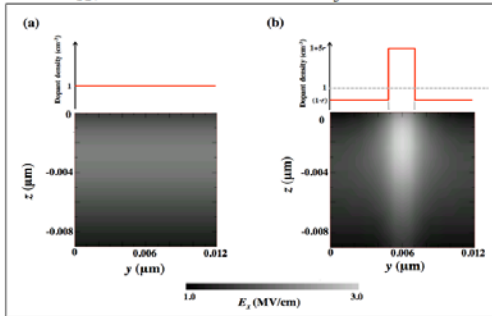


Fig. 5. (a) Distributions of  $E_x$  at the source edge region ( $x = 0.057 \mu\text{m}$ ) of (a) uniform model and (b) non-uniform model.

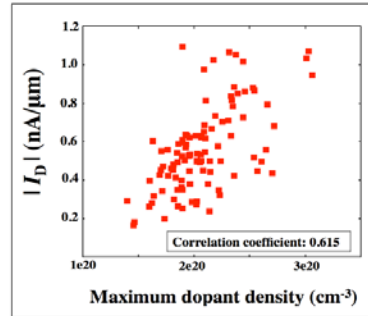
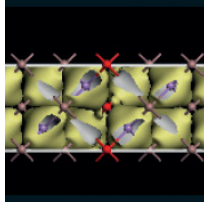


Fig. 6. Scatter plot of drain currents and maximum dopant density.

- [1] W. Y. Cho et al., IEEE Electron Device Lett. 28, 743 (2007)
- [2] N. Damrongplisit et al., IEEE Electron Device Lett. 34, 184 (2013)
- [3] W. Vandenberghe *et al.*, J. Appl. Phys. 109, 124503 (2011)
- [4] HyENEXSS, ver 5.5.7
- [5] E. O. Kane, J. Appl. Phys. 32, 83 (1961)



# International Workshop on Computational Nanotechnology

## P:05 Characterization of topological phase transitions in silicene and other 2D gapped Dirac materials

J C Bolívar Fernández<sup>1</sup>, F de los Santos<sup>1</sup>, J B Roldán<sup>2</sup> and E Romera<sup>1</sup>

<sup>1</sup>Instituto Carlos I de Física Teórica y Computacional, Spain, <sup>2</sup>Departamento de Electrónica y Tecnología de Computadores, Spain

In this work, we have studied the time evolution of electron wave packets in a monolayer of silicene under perpendicular magnetic and electric fields to characterize the topological band insulator transitions. We have found that the periodicities exhibited by the wave packets dynamics (zitterbewegung, classical and revival times) reach maximum values at the charge neutrality points (CNP). Additionally, we have discovered that electron currents reflect the transitions from a topological insulator to a band insulator at CNP too. These results are valid for other 2D gapped Dirac materials analogous to silicene with a buckled honeycomb structure and a significant spin-orbit coupling [1-4].

- [1] E. Romera, J. C. Bolívar, J. B. Roldán and F. de los Santos, Revivals of electron currents and topological-band insulator transitions in 2D gapped Dirac materials, EPL, 115, 20008 (2016).
- [2] M. Calixto and E. Romera, Inverse participation ratio and localization in topological insulator phase transitions, Journal of Statistical Mechanics, P06029 (2015).
- [3] E. Romera and M. Calixto. Uncertainty relations and topological-band insulator transitions in 2D gapped Dirac materials. Journal of Physics: Condensed Matter, 27, 175003 (2015).
- [4] M. Calixto and E. Romera. Identifying topological-band insulator transitions in silicene and other 2D gapped Dirac materials by means of Rényi-Wehrl entropy. EPL, 109, 40003 (2015).

## P:06 study of ballistic transport in phosphorene--nanoribbon-- FETs using empirical pseudopotentials

S Chen<sup>1</sup>, J Fang<sup>2</sup>, W G Vandenberghe<sup>1</sup>, and M V Fischetti<sup>1</sup>

<sup>1</sup>The University of Texas at Dallas, USA, <sup>2</sup>Vanderbilt University, USA

Among the 2D materials currently being considered as possible channel materials for future field-effect transistors, mono- and multi-layer phosphorous (phosphorene) stands out for its promising fabrication and electron-transport properties: Experimental FETs have shown a high on-off current ratio and with a field-effect carrier mobility of the order of  $10^3$  cm<sup>2</sup>/Vs in few-layer phosphorene [1]. Here we present an empirical-pseudopotential study of ballistic quantum transport in monolayer phosphorene in order to assess its potential application in nanoelectronics, following the methodology we have developed before [2].

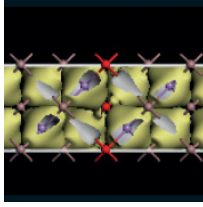
### BAND STRUCTURE CALCULATION AND TRANSPORT SIMULATION

Monolayer phosphorene exhibits a band gap of 1.5 eV [3]. In order to reproduce correctly this experimental observation, we have considered a previously proposed functional form for the local empirical pseudopotential phosphorous [4],

$$V_P(q) = \sum_{j=0}^4 a_j e^{-b_j(q-c_j)^2} [1 - d_j e^{-f_j q^2}]$$

and calibrated it obtaining the band structure shown in Fig. 1. The pseudopotential for the H required to terminate the P dangling bonds was taken from Ref. 5 without modifications:

$$V_H(q) = \begin{cases} b_0 + b_1 q + b_2 q^2 + b_3 q^3 & \text{for } (q \leq 2) \\ b_{-1}/q + b_{-2}/q^2 + b_{-3}/q^3 + b_{-4}/q^4 & \text{for } (q > 2) \end{cases}$$



# International Workshop on Computational Nanotechnology

The parameters are listed in Table 2. Looking at Fig. 1, compared to results obtained using density functional theory (DFT) [6], we obtain a similar dispersion but with the desired larger band gap of 1.5 eV for infinite sheets of monolayer phosphorene. Moving to the phosphorene nanoribbons (PNRs) of interest, we show in Fig. 2 the atomic configuration of a PNR with armchair edges and a width of 16 atomic lines (16-aPNR). The band structure of an unpassivated and an H-passivated 16-aPNR is shown in Fig. 3. The passivated 16-aPNR, which has no dangling bonds band after passivation, has a band gap of 1.36 eV.

We have simulated n-FETs based on such nanoribbons using the methodology presented in Ref. [2]. In order to limit simulation time, we have restricted our attention to a narrow ribbon, a 5-aPNR (*i.e.*, 0.664 nm-wide, with a calculated band gap of 1.92 eV) and a device with a 5.496 nm gate-length. Figure 4 shows the potential and charge density profile. Fig. 5 shows the  $I_{DS} - V_{GS}$  characteristics of a 5-aPNRFET, compared to the (5×5)-SiNWFET and 7-aGNRFET we have studied in Ref. 7, while Fig. 6 shows the on-current per unit width of these three devices. The 5-aPNRFET has a satisfactory subthreshold slope of about 70 mV/decade, but not quite as good as the turn-on behavior of the n-channel Si NWs. Also, the ballistic characteristics of this phosphorene-based FET (Fig. 6) are inferior to SiNW-FETs but superior to aGNR-FETs. Moreover, a relatively low electron mobility ( $\sim 170$  cm<sup>2</sup>/Vs along the armchair direction [8]) is likely to limit even more their performance in realistic situations.

a <sub>i</sub>	b <sub>i</sub>	c <sub>i</sub>	d <sub>i</sub>
-1.02921	0.834517	0.0	0.04
-0.048431	3.18979	0.88964	5.00
-0.11789	0.473922	1.02836	139.2
-0.073056	5.81145	2.4098	

b <sub>i</sub>	c <sub>i</sub>
-0.1416	0.02898
0.000902	-0.3877
0.06231	0.9862
-0.01892	-1.022

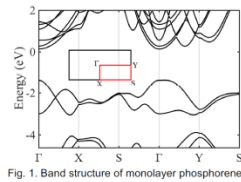


Fig. 1. Band structure of monolayer phosphorene.

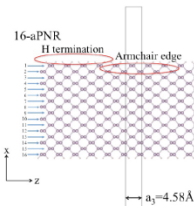


Fig. 2. Atomic model of a 16 armchair-edge phosphorene nanoribbon (16-aPNR). The electron transport direction is along z.

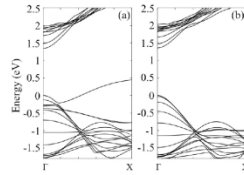


Fig. 3. Band structure of an unpassivated (a) and passivated (b) 16-aPNR.

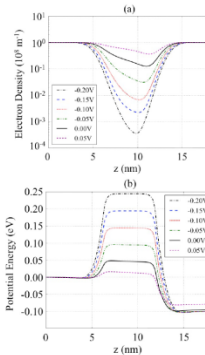


Fig. 4. Average charge-density (a) and potential energy (b) along the channel at  $V_{DS}=0.10$  V and  $V_{GS}$  ranging from -0.20 V to 0.05 V.

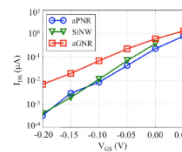


Fig. 5.  $I_{DS}-V_{GS}$  characteristics of a 5-aPNRFET, (5×5)-SiNWFET (0.772 nm side-length, 5.43 nm gate-length), and 7-aGNRFET (0.739 nm-wide, 5.12 nm gate-length) at  $V_{DS}=0.10$  V. The subthreshold slope of the 5-aPNR-FET is about 70 mV/dec, whereas the SiNWFETs exhibit the best electrostatic behavior.

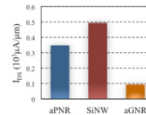
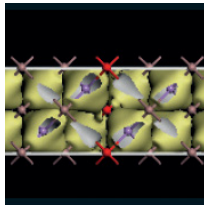


Fig. 6.  $I_{DS}$  for the 5-aPNRFET, SiNWFET, and 7-aGNRFET at  $V_{DS}=0.10$  V and  $V_{GS}-V_T=0.25$  V. The threshold voltage ( $V_T$ ) has been defined as the  $V_{GS}$  at which  $I_{DS}=I_{OFF}=0.1$   $\mu$ A/ $\mu$ m, *i.e.*,  $\sim 10^{-4}$   $I_{ON}$ . The aGNRFET suffers from poor ballistic conduction.

- [1] L. Li *et al.*, Nat. Nanotech. 9, 372--377 (2012).
- [2] J. Fang, W. Vandenberghe, B. Fu, and M. V. Fischetti, J. Appl. Phys. 119, 035701 (2016).
- [3] Z. Guo *et al.*, Adv. Funct. Mater. 25, 6996 (2015).
- [4] L. Bellaiche, S.-H. Wei, and A. Zunger, Phys. Rev. B 54, 17568 (1996).



# International Workshop on Computational Nanotechnology

- [5] L.-W. Wang and A. Zunger, *J. Phys. Chem.* 98, 2158 (1994).
- [6] H. Guo, N. Lu, J. Dai, X. Wu, and X. Zeng, *J. Phys. Chem. C* 118, 14051 (2014).
- [7] J. Fang, S. Chen, W. G. Vandenberghe, and M. V. Fischetti, *IEEE Trans. Elec. Dev.* (submitted, 2017).
- [8] B. Liao, J. Zhou, B. Qiu, M. Dresselhaus, and G. Chen, *Phys. Rev. B* 91, 235419 (2015).

## P:07 Power dissipation and noise in spin-wave-based computing systems

G Csaba<sup>1</sup>, Á Papp<sup>1,2</sup> and W Porod<sup>2</sup>

<sup>1</sup>Peter Pazmany Catholic University, Hungary, <sup>2</sup>University of Notre Dame, USA

Minimizing power dissipation is one of the main drivers behind the quest for emerging electronic devices. Spin-wave-based computing and processing devices are promising candidates in this field. It is claimed that they are both fast and low-power [1][2], which are usually conflicting requirements and are difficult to achieve simultaneously in electronic (CMOS-based) computing systems.

The fact that spin-waves themselves are low-energy excitations, does not necessarily mean that computing systems built from spin-waves will be similarly low-power. There are inefficiencies in the interconversions between the electric and magnetic domains and thermal noise puts an inherent lowest limit on the energy of the spin-wave system [3]. To our knowledge, the present work is the first assessment of fundamental energy limitations in a spin-wave based computing system.

### MODEL SYSTEM

The system we study is sketched in Fig 1 [2]. Electrical inputs at the left-hand side generate a spin-wave distribution in the magnetic thin film. The result of the computation is represented in the interference pattern, which should be picked up and converted back to electrical signals [3].

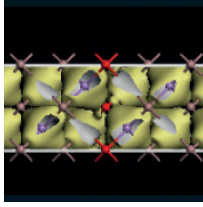
There are a number of physical structures that may serve as input. Most straightforwardly, the Oersted field of a waveguide may generate the spin-wavefront. More localized (short-wave) excitation can be achieved with spin-torque (for magnetic metals) or spin-orbit torque (in case of magnetic insulators) [4]. Signals can be picked up inductively, by a magnetoresistive effect or by inverse spin Hall effect (iSHE).

### DISSIPATION MECHANISMS

Spin wave signals are attenuated by Gilbert damping. In metallic ferromagnets the mean free path of magnons typically up to a few ten times the wavelength of the spin wave, while in magnetic insulators it can be several hundred times their wavelength [5]. Magnetoelectric interfaces both at the input and output side yield to large insertion losses. We estimate that in the case of spin-orbit torque, 5% of the electrical input signal is converted into magnetic energy, the rest is dissipated as Joule heating on the input structure. Similarly, a mere few percent of the spin-wave energy at the output wavefront can be picked up by the output structures.

### ROLE OF NOISE

Low-energy, linear spin-waves give rise to few-ten microvolts of induced AC voltage in micron- scale inductive pick up antennas, iSHE yields DC voltages with similar magnitudes. If such signals have to be picked up with significant bandwidth, thermal noise in the antenna / pick-up structure and the amplifier will become the limiting factor in the device (see Fig 2).



## International Workshop on Computational Nanotechnology

A spin wavefront can be created by a few milliwatts of continuous power consumption, while picking up and amplifying the spin wavefront (i.e. the result of the computation) requires several milliwatts to several ten milliwatts of power per output point, depending on the amplifier construction and bandwidth. The data throughput of the device can be several gigabits per second. Based on these estimate, spin-wave-based devices does not seem to be an energyefficient substitute for logic gates, but they may be very efficient as high-frequency, analog signal processors, for example at RF front-ends.

- [1] Kozhevnikov, Alexander, Frederick Gertz, G. Dudko, Y. Filimonov, and A. Khitun. "Pattern recognition with magnonic holographic memory device." *Applied Physics Letters* 106, no. 14 (2015): 142409. also Chumak, A. V., V. I. Vasyuchka, A. A. Serga, and B. Hillebrands. "Magnon spintronics." *Nature Physics* 11, no. 6 (2015): 453-461.
- [2] Csaba, G., A. Papp, and W. Porod. "Spin-wave based realization of optical computing primitives." *Journal of Applied Physics* 115, no. 17 (2014): 17C741.
- [3] Breitzkreutz, Stephan, Adam Papp, Eugen Egel, Christian Meier, Cenk Yilmaz, Leonhard Heiss, Wolfgang Porod, and Gyorgy Csaba. "Design of on-chip readout circuitry for spin-wave devices." *IEEE Magnetics Letters* (2016).
- [4] Chumak, A. V., A. A. Serga, M. B. Jungfleisch, R. Neb, D. A. Bozhko, V. S. Tiberkevich, and B. Hillebrands. "Direct detection of magnon spin transport by the inverse spin Hall effect." *Applied Physics Letters* 100, no. 8 (2012): 082405.
- [5] Yu, Haiming, O. d'Allivy Kelly, V. Cros, R. Bernard, P. Bortolotti, A. Anane, F. Brandl, F. Heimbach, and D. Grundler. "Approaching soft X-ray wavelengths in nanomagnet-based microwave technology." *Nature communications* 7 (2016).

### P:08 Quantization and analysis of acoustic modes in a rectangular microsound nanowaveguide fixed on a rigid substrate

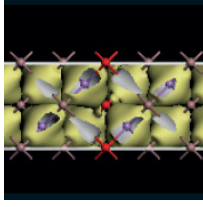
D Datta, A Darbandi, M A Stroschio and M Dutta

University of Illinois at Chicago, USA

Microsound waveguides have been used as delay lines for more than a decade in microwave circuit. With shrinking device sizes there is a need to realize waveguides operating well into the terahertz regime. This article focuses on a waveguide with an isotropic overlay structure deposited on a substrate which has a larger area and much higher rigidity compared to the overlay. Given the known solutions [1] of the completely bound displacement fields inside the overlay; see fig. 1. For the first time the quantization of the displacement fields is performed with respect to normal-mode phonon displacement using following condition [2].

$$\frac{1}{ab} \left[ \int_0^a dx \int_0^b dy (u_x u_x^* + u_y u_y^* + u_z u_z^*) \right] = \frac{\hbar}{2m\omega} \quad (1)$$

where  $m$  = mass of the single atom,  $\omega$  = angular frequency of wave and  $u_x$ ,  $u_y$ ,  $u_z$  is given by-



## International Workshop on Computational Nanotechnology

$$\begin{aligned}
 u_x &= \frac{n\pi}{a} A_3 \left\{ (C(y) - \gamma(y)) + \frac{\Sigma}{\Gamma} [S(y) + \sigma(y)s \frac{g_1}{g_2}] \right\} \cos\left(\frac{n\pi x}{a}\right) e^{-j(\beta z - \omega t)} \\
 u_y &= A_3 \left\{ \frac{\Sigma}{\Gamma} g_1 (C(y) - \gamma(y)) - [S(y)g_1 + \frac{\sigma(y)}{s} g_2] \right\} \sin\left(\frac{n\pi x}{a}\right) e^{-j(\beta z - \omega t)} \\
 u_z &= -j\beta A_3 \left\{ (C(y) - \gamma(y)) + \frac{\Sigma}{\Gamma} [S(y) + \sigma(y)s \frac{g_1}{g_2}] \right\} \sin\left(\frac{n\pi x}{a}\right) e^{-j(\beta z - \omega t)}
 \end{aligned} \quad (2)$$

$$g_1 = \sqrt{\left(k^2 - \frac{n^2\pi^2}{a^2}\right)}, \quad g_2 = \beta^2 + \frac{n^2\pi^2}{a^2}, \quad C(y) = \cos(g_1 y), \quad \gamma(y) = \cos(sy), \quad \sigma(y) = \sin(sy),$$

$$S(y) = \sin(g_1 y), \quad s = \sqrt{\frac{\omega^2 \rho}{\mu} - \beta^2 - \frac{n^2\pi^2}{a^2}}, \quad \Sigma = 2C_0 - \gamma_0 \left(1 - \frac{s^2}{g_2}\right) \text{ and } \Gamma = 2S_0 + \frac{\sigma_0(g_2^2 - s^2)}{s g_1} \text{ where}$$

$$C_0 = C(b), \quad \gamma_0 = \gamma(b), \quad \sigma_0 = \sigma(b), \quad S_0 = S(b), \quad k = \sqrt{\frac{\omega^2 \rho}{\lambda + 2\mu} - \beta^2}, \quad \lambda \text{ and } \mu \text{ are the Lamé's constants}$$

for the overlay material,  $\rho$  (rho) is the density of the overlay material,  $\beta$  and  $\omega$  are the phase constant and angular frequency of the guided wave and  $n$  is a positive integer used for defining the modes. When the quantization condition is satisfied we obtain the constant  $A_3$  as:

$$A_3 = \sqrt{\frac{\hbar}{2M\omega}} \cdot \sqrt{\frac{1}{B}} \quad (3)$$

$$\begin{aligned}
 \text{where } B &= \left[ \left( \frac{g_2}{2} + \frac{1}{2} \left( \frac{\Sigma}{\Gamma} \right)^2 g_1^2 \right) \{ f_s(g_1, b) - 2(f_s(g_1, -s, b) + f_s(g_1, s, b)) + f_s(s, b) \} + \right. \\
 &\left( g_2 \left( \frac{\Sigma}{\Gamma} \right) - g_1^2 \left( \frac{\Sigma}{\Gamma} \right) \right) (f_c(g_1, b) + f_c(g_1, -s, b) + f_c(g_1, s, b)) + \\
 &\left( g_1 s \left( \frac{\Sigma}{\Gamma} \right) - \frac{g_1 g_2}{s} \left( \frac{\Sigma}{\Gamma} \right) \right) (-f_c(g_1, -s, b) - f_c(g_1, s, b) - f_c(s, b)) + \left( \frac{g_2}{2} \left( \frac{\Sigma}{\Gamma} \right)^2 + \frac{1}{2} g_1^2 \right) (1 - f_s(g_1, b)) + \\
 &\left. \left( \frac{g_2}{2} \left( \frac{\Sigma}{\Gamma} \right)^2 2s \frac{g_1}{g_2} + \frac{1}{2} \frac{2g_1 g_2}{s} \right) (f_s(g_1, -s, b) - f_s(g_1, s, b)) + \left( \frac{g_2}{2} \left( \frac{\Sigma}{\Gamma} \right)^2 s^2 \frac{g_1^2}{g_2^2} + \frac{1}{2} \frac{g_2^2}{s^2} \right) (1 - f_s(s, b)) \right] \\
 \text{and } f_s(x, y) &= \frac{1}{2} + \frac{\sin(2xy)}{4xy}; \quad f_c(x, y) = \frac{1}{4xy} - \frac{\cos(2xy)}{4xy}; \quad f_s(x, y, z) = \frac{\sin\{(x+y)z\}}{2(x+y)z}; \quad f_c(x, y, z) = \\
 &\frac{\cos\{(x+y)z\}}{2(x+y)z} - \frac{1}{2(x+y)z}.
 \end{aligned}$$

The phase characteristics of the system are calculated using dispersion curves and are obtained from the two characteristics equations obtained by solving the generalized displacement fields imposing boundary conditions are given in [1] as:

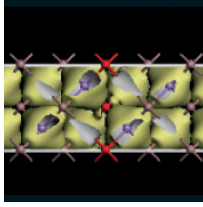
$$4\theta^2(1 - 2\theta^2) - \frac{\theta^2 \sigma_0 S_0}{\sqrt{(1-\theta^2)(P-\theta^2)}} \cdot \{8\theta^4 - 4(P+2)\theta^2 + (4P+1)\} + \gamma_0 C_0 (8\theta^4 - 4\theta^2 + 1) = 0 \quad (4a)$$

$$s = \omega b \sqrt{\frac{(1-\theta^2)\rho}{\mu}} = \frac{(2q+1)\pi}{2} \quad (4b)$$

$$\text{where } P = \frac{\mu}{\lambda + 2\mu}, \quad \theta^2 = \frac{\beta^2}{\omega^2} \cdot \frac{\mu}{\rho} + \frac{n^2\pi^2\mu}{a^2\omega^2\rho}.$$

Three prominent modes can be seen named Longitudinal (L) and Dilatational (D) obtained from Eq. 4a and Shear (S) phase characteristics obtained from Eq. 4b. Phase characteristics of the three above mentioned modes are analyzed for different height to thickness ratio of the overlay.

The suitability of the waveguide structure to behave as a resonator has been evaluated by calculating frequency-quality factor (f. Q) product taking into consideration intrinsic dissipation of the overlay. The calculation at room temperature is being done by plugging in the parameter for silicon.



# International Workshop on Computational Nanotechnology

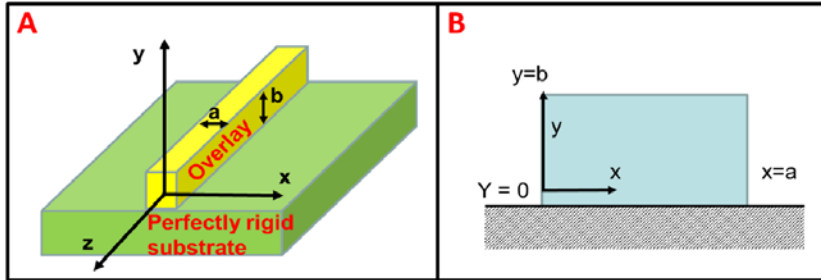


Figure 1: The 3D structure of the microsound waveguide is shown in the fig. A where overlay (yellow) part has much less rigidity compared to the substrate (green) hence substrate assumed to be perfectly rigid. The fig. B shows the rectangular cross-section of the waveguide which is the most common direction for implementing different waveguide structure.

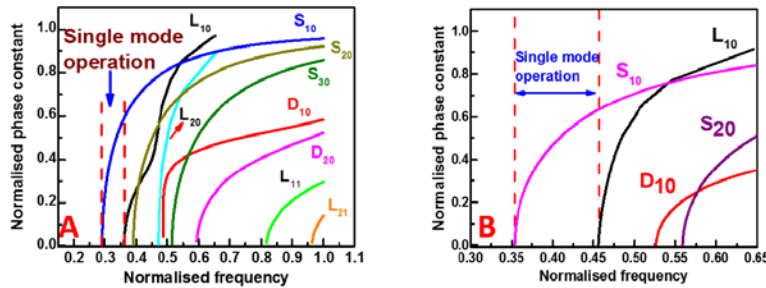


Figure 2: The dispersion curve for the A)  $b/a = 0.3$  B)  $b/a = 0.5$  ratio is given. The single mode operation window for both the ratio of height/width

- [1] Waldron, R.A., 1971. Mode spectrum of a microsound waveguide consisting of an isotropic rectangular overlay on a perfectly rigid substrate. IEEE Transactions on Sonics and Ultrasonics, 18(1), pp.8-15.
- [2] Stroschio, M.A. and Dutta, M., 2001. Phonons in Nanostructures. Cambridge University Press.

## P:09 Effect of quantum confinement on lifetime of anharmonic decay of optical phonon in a confined GaAs structure

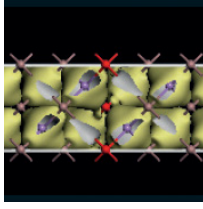
D Datta, K Krishnababu, M A Stroschio and M Dutta

University of Illinois at Chicago, USA

In this research, the role of phonon confinement on the anharmonic decay of an LO is analyzed. Anharmonic interactions describe the decay of phonon modes in GaAs via the Klemens channel [1]. The interaction Hamiltonian for three phonon process can be written as [2] channel [1]. The interaction Hamiltonian for three phonon process can be written as [2]

$$H_{k,j;k',j';k'',j''} = \frac{1}{\sqrt{N}} P(k, j; k', j'; k'', j'') u_{k,j} u_{k',j'} u_{k'',j''} \quad (1)$$

where  $k, k', k''$  are the three phonon wave vectors involved in the annihilation or creation process,  $j, j', j''$  are the polarization of the three phonons and  $N =$  number of unit cells present.  $P$  describes the cubic (anharmonic) coupling. The phonon displacement in normal coordinates is represented as:



## International Workshop on Computational Nanotechnology

$$u_{k,j} = \left( \frac{\hbar}{2m\omega_{k,j}} \right)^{\frac{1}{2}} e'_{k,j} (a_{k,j} e^{i\vec{k}\vec{r}} + a_{k,j}^{\dagger} e^{-i\vec{k}\vec{r}}) \quad (2a)$$

$$u(\vec{r}) = \frac{1}{\sqrt{N}} \sum_q \sum_{j=1,2,3} \left( \frac{\hbar}{2m\omega_{q,j}} \right)^{\frac{1}{2}} (a_{q,j} e^{i\vec{q}\vec{r}} \hat{e}_{q,j} + a_{q,j}^{\dagger} e^{-i\vec{q}\vec{r}} \hat{e}_{q,j}^*) = \frac{1}{\sqrt{N}} \sum_q \sum_{j=1,2,3} \overline{u_{q,j}} \quad (2b)$$

where  $a_{k,j}$ ,  $a_{k,j}^{\dagger}$  denoted the annihilation and creation operator, respectively,  $e'_{k,j}$  is the polarization vector,  $m$  is the reduced mass of the lattice atoms and  $\omega_{q,j}$ , is the frequency of the normal mode. The displacement vector can be represented as following, with the direction of confinement and direction perpendicular to it [1].

$$u(\vec{r}) = e^{\pm i\vec{q}\vec{r}} = u(z) e^{\pm i\vec{q}_{\parallel}\vec{r}_{\parallel}} = (\cos(q_z z) \pm i \sin(q_z z)) e^{\pm i\vec{q}_{\parallel}\vec{r}_{\parallel}} \quad (3)$$

The decay lifetime for phonons can be calculated using Fermi golden rule, the matrix element in Fermi golden rule can be simplified as 1D problem for a quantum-confined structure confined in the z-direction.

$$\frac{1}{V} \int |M|^2_{ave} dV = \frac{1}{L_z} \int u^2(z) dz \quad (4)$$

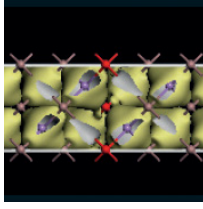
Taking into account the confinement of the LO phonon in the GaAs structure to can be describe by either the slab model ( $V = 0$  at  $\pm L_z/2$ ) or the guided model ( $u = 0$  at  $\pm L_z/2$ ) [1] yields the same value for the average matrix element squared, respectively:

$$|M|^2_{ave} = \frac{1}{\pi} \int_{-\frac{\pi}{2}}^{\frac{\pi}{2}} \sin^2 y dy = \frac{1}{\pi} \int_{-\frac{\pi}{2}}^{\frac{\pi}{2}} \cos^2 y dy = \frac{1}{2} \quad (5)$$

These results indicate that the decay rate for the lowest LO phonon mode in either the slab or the guided model is approximately half that of the bulk phonon.

In this research, the confinement effect on the optical phonon decay lifetime in confined GaAs quantum structures is considered. This analysis is based on the three phonon interaction Hamiltonian; the phonon displacement vectors are defined in order to perform the calculation of the matrix element via the Fermi golden rule to estimate the lifetime for the Klemens channel in confined GaAs structures.

- [1] Strocio, M.A. and Dutta, M., 2001. *Phonons in Nanostructures*. Cambridge University Press.
- [2] Bhatt, A.R., Kim, K.W. and Strocio, M.A., 1994. Theoretical calculation of longitudinal-optical-phonon lifetime in GaAs. *Journal of Applied Physics*, 76(6), pp.3905-3907.



# International Workshop on Computational Nanotechnology

## P:10 Quantized acoustic-phonon modes in a non-piezoelectric nanowaveguide

M Mazouchi, M Dutta and M A Strosio

University of Illinois at Chicago, USA

To reach the terahertz frequency domain, size reduction of the resonator down to a few nanometers is required. Here, for the first time, we take the necessary step of quantizing the acoustic shear modes in an isotropic non-piezoelectric waveguide structure, using the general unquantized equations presented earlier by Auld [1]. In this work, a thin plate of infinite length with the thickness of  $t$  and width of  $w$  is considered. To avoid the spurious frequency responses produced by other modes of the structure which rests very close to the desired resonance, the plate is thickened in the area where energy trapping is to be realized (Fig. 1). The thickened region has the thickness of  $t$  with the lateral dimension of  $w'$ , and to confine the resonance fields near the thickened part and far from the edges of the plate;  $w' \cong t$  is assumed. In this ridged waveguide, the shear horizontal (SH) waves are polarized in  $x$  direction and propagating along the  $z$ -axis. By adopting the notations in [1], and considering the fundamental mode of  $n = 1$  and  $m = 1$  along with the assumption of  $t \cong t'$ , the unquantized acoustic-mode displacements and stress fields can be written as follows:

$$U_x = \begin{cases} \cos \left[ \frac{\pi}{t'} \left( y + \frac{t'}{2} \right) \right] C e^{\gamma_1 z}, & z < -\frac{w'}{2} \\ \cos \left[ \frac{\pi}{t'} \left( y + \frac{t'}{2} \right) \right] (A e^{-i\beta_1 z} + B e^{+i\beta_1 z}), & -\frac{w'}{2} < z < \frac{w'}{2} \\ \cos \left[ \frac{\pi}{t'} \left( y + \frac{t'}{2} \right) \right] D e^{-\gamma_1 z}, & z > \frac{w'}{2} \end{cases} \quad (1)$$

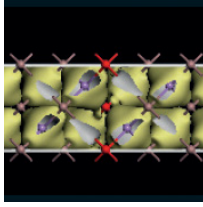
$$\beta_1^2 = \left( \frac{\omega}{v_s} \right)^2 - \left( \frac{\pi}{t} \right)^2, \quad (2)$$

$$T_{xz} = \begin{cases} \gamma_1 \cdot c_{44} \cdot \cos \left[ \frac{\pi}{t'} \left( y + \frac{t'}{2} \right) \right] C e^{\gamma_1 z}, & z < -\frac{w'}{2} \\ -i\beta_1 c_{44} \cdot \cos \left[ \frac{\pi}{t'} \left( y + \frac{t'}{2} \right) \right] (A e^{-i\beta_1 z} - B e^{+i\beta_1 z}), & -\frac{w'}{2} < z < \frac{w'}{2} \\ -\gamma_1 \cdot c_{44} \cdot \cos \left[ \frac{\pi}{t'} \left( y + \frac{t'}{2} \right) \right] D e^{-\gamma_1 z}, & z > \frac{w'}{2} \end{cases} \quad (3)$$

where  $\beta_1$  is the wave vector of the wave,  $\gamma_1 = -i\beta_1$ , A, B, C and D are the four unknown wave amplitudes. By solving the boundary conditions, where  $U_x$  and  $T_{xz}$  are continuous at  $z = \pm \frac{w'}{2}$  for two cases of (i) even symmetry modes ( $B = A, D = C$ ) and, (ii) odd symmetry modes ( $B = -A, D = -C$ ) with the assumption of  $t = t'$ , the number of unknown wave amplitudes can be reduced. Now, by following the quantization procedure described by Strosio et al. in [2], the normalization constant of the SH acoustic modes can be obtained as follows:

$$\frac{1}{tw} \left( \int_{-\frac{t}{2}}^{\frac{t}{2}} dy \int_{-\frac{w}{2}}^{\frac{w}{2}} dz \{U_x \cdot U_x^*\} + \int_{-\frac{t}{2}}^{\frac{t}{2}} dy \int_{-\frac{w'}{2}}^{\frac{w'}{2}} dz \{U_x \cdot U_x^*\} + \int_{\frac{t}{2}}^{\frac{t}{2}} dy \int_{\frac{w'}{2}}^{\frac{w}{2}} dz \{U_x \cdot U_x^*\} \right) = \frac{\hbar}{2m\omega} \quad (4)$$

where  $m$  is the atomic mass and  $\omega$  is the wave angular frequency. Finally, by performing the integration indicated in Eq. 4, the amplitude  $C$  is found to be,



# International Workshop on Computational Nanotechnology

$$C = \sqrt{\frac{\hbar}{2m\omega}} \cdot \frac{1}{\sqrt{\frac{1}{2w\gamma_1}(e^{-w'\gamma_1} - e^{-w\gamma_1}) + \frac{w'\gamma_1^2}{4w\beta_1^2}e^{-w'\gamma_1} \cdot \left(\frac{1 + \sin(\beta_1 w')}{\beta_1 w'}\right) \frac{1}{\sin^2(\frac{\beta_1 w'}{2})}}}, \quad (5)$$

for the even symmetry modes and

$$C = \sqrt{\frac{\hbar}{2m\omega}} \cdot \frac{1}{\sqrt{\frac{1}{2w\gamma_1}(e^{-w'\gamma_1} - e^{-w\gamma_1}) + \frac{w'\gamma_1^2}{4w\beta_1^2}e^{-w'\gamma_1} \cdot \left(\frac{1 - \sin(\beta_1 w')}{\beta_1 w'}\right) \frac{1}{\cos^2(\frac{\beta_1 w'}{2})}}}, \quad (6)$$

for the odd symmetry modes.

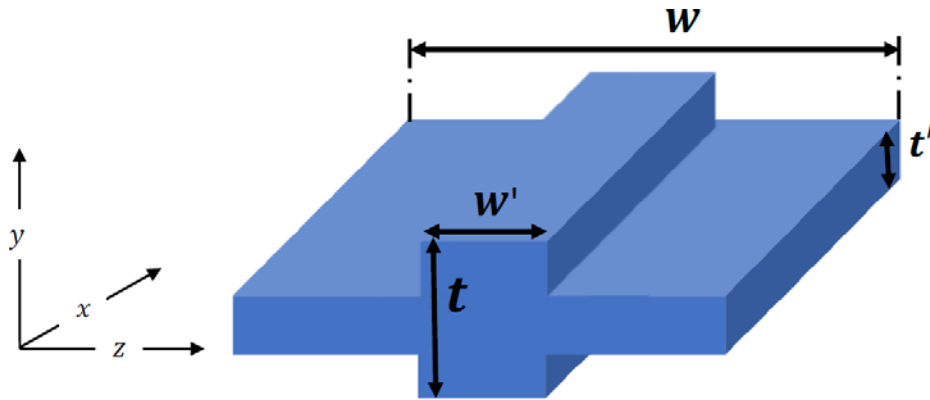
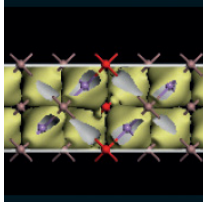


Fig. 1: Acoustic SH mode non-piezoelectric nanowaveguide designed by thickening the central region of the thin plate.

2

- [1] B. A. Auld, Acoustic fields and waves in solids, ISBN: 978-5-88501-343-7 (1973).  
 [2] Strocio et al., Phys. Rev. B 48, 1936–1938, doi: 10.1103/PhysRevB.48.1936 (1993).



## P:11 Quantized acoustic-phonon shear horizontal modes in a piezoelectric nanoresonator

M Mazouchi, M Dutta and M A Stroschio

University of Illinois at Chicago, USA

To obtain high resonant frequencies of the order of sub-terahertz frequencies, the dimensions of a resonator need to be scaled down to the nanometer regime. As device dimensions shrink, the fundamental physics of phonon propagation and interaction is changed. In this study, to simplify the calculations of the quantum-mechanical coefficients, for the very first time we applied a quantization prescription to the classical acoustic-shear horizontal (SH) modes confined in an infinite piezoelectric nanoresonator. Here, we quantized the displacement amplitudes of the modes using the unquantized equations presented by Auld [1], in a way that each mode has the appropriate quantum-mechanical energy. As depicted in Fig.1, we consider an infinite piezoelectric X-cut hexagonal plate of a 6mm crystal with thickness,  $t$ , along with two perfectly conducting electrodes away from the surfaces of the plate by a gap of  $h$ . The coordinate system used in this problem is shown in Fig. 1. Here, the assumption is that the plate has stress-free boundaries and its thickness is small enough for the quasi-static approximation to be valid. We only consider the x-polarized particle displacement which is electrically coupled to the generated potential. The unquantized acoustic SH displacement wave propagating in the y direction can be written as follows [1]:

$$U_x = \begin{cases} A \cos(ky), & n = 0,2,4, \dots \\ A \sin(ky), & n = 1,3,5, \dots \end{cases} \quad (1)$$

where  $k = \frac{n\pi}{t}$  is the wave vector, and  $A$  is the unknown amplitude of the acoustic wave. Now we can obtain the normalized expression of classic acoustic SH modes confined in the nanoresonator depicted in Fig. 1, for two cases of (i) even symmetry modes and, (ii) odd symmetry modes, by following the general quantization procedure discussed by Stroschio et al. [2],

$$\frac{1}{t} \int_0^t dy \{U_x, U_x^*\} = \frac{\hbar}{2m\omega_n} \quad (2)$$

where  $\omega$  is the wave angular frequency and  $m$  is the atomic mass. Substituting the displacement fields given in Eq. 1 into Eq.2, yields

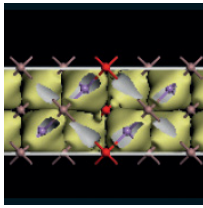
$$\frac{A^2}{n\pi} \int_0^{n\pi} \cos^2(u) du = \frac{\hbar}{2m\omega_n} \quad (3)$$

for the even symmetry modes and

$$\frac{A^2}{n\pi} \int_0^{n\pi} \sin^2(u) du = \frac{\hbar}{2m\omega_n} \quad (4)$$

for the odd symmetry modes, so that

$$A^2 = \frac{\hbar}{m\omega_n} \quad \text{for all } n. \quad (5)$$



# International Workshop on Computational Nanotechnology

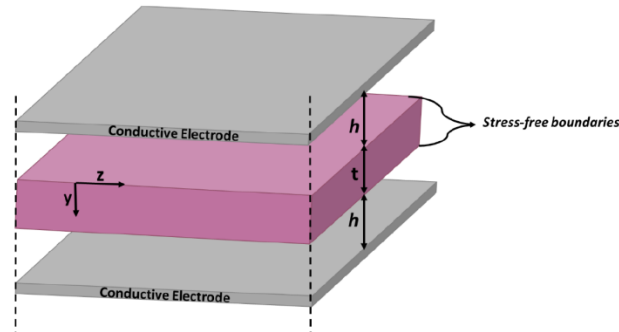


Fig. 1: Quantization of acoustic SH modes in an unbounded piezoelectric x-cut hexagonal crystal (class 6mm) nanoresonator.

- [1] B. A. Auld, Acoustic fields and waves in solids, ISBN: 978-5-88501-343-7 (1973).
- [2] Stroschio et al., Phys. Rev. B 48, 1936–1938, doi: 10.1103/PhysRevB.48.1936 (1993).

## P:12 Exchange-coupled majority logic gate

H Dey, G Csaba, and W Porod

University of Notre Dame, USA

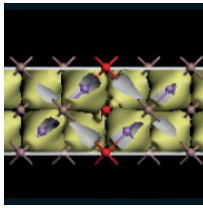
Magnetic dipole-field-coupling between adjacent single-domain nanomagnets has long been used to realize logic gates [1]. It has recently been demonstrated that much stronger lateral coupling can be achieved between two neighboring nanomagnets, if they both are antiferromagnetically exchange-coupled to a common bottom magnetic layer [2]. This paper presents a simulation study on majority logic gate, using this novel coupling mechanism as a building block.

### PHYSICAL STRUCTURE OF THE EXCHANGE- COUPLED SYSTEM

Two magnetic layers separated by a non- magnetic layer can either point to parallel or antiparallel directions in their ground state (fig.1 (top left and right)), depending on the thickness of the non-magnetic layer [3]. If the ground state is antiparallel, the layers are called antiferromagnetically exchange-coupled. However, if the top magnetic layer is patterned into two closely-spaced single- domain nanomagnets, the magnets force each other to parallel direction, both being antiparallel to the bottom magnetic layer (fig. 1(bottom)) [2]. The competition between lateral dipole coupling energy between the magnets, and the exchange coupling energy between the layers in vertical direction determines the ground state of this system. If the exchange coupling energy overwhelms the dipole coupling energy, the nanomagnets settle into parallel direction. Stronger coupling between the neighboring elements can effectively increase the energy barrier between stable round states, and make the system more immune to thermal fluctuations and process variations, which can cause random errors in complex systems by obliterating the energy barrier.

### NUMERICAL SIMULATIONS

In fig. 2, a typical majority gate structure is shown for different input/output combinations. Given the state of input A (0 or 1), the computing magnet (M) performs a logical AND or OR operation between the other two input magnets (B, C), respectively. The computing (M) and output (Out) magnets were clocked along their



# International Workshop on Computational Nanotechnology

hard axis by applying a 1 T magnetic field, and then allowed to relax as the field was gradually reduced to zero.

The micromagnetic simulations using OOMMF clearly show logically correct output states for the given input combinations. Unlike a dipole-coupling based majority logic gate, the state of the computing magnet is buffered to the output magnet instead of being inverted. This is due to the dominance of exchange-coupling over the dipole-coupling between them. The bottom layer finds an energetically favorable domain configuration (fig. 2).

We are not aware of any studies on the logic applications of exchange-coupled and patterned films. Besides being an interesting model system, such systems can be engineered to build dense, 3-D magneto-electronic platform for magnetic logic and data storage. We are currently studying this system both experimentally and via further simulation and analytical methods.

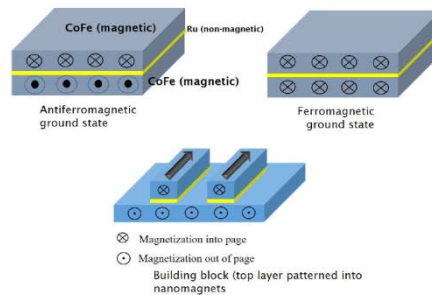


Figure 1: Exchange-coupled nanomagnet system: (top left and right) the antiferromagnetic and ferromagnetic ground state (bottom) building block showing nanomagnets pointing to same direction [2].

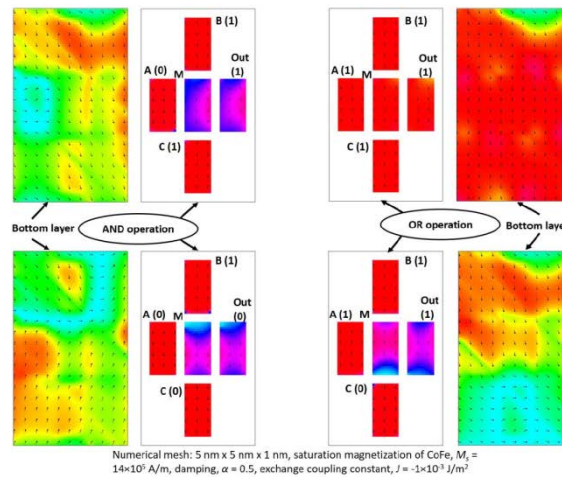
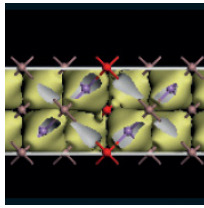


Figure 2: Simulated magnetizations of the exchange-coupled majority logic gates: (left column) A=0: AND operation between the inputs B and C (right column) A=1: OR operation between B and C.

- [1] Imre, A., G. Csaba, L. Ji, G.H. Bernstein, and W. Porod. "Majority logic gate for magnetic quantum-dot cellular automata." *Science* 80, pp. 1-4 (2006).
- [2] Dey, H., G. Csaba, G.H. Bernstein, and W. Porod. *Exchange coupling between laterally adjacent nanomagnets.* "Nanotechnology 27, 395202 (2015).
- [3] Fullerton, E. et al., "Antiferromagnetically coupled magnetic media layers for thermally stable high density recording", *Applied Phys Lett*, vol. 77, 3806,2000.



## P:13 Multi-subband ensemble Monte Carlo simulator for 3D electron devices

L Donetti, C Sampedro, F G Ruiz, A Godoy and F Gamiz

Universidad de Granada, Spain

To study non-planar MOS devices with multiple gates we have developed a Multi- Subband Ensemble Monte Carlo (MS- EMC) simulator for 3D devices, coupling the solution of 3D Poisson Equation (PE), 2D Schrödinger Equation (SE) and 1D MC transport.

### II. THE SIMULATOR

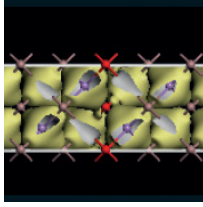
To simulate a 3D device we employ the space-mode approach [1], where the SE is solved in several cross sections of the device perpendicular to the transport direction. The MC approach is then applied to carriers in every subband considering 1D transport. Self-consistency is obtained by solving the 3D PE in the whole device.

A flow chart of the simulation strategy for a given value of the gate bias  $V_G$  is reported in Fig. 1. The algorithm starts with  $V_{DS}=0$  V and a self-consistent solution of SE and PE in equilibrium (w/o transport) is found employing a predictor-corrector method. This allows the initialization of the MC simulator employing the equilibrium Fermi- Dirac distribution for each subband. Then a self-consistent MC, PE, SE loop is started. In a first phase the boundary conditions at the drain are changed step by step in order to reach the desired value of  $V_{DS}$ . After that, the boundary conditions are kept fixed while a self-consistent solution for the potential is reached within a prescribed tolerance. Finally, the current is computed while preserving self-consistency. This self- consistent procedure is repeated for increasing values of  $V_{DS}$ .

The simulation domain is represented using a 3D finite element mesh: first a 2D triangular mesh of the device cross section is built and then the 3D one is built by extrusion. The finite element mesh allows a good representation of complex geometries (e.g. round nanowires, rounded corners, leaning sidewalls in FinFETs) and a natural formulation of the equations (PE, SE) near material boundaries. Different properties are mapped to nodes (e.g. the potential), to elements (e.g. affinity, dielectric constant, energy gap, etc.) or even on nodes as seen from each element (for example the conduction band which depends on both the electrostatic potential of the node and the material properties of the element).

The SE is solved in several 2D cross sections of the device employing triangular finite elements. Non-parabolic corrections are added to energy levels and to the band structure [2]. To improve the MC statistics, especially in the sub-threshold regime, non-uniform particle weights are employed which depend on particle energy [3]. At this stage acoustic and optical phonon scattering has been implemented [4]. For the scattering events, the simulator takes into account the Pauli's exclusion principle: to do that the occupation function  $f_{\mu i}(k)$  is computed and updated for every subband  $\mu$  and cross-section  $i$  [5].

We simulated FET devices based on Si nanowires in  $\langle 100 \rangle$  direction with diameter  $D=6$  nm,  $\text{SiO}_2$  thickness  $T_{ox}=1$  nm, gate length  $L_G=14$  nm, undoped channel and gate work function 4.65 eV. Source and drain doping is  $N_{SD}=1 \times 10^{20} \text{ cm}^{-3}$ , with underlap  $L_{sp}=2$  nm and Gaussian distribution with  $\sigma=0.8$  nm. Some results are shown in Figs. 2-8, including electron wave- functions, output and transfer characteristics, subband energy profiles and populations. In Fig.4 we compare the subthreshold behavior of devices with  $L_G$  down to 8 nm: notice that the statistical error is relevant only for current values  $< 1$  nA.



# International Workshop on Computational Nanotechnology

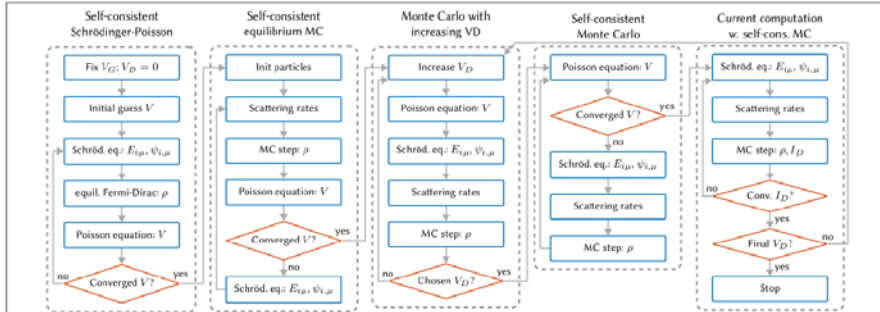


Fig. 1: Block diagram for the simulation of an  $I_D$ - $V_D$  curve, which is repeated, if needed, for different values of  $V_G$ .

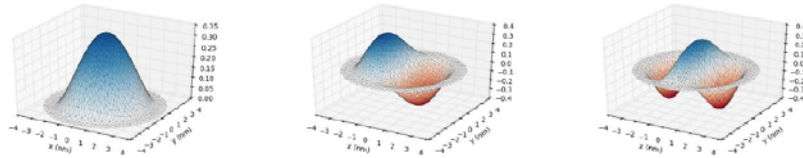


Fig. 2: Wave functions of the first 3 subbands of the  $\Delta_1$  valley in the middle of the channel for  $V_G=0.5$  V,  $V_D=0.05$  V.

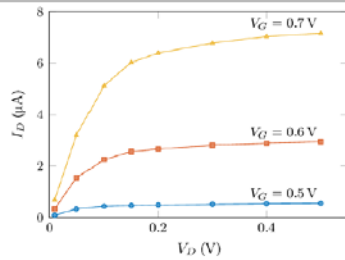


Fig. 3: Output characteristic of the device with  $L_G=14$  nm.

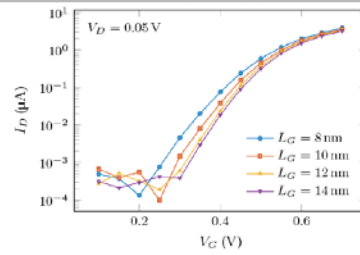


Fig. 4: Transfer characteristic of devices with different  $L_G$ .

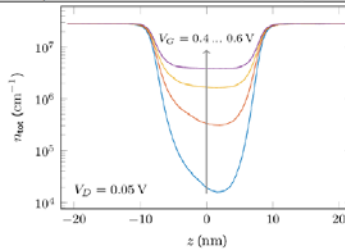


Fig. 5: 1D electron density for different values of  $V_G$ .

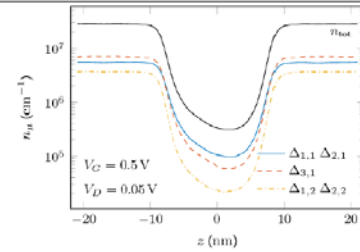


Fig. 6: Population of the lowest energy subbands.

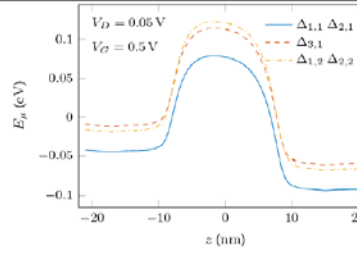


Fig. 7: Energy profile of the lowest energy subbands.

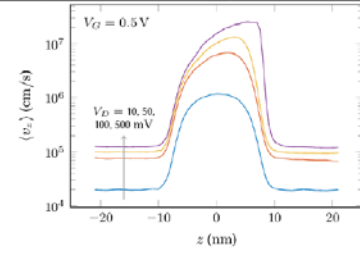
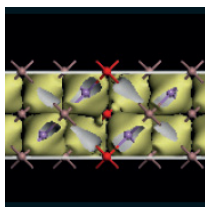


Fig. 8: Average velocity profiles for increasing values of  $V_D$ .

- [1] R. Venugopal, Z. Ren, S. Datta, M. S. Lundstrom, and D. Jovanovic, Journal of Applied Physics, 92(7), p. 3730, 2002.
- [2] S. Jin, M. V. Fischetti, and T.-w. Tang, Journal of Applied Physics 102, p. 083715, 2007
- [3] A. Pacelli, U. Ravaioli, Solid-State Electronics, 41(4), p. 599, 1997.
- [4] A. Godoy, F. Ruiz, C. Sampedro, F. Gámiz, U. Ravaioli, Solid-State Electronics 51, p. 1211, 2007.
- [5] P. Lugli and D.K. Ferry, IEEE Transactions on Electron Devices 32(11), p. 2431, 1985.



# International Workshop on Computational Nanotechnology

## P:14 Charge corrections from exact electrostatics for metal-oxide interfaces

T R Durrant<sup>1</sup>, S T Murphy<sup>2</sup>, M B Watkins<sup>3</sup> and A L Shluger<sup>1</sup>

<sup>1</sup>University College London, <sup>2</sup>Lancaster University, UK, <sup>3</sup>University of Lincoln, UK

Density functional theory (DFT) is a workhorse of electronic structure theory. When simulating charged defects, the use of periodic boundary conditions (PBC) ensures an accurate description of the host crystal's bandstructure, but negatively introduces fictitious interactions with image charges in neighbouring cells [1]. These interactions are large when the defect is in a high charge state, or when some dimensions of the simulation cell are small. This last case is especially severe when expensive hybrid functionals are utilised to study multiple interfaces. Several methods to correct for this interaction exist in the literature for the bulk case and are widely used to study charged defects [2-5]. Equivalent methods for surfaces and interfaces with varying dielectric profile are now starting to be developed [6].

We have been developing a new method that can be applied to this problem, by extending previous work based on charged molecular fragments in vacuum [7] to crystals. Using the newly released electrostatics solver DL\_MG, we have extended this method to interfaces and defect clusters. We have validated our electrostatic method for bulk problems, where it is important to well describe the internal response of the defect containing supercell. This behaviour is shown in Figure 1. We found a strong correspondence with the Lany-Zunger method for bulk crystals [4].

Now we have been applying the method to more complex interface systems, such as islands of MgO grown on a Ag substrate. This is shown in Figure 2. Such systems show very different behaviour, due to the metal substrate. When electrons or holes are transferred from the defect to the metal substrate, they occupy delocalised states and can lead to surface dipoles. The physics of this process is explored.

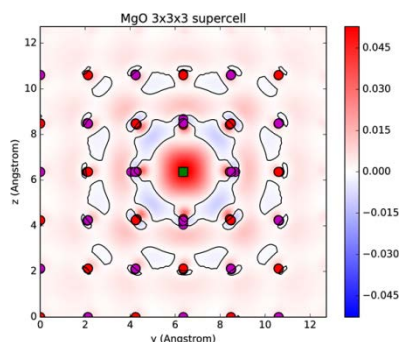
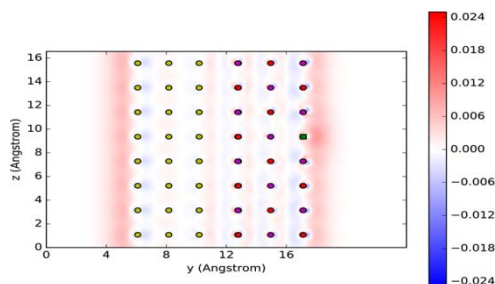
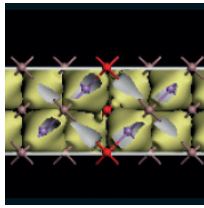


Figure 1 Internal polarisation response of a bulk supercell of MgO containing an  $F^{2+}$  centre, denoted by the green square. The clear bands of positive and negative polarisation show the ionic response of the host crystal to the charge of the defect complex, and act to reduce the defects interaction with it's own periodic images.





## International Workshop on Computational Nanotechnology

Figure 2 A similar plot for MgO (right three layers) grown on an Ag substrate (left three layers). An  $F^+$  defect is present at the surface of the MgO film, denoted by a green square. Surface models show significantly greater movement of charge. In this case, there is a clear accumulation of positive charge on the surfaces of the interface model.

- [1] C Freysoldt, B Grabowski, T Hickel and J Neugebauer, *Rev. Mod. Phys.* 86 253 (2014)
- [2] H Komsa, T Rantala and A Pasquarello, *Physica B* 407 3063 (2012)
- [3] C Freysoldt, J Neugebauer and C Van de Walle, *Phys. Rev. Lett.* 102 016402 (2009)
- [4] S Lany and A Zunger, *Phys. Rev. B* 78 235104 (2008)
- [5] G Makov and MC Payne, *Phys. Rev. B* 51 4014 (1995).
- [6] H Komsa and A Pasquarello, *Phys. Rev. Lett.* 110 095505 (2013)
- [7] I Dabo, B Kozinsky, N E Singh-Miller and N Marzari, *Phys. Rev. B* 77 115139 (2008).

### P:15 Monte Carlo simulations of electron transport in bulk GaN

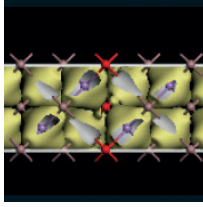
S Forster, B Ubochi and K Kalna

Swansea University, UK

Gallium Nitride (GaN) based transistors have become increasingly attractive for radio frequency (RF) and power applications due to their excellent material properties [1]. This has led to benefits in circuit performance and a reduction in both the size and the cost of RF and power electronic circuits. Although the desire for GaN based transistors, for example, the High Electron Mobility Transistors (HEMTs) has increased over the years, some reliability issues such as current collapse and the DC/RF dispersion persist. A physical understanding of the cause for these issues is difficult to obtain through experimental observations only. Consequently, the need for a physical based modelling is urgently needed. Physically based simulations are usually differentiated by their levels of accuracy and computational cost even other criteria might also play a role.

In this work, we have used the Monte Carlo (MC) transport model to study the effects of material parameters (which are not well known in the GaN) on electron transport in a bulk GaN. Additionally, we have studied the effects of impurity scattering on electron mobility. By assuming that the transport properties in the bulk GaN at high electron concentrations are similar to that of the two-dimensional electron gas (2DEG) [2], we expect that the data we obtain can easily be used to accurately predict the DC and RF performance of GaN based HEMTs.

The band structure of GaN we have considered comprises of a four-valley model of the conduction band namely the  $\Gamma_1$ , U,  $\Gamma_3$  and K valleys as shown in Fig. 1. In the models, we have assumed an anisotropic non-parabolic approximation of the band structure. In general, we thus consider GaN in wurtzite phase using parameters reported in Ref. [3] with the addition of the K valley. Fig. 2 compares the variation of drift velocity with the applied electric field. Our results are in a good agreement with experimental data [4] and other MC simulations [4, 5]. Furthermore, we have varied the dislocation density in order to study the effect of a dislocation scattering on the electron drift velocity. We report in Fig. 2 that increasing the dislocation density by an order of magnitude reduces the saturation velocity by half although the peak drift velocity appears to be unaffected. Fig. 3 shows the gradual reduction in mobility, from a steady mobility of approximately  $600 \text{ cm}^2\text{V}^{-1}\text{s}^{-1}$  to almost zero when the ionised impurity concentration exceeds  $10^{17} \text{ cm}^{-3}$ . The mobility is observed to be approximately constant when the neutral impurity concentration is varied, fluctuating about an average value approximately of  $620 \text{ cm}^2\text{V}^{-1}\text{s}^{-1}$  (see Fig. 4) which agrees quite well with experimental measurements [2].



# International Workshop on Computational Nanotechnology

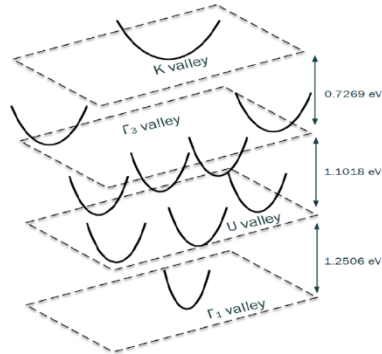


Figure 1: Band structure of Gallium Nitride indicating the four valleys that have been considered in our simulations.

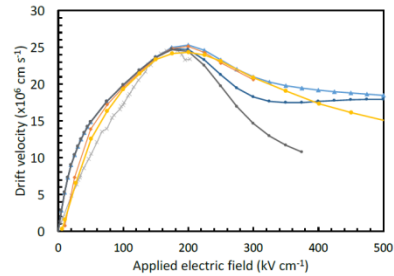


Figure 2: Electron drift velocity as a function of applied electric field in bulk GaN where the dislocation density has been increased by an order of magnitude comparing data from an ensemble Monte Carlo simulations to both experimental data [4] and other Monte Carlo simulations [3, 5].

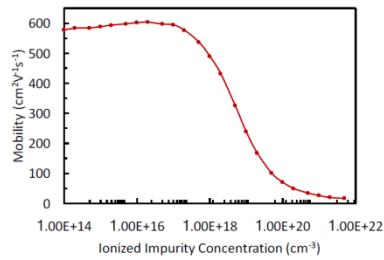


Figure 3: Electron mobility as a function of ionized impurity concentration in bulk GaN obtained from our ensemble Monte Carlo simulations.

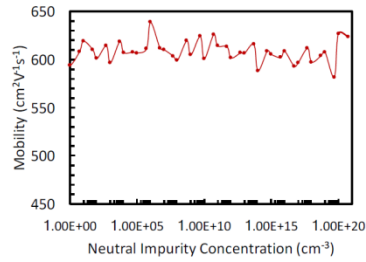
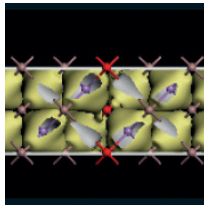


Figure 4: Electron mobility as a function of neutral impurity concentration obtained from our ensemble Monte Carlo simulations showing variations of the runs since the neutral impurity scattering has negligible effect on the mobility.

- [1] S. Faramehr, K. Kalna, and P. Igić, *Semicond. Sci. Technol.* 29, 25007 (11pp), Feb. 2014.
- [2] M. Shur, B. Gelmont, and M. A. Khan, *J. Electron. Mater.* 25, 777-785, May 1996.
- [3] M. Aldegunde, A. Loureiro, B. Benbakhti, and K. Kalna, in *Proc. UK Semiconductors*, Jul. 2010.
- [4] J. M. Barker, D. K. Ferry, D. D. Loleske, and R. J. Shul, *J Appl. Phys.* 97, 063705, 2005.
- [5] S. Yamakawa, R. Akis, N. Faralli, M. Saraniti, and S. M. Goodnick, *J. Phys.: Condens. Matter*, 21, 174206 (16pp), 2009.



## P:16 Scaling of Tunnel FETs

K Fukuda, H Asai, J Hattori, Y Morita, T Mori, W Mizubayashi, M Masahara, S Migita, H Ota, K Endo and T Matsukawa

National Institute of Advanced Industrial Science and Technology (AIST) Japan

Scaling of tunnel FETs is discussed using device simulation with nonlocal band-to-band tunneling model. Impacts of channel length, drain dopant level, SOI (or Fin) thickness are systematically investigated. The effects of the scaling are quite different from those of conventional MOSFETs, especially for their channel thickness dependence.

Tunnel FET (TFET) is a potential candidate for the low power transistor as an alternative to a MOSFET [1]. The authors developed several types of TFETs on matured silicon technology. These TFETs are successfully modeled by device simulation with the nonlocal band-to-band tunneling (BTBT) model [2][3], and recently, the drain bias dependence of long channel TFET characteristics is well explained by the same approach [4]. These series of studies are the base for further investigations of the scaling of TFETs, which is an important issue to determine the future of TFETs.

Fig. 1 shows the cross sections of p-type silicon (a) SOI and (b) Fin TFETs discussed in this work. For simplicity, source and drain junctions are at the gate edges, channel dopant is constant and weakly p-type, effective oxide thickness is 1 nm, the supply voltage is 0.5 volt. The nonlocal BTBT model is implemented as in ref. [1]. The drain bias dependence of an SOI TFET with a gate length of 500 nm is shown in Fig. 2, and the physics behind the dependence is discussed in ref. [4].

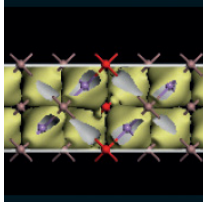
Gate length dependence of the SOI TFET  $I_D$ - $V_G$  characteristics is shown in Fig. 3. Below 10 nm, the source-to-drain direct tunneling is caused which cannot be controlled by gate voltage. This punch-through between source and drain may be weakened by low drain dopant concentration, such as  $10^{18}$  cm<sup>-3</sup>, but not so effectively.

Fin-TFET realizes the double current compared with the SOI-TFET both for on-current ( $I_{ON}$ ) and off-current ( $I_{OFF}$ ) as shown in Fig. 4 (a). Fin-thickness dependence is also shown in Fig. 4 (a), where ( $I_{OFF}$ ) increases more than  $I_{ON}$  for thinner fins. In Fig. 4 (b), the same curves are adjusted to the same  $I_{OFF}$ 's by changing the gate work-functions. The  $I_{ON}$  increases for the same  $I_{OFF}$  for fin thicknesses below 10 nm.

Fig. 5 shows fin thickness dependence of gate length 10 nm TFETs. The fin thickness scaling is not so effective in suppressing the short channel punch-through.

Fig. 6 shows two-dimensional distribution of the BTBT generation rates for the gate length of 30 nm and the fin thickness of 5 nm. Hole generation rate peaks for the front and the back gates are located nearly at the center of the fin thickness, and the electric field becomes larger under the control of the front and back gates.

Effects of TFET device scaling are studied using device simulation. Channel length affects  $I_{ON}$  -  $I_{OFF}$  below 20 nm, and source-to-drain punch-through occurs below 10 nm. In Fin-type TFETs,  $I_{OFF}$  increases for thinner Fin above 20 nm more than  $I_{ON}$ . When  $I_{OFF}$  is adjusted,  $I_{ON}$  increases for fin thickness below 7 nm. However the fin thickness scaling is not effective for short channel punch-through of gate length below 10 nm. Thus TFET-scaling is quite different from MOSFET-scaling.



# International Workshop on Computational Nanotechnology

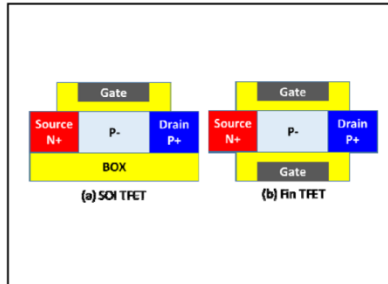


Fig. 1. Schematics of (a) SOI and (b) Fin TFETs studied in this work.

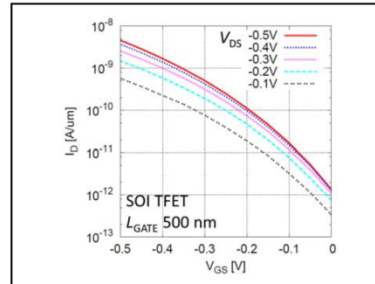


Fig. 2. Drain bias dependence of  $I_D$ - $V_G$  characteristics of an SOI TFET of a 500 nm gate length.

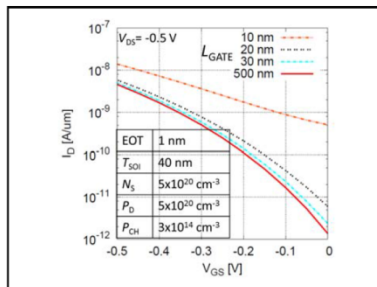


Fig. 3. Channel length dependence of  $I_D$ - $V_G$  characteristics of the SOI-TFET.

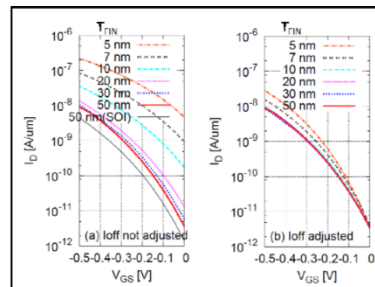


Fig. 4. Thickness dependence of Fin TFET characteristics (a) without and (b) with  $I_{off}$  adjustment.  $L_{GATE}$  is 500 nm.

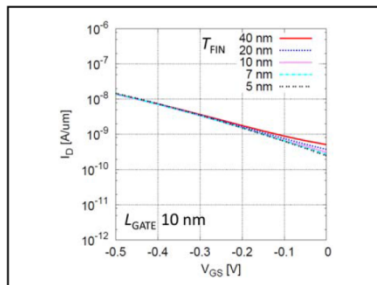


Fig. 5. Fin thickness dependence of Fin TFET with gate length of 10 nm. Short channel punch-through is not suppressed effectively by fin-thickness scaling

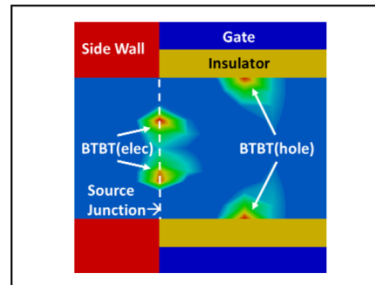
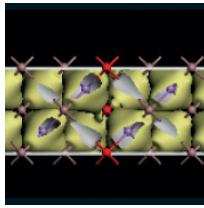


Fig. 6. 2D distribution of the BTBT generation rates for  $L_{GATE}=30$  nm and  $T_{FIN}=5$  nm case. The gate and drain voltages are -0.5 V.

- [1] Ionescu, A. M., and H. Riel, Nature 479.7373, 2011.
- [2] K. Fukuda et al. "On the nonlocal modeling of tunnel-FETs." SISPAD, 2012.
- [3] K. Fukuda et al. "Predictivity of the non-local BTBTmodel for structure dependencies of tunnel FETs." IWCE, 2014.
- [4] K.Fukuda et al., "On the drain bias dependence of tunnel FETs," Proc. SSDM, 2016.



## P:17 Monte Carlo analysis of impact ionization processes and band-to-band tunneling in In<sub>x</sub>Ga<sub>1-x</sub>As PIN ungated devices

B G Vasallo<sup>1</sup>, T González<sup>1</sup>, V Talbo<sup>2</sup>, Y Lechoux<sup>3</sup>, N Wichmann<sup>3</sup>, S Bollaert<sup>3</sup> and J Mateos<sup>1</sup>

<sup>1</sup>Universidad de Salamanca, Spain, <sup>2</sup>Université Grenoble Alpes INAC-PHELIQS, France, <sup>3</sup>Institute d'Électronique, France

Impact-ionization (II) metal-oxide-semiconductor FETs (I-MOSFETs) [1] are in competition with tunnel-FETs (TFETs) [2] to achieve the best behavior for ultra-low subthreshold-swing (SS) logical circuits. In particular, narrow-bandgap III-V I-MOSFETs are being explored as promising devices because of the low values of SS and ON-state drain-to-source voltage  $V_{DS}$ . However, in III-V structures band-to-band tunneling emerges for lower applied  $V_{DS}$  than II processes, thus hindering the development of III-V I-MOSFETs.

In order to facilitate the design process of III-V I-MOSFETs from the physical point of view, this work reports the development of a Monte Carlo (MC) simulator able to reproduce the internal quantities of ungated diodes at the basis of I-MOSFETs or TFETs. Our simulator incorporates the II events by means of the Keldysh approach [3], where the probability per unit time of having an II process is  $P(E) = S [(E - E_{th})/E_{th}]^2$  when  $E > E_{th}$ ,  $E$  being the electron kinetic energy,  $E_{th}$  the ionization threshold energy and  $S$  a measure of the softness or hardness of the threshold. To take into account band-to-band tunneling, the transmission coefficient  $T_C$  along the longitudinal dimension is determined for each energy following the Wentzel-Kramers-Brillouin (WKB) method, considering the shape of the energy barrier provided by MC simulations [4]. The expression for the transmission coefficient involves a global proportionality constant  $K$  that includes, among other quantities, the electron and hole effective masses during the tunnel transmission and the Richardson constant [4]. Both  $S$  and  $K$  are typically considered as adjustable parameters to reproduce the experimental I-V curves. This MC model has been validated by comparison with the experimental measurements of an ungated In<sub>0.53</sub>Ga<sub>0.47</sub>As 100 nm PIN diode, using  $S=2 \times 10^{12} \text{ s}^{-1}$  for  $P(E)$  and  $K=10^{21} \text{ Am}^{-1} \text{ s}^{-1}$  for  $T_C$ .

The internal quantities of In<sub>0.53</sub>Ga<sub>0.47</sub>As, In<sub>0.7</sub>Ga<sub>0.3</sub>As and InAs ungated PIN devices have been evaluated considering tunnel events or II processes independently, at the onset of the ON-state current. To illustrate these results, Fig. 1 presents the MC values of the number of electron-hole pairs generated by tunnel events or II processes and the energy bands for -3.1 V applied to the In<sub>0.7</sub>Ga<sub>0.3</sub>As structure. Tunneling, linked to the shape of the energy bands, is responsible for the onset of  $I_{ON}$ , the threshold voltage  $V_{T,tunnel}$  being about -2.8 V, much lower than that found for In<sub>0.53</sub>Ga<sub>0.47</sub>As, around -3.8 V. When considered in the simulations, II processes, originated by electrons coming from the p-side of the device, take place mainly in the n-side of the intrinsic area and the n+ region. The value of  $V_T$  linked to II events is  $V_{T,II} \sim -3.1 \text{ V}$ , while in the In<sub>0.53</sub>Ga<sub>0.47</sub>As structure no current due to II processes is found at least up to -5.0 V when only II is considered. In case II and tunnel processes are jointly accounted for in the simulations, II processes do take place for  $x=0.53$ , triggered by tunneled carriers. Interestingly, when increasing the proportion of In, thus reducing the bandgap, the decrease in  $V_{T,II}$  is much more pronounced than that in  $V_{T,tunnel}$ . Semiconductors with lower bandgap, as InAs and InSb, must be analyzed to check if II can dominate the onset of the current.

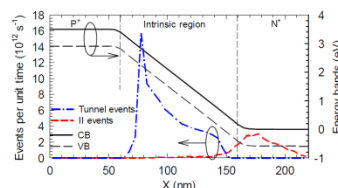
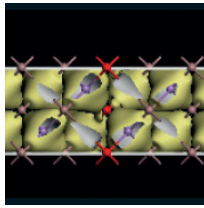


Fig. 1. MC values of the electron-hole pairs generated by tunnel events or II processes curves per unit time and energy bands for -3.1 V for the In<sub>0.7</sub>Ga<sub>0.3</sub>As 100 nm PIN diode, being  $S=2 \times 10^{12} \text{ s}^{-1}$  and  $K=10^{21} \text{ Am}^{-1} \text{ s}^{-1}$ .



## International Workshop on Computational Nanotechnology

- [1] Q. Huang, R. Huang, Z. Wang, Z. Zhan and Y. Wang, Appl. Phys. Lett., 99, 083507 (2011)
- [2] W.Y. Choi, J.Y. Song, J.D. Lee, Y.J. Park and B.-G. Park, IEEE IEDM, 955 (2005)
- [3] B. G. Vasallo, J. Mateos, D. Pardo and T. González, J. Appl. Phys. 94, 4096 (2003)
- [4] D. Moro-Melgar, J. Mateos, T. González and B. G. Vasallo, J. Appl. Phys., 116, 234502 (2014)

### **P:18 Multi-scale nonequilibrium green's function method for LEDs: Balance of thermalization and tunneling**

J Geng<sup>1</sup>, P Sarangapani<sup>1</sup>, B Browne<sup>2</sup>, C Wordelman<sup>2</sup>, E Nelson<sup>2</sup>, T Kubis<sup>1</sup> and G Klimeck<sup>1</sup>

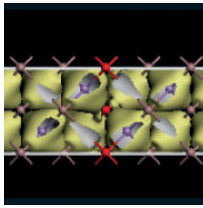
<sup>1</sup>Purdue University, USA <sup>2</sup>Lumileds, USA

GaN/InGaN multi-quantum-well (MQW) structures are the core technology of most mid-to-high power blue light-emitting diodes (LED). Their optimization requires a quantitative understanding of the nanoscale carrier flow. Typical LEDs are characterized by high carrier density regions such as n-GaN/p-GaN leads and InGaN quantum wells (QW). The charge transport is based on both tunneling and thermionic emission. In this work, a multi-scale quantum transport model for efficient and quantitative modeling of a commercial LED is applied [1,2] and augmented to include nonlocal quantum effects. This method is based on the nonequilibrium Green's function (NEGF) formalism to compute the dynamics (states) and the kinetics (filling of states) in the entire extended complex device. The model results agree with experimental I-V curves quantitatively. In this work, we provide a quantitative assessment of long-range tunneling in LEDs. II.

The methodology is based on carrier scattering versus carrier tunneling oriented partitioning of the device as shown in Fig. 1. The n-GaN/p-GaN layers and QWs have extremely high carrier densities. Since the carrier scattering is very strong in these regions, they are considered local equilibrium carrier reservoirs with local quasi Fermi levels. In each reservoir, an imaginary optical potential ( $\eta = 0.1\text{eV}$  according to photoluminescent (PL) measurements [3]) is included in the diagonal of the Hamiltonian [4] to mimic the scattering. Current conservation is ensured by self-consistently solving the local Fermi levels [2]. Figure 1 shows all current paths through barrier #4 as an example. In the previous work, all the current paths coupling more than two QW were not considered. In this work, the model is expanded to allow for transport current coupling multiple QWs. 'Hot carrier' formation is allowed in this way. III.

The model is applied to simulate a commercial GaN/InGaN blue LED (see Fig. 1). Figure 2 plots the electron and hole densities with band diagrams and local Fermi levels. Electrons are well transported across the MQW, as indicated by low Fermi level drop ( $\sim 25\text{meV}$ ) and well spread-out carrier distribution. In contrast, the hole Fermi level drop ( $\sim 180\text{meV}$ ) is much larger and as a result the hole distribution is skewed towards the p-side. A realistic ( $0.1\text{eV}$ ) and a reduced ( $0.01\text{eV}$ )  $\eta$  value were simulated and compared. For each  $\eta$ , two sets of simulations were performed. The first set (denoted as 'short') includes only nearest neighbor QW currents. The second set (denoted as 'long') includes all transport components across different QWs. Larger  $\eta$  leads to higher thermionic emission due to more broadened states. The majority of current conduction occurs below the barriers, and decays significantly with longer coupling range. Figure 3 and 4 compares the I-V and internal quantum efficiency (IQE) for different  $\eta$  values and coupling ranges. For larger  $\eta$ , the IQE droops became worse. This is because higher scattering reduces the mobility in the QWs, which leads to more holes piling up at the p-side (see Fig. 2) and thus increases nonradiative losses. The I-V at  $0.1\text{eV}$  agrees quantitatively with experimental results. The effect of long-range coupling is only observable at low scattering case ( $\eta=0.01\text{eV}$ ). Realistic thermalization in LEDs prevent the hotcarrier formation.

An efficient, multi-scale NEGF based transport model was applied on a commercial LED structure. Complete thermalization in the LED QWs has been confirmed. Reducing the scattering rate by 1 order of magnitude, however, allows for the formation of 'hot carriers' due to long range tunneling.



# International Workshop on Computational Nanotechnology

Fig. 2. (a) Conduction band profile with electron density and (b) valance band profile with hole density for  $\eta=0.1\text{eV}$ . Note that local Fermi levels (red dashed lines) are only defined in the equilibrium regions of Fig. 1 only. The Fermi level lines are meant to guide the eye.

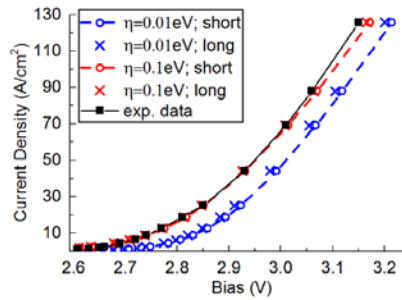


Fig. 3. I-V characteristics with different scattering strengths ( $\eta$ ) and tunneling ranges (short vs. long). Larger  $\eta$  suppresses long-range tunneling and long range tunneling can be neglected. The simulated I-V at  $\eta = 0.1\text{eV}$  agrees quantitatively with experimental results (black squares).

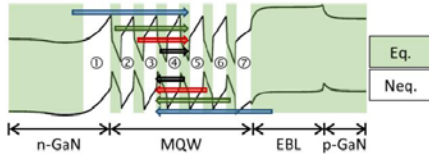


Fig. 1. LED structure considered in this work. Equilibrium (eq - green) and non-equilibrium (neq - white) regions are highlighted. As an example, various tunneling paths through barrier #4 are illustrated with arrows of different colors.

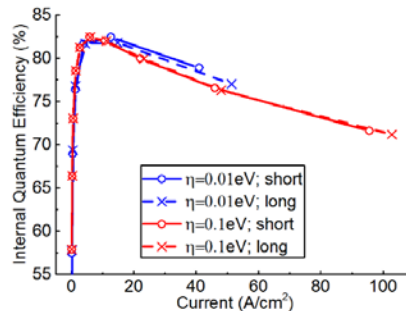
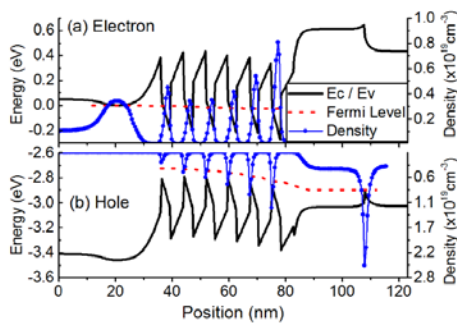
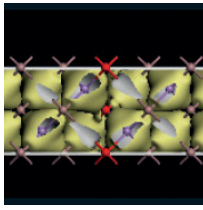


Fig. 4. Internal quantum efficiency (IQE) with different scattering strengths ( $\eta$ ) and tunneling ranges. Carriers become more thermalized at higher values of  $\eta$ . This yields charge accumulation at p-side and causes the efficiency droop.

- [1] J. Geng, et al., Proceedings of the 16<sup>th</sup> International Conference on Numerical Simulation of Optoelectronic Devices, 107, (2016).
- [2] J. Geng, et al., Proceedings of SPIE Photonics West 2017, accepted.
- [3] O'Donnell, et al., Appl. Phys. Lett. 70, 1843, (1997).
- [4] Gerhard Klimeck, et al., Appl. Phys. Lett. 67, 2539, (1995).
- [5] J. Fonseca, et al., J. of Comput. Elec. 12, 592, (2013).



# International Workshop on Computational Nanotechnology

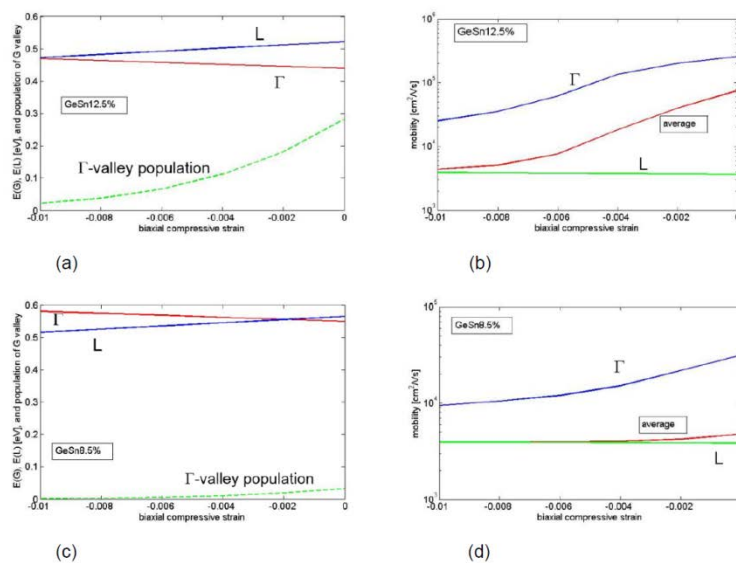
## P:19 Electron and hole mobility calculation in GeSn alloys

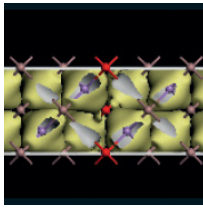
Z Ikonić

University of Leeds, uk

The recent advances in growth of group-IV (SiGeSn) materials are primarily directed towards their photonics applications, taking advantage of the direct band gap achievable for suitable composition and strain conditions. However, there are also good prospects of using these materials for electronic devices, where the band gap directness also offers distinct advantages (a higher electron mobility) over what is achievable in indirect gap alloys, accompanied with the benefits coming from mature and cost-effective fabrication on Si platform. Increased electron mobility is expected in direct-gap alloys because of a considerably lower  $\Gamma$ -electron effective mass in GeSn, compared to mass in Ge. Mobility is influenced by both the material composition and strain, and one way of using SiGeSn is as stressor material, to control the mobility in Ge, and the other would use it as active (conducting) material in CMOS type devices.

Here we present results of both electron and hole mobility calculation in GeSn bulk alloys. The band structure was calculated using effective mass with nonparabolicity for the conduction band indirect valleys, and 8-band k.p method [1], stabilised against spurious solutions, for holes and  $\Gamma$ -electrons, and linear deformation potentials in both cases. Mobility is then calculated in the conventional way [2,3], by finding the momentum relaxation times of carriers, due to: acoustic phonon, optical phonon (deformation potential), intervalley scattering, alloy disorder and ionised impurity scattering (however, scattering on defects / dislocations was not included because of insufficient data available, so the results may be somewhat optimistic). Examples of the dependence of mobility on alloy composition, strain, and doping density are given in Fig.1(a-f) for electrons and Fig.1(g,h) for holes. Generally, the mobility of  $\Gamma$ -electrons, and then also the average mobility, is indeed found to be very high provided the alloy is strongly direct, i.e. that the L valley is well above the  $\Gamma$ -valley, primarily because this suppresses strong intervalley  $\Gamma$ -L scattering. Aside from this effect, the alloy composition does not have a major influence because the alloy disorder does not give a very strong contribution to total scattering. In case of holes, the mobility primarily benefits from strain, either compressive or tensile, by removing the HH-LH scattering, while the alloy composition has a smaller influence.





# International Workshop on Computational Nanotechnology

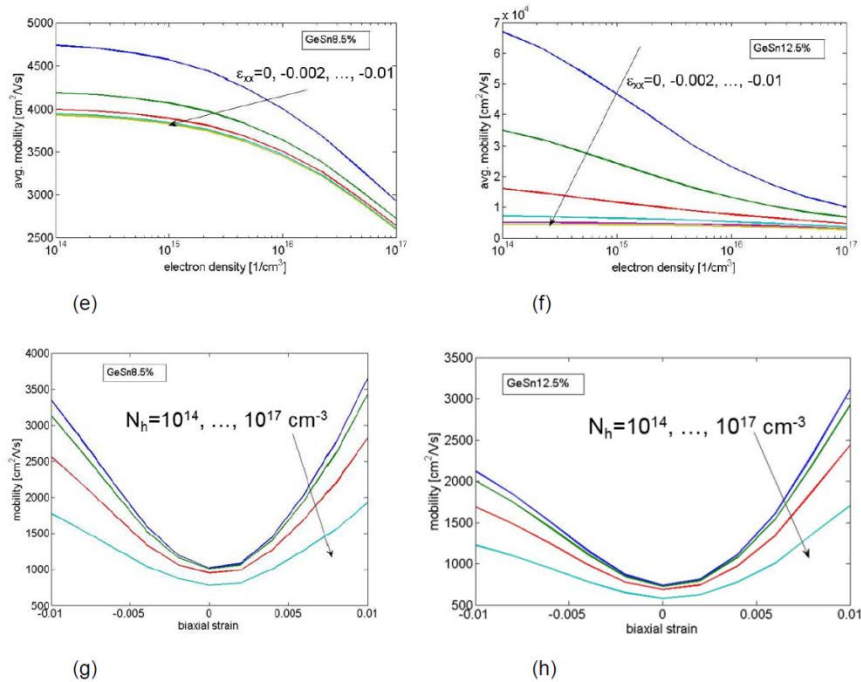


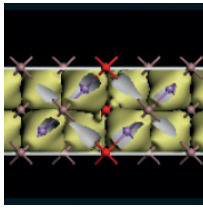
Fig. 1. (a,c) GeSn c.b. valley edges (solid) and  $\Gamma$ -population (dashed), low-density electron mobility (b,d), its dependence on electron density (e,f), and hole mobility (g,h) in strained GeSn at  $T=300\text{K}$ .

## P:20 Transport modelling and design of GaN/AlN based unipolar (opto-)electronic devices, and interface quality effects

A Grier<sup>1</sup>, A Valavanis<sup>1</sup>, C Edmunds<sup>2</sup>, J Shao<sup>2</sup>, J D Cooper<sup>1</sup>, G Gardner<sup>2,3</sup>, M J Manfra<sup>2,3</sup>, O Malis<sup>2</sup>, D Indjin<sup>1</sup>, Z Ikonjić<sup>1</sup> and P Harrison<sup>4</sup>

<sup>1</sup>University of Leeds, UK, <sup>2</sup>Purdue University, USA, <sup>3</sup>Birck Nanotechnology Center, USA, <sup>4</sup>Sheffield Hallam University, UK

The AlGaN/GaN material system has been proposed as a highly promising alternative to more conventional III-V's for various optoelectronic devices, e.g. quantum cascade lasers (QCL), photodetectors and electronic devices like resonant tunnelling diodes (RTD). The high LO-phonon energy in GaN should significantly reduce the thermal degradation effects coming from phonon-assisted relaxation, which could allow lasing at higher THz frequencies, and higher operation temperature [1]. A detailed understanding of electron transport in AlGaN/GaN heterostructures is crucial for optimizing devices performance. RTDs are interesting in their own right, and also as the simplest devices in which vertical tunneling and scattering transport can be investigated, both experimentally and theoretically: the experience can then be transferred to the design of more complicated devices. We have therefore investigated electron transport in epitaxially grown nitride-based RTDs, as well as in sequential tunneling devices [2]. The density-matrix model developed for this purpose is shown to be able to reproduce the experimental I-V characteristics. Scattering-induced broadening effects (largely coming from interface roughness) are found to have a strong influence on current magnitude and peak-to-valley ratios, highlighting critical optimization parameters for III-nitride unipolar electronic and optoelectronic devices. Investigation of AlGaN QCLs, also performed by the density matrix method, shows that a realistic level of interface roughness (found from RTD modelling) would degrade the



# International Workshop on Computational Nanotechnology

gain and operating temperature of some previous designs. These can be improved by a structure optimization, based on a genetic algorithm [3], however further improvements of the material quality are essential for III-nitride QCLs to demonstrate their full potential.

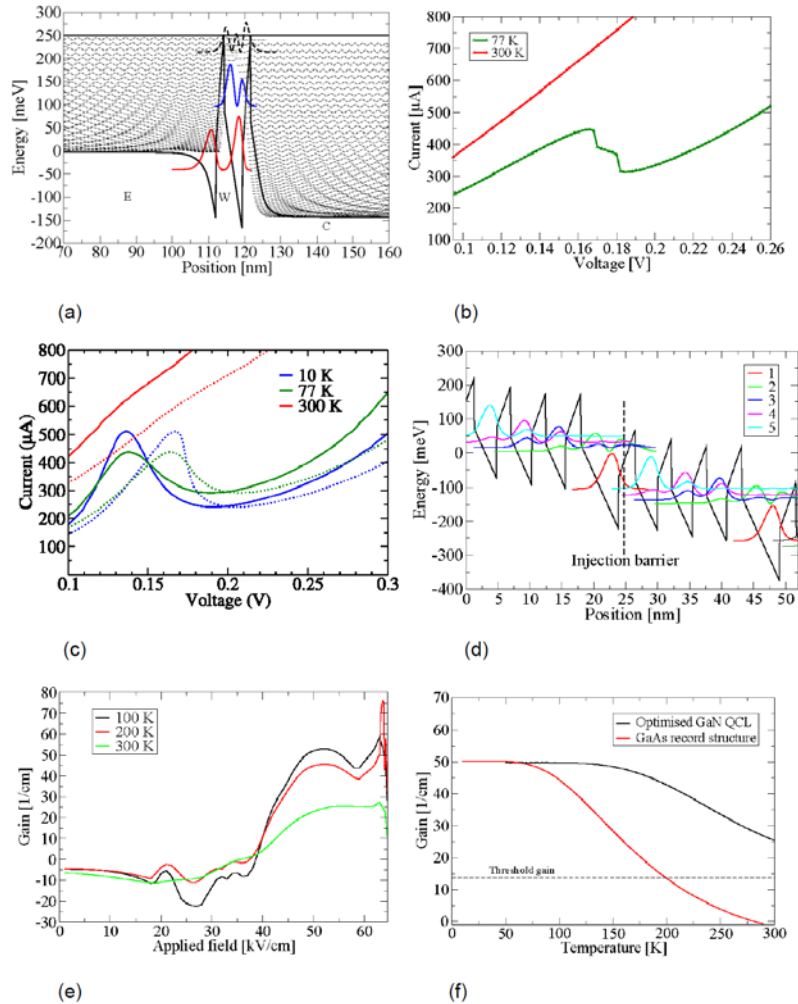
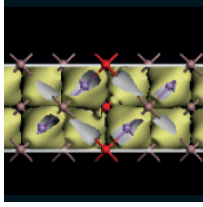


Fig.1. (a)  $\text{Al}_{0.18}\text{Ga}_{0.82}\text{N}(4.9\text{nm})/\text{GaN}(2.4\text{nm})$  RTD structure and states, (b) measured and (c) calculated I-V characteristics for the interface roughness parameters  $\Lambda=10\text{nm}$  and  $\Delta=0.28\text{nm}$ , (d) optimised  $2.6/3.5/2.2/3.3/2.2/3.1/2.4/5.9\text{nm}$  ( $\text{Al}_{0.08}\text{Ga}_{0.92}/\text{GaN}$ ) QCL structure, its calculated (e) gain-bias, and (f) gain-temperature dependence.

- [1] E. Bellotti, K. Driscoll, T. D. Moustakas, and R. Paiella, "Monte Carlo study of GaN versus GaAs terahertz quantum cascade structures," *Appl. Phys. Lett.*, 92, 101112 (2008).
- [2] A. Grier, A. Valavanis, C. Edmunds, J. Shao, J. D. Cooper, G. Gardner, M. J. Manfra, O. Malis, D. Indjin, Z. Ikonić, and P. Harrison, "Coherent vertical electron transport and interface roughness effects in AlGaIn/GaN intersubband devices", *J. Appl. Phys*, 118, 224308 (2015).
- [3] A. Grier, "Modelling the optical and electronic transport properties of AlGaAs and AlGaIn intersubband devices and optimisation of quantum cascade laser active regions", PhD Thesis, University of Leeds, 2015.



# International Workshop on Computational Nanotechnology

## P:21 Investigation of hot-carrier effects using a backward Monte Carlo method and full bands

M Kampl and H Kosina

TU Wien, Austria

Degradation models for MOSFETs require accurate knowledge of the carrier distribution function which is determined by the Boltzmann equation. This equation can be solved by the Monte Carlo method. However, calculation of the high-energy-tail of the carrier distribution which requires the simulation of statistically rare events often poses a problem on the standard Monte Carlo methods. Using a backward Monte Carlo algorithm it is possible to selectively simulate the rare events of interest and to avoid simulation of the uninteresting common events. A stable backward Monte Carlo algorithm has been implemented in a full-band Monte Carlo code and its properties have been analyzed. High-energy tails of the distribution function and I/V curves in the sub-threshold regime can be easily calculated with this new method.

The physically transparent and commonly used forward Monte Carlo (FMC) method produces a large statistical error when used for the simulation of statistically rare events. In the field of semi-classical transport, the backward Monte Carlo (BMC) method has been proposed at the end of the 1980's [1] [2]. These early algorithms turned out to be numerically unstable as the transition rates did not satisfy the principle of detailed balance. In 2003 a numerically stable algorithm was proposed [3]. Because now the backward transition rates obey the principle of detailed balance, a runaway of the energy along a backward trajectory is avoided. The BMC method uses the scattering rates of the FMC method [3] and can thus be easily implemented in an already existing Monte Carlo simulator, Vienna Monte Carlo (VMC).

The principle of the BMC method is to create a set of rare events in phase space, and to trace the trajectories back in time until they reach a contact. From the known distribution function (DF) at the contact the statistical weight of the backward trajectory, consequently its contribution to the estimator of interest, is determined.

### THE BACKWARD MONTE CARLO METHOD

A stable estimator for the DF in a given point  $(\vec{k}_0, \vec{r}_0)$  is given by [3]:

$$f(\vec{k}_0, \vec{r}_0) = \frac{1}{M} \sum_{i=1}^M f_b(\vec{k}_{b,i}, \vec{r}_{b,i}) e^{\sum_j \Delta E_j / k_B T}, \quad (1)$$

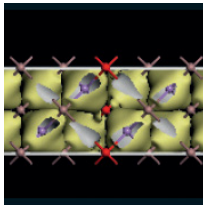
where  $f_b$  represents the boundary distribution at the contact,  $M$  is the number of backward trajectories injected at the point  $(\vec{k}_0, \vec{r}_0)$  and  $\sum_j \Delta E_j$  is the sum of all energy changes due to phonon emission and phonon absorption processes.

This approach allows one to calculate the DF in only one point of the device, neglecting all other trajectories which do not pass through that point. Monte Carlo estimators for statistical averages of the form

$\langle A \rangle = \int A(\vec{k}_0, \vec{r}_0) f(\vec{k}_0, \vec{r}_0) d^3 k d^3 r$  can be derived from (1) straightforwardly.

We investigated a 65 nm MOSFET presented in [5].

To calculate the current, we generate the states  $\vec{k}_0$ , from a Maxwellian distribution at different temperatures and the positions  $\vec{r}_0$  in the channel cross section where the energy barrier has its maximum. The BMC method allows to compute the whole I/V curve, including the sub-threshold region as shown in Figure 1. The statistical error of the current as a function of the injection temperature is plotted in Figure 2. While the estimated current is independent of this temperature, the statistical error shows a clear minimum where the



# International Workshop on Computational Nanotechnology

injection distribution most closely resembles the real distribution. The energy distribution is calculated point-wise in energy at some fixed locations at the interface, see Figure 3.

Additionally, a combined backward-forward MC (BFMC) method has been developed. After having calculated a backward trajectory from the starting point  $\vec{k}_0, \vec{r}_0$ , a weighted forward trajectory is started from that point as well, see Figure 4. The combined backward-forward technique has been used to calculate the acceleration-integral employed for hot-carrier degradation modeling, see Figure 5.

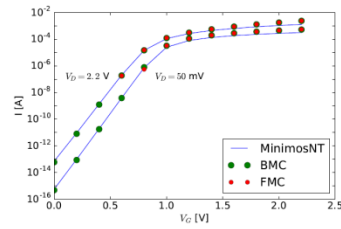


Fig. 1. Transfer characteristics of an nMOS device, simulated with MinimosNT [4] (drift-diffusion), the FMC and BMC methods. Drain voltage is varied between 2.2 V and 50 mV. Each point of the Monte Carlo methods is calculated with  $10^6$  trajectories.

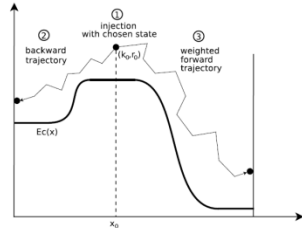


Fig. 4. Principle of the BFMC method for a MOSFET. The injected particle has a chosen state in  $r$ - and  $k$ -space. It is traced back in time to its origin to calculate the weight (probability) of itself. The observables are calculated from the weighted forward trajectory.

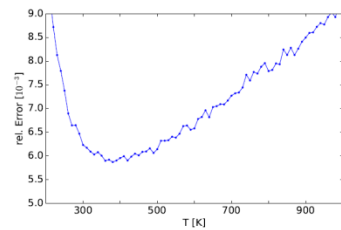


Fig. 2. Relative error of the BMC estimator on a 65 nm nMOS channel at  $V_{GS} = 0.6$  V and  $V_{DS} = 2.2$  V with different injection temperatures.

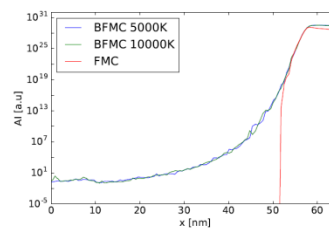


Fig. 5. The results of the acceleration integral [5] from two BFMC simulations, at different injection temperatures, and one FMC simulation with  $10^{10}$  scattering events were compared with each other. Furthermore the graph shows that the backwards estimator is independent of the injection temperature.

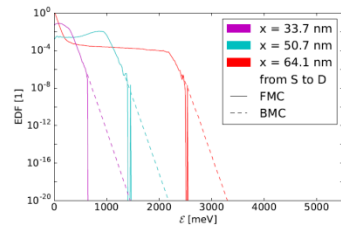
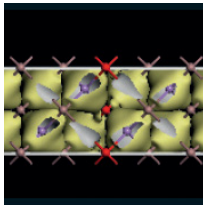


Fig. 3. Energy distribution at some cuts through a 65 nm nMOS channel at  $V_{GS} = 2.2$  V and  $V_{DS} = 2.2$  V. Solid lines show FMC at with  $10^{10}$  scattering events. Dashed lines show BMC with  $10^4$  trajectories per energy point.

- [1] C. Jacoboni, P. Poli, and L. Rota, "A new Monte Carlo technique for the solution of the Boltzmann transport equation," *Solid-State Electron*, vol. 31, no. 3/4, pp. 523 – 526, 1988.
- [2] M. Nedjalkov and P. Vitanov, "Iteration approach for solving the Boltzmann equation with the Monte Carlo method," *Solid-State Electron*, vol. 32, no. 10, pp. 893 – 896, 1988.
- [3] H. Kosina, M. Nedjalkov, and S. Selberherr, "A Stable Backward Monte Carlo Method for the Solution of the Boltzmann Equation," in *Lecture Notes in Computer Science*, vol. 2907. Springer, 2003, pp. 170–177.
- [4] *Minimos-NT User Manual - Release 2016.09*. [Online]. Available: [www.globaltcad.com](http://www.globaltcad.com)
- [5] S. E. Tyaginov, M. Bina, J. Franco, D. Osintsev, O. Triebel, B. Kaczer, and T. Grassler, "Physical Modeling of Hot-Carrier Degradation for Short- and Long-channel MOSFETs," in *Conference Proceedings of International Reliability Physics Symposium*, 2014, pp. XT16.1 – XT16.8.



# International Workshop on Computational Nanotechnology

## P:22 Lindblad-based Markov approach to spatiotemporal quantumdynamics of wave packets in nanostructures

F Lengers, R Rosati, T Kuhn and D E Reiter

Universität Münster, Germany

The ultrashort time and length scales involved in carrier dynamics like carrier capture or ultrafast and highly localized optical generation inside a nanostructure call for a suitable quantum mechanical treatment of the dynamics. Fully quantum mechanical treatments like quantum kinetic approaches [1] describe these processes very well, but are limited to low-dimensional systems or systems with sufficiently high symmetry as well as rather short times. Those limitations result from the computational complexity as well as from instabilities due to interference phenomena of the dynamical variables. Those problems call for a suitable approximation scheme. We here introduce a Lindblad single-particle (LSP) equation of motion, which is obtained by a proper tailoring [2] of the superoperator provided by a recently introduced Markov approach [3,4]. Although in general nonlinear, the latter is still able to preserve the positivity of the density matrix in any circumstance, in contrast to conventional Markov approximations [4].

In this contribution we will discuss the dynamics of traveling wave packets in a semiconductor quantum wire with an embedded quantum dot under the influence of carrier-light, carrier-carrier and carrier-phonon interaction. During the local optical excitation localized electron and hole wave packets are generated. Because of the spatial localisation, the description of the wave packet dynamics in the density matrix formalism includes both occupations of the quantum wire states and coherences between the states, i.e. diagonal and off-diagonal elements of the density matrix. The excited electron and hole wave packets then travel along the quantum wire with velocities depending on the respective effective masses and excess energy of the optical pulse whilst being subject to interactions. These interaction processes lead to transitions between the quantum wire states, which affects both occupations and coherences. When an embedded quantum dot inside the quantum wire is present the carrier-phonon interaction leads to capture processes into the localized states. We study the carrier capture using the LSP approach and compare it to a quantum kinetic (QK) approach. We show that the essential features of the carrier capture process are well described by the LSP approach (Fig. 1, left panel) when compared to the QK approach (Fig. 1, right panel) while the computational complexity is greatly reduced.

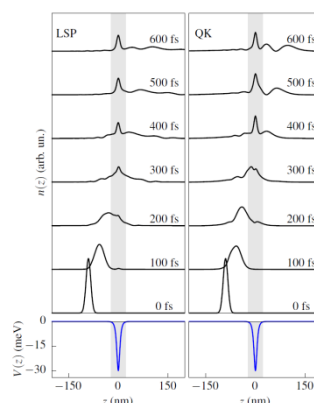
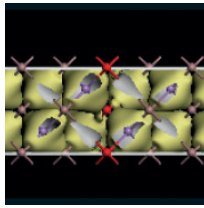


Figure 1: Comparison of electron density dynamics. The solid lines in the two upper panels show the dynamics when carrier-phonon interaction is considered within the Lindblad based approach (LSP, left panel) and the quantum kinetic approach (QK, right panel). The quantum dot is described by the potential depicted in the two lower panels.



# International Workshop on Computational Nanotechnology

- [1] D. Reiter et al., Phys. Rev. B 75, 205327 (2007).
- [2] R. Rosati et al., submitted.
- [3] D. Taj et al., Eur. Phys. J. B 72, 305-322 (2005).
- [4] R. Rosati et al., Phys. Rev. B 90, 125140 (2014).

## **P:23 Impact of the gate and external insulator thickness on the static characteristics of ultra-scaled silicon nanowire FETs**

D Logoteta<sup>1</sup>, N Cavassilas<sup>1</sup>, M Pala<sup>2</sup>, A Cresti<sup>3</sup> and M Bescond<sup>1</sup>

<sup>1</sup>Aix-Marseille Université, France, <sup>2</sup>Université Paris-Saclay, France, <sup>3</sup>Université Grenoble Alpes, France

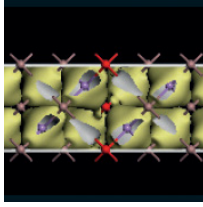
The geometries routinely considered for the numerical simulation of nanoelectronic devices within quantum self-consistent models do not result in a realistic description of the electrostatic potential in the insulator covering the access regions. The thickness chosen for this latter is indeed typically too small with respect to the decay length of electric field and the gate is modeled with thickless stripes, preventing any account for fringe fields. More realistic geometries are considered only in the framework of simpler transport models, in order to provide semianalytical descriptions of parasitics [1], [2], [3] or perform extensive explorations of the design parameter space [4], [5].

We propose a full quantum simulation study focusing on gate-all-around ultra-scaled silicon nanowire field effect transistors (NW FETs), aimed to investigate the impact of extending the simulation domain so as to include a larger part of the gate electrode and of the insulator enveloping the source and drain extensions.

Our simulation approach relies on an effective mass Hamiltonian fitted on tight-binding band structure computations [6] and is based on the self-consistent solution of the transport equations within the non-equilibrium Green's function formalism and of the Poisson equation. The electron scattering with acoustic and optical phonons is taken into account within the self-consistent Born approximation.

The geometries compared in this study are sketched in Fig. 1. The geometry A is the simplest and most widely used one, in which the gate corresponds to a wrapping surface belonging to the boundary of the simulation domain. On the contrary, the geometry B models the gate as a three-dimensional shell; the value of 5 nm set for its thickness has been verified to guarantee a reasonable stabilization of the results against any further increase. In order to investigate the interplay with different degrees of quantum confinement and short channel effects, we consider NW FETs with two different transversal crosssections (2x2 and 5x5 nm<sup>2</sup>), gate lengths (5 and 10 nm) and gate underlaps (0 and 3 nm).

Our results highlight deviations between the two models both in the subthreshold region and at large gate overdrives. As illustrated in Fig. 2 and in the top panel of Fig. 3, accounting for the fringe field of the gate in the B arrangement can dramatically improve the electrostatic integrity and consequently the subthreshold swing with respect to the A case. This effect is particularly pronounced in the wider and shorter devices, as a consequence of the less effective gate control. In the narrower devices, due to the weaker pinning in the doped source region, at large overdrive the gate fringes can induce a sizeable bottom shift in the lowest subband with respect to the A case (bottom panel of Fig. 3). This effect, stronger in the ballistic regime and quite weakly dependent on the gate length, results in an increase of the current in the B arrangement with respect to the A one. The overall impact on the estimation of the device performance for several representative configurations is summarized in Table 1, which indicates that the  $I_{ON}=I_{OFF}$  ratio computed with the A geometry can suffer from large underestimations as compared to the results obtained with the B geometry.



# International Workshop on Computational Nanotechnology

The discrepancies between the two models in terms of sensitivity to the discrete dopant variability are addressed in Fig. 4 and Fig. 5. Two arrangements of discrete dopants, denoted as (1) and (2), are considered, differing in the distance between the dopants and the gated region of the nanowires. The difference of the currents in the case (1) and (2) divided by their average is taken as a measure of the sensitivity of the devices. A close inspection of the curves in Fig. 5 for high values of the gate voltage indicates that the relative deviation of the sensitivity between the devices described with the model *A* or *B* can be significant.

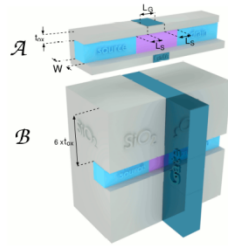


Fig. 1. Sketch of the considered geometries. SiO<sub>2</sub> is chosen as the insulator material. The gate oxide thickness is  $t_{ox} = 1$  nm. The source and drain extensions are 12 nm long and are n-doped with concentration  $10^{20}$  cm<sup>-3</sup>.  $L_G$  and  $L_S$  denote the gate and spacer length, respectively.

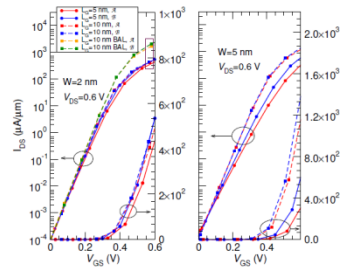


Fig. 2. Transfer characteristics for nanowires with  $W = 2, 5$  nm,  $L_G = 5, 10$  nm and  $L_S = 3$  nm. For the case  $W = 2$  nm and  $L_G = 10$  nm also the ballistic curves (BAL) are shown. All the curves have been horizontally shifted in order to set  $I_{DS} = I_{OFF} = 10^{-4}$   $\mu A/\mu m$  at  $V_{GS} = 0$  V.

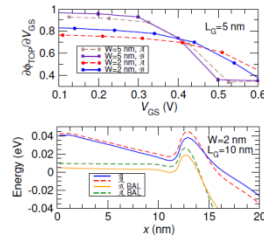


Fig. 3. *Top*: derivative of the potential  $\phi_{TOP}$  of the top of the source-to-drain barrier with respect to the gate voltage corresponding to some of the transfer characteristics in Fig. 2. *Bottom*: detail of the lowest subband in the source region corresponding to the points enclosed within a rectangle in Fig. 2. The subbands referring to the dissipative regime have been vertically shifted of 0.02 eV for clarity. The Fermi level at the source contact equals 0 eV.

	$L_G = 3$ nm		$L_G = 9$ nm	
	$L_C = 5$ nm	$L_C = 10$ nm	$L_C = 5$ nm	$L_C = 10$ nm
$W = 2$ nm	53%	28%	26%	10%
$W = 5$ nm	122%	117%	21%	29%

TABLE I  
PERCENTAGE INCREASE OF THE  $I_{ON}/I_{OFF}$  RATIO IN THE  $\mathcal{B}$  GEOMETRY WITH RESPECT TO THE  $\mathcal{A}$  ONE IN THE BALLISTIC (BAL) AND DISSIPATIVE (PHON) REGIME.  $I_{OFF}$  IS SET TO  $10^{-4}$   $\mu A/\mu m$ .

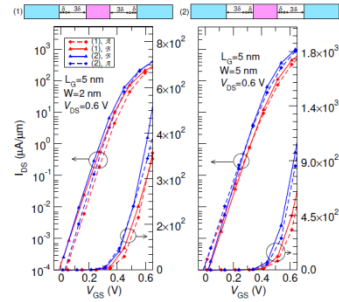


Fig. 4. Transfer characteristics for nanowires with  $W = 2, 5$  nm and  $L_G = 5$  nm in the presence of two discrete dopants at the center of the nanowire transversal cross-section, located symmetrically with respect to the gate. The top of the figure illustrates the two different arrangements considered, denoted by (1) and (2).  $\delta = 1.5$  nm. Each couple of curves ( $I_{DS}^{(1)}, I_{DS}^{(2)}$ ) referring to the same geometry has been horizontally shifted in order to set to  $10^{-4}$   $\mu A/\mu m$  the value of the arithmetical average  $(I_{DS}^{(1)} + I_{DS}^{(2)})/2$  at  $V_{GS} = 0$  V.

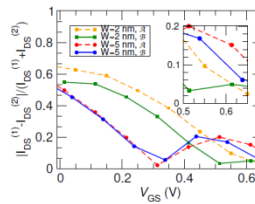
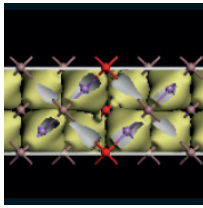


Fig. 5. Deviation of the value of the current relative to the average  $|I_{DS}^{(1)} - I_{DS}^{(2)}| / (I_{DS}^{(1)} + I_{DS}^{(2)})$  for the couples of transfer characteristics  $\{I_{DS}^{(1)}, I_{DS}^{(2)}\}$  in Fig. 4 referring to the same geometry and to a different arrangement of dopants. The inset shows an enlargement for high  $V_{GS}$ .

- [1] P. Liang et al., J. Phys. D Appl. Phys. 116, 215109 (2008).
- [2] S. Kim et al., IEEE-Trans. Electron Dev. 53, 2143 (2006).
- [3] S. Venugopalan et al., Solid State Electron. 67, 79 (2012).
- [4] A. Sachid et al., IEEE Electron Device Lett. 29, 128 (2008).
- [5] H. Zhao et al., IEEE-Trans. Electron Dev. 55, 1177 (2008).
- [6] K. Nehari et al., Solid State Electron. 50, 716 (2006).



# International Workshop on Computational Nanotechnology

## P:24 Towards a full self-consistently coupled drift diffusion and Monte Carlo simulator to model silicon heterojunction solar cells

P Muralidharan, S M Goodnick and D Vasileska

Arizona State University, USA

The Drift-Diffusion (DD) model has been extensively used to model solar cells of all types. This model provides an efficient and reasonably accurate way to simulate solar cells as long as the physics doesn't stray too far away from the assumptions used to derive the DD model. However, with the advent of 2nd and 3rd generation solar cells [1], novel device structures and new materials have tested the limits of traditional methods.

Our work focuses on an amorphous silicon (a-Si)/crystalline silicon (c-Si) heterojunction solar cell (SHJ), also referred to as a HIT cell [2]. The strong band bending and high electric field at the heterointerface of this cell leads to a non-Maxwellian energy distribution of photogenerated carriers [3]; this, in turn, violates some of the assumptions made in the derivation of the DD model from the Boltzmann transport equation (BTE). The DD model is not ideal for studying regions where the electric field varies rapidly over a very short distance; the distribution function becomes non local in such scenarios and the local electric field based description of the DD model is no longer applicable.

The Monte Carlo (MC) solution to the BTE is an ideal tool to study the distribution function in high field scenarios but has some limitations when it is considered as a global simulator. It becomes quite inefficient in regions where the field is low, whereas DD models can perform very efficiently and accurately in these areas. Thus, by coupling both these solvers it is possible to combine their advantages to create a computationally efficient and accurate solver [4].

Coupled DD and MC hybrid solvers have been implemented in the past to study hot carrier effects in MOSFET's [5]. In this paper we have utilized this concept to study high field effects and interfacial transport in a SHJ solar cell. This is the first stage of our modeling effort to build a fully self consistent multiscale solver that can describe transport across various length and time scales.

The hybrid solver consists of a DD solver and an MC solver. The DD solution is applied to the quasi-neutral areas which have low electric fields and the MC solution to the regions near the heterointerface which have high electric fields.

At first the DD solution is applied to the entire SHJ to determine the fields, potentials, carrier densities and currents in the device. Then the region to apply the MC solution is identified based on a critical electric field. Special care has to be taken to make sure the input carrier distribution is strongly correlated to the DD solution at the MC-DD boundary [6].

The initial DD solution calculates the current that in turn serves as the flux boundary condition for the MC. Figure 1. shows a schematic diagram of the HIT cell and the different domains that are being implemented to realize the multiscale solver; in previous works we have developed the MC and kinetic Monte Carlo (KMC) modules [7]. The solvers are said to be current matched when the MC solver reproduces the DD injection current. The current is calculated by analyzing the slope of the cumulative charge vs. time.

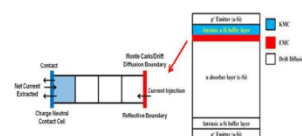
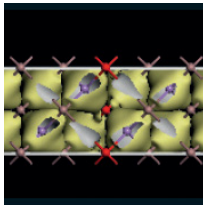


Fig 1. (Right) Schematic diagram of HIT cell and the different simulation domains. (Left) Schematic representation of the boundary conditions for MC - DD coupling.



## International Workshop on Computational Nanotechnology

The MC solver treats photogenerated holes at the heterointerface [8]. The MC solver is placed in the depletion region of a p-i-n junction on the 'n' side which gives rise to some crucial problems. There is orders of magnitude difference in hole density in terms of the densest cell and the least dense cell which leads to a lot of noise in the extracted current from the MC. We make some assumptions to account for the generation and recombination process that take place near a contact in a solar cell. The application of a MC solver is applicable if, 1) it is placed in an area where the photogenerated carriers have a diffusion length greater than its distance to the contact and 2) it is placed close to the front contact where the high frequency photo generation is not going to contribute to the short circuit current.

Once the solvers are current matched, coupling coefficients are extracted from the MC and the DD equations are solved again to get the new injection conditions for the MC [9]. Thus, the self consistent Gummel loop is completed.

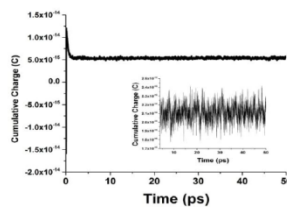


Fig 2. Cumulative charge vs. time extracted from the MC domain.

Figure 2 shows a cumulative charge vs. time plot for an injection of 50 mA/cm<sup>2</sup> into the MC domain. The vastly varying carrier density in the domain combined with low current injection makes it very hard to extract a coherent slope by creating a lot of noise in the MC results.

The time taken for the simulations are heavily dependent on the current injection from the DD and the MC domain population describing the depletion region charge density.

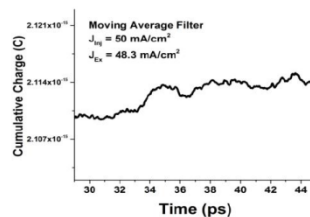
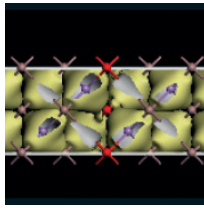


Fig 3. Moving average filter applied to fig. 2.

Figure 3 shows a moving average filter that is applied to the cumulative charge in order to reduce the noise. The solvers are said to be current matched if the injection current lies within  $\pm 3\sigma$  of the extracted current. By following the method described in this paper we are able to current match the DD and the MC solvers. Our current work is focused on extracting coupling coefficients from the MC to complete the self consistent Gummel cycle.

- [1] Martin A. Green, *Physica E: Low-dimensional Systems and Nanostructures*, Volume 14, Issues 1-2, Pages 65-70, 2002.
- [2] K. Masuko *et al.*, *IEEE Journal of Photovoltaics*, Vol 4., pp. 1433-1435, 2014.
- [3] K. Ghosh *et al.*, *Phys. Status Solidi A*, 210, No.2, pp 413-319, 2013.
- [4] H. Kosina and S. Selberherr, *IEEE Transactions on Computer-Aided Design of Integrated Circuits and Systems*, vol. 13, no. 2, pp. 201-210, 1994.
- [5] J. M. Hignman *et al.*, *IEEE Transactions on Electron Devices*, vol. 36, no. 5, pp. 930-937, 1989.
- [6] D. Y. Cheng *et al.*, *IEEE Transactions on Computer-Aided Design of Integrated Circuits and Systems*, vol. 7, no. 9, pp. 1017-1026, 1988.



- [7] P. Muralidharan *et al.*, *42nd IEEE Photovoltaic Specialist Conference (PVSC)*, pp. 1-4, 2015.
- [8] P. Muralidharan *et al.*, *40th IEEE Photovoltaics Specialists Conference*, pp 2519-2523, 2014.
- [9] S. Bandyopadhyay *et al.*, *IEEE Transactions on*

## P:25 Characterisation of a tunnel field-effect transistor using 2D TCAD simulations

D Nagy<sup>1</sup>, A J García-Loureiro<sup>1</sup>, <sup>2</sup>K Kalna and <sup>1</sup>N Seoane

<sup>1</sup>University of Santiago de Compostela, Spain, <sup>2</sup>Swansea University, UK

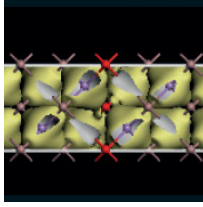
In conventional MOSFETs, the subthreshold swing (SS) has a fundamental limit of 60 mV/dec at room temperature that affects the minimum power consumption achievable when the device is turned off [1], [2]. Such constraint is one of the limiting factors of MOSFETs for low power devices. One of the promising solutions are tunnelling-FETs (TFETs) that demonstrated a much steeper SS with a very small leakage current ( $I_{OFF}$ ) because their operation is based on the band- to-band tunnelling (BTBT). The main drawback of TFETs are their low on-current ( $I_{ON}$ ) [3]-[5]. Various approaches aim to overcome the ( $I_{ON}$ ) issue and one of them, examined in this paper, is a modified structure of a conventional TFET by adding an extra layer between the gate-dielectric and the  $p-i-n$  junction to increase the tunnelling area. The aim of this paper is to investigate the performance of a parallel electric field (PE) TFET based on the experimental device [4].

The device is an  $n$ -type PE-TFET with a gate length of 1  $\mu\text{m}$  as shown in Fig. 1. The epi-layer and the SOI have an intrinsic doping of  $1.0 \times 10^{15} \text{ cm}^{-3}$ , the  $p$ -type source has a concentration  $3.7 \times 10^{19} \text{ cm}^{-3}$  and the  $n$ -type a doping of  $2.7 \times 10^{20} \text{ cm}^{-3}$ . The work function of the metal gate (TiN) is 4.8 eV. Simulations have been performed using Silvaco ATLAS version 5.20.2.R [6]. The simulations account for both the local and non-local BTBT, for the band-gap narrowing (BGN), the local and non-local trap assisted tunnelling, the Shockley-Read-Hall recombination, Auger generation, the impact ionization effects and finally the thermionic emission transport model at semiconductor-semiconductor interfaces.

Fig. 2 shows the  $I_D - V_G$  characteristics at high (1.0 V) drain bias comparing simulations with experimental data which is very close at large gate biases. The simulations can reveal details of device architecture since  $I_{OFF}$  increases dramatically with a drain-to-gate distance ( $D$ ) while ( $I_{ON}$ ) shows a minimal change. They determine  $D \leq 5 \text{ nm}$  as oppose to experimentally reported of 20 nm which would underestimate  $I_{OFF}$  by orders of magnitude. Fig. 3 shows that electron density is larger near the epi-channel junction when the  $D = 0 \text{ nm}$  than  $D = 5 \text{ nm}$  which results in a larger  $I_{OFF}$ . Fig. 4 shows a band- profile when the device is in OFF- ( $V_G = 0.3 \text{ V}$ ) and ON- mode ( $V_G = 2.5 \text{ V}$ ), respectively, for  $D = 0$  and  $D = 5 \text{ nm}$  at  $V_D = 1.0 \text{ V}$ . Note that at the OFF-mode, the current is due to the tunnelling near the drain side while, at the ON-mode, the tunnelling current occurs both near the epi-layer edge on the source side as well as at the source-intrinsic layer junction. The change in  $D$  from 0 to 5 nm reduces the  $I_{OFF}$  around 90% and introduces a shift of 0.1 V in the  $V_G$ . Fig. 5 shows that as the relative permittivity ( $\epsilon_r$ ) of the high- $\kappa$  layer under the gate is increased, the  $I_D - V_G$  curve shifts upwards (increased current). Fig. 6 shows how the doping of the source and drain regions affects the performance of the device. A decrease in the source doping by 35% will decrease the ON-current by around 48% at  $V_G = 2.5 \text{ V}$  and  $V_D = 1.0 \text{ V}$  while an increased in the drain doping by 48% increases the OFF-current by about 58% at  $V_G = 0.5 \text{ V}$  and  $V_D = 1.0 \text{ V}$ . Fig. 7 studies the effect of the LOV length. When LOV is reduced from 150 nm to 100 nm, the current at  $V_G = 2.5 \text{ V}$  and  $V_D = 1.0 \text{ V}$  is reduced by around 23%. Finally, Fig. 8 shows variations in a thickness of the epi-layer from 2 nm to 1 and 3 nm and found that as the epi-layer thickness is increased the  $I_D$  is reduced for all the  $V_G$ .

We have simulated an  $n$ -type PE-TFET device with 1.0  $\mu\text{m}$  gate length using DD simulations enhanced by tunnelling models calibrated against the experimental device in Ref. [4] with a good agreement at low and high drain biases. The most significant outcome of this study is that the distance between the gate and drain





## P:26 Impact of layer rotational misalignment on the transport properties of van der Waals tunnel field effect transistors

A Cresti<sup>1</sup>, J Cao<sup>1</sup> and M Pala<sup>2</sup>

<sup>1</sup> Université Grenoble Alpes, France, <sup>2</sup> Université Paris-Saclay, France

2D materials are a promising option for the realization of ultra-low-power tunnel field effect transistors (TFETs) thanks to their thinness, the absence of dangling bonds and the large band structure variety [1]. In this work, we study the impact of layer misorientation on the transport properties of a vertical TFET based on a MoS<sub>2</sub>/WTe<sub>2</sub> van der Waals (vdW) heterojunction [2]. To this aim, we use an effective mass Hamiltonian model and the non-equilibrium Green's function approach self-consistently coupled with the 3D Poisson equation for an accurate description of the system electrostatics. The effect of electron-phonon interaction is included within the self-consistent Born approximation. We consider both acoustic phonons within the elastic approximation and dispersionless optical phonons with parameters taken from [3].

The simulated vdW-TFET is shown in Fig. 1(a) and consists in a WTe<sub>2</sub> bottom layer acting as source and a MoS<sub>2</sub> top layer acting as drain. When the MoS<sub>2</sub> and the WTe<sub>2</sub> monolayers are stacked with a relative rotation angle  $\theta$ , the hexagonal Brillouin zones of the two original layers are also rotated by  $\theta$  around the  $\Gamma$  point, as shown in Fig. 1(b).

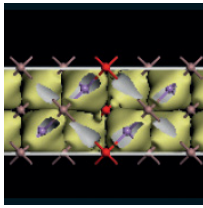
Hence, the MoS<sub>2</sub> conduction bands with valleys at the K and K' points are shifted from the corresponding WTe<sub>2</sub> valence bands, thus resulting in indirect band gaps between the two layers.

Fig. 2(e) shows the transfer characteristic IDS-VTG of the device for different rotation angles  $\theta = 0, 10.5^\circ$  and  $21^\circ$ . As can be seen, the rotational misalignment determines a significant current decrease. As schematized in Fig. 2(a-d), this is due to the interlayer tunneling reduction induced by the valley shift, which implies that a larger momentum change is needed by electrons to pass from one band to the other one. The impact on the subthreshold swing (SS) is quite modest, whereas the on-state current depends considerably on the rotation angle.

To analyze this behavior, Fig. 3 shows the interlayer tunneling current density for the vdW-TFET in the on-state with  $\theta = 10.5^\circ$  and  $\theta = 21^\circ$ . As shown in Fig. 3(a), for relatively small rotation angles, the tunneling occurs inside the overlap region. On the contrary, for larger angles the tunneling is localized at the edges of the overlap region, see Fig. 3(b), while it is very weak in the central area due to the fact that phonons alone are not able to scatter the electrons over a large  $\Delta k$ .

Conversely, the sharp edges of the overlap region are source of short-range scattering, and thus allow the electrons to change their momentum and to tunnel between the shifted valleys.

Since at room temperature the interlayer tunneling can be assisted also by phonons, in Figs. 4(a,b), we consider the most unfavorable configuration ( $\theta = 21^\circ$ ) for the vdW-TFET and artificially tune the deformation potential for acoustic ( $D_{ac}$ ) and optical phonons ( $D_{op}$ ). The increase of the phonon scattering strength results in a substantial on-current enhancement. As illustrated in Fig. 2(d), the electron tunneling can be triggered by two different mechanisms: one is the change of the momentum and the other is the optical phonon absorption, which promotes electrons to higher energy levels. Figs. 4(a,b) indicate that an increase of  $D_{ac}$  and  $D_{op}$  results in similar on-state currents, which suggests that the increase of IDS is more likely due to the momentum scattering.



# International Workshop on Computational Nanotechnology

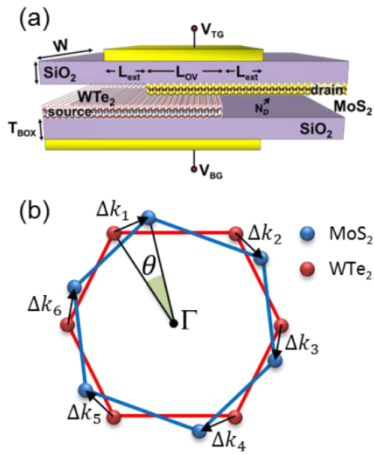


Figure 1. (a) Simulated van der Waals TFET. Tunnelling, driven by the top gate potential  $V_{TG}$ , occurs in the overlap region. (b) Brillouin zones (red and blue hexagons) of the two misoriented monolayers. The indirect gaps are indicated by the six vectors  $\Delta k_i$ .

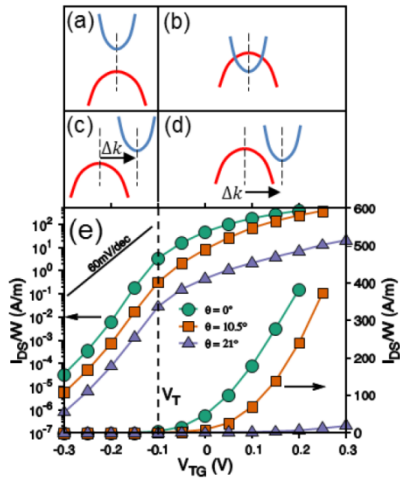


Figure 2. Schematics of the alignment of the MoS<sub>2</sub> conduction and WTe<sub>2</sub> valence bands (a,b) without and (c,d) with rotational misalignment. With the rotation, the band gap becomes indirect with a shift vector  $\Delta k$ . Panels

(a,c) correspond to the subthreshold  $V_{TG} < V_T$ , and panels (b,d) correspond to  $V_{TG} > V_T$ . (e) Transfer characteristics for different values of the rotation angles  $\theta = 0, 10.5^\circ$  and  $21^\circ$ , at  $V_{DS} = 0.3V$ . Other parameters are:  $D_{ac} = 3$  eV,  $L_{ext} = 5$  nm,  $L_{ov} = W = 20$  nm,  $T_{BOX} = 1$  nm and  $N_D = 4 \times 10^{12} \text{ cm}^{-2}$ .

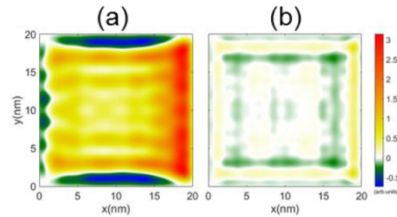


Figure 3. Spatial distribution of the inter-layer tunnelling current in the on state ( $V_{TG} = 0.2V$ ) for misorientation angles of (a)  $10.5^\circ$  (b) and  $21^\circ$ . For large angles, tunnelling is concentrated along the edges of the region of overlap between the two layers.

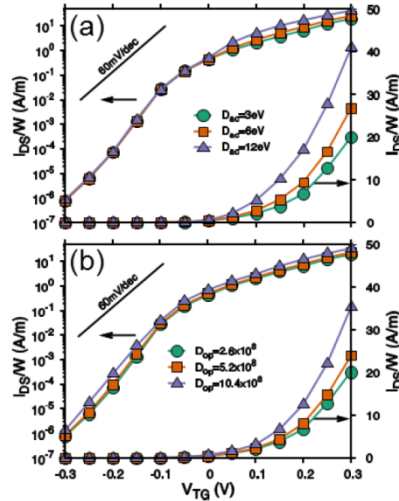
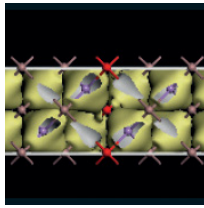


Figure 4. Transfer characteristics for different values of (a) acoustic deformation potential  $D_{ac}$  and (b) optical deformation potential  $D_{op}$ , with the rotation angles  $\theta = 21^\circ$ , at  $V_{DS} = 0.3$  V. The optical phonon energy is  $\hbar\omega = 50$  meV. Other parameters are as in Fig.2.

- [1] T. Roy, M. Tosun, M. Hettick, G. H. Ahn, C. Hu, and A. Javey, Applied Physics Letters, 108, (2016) 083111.
- [2] J. Cao, D. Logoteta, S. Özkaya, B. Biel, A. Cresti, M. G. Pala, and D. Esseni, IEEE Transactions on Electron Devices, 63, (2016) 4388.
- [3] K. Kaasbjerg, K. S. Thygesen, and K. W. Jacobsen, Physical Review B, 85, (2012) 115317.



## International Workshop on Computational Nanotechnology

### P:27 Do we really need the collapse law when modelling quantum transport in electron devices?

D Pandey<sup>1</sup>, Z Zhan<sup>1</sup>, E Colomés<sup>1</sup>, G Albareda<sup>2</sup> and X Oriols<sup>1</sup>

<sup>1</sup>Universitat Autònoma de Barcelona, Spain, <sup>2</sup>Universitat de Barcelona, Spain

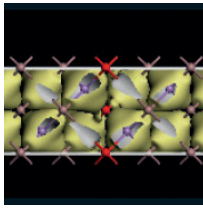
A well-known challenge in quantum theory is the description of the measurement process [1,2]. After more than one century since the birth of quantum mechanics, this fundamental problem still remains timely. In fact, our basic conception of quantum reality depends on how we ultimately solve this problem. The usual formulation of quantum mechanics (the so-called orthodox theory) argues that two fundamental laws describe the evolution of any system: (i) a unitary and linear law (given for example by the Schrödinger equation) when the system evolves without being measured and (ii) a non-unitary and non-linear law (the so-called collapse law) when it is being measured.

In principle, the correct modelling of any electron device within the orthodox theory requires including both laws. However, there is a large list of quantum transport models in the literature that do not treat explicitly the collapse law, but they only include analytical or numerical solutions of the Schrödinger (parabolic band structure) or Dirac (linear band structure) equations. Notice that it is well-known that the measurement problem cannot be generally solved in a quantum system by invoking decoherent phenomena (like phonon or impurity collisions) alone. One of the reasons that can explain why the measurement problem is usually forgotten in the quantum modelling of electron devices is that there is no such problem in classical or semi-classical modelling.

In this conference we will explain for which type of observables we can expect to induce erroneous predictions of the performance of quantum devices when neglecting the measurement problem. Based on ergodic arguments, the DC performance of quantum devices does not require the post-evolution of the system after measurement and the collapse law can be ignored (like in the successful Landauer model). However, the computation of (zero or high frequency) noise through the correlations of the measured currents at different times requires the inclusion of the collapse law (see Figs. 1 and 2). Similarly, for high frequency (AC) predictions beyond the quasi-static approximation, where a multi-time measurement of the current is necessary, the collapse law plays also a significant role (see Figs. 3).

In this conference we will also argue that there exist alternative valid theories that allow us to solve the measurement problem in a rather trivial manner [2-5]. For example, in addition to the wavefunction, Bohmian theory introduces well defined quantum trajectories in the description of a quantum state. In this way, this theory is able to solve the measurement problem without the need of invoking the collapse law. Following these ideas, the group of Dr. Oriols has developed a quantum electron transport simulator, the so-called BITLLES simulator [6], that can be used to model the DC, AC or high-frequency performance of any quantum device without the need of any further conceptual difficulty associated to the quantum measurement problem [2-4] (see Figs. 1, 2, 3).

In summary, we provide two answers to the question posed in the title. First, if you want to use the orthodox theory to provide noise and AC predictions beyond the quasi-static approximation you do effectively need the collapse law. Contrarily, the answer is no if you choose to model your quantum device with an alternative formulation of quantum mechanics. For example, within Bohmian mechanics, a general purpose simulator can be developed to provide DC, AC and noise performances of state-of-the-art nanoscale devices without the need of invoking the collapse law [2-4].



# International Workshop on Computational Nanotechnology

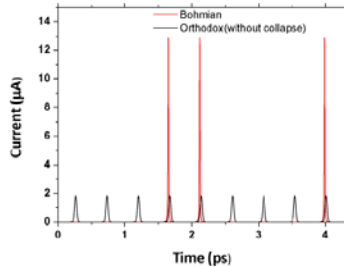


Fig1. Time dependent simulation of the electrical current measured in the collector terminal of a RTD device for a constant flux of injected electrons (all with the same energy) impinging upon a double barrier. The transmission coefficient is  $T=0.436$ . Two different models are used in the current computation: (i) (in black) we use the orthodox model without collapse law to compute quantum transport by just solving the time-dependent solution of the Schrödinger equation. (ii) in red, a Bohmian solution which uses the orthodox wave function plus trajectories that include the randomness of the measurement problem by the selection of the initial position of the trajectory that determines if the electron is either transmitted or reflected. The charge transmitted in each pulse is the average value  $qT$  (being  $q$  the electron charge) in the first model and  $q$  or  $0$  in the second one. Notice that the average results (DC current) of both models are identical.

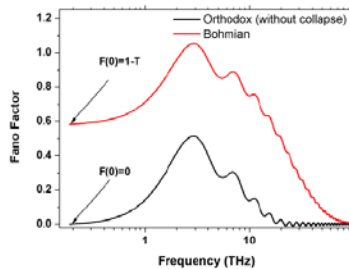


Fig.2 The noise of the electrical current corresponding to the two transport models considered in Fig 1. Fano factor,  $F(0)=S(0)/(2qI)$ , defined as the power spectral density at zero frequency  $S(0)$  divided by the average current  $I$  and the electron charge  $q$ , is plotted. The first model (black line) provides zero noise at low frequency  $F(0)=0$  since there is no randomness in its current in Fig. 1. Notice that the Schrödinger equation alone (without the collapse law) is a deterministic equation without randomness. The second model (red line) provides a Fano factor equal to  $F(0)=1-T=0.564$  due to the randomness of its current seen in Fig 1. The value corresponds to the well-known result of the fluctuations in the current due to the tunnelling barrier with transmission coefficient  $T$  (such process follows a Binomial probability distribution with probability equal to  $T$ ). Notice the differences in the spectrum of the noises of both models at either zero or high frequencies.

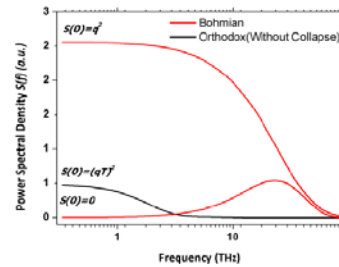
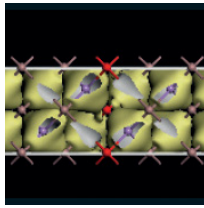


Fig.3 Power spectral density  $S(f)$  corresponding to the simulation of one single electron of figure 1 (not a constant flux) computed with the two models considered in this work. Since transmitted and reflected particles have the same description in the first model (black line) only one plot is represented. In the second model (red lines), we plot  $S(f)$  corresponding to a reflected particle and another  $S(f)$  for a transmitted one. At zero frequency, when a large flux of particles is considered, both models provide the same average value of  $S(0)$  which corresponds to the DC results. The two red lines averaged by the transmission coefficient corresponds to the black line at  $S(0)$ . However, at high frequency, important differences remain. As seen in figure 1, the result of the second model corresponds to thinner and higher current pulses that are later translated in the presence of  $S(f)$  at higher frequencies in the power spectral density.

- [1] X.Oriols and D.K.Ferry, JCE, 12(3), 317-330 (2013)
- [2] X.Oriols and J.Mompart, Applied Bohmian Mechanics (2012) ISBN: 978-981-4316-39-2
- [3] A. Benseny et al. European Physical Journal D, 68, 286 (2014)
- [4] X. Oriols, PRL, 98 (2007) 066803.
- [5] D. Marian, N. Zanghì and X. Oriols, PRL, 116 (2016) 110404.
- [6] <http://europe.uab.es/bitlles>.



# International Workshop on Computational Nanotechnology

## P:28 Electric field modulation of phosphorene nanoribbons' electronic properties

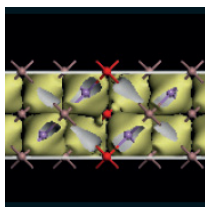
S Soleimanikahnoj, C-H Hsu and I Knezevic

University of Wisconsin-Madison, USA

Black phosphorus can be peeled down to a few monolayers by mechanical exfoliation [1]. The resulting two-dimensional structure is referred to as phosphorene. Single-layer phosphorene has a direct band gap of 1.45 eV at the  $\Gamma$  point of a rectangular Brillouin zone [1]. The gap remains direct in multilayer phosphorene, which makes this material suitable for electronic and optoelectronic applications [2]. The gap decreases with increasing number of layers and reaches a value of 0.3 eV in the bulk [3]. Furthermore, the puckered crystal structure in phosphorene leads to a high tunability of the bandstructure by strain and electric field. For instance, applying an electric field normal to the layers reduces the band gap due to a giant Stark effect [4]. The bandgap closes at a critical electric field, which marks a transition from a moderate-gap semiconductor to a semimetal. This bandgap closing is associated with the emergence of remarkable topological properties of biased phosphorene, as well as drastic changes in its electronic behavior [5]. Although the effect of electric field on electronic properties of multilayer layer phosphorene is understood, the possible use of electric field modulation in tuning the electronic characteristics of phosphorene-based nanostructures is fairly unexplored.

In this paper, we investigate the tunability of the electronic properties of phosphorene nanoribbons (PNRs) by an external electric field. In PNRs, edge termination plays an important role in determining electronic dispersion. In particular, PNRs with zigzag and skewed armchair edges are metallic while other edge terminations lead to insulating behavior. Focusing on metallic multilayer PNRs, we show that there are twofold-degenerate bands within the bulk gap, which govern electronic transport. The wave functions associated with these bands are localized near the ribbon edges. We propose a dual-edge-gate structure that affects these midgap states and drives the conducting-to-insulating transition in single layer and bilayer PNRs, thus enabling field-effect transistor action compatible with modern nanoelectronics, and potentially leading to new PNR-based devices.

The bandstructure of bilayer phosphorene is described by a fifteen-nearest neighbors tight binding Hamiltonian [6]. The band structures of a bilayer zigzag PNRs (ZPNRs) is shown in Fig. 1(a). One can see the presence of midgap bands (red curves) completely detached from the other bands (shown in blue). For ZPNRs, each layer of phosphorene contributes one band of twofold-degenerate midgap states, making a total of four midgap states for bilayer ZPNRs. The ribbon is metallic, since the Fermi level (dashed line) passes through the midgap bands and is energetically far from the other states. Consequently, charge transport is governed by the midgap states. The probability density associated with the wave function for the midgap state at  $k = 0$ , marked in Fig. 1(a), is plotted along the width in Fig. 1(d). The probability density peaks near the edges and decays towards the bulk. Hence, charge transport in ZPNRs should be controllable by applying a perpendicular electric field to the edges, where the electrons in midgap states around the Fermi level are likely to reside. When a perpendicular electric field is applied to the edges of metallic PNRs [solid line boxes in Fig. 1(d)], it strongly affects the midgap state which have a high probability density right under the gate. This leads to an energetic shift of midgap states, proportional to the amplitude of the field [see Fig. 1(b)]. Increasing the field beyond a critical value leads to a complete separation of the midgap bands and a transition to insulating behavior [see Fig. 1(c)]. At the conference, we will discuss several device structures that rely on the tunability of midgap states by edge gates.



# International Workshop on Computational Nanotechnology

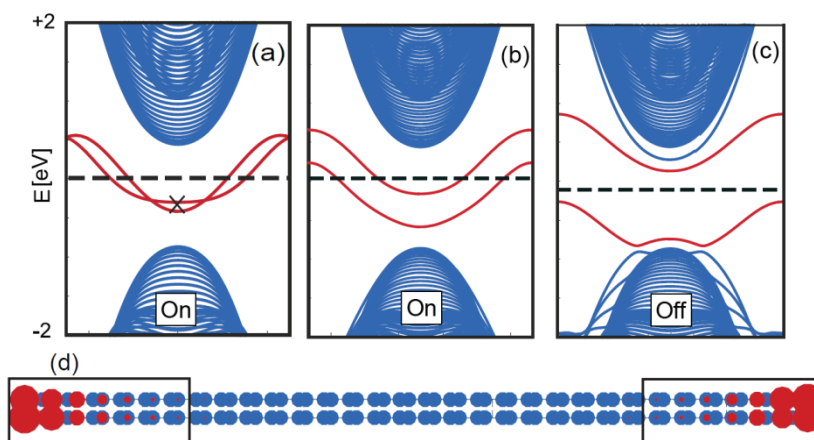
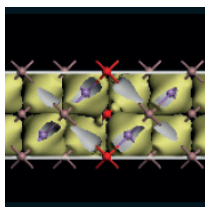


Fig. 1: (a) Band structure of an unbiased bilayer zigzag PNR. (b) Band structure of a zigzag bilayer PNR when the electric field applied to the edges is nonzero but below the critical value. (c) Band structure of zigzag bilayer PNR beyond the critical electric field. (d) On-site probability density of the state whose energy is marked by "x" in panel (a). The red circles denote the probability density, with the larger circles representing higher probability density.

- [1] H. Liu, A. T. Neal, Z. Zhu, Z. Luo, X. Xu, D. Tomanek, and D. Peide, Phosphorene: an unexplored 2D semiconductor with a high hole mobility, *ACS Nano* 306, 4033 (2014).
- [2] Y. Jing, Q. Tang, P. He, Z. Zhou and P. Shen, Small molecules make big differences: molecular doping effects on electronic and optical properties of phosphorene, *IOP Nanotechnology* 26, 095201 (2015).
- [3] S. Zhang, J. Yang, R. Xu, F. Wang, W. Li, M. Ghufran, Y. W. Zhang, Z. Yu, G. Zhang, Q. Qin, and Y. Lu, Extraordinary photoluminescence and strong temperature/angle-dependent Raman responses in few-layer phosphorene, *ACS Nano* 8, 9590 (2014).
- [4] G. Qin, Q. Yan, Z. Qin, S. Yue, M. Hu and G. Su, Anisotropic intrinsic lattice thermal conductivity of phosphorene from first principles, *Physical Chemistry Chemical Physics* 17, 4854 (2015).
- [5] Q. Lui, X. Zhang, L. B. Abdalla, A. Fazio, and A. Zunger, Switching a Normal Insulator into a Topological Insulator via Electric Field with Application to Phosphorene, *Nano. Lett.* 15, 1222 (2015).
- [6] A. N. Rudenko, S. Yuan, and M. I. Katsnelson, Toward a realistic description of multilayer black phosphorus: From G W approximation to large-scale tight-binding simulations, *Phys. Rev. B* 92, 085419 (2015).



# International Workshop on Computational Nanotechnology

## P:29 Hole Trapping in Amorphous $\text{HfO}_2$ and $\text{Al}_2\text{O}_3$ as a source of positive charging

J Strand<sup>1</sup>, O Dicks<sup>1</sup>, M Kaviani<sup>2</sup> and A Shluger<sup>1,2</sup>

<sup>1</sup>University College London, UK, <sup>2</sup>WPI-AIMR Tohoku University, Japan

Positive charging in Si/SiO<sub>2</sub>/HfO<sub>2</sub> stacks is usually associated with defects in the interface SiO<sub>2</sub> layer. Implementation of high mobility substrates, such as Ge and III-Vs, will see the gate dielectric exposed to hole trapping. Thin HfO<sub>2</sub> and Al<sub>2</sub>O<sub>3</sub> layers deposited on, for example, Ge are usually amorphous [1]. To understand the ultimate behaviour of high- $\kappa$  dielectrics in such devices we compare hole trapping in crystalline and amorphous HfO<sub>2</sub> and Al<sub>2</sub>O<sub>3</sub> using DFT modelling. Nine periodic models of a-HfO<sub>2</sub>, each containing 324 atoms, have been generated using classical MD and a melt and quench procedure. Further optimization of the volume and geometry of these structures was performed using DFT as implemented in the CP2K code [2] with the PBE0-TC-LRC functional. The model a-Al<sub>2</sub>O<sub>3</sub> structures produced using the same method and contained 360 atoms.

The trapping of hole polarons on O atoms in m-HfO<sub>2</sub> and  $\alpha$ -Al<sub>2</sub>O<sub>3</sub> has been previously predicted theoretically [3, 4]. Recent calculations [5] predicted that holes can trap only at three-coordinated O sites in the bulk of m-HfO<sub>2</sub> with a trapping energy of 0.18 eV and with much larger trapping energies at surfaces, featuring two-coordinated O sites. Structural variations, such as under-coordination or elongated bonds, serve as precursor sites where holes can trap spontaneously in a-HfO<sub>2</sub> and a-Al<sub>2</sub>O<sub>3</sub> [6]. In both materials over 90% of the hole spin density is localized on two O atoms. The characteristic atomic configurations of the polaron are shown in Fig. 1. The average hole trapping energies (thermal ionization energies) are 1.4 eV in a-HfO<sub>2</sub> and 1.2 eV in a-Al<sub>2</sub>O<sub>3</sub>. The distribution of hole trapping energies is shown in Fig. 3. We also find that both cells contain up to four precursor sites.

In m-HfO<sub>2</sub> two hole polarons form a stable bi-polaron state with the binding energy of 0.65 eV. This state is stabilized by forming of an O-O dimer. In a-HfO<sub>2</sub> the formation of hole bi-polaron takes place spontaneously at structural precursor sites. In both the amorphous and monoclinic cases, the O-O dimer formed has a bond length of 1.5 Å. Hole bi-polarons also form in a-Al<sub>2</sub>O<sub>3</sub> again with an O-O bond length of 1.5 Å. The relaxation of surrounding ions is asymmetric (Fig. 2). In both oxides this involves ionic displacements exceeding 0.5 Å. This large structural reorganisation means that Hf-O, or Al-O, bonds are greatly weakened, suggesting the possibility of further defect creation.

### 2. FIGURES

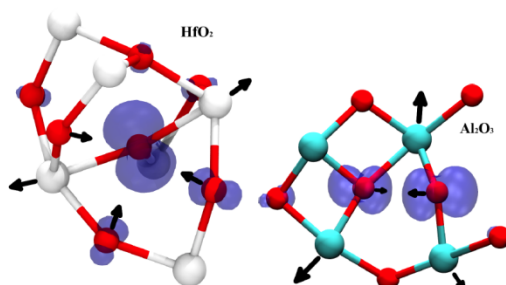
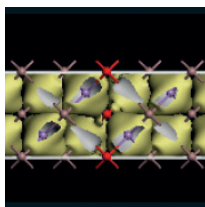


FIGURE 1. Configurations of hole polarons in a-HfO<sub>2</sub> and a-Al<sub>2</sub>O<sub>3</sub>. Red indicates O ions, cyan Al ions and white Hf ions. Spin density is indicated by the blue iso-surfaces. Arrows indicate direction of ionic displacements due to polaron trapping.



# International Workshop on Computational Nanotechnology

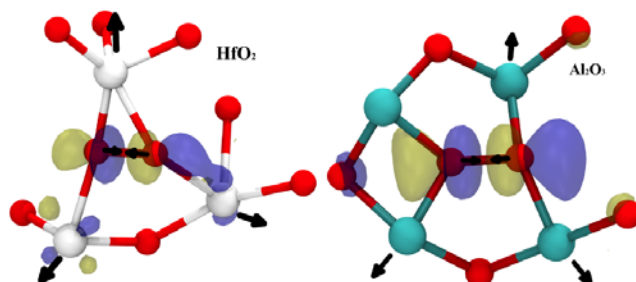


FIGURE 2. Configurations of bi-polarons in  $\alpha\text{-Al}_2\text{O}_3$  and  $\alpha\text{-HfO}_2$ . The colored surfaces correspond to the unoccupied KS state of the bipolaron, with blue indicating a positive isovalue and yellow indicating a negative isovalue.

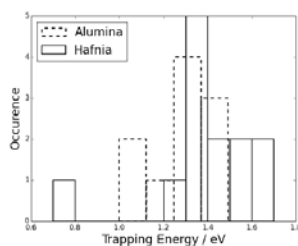
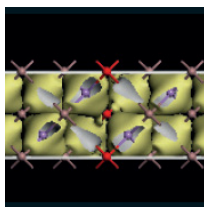


FIGURE 3. Trapping energies of single hole polarons in  $\alpha\text{-Al}_2\text{O}_3$  and  $\text{HfO}_2$ . Energies given are referenced to delocalized hole at the top of the valence band.

- [1] A Delabie, R Puurunen, B Brijs, M Caymax, T Conard, B Onsia, O Richard, W Vandervorst, C Zhao, M M Heyns, et al. Atomic layer deposition of hafnium oxide on germanium substrates. *Journal of applied physics*, 97(6):064104, 2005.
- [2] M Guidon, J Hutter, and J VandeVondele. Robust periodic hartree-fock exchange for large-scale simulations using gaussian basis sets. *Journal of chemical theory and computation*, 5(11):3010-3021, 2009.
- [3] A Ramo, Dand Shluger, J Gavartin, and G Bersuker. Theoretical prediction of intrinsic self-trapping of electrons and holes in monoclinic hfo 2. *Physical review letters*, 99(15):155504, 2007.
- [4] JB Varley, A Janotti, C Franchini, and CG Van de Walle. Role of self-trapping in luminescence and p type conductivity of wide-band-gap oxides. *Physical Review B*, 85(8):081109, 2012.
- [5] K McKenna, M Wolf, A L Shluger, S Lany, and A Zunger. Two-dimensional polaronic behavior in the binary oxides m- hfo 2 and m- zro 2. *Physical review letters*, 108(11):116403, 2012.
- [6] M Kaviani, J Strand, V Afanas' ev, and A Shluger. Deep electron and hole polarons and bipolarons in amorphous oxide. *Physical Review B*, 94(2):020103, 2016.



# International Workshop on Computational Nanotechnology

## P:30 Electron transport in defective metallic and semiconducting carbon nanotubes: An improved RGF-based $O(N)$ approach

F. Teichert<sup>1,2,3</sup>, A. Zienert<sup>2</sup>, J. Schuster<sup>1,3</sup> and M. Schreiber<sup>1,2</sup>

<sup>1</sup>TU Dresden, Germany, <sup>2</sup>Chemnitz University of Technology, Germany, <sup>3</sup>Fraunhofer Institute for Electronic Nano Systems (ENAS), Germany

We present electron transport calculations for metallic and semiconducting carbon nanotubes (CNTs) with randomly positioned realistic defects. For this purpose we use our new and very efficient RGF-based  $O(N)$  algorithm [1]. Based on this approach we are able to handle CNTs of realistic size up to several microns with up to thousands of defects. From our model calculations, simple analytic expressions are derived to express the conductivity of CNTs featuring arbitrary defect mixtures and different chiralities.

Although nearly ideal CNTs can be produced selectively under very clean laboratory conditions, during any step of the device fabrication at the wafer level going towards mass production methods, defects are introduced to all CNT devices fabricated so far. While many of the theoretical studies deal with ideal CNTs, it is of big interest to focus more on defective CNTs to know how different defects affect the electronic transport properties of CNTs. We treat this task from a theoretical point of view. This is a challenging task due to the huge number of atoms to be considered for defective systems. The usage of density functional theory (DFT), which scales cubically with the number of atoms, becomes unpractical for this purpose.

We use hybrid models like the density-functional-based tight binding (DFTB) model which combine the fastness of the tight binding approach with the good accuracy of DFT. Furthermore, we use the common quantum transport theory in combination with a fast, linearly scaling recursive Green's function formalism (RGF), allowing us to treat the electronic transport problem quantum-mechanically. But the further development and improvement of such theoretical methods is also an important task to overcome the system size limitations.

In the first part of our contribution we present two new and very efficient RGF-based approaches. The first algorithm accelerates the common RGF for the case of defective quasi-1D systems [1].

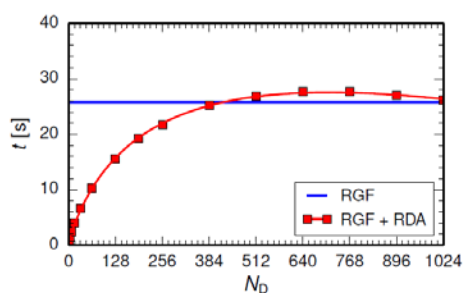


**Figure 1:** Calculation time as a function of the number of defects within a test system, which contains a fixed number of 1024 cells. The improved RGF+RDA is compared to the common RGF.

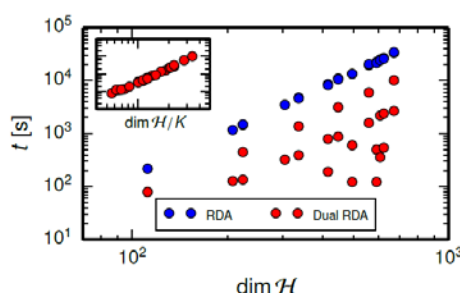
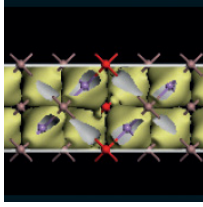


**Figure 2:** Calculation time as a function of the dimension of the Hamiltonian matrix of the periodic unit cell. The improved Dual-RDA is compared to the common RDA. Inset: Scaled data, where  $K$  is the number of sub-cells.

This is achieved by using the iteration steps of the renormalization decimation algorithm (RDA), leading to a smaller effective system. The resulting computational complexity scales linearly with the number of defects, instead of linearly with the total system length for the conventional approach. We show how the scaling of the calculation time depends on the defect density, leading to significant reductions for less defects and small unit cells (RGF+RDA, figure 1). We apply this algorithm to defective metallic armchair CNTs. The second approach treats the problem of periodic quasi-1D systems with large unit cells, which can be treated by the common RDA. However, this gets more inefficient for the larger cells as the calculation time scales



# International Workshop on Computational Nanotechnology

quadratic with the number of atoms. Based on the DFTB model, we present how to reduce the calculation time by simply subdivide and conquer (Dual-RDA, figure 2). We demonstrate the application of the algorithm for semiconducting chiral CNT with different unit cell lengths.

In the second part we show the results we got for the electronic transport through defective CNTs by using our algorithm improvements. For this, we focus on mono- and divacancies, which are the most common defects. In general, our approach can be extended easily to cover arbitrary defect types. In our previous publication [2] transmission spectra of defective metallic armchair CNTs are studied comprehensively and diameter-dependent localization exponents are extracted (figure 3a, 3b). We extend this work to defect mixtures and show that the total localization exponent can be expressed by linear combinations of those of CNTs with one defect type, which can be used to estimate the conductance of arbitrary defective CNTs. Finally, we focus on defective semiconducting  $(m,n)$ -CNTs of different chirality and present the influence of the structural parameters on the conductivity and the localization exponent. The diameter dependence can be described like for the metallic CNTs, but a distinction into three groups must be done. The investigation of the chirality dependence shows no significant influence (figure 3c).

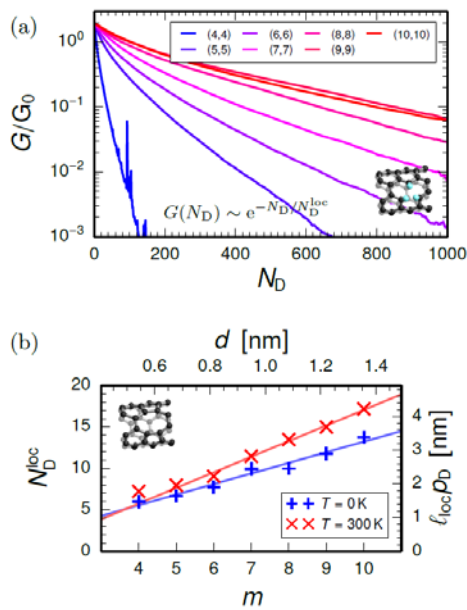
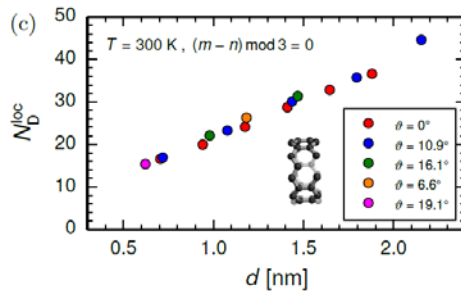


**Figure 3:**

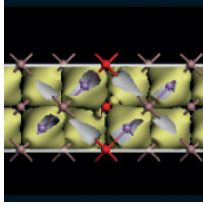
(a) Conductance of metallic armchair CNTs as a function of the number of defects therein. Different tube diameters are denoted by color.

(b) Localization exponent of metallic armchair CNTs as a function of the tube diameter. Different temperatures are denoted by color.

(c) Localization exponent of defective semiconducting zig-zag and chiral CNTs as a function of the tube diameter. Different chiralities are denoted by color.



- [1] F. Teichert et al., J. Comput. Phys., submitted  
 [2] F. Teichert et al., New J. of Phys. 16 (2014) 123026.



## P:31 A mobility model for TCAD simulation of current variation by random discrete dopant

H I Yu, D W Kim, S M Lee and Y J Park

Seoul National University, South Korea

As the device size is rapidly scaling down, the variation of the drive current by random discrete dopant (RDD) becomes very important [1]. Contrary to the conventional MOSFET where the RDD in the channel region mainly contributes to the performance variations, the RDD fluctuation in the source/drain area can significantly influence the performance of the DRAM cell because the source/drain doping concentration needs to be kept low in the DRAM cell in order to suppress the junction and gate induced drain leakage (GIDL) [2].

The drift-diffusion (DD) solver can give unphysical results when it is applied to study the influence of the RDD without care because the adopted mobility models were typically derived from the homogeneous doping concentration, and they may not be valid when the atomistic doping profile is employed. Several groups are trying to solve these artifacts [3]. In this paper, we propose a method that can effectively eliminate these artifacts by correcting the doping dependent mobility model.

As a test structure, we consider a n-type silicon resistor of dimensions 20 nm × 20 nm × 140. Several random samples are generated with different dopant positions on intrinsic silicon for the given doping density. Discrete region length is 100nm. A continuous doping region is interposed between the contacts and the discrete zone to avoid any influence related to the boundary conditions. To resolve the carrier localization by discrete dopant, density gradient (DG) method with fine mesh is adopted [4]. As a reference, a continuous doped resistor with the same concentration as the discrete one was prepared. [Fig. 1-(a)]

For the low-field doping dependent mobility model, the Masetti model [5] is employed. As for the high-field saturation, we adopt the driving force from the gradient of the quasi-Fermi potential in order to avoid errors due to local electric field from individual dopants. The bandgap-narrowing (BGN) model is turned off. Fig. 2 compares the current of the resistor as a function of the doping concentration obtained from the reference continuous doping profile and from the ensemble average of the discrete dopant profiles.

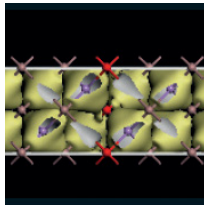
When the doping-dependent mobility model is used together with the discrete doping profile without any correction, the model overestimates the current as there exist many mesh elements without any doping such that current can flow through the intrinsic path. In addition, this behavior is sensitive to the mesh spacing such that it is very difficult to obtain a robust and consistent result. In order to resolve this issue, we smooth the discrete doping profile for the mobility calculation by applying the Sano method [6] where the cut-off parameter ( $K_c$ ) is calibrated as a function of the doping concentration in order to reproduce the current of the continuous doping profile. On the other hand, the discrete doping profile is employed without smoothing in the Poisson equation to capture the effects of the discrete dopant on the electrostatic potential.

Table. 1 shows the cut-off parameters for each doping concentration. From this, we can obtain the following equation by polynomial regression the relationship between doping concentration and  $K_c$ .

$$K_c = -0.004944073 \times (N_d)^3 + 0.6569125 \\ \times (N_d)^2 - 28.74891 \times (N_d) \\ + 430.6536$$

This  $K_c$  is used as a new fitting parameter for doping dependent mobility correction.

Fig.3 shows the result of applying fitting parameter to analytic doping profile. In the case of analytic doping, several arbitrary sections were divided to reflect the gradual doping change, and a fitting parameter



# International Workshop on Computational Nanotechnology

corresponding to the average doping concentration of each section was applied. Fig.4 means  $K_c$  extracted from the above relationship agrees well with the analytic doping profile used in general devices.

We proposed a modified doping dependent mobility model considering a wide range of doping concentrations and confirmed that the model has good agreement.

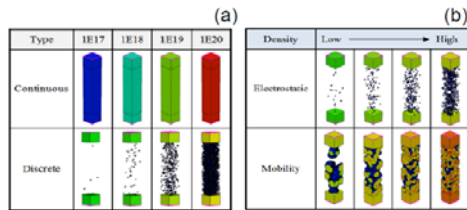


Fig.1. (a) N-type silicon resistor to compare the difference between continuous doping and discrete doping (b) Doping profiles as the input to TCAD simulation of the electrostatic potential and mobility

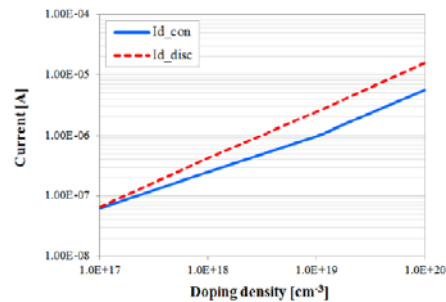


Fig. 2. Comparison of the I–V characteristics of the samples with continuous doping and discrete doping

Doping conc. [ $\text{cm}^{-3}$ ]	Cut-off parameter
1.0E+17	4.170E+06
1.0E+18	5.700E+06
1.0E+19	1.132E+07
1.0E+20	2.439E+07

Table. 1. Correction cut-off parameter ( $K_c$ ) for each doping concentration

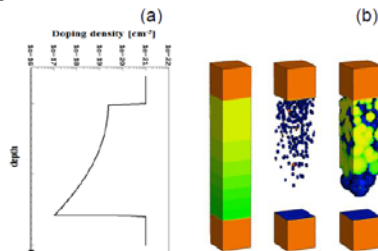


Fig.3 (a) Doping profile in the depth direction (b) reference analytic doping (left), for electrostatic (mid), for mobility (right) doping

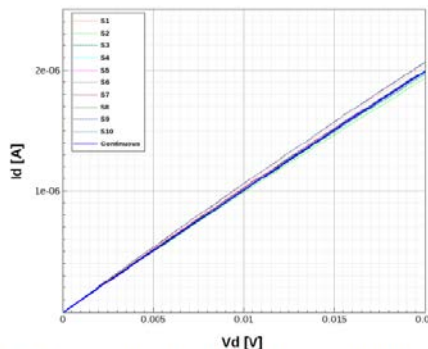
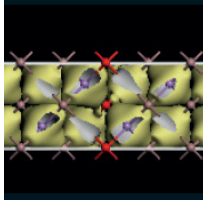


Fig. 4. I-V characteristics with newly extracted fitting parameters.

- [1] X. Tang, V. K. De, and J. D. Meindl, "Intrinsic MOSFET parameter fluctuations due to random dopant placement," IEEE Trans. VLSI System, vol. 5, no. 4, pp. 369-376, Dec. 1997
- [2] J.M. Park, Y.S. Hwang, S.-W. Kim, S.Y. Han, J.S. Park et al., "20nm DRAM: A new beginning of another revolution", IEDM.2015. 677-679
- [3] S.M. Amoroso, A. R. Brown, A. Asenov, "A Mobility Correction Approach for Overcoming Artifacts in Atomistic Drift-Diffusion Simulation of Nano-MOSFETs". IEEE Trans. Electron Devices, VOL. 62, NO. 6, JUNE 2015
- [4] G. Roy, A. R. Brown, A. Asenov, and S. Roy, "Quantum aspects of resolving discrete charges in 'atomistic' device simulations," J. Comput. Electron., vol. 2, nos. 2–4, pp. 323–327, Dec. 2003.
- [5] G. Masetti, M. Severi, and S. Solmi, "Modeling of carrier mobility against carrier concentration in arsenic-, phosphorus-, and boron-doped silicon," IEEE Trans. Electron Devices, vol. 30, no. 7, pp. 764–769, Jul. 1983.
- [6] Sano N, Matsuzawa K, Mukai M, Nakayama N. "On discrete random dopant modeling in drift-diffusion simulations", Microelectronics Reliability 42 (2002) 189-199.



# International Workshop on Computational Nanotechnology

## P:32 Spin recovery in the 25 nm gate length InGaAs field effect transistor

B Thorpe<sup>1</sup>, K Kalna<sup>1</sup>, F Langbein<sup>2</sup> and S Schirmer<sup>1</sup>

<sup>1</sup>Swansea University, UK, <sup>2</sup>Cardiff University, UK

In recent years, there has been an increasing interest in electron spin and its potential for use in semiconductor devices enabling the creation of novel devices with a wide variety of potential applications [1, 2]. Amongst the most promising of these devices are spin field effect transistors (SpinFETs) which are considered a future candidate for high performance computing and memory applications with ultra-low power consumption [3, 4, 5].

A thorough understanding of the dynamics of electron spins inside real semiconductor materials and device structures is crucial to making use of the spin as part of the device operation. To this end, we apply finite-element quantum-corrected ensemble Monte Carlo simulations with electron spin to a nanoscale III-V field effect transistor to investigate a spin transport within a realistic semiconductor device.

The simulation was adapted to include electron spin as a separate degree of freedom using the spin density matrix  $\rho_0(t)$  [6].

$$\rho_0(t) = \begin{pmatrix} \rho_{\uparrow\uparrow}(t) & \rho_{\uparrow\downarrow}(t) \\ \rho_{\downarrow\uparrow}(t) & \rho_{\downarrow\downarrow}(t) \end{pmatrix} \quad (1)$$

where  $\rho_{\uparrow\uparrow}$  and  $\rho_{\downarrow\downarrow}$  represent the probability of finding the electron in either a spin up or spin down state and  $\rho_{\uparrow\downarrow} / \rho_{\downarrow\uparrow}$  represent the coherence. This can be parametrized by the electron spin-polarization vector as  $S_\zeta = Tr(\sigma_\zeta \rho_0(t))$  where  $\zeta = x, y, z$ , and  $\sigma_\zeta$  are the Pauli matrices.

The spin-orbit interaction consists of two terms the Dresselhaus Hamiltonian ( $H_D$ ) which accounts for spin-orbit coupling as a result of bulk inversion asymmetry of the crystal, and the Rashba Hamiltonian ( $H_R$ ) which accounts for spin-orbit coupling due to structural inversion asymmetry of the quantum well.

$$H_D = \beta \langle k_y^2 \rangle (k_z \sigma_z - k_x \sigma_x) \quad H_R = \eta (k_z \sigma_x - k_x \sigma_z) \quad (2)$$

Here  $x$  is taken to be the transport direction along the device channel and  $y$  the growth direction of the quantum well and  $k_x^2, k_z^2 \ll \langle k_y^2 \rangle$ .

Discretizing the equations, we obtain the update rule for the density matrix,

$$\rho(t + \tau) = e^{-i(H_R + H_D)\tau/\hbar} \rho(t) e^{i(H_R + H_D)\tau/\hbar}. \quad (3)$$

Using basic matrix algebra it can easily be shown that

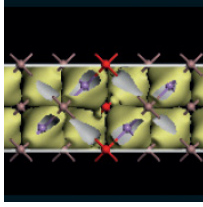
$$e^{-i(H_R + H_D)\tau/\hbar} = \begin{pmatrix} \cos(|\alpha|\tau) & i \frac{\alpha}{|\alpha|} \sin(|\alpha|\tau) \\ i \frac{\alpha^*}{|\alpha|} \sin(|\alpha|\tau) & \cos(|\alpha|\tau) \end{pmatrix} \quad (4)$$

With

$$\alpha = \hbar^{-1} [(\eta k_z - \beta \langle k_y^2 \rangle k_x) + i(\eta k_x - \beta \langle k_y^2 \rangle k_z)]. \quad (5)$$

This shows that the evolution of the spin polarization vector is equivalent to a rotation determined by the direction of the electron momentum.

Using this simulator, we investigated the spin dynamics across the channel of an  $\text{In}_{0.3}\text{Ga}_{0.7}\text{As}$  MOS-FET (Fig. 1). The device we study is similar to the Datta-Das spin-FET [3] except that only the source



# International Workshop on Computational Nanotechnology

electrode is ferromagnetic. We simulated the effects of varying both the drain and gate biases and the application of mechanical strain. The simulation results are interesting because they suggest that the polarisation of the electrons initially decays as they traverse the device, as expected, but partially recovers as the electrons approach the drain (see Fig. 2a).

As the drain electrode was deliberately chosen to be non-magnetic, the recovery of the magnetization cannot be attributed to existing polarized carriers inside the drain but must be assumed to be due to partial re-phasing of electron spins resulting in a net magnetization. Finally the decay and the recovery depend on the gate voltage (Fig. 2b) and can therefore be controlled we also see a similar dependence on the applied strain which has the potential to be used in the operation of a nanoscale strain sensor.

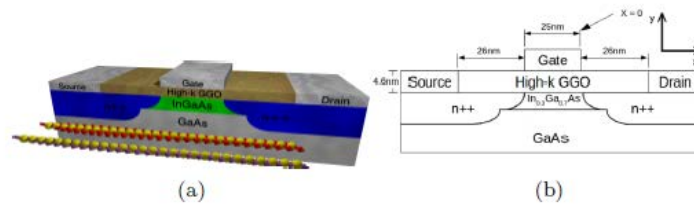


Figure 1: (a) 3D model of  $\text{In}_{0.3}\text{Ga}_{0.7}\text{As}$  MOSFET showing spin polarization of electrons along  $n$ -channel with 4% strain in the [001] direction (Red) and unstrained (Purple). (b) Schematic of  $\text{In}_{0.3}\text{Ga}_{0.7}\text{As}$  MOSFET.

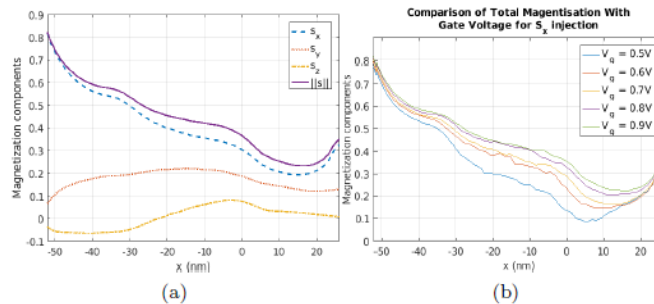
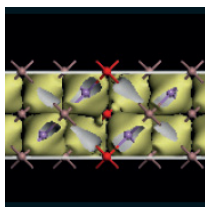


Figure 2: (a) Magnetisation components vs. position along the channel (averaged over 10 runs) taken for  $S_x$  injection at  $t = 8ps$ , i.e., after a steady state was reached. (b) Total magnetisation versus position at  $t = 8ps$  with different gate voltages ( $V_g$ ) and a fixed source-drain voltage ( $V_d$ ) of 0.9 V.

- [1] D. D. Awschalom, L. C. Bassett, A. S. Dzurak, E. L. Hu, and J. R. Petta, "Quantum spintronics: Engineering and manipulating atom-like spins in semiconductors," *Science*, vol. 339, no. 6124, pp. 1174–1179, 2013.
- [2] S. Wolf, D. D. Awschalom, R. A. Buhrman, J. M. Doughton, S. von Molnár, M. L. Roukes, A. Y. Chtchelkanova, and D. M. Treger, "Spintronics: A spin-based electronics vision for the future," *Science*, vol. 294, no. 5546, pp. 1488–1495, 2001.
- [3] S. Datta and B. Das, "Electronic analog of the electrooptic modulator," *Applied Physics Letters*, vol. 56, no. 7, pp. 665–667, 1990.
- [4] S. Sugahara and M. Tanaka, "A spin metaloxidesemiconductor field-effect transistor using half-metallic-ferromagnet contacts for the source and drain," *Applied Physics Letters*, vol. 84, no. 13, pp. 2307–2309, 2004.
- [5] "International technology roadmap for semiconductors (ITRS)." <http://www.itrs2.net/2013-itrs.html>, 2013.
- [6] M. Shen, S. Saikin, M.-C. Cheng, and V. Privman, "Monte carlo modeling of spin fets controlled by spinorbit interaction," *Mathematics and Computers in Simulation*, vol. 65, pp. 351–363, 2004.



## International Workshop on Computational Nanotechnology

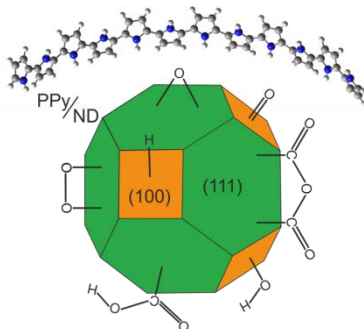
### P:33 Computing interfacial properties of polypyrrole on diamond nanoparticles for photovoltaic applications

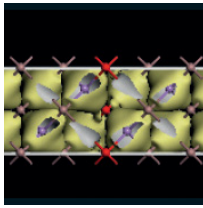
Petra Matunová<sup>1,2</sup>, Vít Jirásek<sup>1</sup>, Bohuslav Rezek<sup>1,2</sup>

<sup>1</sup>Institute of Physics of the Czech Academy of Sciences, Czech Republic, <sup>2</sup>Czech Technical University, Czech Republic

Low-cost and high-efficiency renewable energy is nowadays increasing in importance [1]. Diamond-based inorganic-organic hybrid systems may have an immense, yet still mostly unexplored potential in photovoltaic solar cells. That was suggested for instance by previously measured transfer of photo-generated charge between bulk diamond and polypyrrole (PPy) [2–4] or other organic molecules [5]. In this work, we focus on studying interactions of PPy with diamond nanoparticles (so-called nanodiamonds - NDs) by computational methods in order to reveal and better understand effects possibly brought about by the nanoscale features. Density functional theory (DFT) is employed, particularly the B3LYP functional and the 6-31G(d) basis set are used. We compare PPy in chemisorbed and physisorbed configurations on the most probable (111) and (100) ND surface slabs [6,7], having the most common hydrogen-terminated surfaces [8], as well as frequently present oxygen, hydroxyl, carboxyl, and anhydride terminated surfaces. Consistently for hydrogenated and oxidized ND surfaces, calculated binding energies ( $E_B$ ) indicate exothermic and endothermic character for physisorbed and chemisorbed structures, respectively. For the oxidized ND surfaces, though, the analysis reveals significant role of hydrogen bonds in the physisorption of PPy. In some cases, we obtain more positive values, up to 4.44 eV for physisorbed structures (for PPy on peroxide-terminated  $1 \times 1$  (111) ND surface slab) and up to -0.90 eV for chemisorbed structures (for 1-bond contact of PPy on epoxide-terminated  $2 \times 1$  (111) ND surface slab). Generally, the one-bond contact is energetically more favorable than the two-bond contact. Interaction energies ( $E_{int}$ ) confirm covalent and non-covalent bonds for all the chemisorbed and physisorbed structures, respectively. Charge transfer ( $\Delta q$ ) is observed for all the interfacial structures. The highest charge transfer was obtained for PPy physisorbed on peroxide-terminated  $1 \times 1$  (111) ND surface slab ( $\Delta q = 0.23 e^-$ ). For the hydrogen-terminated NDs, the charge transfer is the most pronounced in the case of one-bond contact of PPy chemisorbed on  $1 \times 1$  (111) ND surface slab ( $-0.11 e^-$ ). Moreover, in a significant number of cases we obtain a spatial separation of HOMO and LUMO at the interface, which seems promising for photovoltaic applications. Simulations addressing an amorphous carbon layer on the surface are beyond the scope of this work. However, they are already in progress in order to model detonation nanodiamond (DND) particles more appropriately. For a better understanding of the observed phenomena and further improvement of the models, simultaneous experimental work is being done, for instance corroborating the bonding character between PPy and NDs [9].

Figure: Schematic of truncated octahedral ND functionalized with various oxygen-containing groups, and PPy chain adsorbed on the surface. (111) ND facets are in green, (100) ND facets are in orange, C atoms of PPy are in gray, H atoms of PPy are in white, and N atoms of PPy are in blue.





## International Workshop on Computational Nanotechnology

- [1] B. R. Saunders and M. L. Turner, *Adv. Colloid Interface Sci.* 138, 1 (2008).
- [2] B. Rezek, J. Čermák, A. Kromka, M. Ledinský, and J. Kočka, *Diam. Relat. Mater.* 18, 249 (2009).
- [3] P. Galář, J. Čermák, P. Malý, A. Kromka, and B. Rezek, *J. Appl. Phys.* 116, 223103 (2014).
- [4] B. Rezek, J. Čermák, A. Kromka, M. Ledinský, P. Hubík, J. J. Mareš, A. Purkrt, V. Cimrová, A. Fejfar, and J. Kočka, *Nanoscale Res. Lett.* 6, 1 (2011).
- [5] Y. L. Zhong, A. Midya, Z. Ng, Z.-K. Chen, M. Daenen, M. Nesladek, and K. P. Loh, *J. Am. Chem. Soc.* 130, 17218 (2008).
- [6] H. Yang, L. Xu, C. Gu, and S. B. Zhang, *Appl. Surf. Sci.* 253, 4260 (2007).
- [7] D. Petrini and K. Larsson, *J. Phys. Chem. C* 112, 3018 (2008).
- [8] P. Matunová, V. Jirásek, and B. Rezek, *Phys. Status Solidi A* 213, 2672 (2016).
- [9] D. Miliáieva, S. Stehlik, P. Stenclova, and B. Rezek, *Phys. Status Solidi A* 213, 2687 (2016).

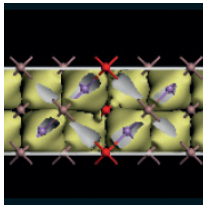
### P:34 Wigner modelling of surface roughness in quantum wires

P Ellinghaus, J Weinbub, M Nedjalkov, and S Selberherr

TU Wien, Austria

Aggressively scaled Moore devices, such as FinFETs and nanowire transistors, are designed around the concept of spatial confinement, where electrons are not point-like particles with a continuous spectrum of the momentum: The finite electron size precludes - according to the Heisenberg principle - a well-determined momentum component. Physical processes are usually modelled by a decomposition of the problem into transport and eigenvalue tasks. In quantum wires, the transport is along the wire, where homogeneous conditions are assumed, while the eigenvalue problem in the transverse plane is posed in terms of eigenfunctions and energy subbands. Within this approach shape variations (e.g. roughness) are treated as perturbations which give rise to scattering. Scattering probability models based on the Fermi Golden Rule depend explicitly on the in-plane eigenfunctions, while the subband energies appear in the energy conserving delta function. The eigenvalue problem can be solved either for an ideal wire or with account for the rough interface [1]. A statistical averaging is performed, which gives rise to a roughness-aware, but homogeneous model as long as the probability is independent of the position along the wire. The electron dynamics is captured by the long-time limit of the electron-surface potential interaction process.

In this work, we use the Wigner function approach to simulate the time-dependent electron dynamics in the presence of surface potential variations. The generic process is tunnelling; no artificial borders are introduced. Identical, minimum uncertainty Wigner states [2]  $f_w = N \exp\{(r - r_0)^2 / \sigma^2\} \exp\{(k - k_0)^2 2\sigma^2\}$  are periodically injected, with  $r_0$  centered in the source contact of the wire and  $\sigma_{x,y} = 2nm$ , corresponding to the equilibrium distribution around  $k_0$  with the effective mass  $m^* = 0.19$  at  $T = 300K$ . A signed particle method [3][4] with coherence length  $L_x = L_y = 45nm$  is applied. The behavior of currents and densities in the time domain provides rich information about the involved physics. Figure 1 shows an initial penetration in the walls, until the potential modifies the initial distribution with the evolution of the electrons along the channel. The current, calculated with the Ramo-Shockley theorem, linearly increases due to the  $5fs$  periodic injection of electron states. After  $400fs$ , steady-state conditions are reached. Figure 2 compares densities of the ideal and the rough wire. The latter is obtained by superimposing variations of the potential with a correlation function  $L_0 \exp\{\Delta x / c_l\}$  [5] on the ideal geometry. The assumption for homogeneous conditions is challenged in both cases, in particular the source and drain regions are well identified in the ideal case. Figure 3 shows the current evolution in the time domain for three different values of  $k_{o,y}$ . States with a higher  $k_{o,y}$  travel faster, therefore a steady-state is reached earlier. Moreover, the



# International Workshop on Computational Nanotechnology

effect of the surface roughness is also less pronounced. The difference of the wave vector probability distributions (cf. Figure 4) shows both a reduction of the probability for high  $k$  values and the existence of negative  $k$  values due to the quantum reflection caused by the rough potential.

We conclude that the homogeneous conditions may be disturbed in considerable parts near the wire contacts, when the system is open. The effect of the non-ideal surfaces depends not only on the geometry of the wire, but also on the boundary conditions imposed on the electron system.

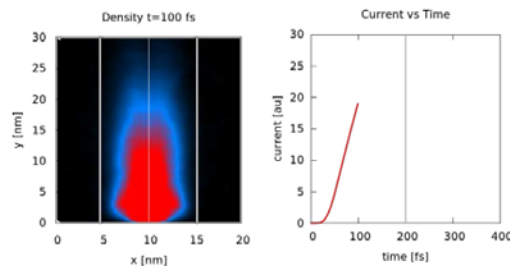


Figure 1. 100 fs evolution of density and current. The 5nm wide 0.8eV potential walls smoothly drop to zero for a distance of 2nm towards the middle of the channel. The electron states are centered around  $r_0$  given by  $x = 10\text{nm}, y = 0\text{nm}$ . Tunnelling is the only process which controls the penetration of the electrons into the walls.

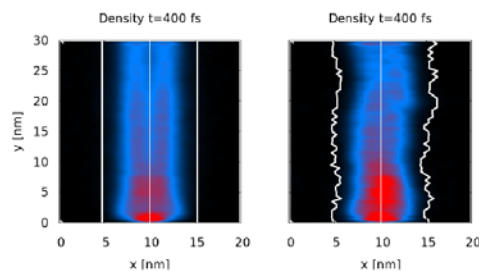


Figure 2. After 400 fs evolution the system reaches steady-state. The potential variations are characterized by a mean offset of 0.5nm and a correlation length of 5nm. The density is homogeneous in the middle half of the ideal wire.

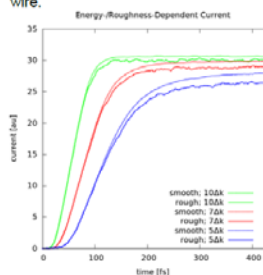


Figure 3. Current evolution for different values of  $k_{0,y}$ ;  $\Delta k$  corresponds to 1meV.

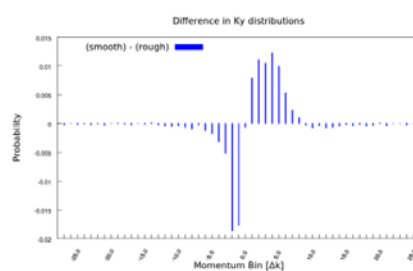
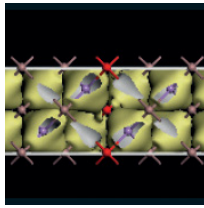


Figure 4. Difference of the ideal and rough wave vector distributions in transport direction.

**Acknowledgments.** We acknowledge funding from the EU SUPERAID7 project 688101. The financial support by the Austrian Federal Ministry of Science, Research and Economy and the National Foundation for Research, Technology and Development is gratefully acknowledged. The computational results have been achieved using the Vienna Scientific Cluster (VSC).

- [1] S. Jin, M. Fischetti, and T. Tang, J. Appl. Phys. 102, 083715 (2007)
- [2] D. Querlioz and P. Dollfus, Wiley-ISTE, ISBN: 978-1-84821-150-6 (2010)
- [3] M. Nedjalkov, D. Querlioz, P. Dollfus, and H. Kosina, in: Springer, ISBN: 978-1-4419-8839-3 (2011)
- [4] P. Ellinghaus, PhD Thesis, <http://www.iue.tuwien.ac.at/phd/ellinghaus/> (2016)
- [5] S. Goodnick and D.K. Ferry, Phys. Rev. B 32, 8171 (1985)



# International Workshop on Computational Nanotechnology

## NEGF through finite-volume discretization

M Thesberg and [H Kosina](#)

TU Wien, Austria

As device sizes have been pushed to the nanometers, the need for numerical methods capable of describing the more quantum-mechanical nature of flow at those scales has become pressing. The Non-Equilibrium Green's Function (NEGF) method has filled this need nicely, with its capacity to describe both the ballistic and diffusive transport regimes, as well as all regimes in between.

Most common implementations of the NEGF approach are done using the Finite-Difference Method (FDM) on uniform grids. This discretization scheme allows one to study many types of planar devices, such as MOSFETs, superlattices and planar heterojunctions. Within this paradigm, carrier scattering can be included through the self-energy approach, almost always under the assumption of local interaction, and a number of specialized numerical schemes have been developed, such as the Recursive Green's Function (RGF) method, to solve the resulting linear algebra in an efficient manner.[1]

However, there are a number of important fields of nano-technology where the nano-structures of interest are decidedly non-planar. Examples include: thermoelectrics, where nano-granular systems are of interest; so-called invisible dopant or shell-antishell systems with spherical structures; and systems of nano-inclusions or nano-voids, which have a number of applications. In these systems, a numerical approach capable of handling incoherent and coherent transport on structures of generic shape is required.

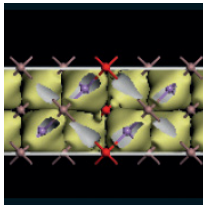
In this talk, we will present work on an implementation of the NEGF method using a Finite-Volume Method (FVM) approach, capable of describing: unstructured-grids, carrier scattering at the self-energy level, anisotropic effective masses, and coupling with classical partial differential equations of charge (i.e. Poisson's equation) and heat (i.e. Fourier's law) within the same discretization scheme.

Here we introduce an extension of the Vienna Schroedinger-Poisson (VSP) solver[2] adapted for the NEGF approach, with electron-phonon scattering, within the effective mass model. Discretization is based on an element-based FVM approach, which is ultimately derived from a conservation law formalism and thus guarantees charge conservation at each element. This makes it well suited for the treatment of anisotropic flow. An important aspect of the solver is the treatment of the open-boundary and the derivation of the appropriate form of the contact self-energy, which although well known for FDM and FEM approaches,[3] requires special consideration for FVM.

Furthermore, the use of an FVM approach allows for seamless coupling with not just a Poisson's equation treatment of charge, but a Fourier's law treatment of classical heat flow.

During the talk specific examples, drawn from the field of nano-structured thermoelectrics, demonstrating both: decoherence of flow, with increasing electron-phonon scattering strength, in non-planar structures; as well as the results for a coupled "quantum charge" - "classical heat" transport simulation, indicating self-heating effects. will be explored.

This talk will discuss new results from the extension of the Vienna Schroedinger-Poisson (VSP) solver to include the NEGF model on unstructured-grids within a Finite-Volume discretization approach, with electron-phonon scattering and the ability to seamlessly couple with classical heat flow equations.



# International Workshop on Computational Nanotechnology

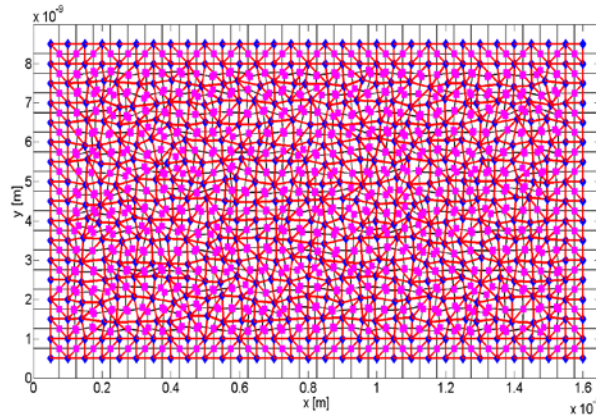


Fig. 1. Sample, random unstructured mesh of arectangular 15 nm by 7.5 nm channel. The blue diamonds represent vertices, or the defined system points. From them Voronoi cells are constructed (black) and divided into triangles (i.e. 2D simplices), which form the base element of the approach. Pink squares represent the circumcenters of these elements. The shown grid is intentionally randomized in order to demonstrate a non-uniform grid.

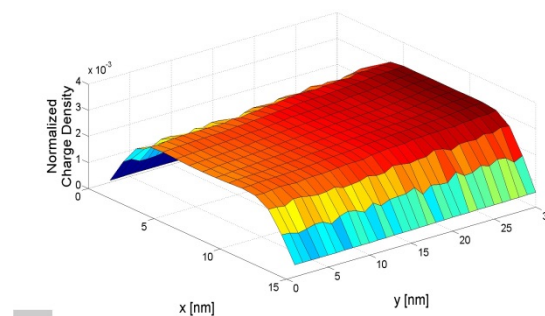


Fig. 2. Normalized charge density for the same grid, showing a flat well behaved distribution of charge in the confined channel.

- [1] Lake, R., Klimeck, G., Bowen, R.C. and Jovanovic, D.,1997. Single and multiband modeling of quantum electron transport through layered semiconductor devices. *Journal of Applied Physics*, 81(12), pp.7845-7869.
- [2] Baumgartner, O., Stanojevic, Z., Schnass, K., Karner, M. and Kosina, H., 2013. VSP—a quantum-electronic simulation framework. *Journal of Computational Electronics*, 12(4), pp.701-721.
- [3] Jiang, H., Shao, S., Cai, W. and Zhang, P., 2008. Boundary treatments in non-equilibrium Green's function (NEGF) methods for quantum transport in nano-MOSFETs. *Journal of Computational Physics*, 227(13), pp.6553-6573.

**Institute of Physics**

76 Portland Place, London W1B 1NT, UK

Telephone: +44 (0)20 7470 4800

**[www.iop.org/conferences](http://www.iop.org/conferences)**

Registered charity number 293851 (England & Wales) and SC040092 (Scotland)